The novel role of cyclic GMP-mediated autophagy induction

By:
Ben Aden Phillips

A thesis submitted in partial fulfilment of the requirements for the degree of
Doctor of Philosophy

The University of Sheffield
Faculty of Science
Department of Biomedical Science

Submission Date
14th March 2021

darkest place I thought I would never leave, and will continue to help me for years to come. And thank you to my mentor, Amanda Marples. Our weekly meetings were the highlight, from the conversations about neon hair dyes and skateboarding, to venting about my dot-counting-related meltdowns (sorry!). But most importantly, you reminded me how to believe in myself when I didn't think I could.

Finally, I would like to thank those who have provided love and support over the years, and helped shape me into the person I am. To my sister, Carrie, for the late night Netflix binges, letting me puppy-sit Ivor, and the many Pokémon adventures. To my friends, Louise, Eve and Carly, for the trips to pub to unwind, the forest raves, letting me befriend all your cats, and being my anchors through many storms. To Helen for all the festival adventures, and sharing my love of a well presented graph. To Lexie and Roadkill for all the gigs, parties and listening to my rants about failed experiments. To Myles for his infectious optimism, and our excursions around Yorkshire. To Maureen Harris, for the impromptu champagne and Gay Disco parties, and forgiving me when I stained her kitchen red with Glühwein. To Lawrence and Maureen Peachey for the many words of wisdom and encouragement. Friends are the family you chose, and I am so fortunate to have been chosen by such amazing people.

Acknowledgements Part 2 – The Pandemic Special

It is customary for New Year celebrations to come with resolutions for the upcoming year: to eat healthier food, to drink less alcohol, to start going to the gym. One of the few highlights of 2020 was a valid excuse to break them all, particularly the gym because you couldn't leave the house. The Covid-19 pandemic spread worldwide, bringing with it fear and uncertainty, upheaval of all aspects of our lives, and widespread suffering and death. In spite of this turmoil, there were individuals who took it upon themselves to adapt to this "new normal" and, through online events, bring both hope and happiness into the lives of others.

Thank you to Mark Haigh (aka DJ Kark) and Peter Sawyer (aka DJ Peewee), the two parts of the DJ duo Karkasaurus. They organised and ran multiple events throughout the pandemic, providing an online platform for people to socialise and enjoy music while stuck indoors and live-music venues had to close. In addition, they raised money for several charities in the process, such as Beat:Cancer, making their efforts all the more noteworthy. A personal favourite was their regular GRRRadio event, which introduced me to new music and DJs (who are also all amazing!), and reminded me that not everything in the world is awful. Because no matter how bad things get, they can always be improved with dancing and dinosaurs.

Thank you to Lee Holder (aka DJ Lee Chaos) and Tes Matthews (aka DJ Duracell Bunny) who together created the Chaos Emergency Doof Broadcast, a weekly online event and another platform for people to connect and socialise. While writing, this event is ongoing and they're close to their 100th show. They have both hosted and participated in multiple online events, also raising money for charity in the process. They have brought limitless entertainment and amusement, from trash-wine anthems to kazoo interludes, and have never failed to brighten my day. And I solemnly swear no maths was done during your sets or events.

Thank you to those who unknowingly contributed to my sanity during this chaotic period, and also to everyone else who rose to this challenge in providing respite from reality.

Abstract

Macroautophagy (hereafter autophagy) is the process through which portions of the cytosol are sequestered within double-membrane bound autophagosomes. Captured cytosolic contents are subsequently delivered to lysosomes for catabolic degradation. Under optimal growth conditions, autophagy functions to maintain homeostasis through removal of protein aggregates, degradation of long-lived proteins, and recycling of excess organelles, to name a few. Under sub-optimal conditions, autophagy can be rapidly induced and functions as an adaptive mechanism to promote cell viability. The best documented stimulator of autophagy is nutrient deprivation, which acts via the canonical signalling pathway involving mechanistic Target of Rapamycin (mTOR) and AMPK. Additional, autophagy modulating, upstream signalling pathways have been described, which include Akt/PKB, MAPK/ERK1 and p53. A diverse array of environmental stressors have also been reported to affect autophagy, many of which utilise these established canonical pathways.

Compressive force has been shown to induce autophagy in both the soil dwelling amoeba, *Dictyostelium discoideum*, and mammalian cells. In both instances, the autophagic response was proportional to the force magnitude and greater than nutrient starvation induction. However, involvement of established autophagy signalling proteins was ruled out, indicating signalling occurred via an unknown non-canonical mechanism. Currently, the underpinning signalling pathways linking mechanical stimulation and autophagy remain elusive. Using *D. discoideum*, we present novel findings that sustained compression can stimulate production of the secondary messenger cyclic GMP (cGMP). Furthermore, the membrane-permeant cGMP analogue (8Br-cGMP) potently induced autophagy in a dose-responsive manner similar to compression. As hyper-osmotic stress (hyper-OS) drives cGMP production, this stimulus was tested and shown to elicit a strong, dose-dependent, autophagic response similar to compression. For both stimuli, however, cGMP signalling was dispensable as autophagy was unaffected by ablation of guanylyl cyclases or the cGMP-regulated kinase, GbpC. While the signalling pathway(s) linking mechanical compression with autophagy induction remain elusive, our findings do, however, highlight a previously unreported mechanism. Subsequent phosphoproteomic analysis has provided candidate proteins which could facilitate this cGMP-induced autophagy. Clearly, the complex web of signalling pathways affecting autophagy is not yet fully resolved. Our findings add to the growing repertoire of stressors which modulate autophagy, and provide promising avenues for future research.

Contents

Chapter 1

Introduction

1.1 Autophagy

Macroautophagy (hereafter autophagy) is the process whereby cytosolic material is degraded in bulk. First described in 1960 and subsequently reviewed later that decade (De Duve and Wattiaux, 1966), autophagy was understood to be a constitutive, homeostatic process which maintained cell viability. This remained the case until seminal work in the budding yeast, *Saccharomyces cerevisiae*, identified core autophagy protein genes (Funakoshi *et al.*, 1997; Matsuura *et al.*, 1997), ultimately securing a Nobel Prize in Medicine in 2016. Since the discovery of these core autophagy genes (initially called Apg but referred to now as Atg), autophagy is known to be a dynamic process which can be activated in response to a host of stressors. This has led to an explosion of research into the degradative pathway, with autophagy now being attributed to a range of pathological diseases and disorders in both agonistic and antagonistic contexts, in addition to cell maintenance and survival.

Autophagy involves the sequestration of cytoplasmic material of varying size within a double membrane vesicle called an autophagosome. Captured material can include proteins, complexes and aggregates, as well as whole organelles. Once encapsulated, the autophagosome is delivered to the lysosomal machinery and the luminal contents are degraded by hydrolytic enzymes (Figure 1.1A-C). Other variations of autophagy exist regarding content delivery mechanisms, and specialisations relating the degraded cargoes. Micro-autophagy involves small-scale degradation of cytoplasm by invagination of lysosomal membrane (Kunzt *et al.*, 2004), whereas chaperone-assisted autophagy (CASA) delivers misfolded proteins directly to degradative machinery (Cuervo and Dice, 2000; Salvador *et al.*, 2000). Specialised autophagy processes specific to selective cargoes also exist, such as mitophagy (mitochondria), xenophagy (intracellular pathogens), and pexophagy (peroxisomes), to name a few. These processes all impinge on a tightly regulated, systematic pathway for the capture, degradation and ultimate recycling of biomolecules (Figure 1.1D).

1.1.1 Autophagy mechanisms and core machinery

The autophagic process has been identified in almost all eukaryotic organisms, ranging from yeast, plants and amoeba, to mammalian organisms. Both genomic and experimental approaches indicate the core autophagic machinery is highly conserved across organisms (Yang and Klionsky, 2010). Due to the many genes involved, and the degree of conservation across divergent species, autophagy likely arose from an evolutionarily ancient common ancestor rather than independent parallel evolution events. Some specialisations have been noted, however, such as in budding yeast which contains additional Atg genes not present in other species (King, 2012). The system involves several key complexes which drive the initiation and nucleation of the phospholipid phagophore, followed by two ubiquitin-like conjugation reactions which drive phagophore membrane expansion and eventual closure prior to delivery (Figure 1.1).

Initiation is driven by the ULK/Atg1 complex which mediates the early stages of autophagy. In *Dictyostelium*, this is composed of Atg1 (Otto *et al.*, 2003), Atg13 (Mesquita *et al.*, 2015) and Atg101 (Mesquita *et al.*, 2015). In mammalian cells, this complex is composed of the central Atg1 protein, called

2
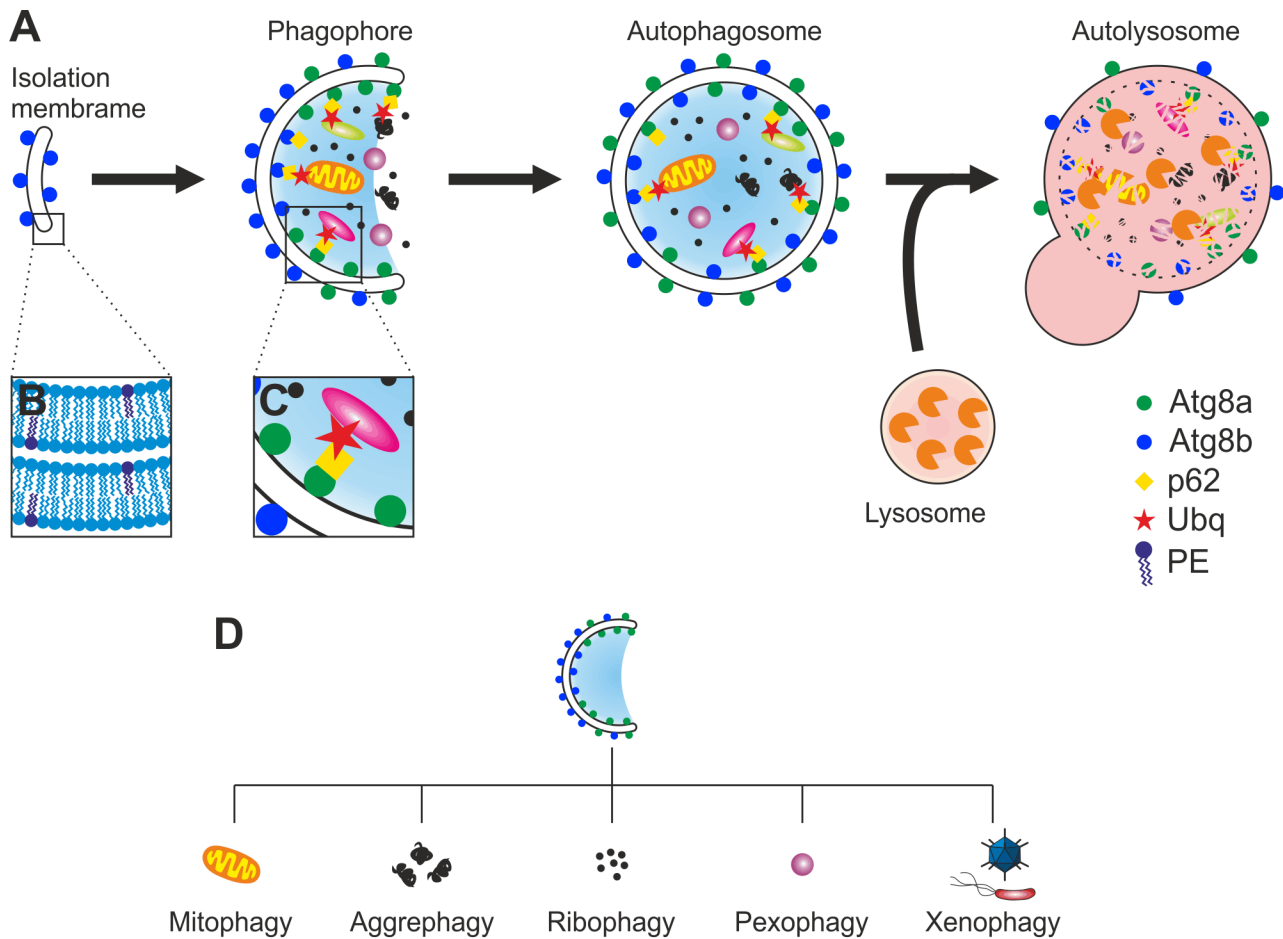
Figure 1.1 **Schematic depiction of autophagy and cargo-specific forms.** (A) Autophagosome biogenesis begins with the *de novo* formation of the isolation membrane, a double phospholipid bilayer (B) with Atg8b attached to phosphatidylethanolamine (PE) lipids. As membrane is delivered, the membrane expands to a phagophore, at which point Atg8a associates, also covalently linked to PE. Cargo ear-marked for degradation, e.g. ubiquitinated protein linked to Atg8 via p62 adaptor protein (C), gets loaded into the developing lumen. Content may include random portions of cytosol containing proteins, aggregates or small organelles. The phagophore then closes to form an autophagosome with a contained lumen. This subsequently fuses with lysosomes, which deliver catabolic enzymes, forming an autolysosome. The autophagosome lumen pH becomes acidic, and the catabolic enzymes degrade the inner membrane bilayer and lumenal contents. Catabolised content is then recycled. (D) Autophagy can degrade specific cargos, rather than random portions of the cytosol. Some examples are shown with the respective terminology.

ULK for Unc-51-like kinase, along with Atg13, Atg101 (Mercer *et al.*, 2009) and focal adhesion kinase family interacting protein of 200kDa (FIP200; Hara *et al.*, 2008). Currently, there is no known FIP200 homologue in *Dictyostelium*. When knocked out, the putative *Dictyostelium* FIP200 gene identified by bioinformatics (Calvo-Garrido *et al.*, 2010) presented an inconsistent phenotype to FIP200 knockouts in other model organisms and was subsequently renamed autophagy regulator B (AreB; Mesquita *et al.*, 2015). The yeast complex also has a similar architecture, comprising Atg1, Atg13 and Atg17 (homologue of FIP200), but lacks Atg101.

Atg1 is a serine/threonine protein kinase first identified in yeast and shown to be involved in the autophagic process (Matsuura *et al.*, 1997). Soon after, mammalian Atg1 homologues Unc-51-like kinase (ULK) 1 and 2 were uncovered in humans (Kuroyanagi *et al.*, 1998) and mice, and later the *D. discoideum* *atg1* gene was identified (Otto *et al.*, 2004). While the *C. elegans* homologue Unc-51 had been identified earlier (Ogura *et al.*, 1994), its role in autophagy was not determined until comparisons were drawn with

yeast Atg1 (Matsuura *et al.*, 1997). Across these varied organisms, the Atg1 proteins show high levels of conservation (Mizushima, 2010). In mammalian systems, siRNA knockdown showed ULK1 was essential for autophagy whereas ULK2 was dispensable (Chan *et al.*, 2007). Subsequent research, however, has shown that ULK2 does contribute to autophagy and exhibits redundancy (Hara *et al.*, 2008; McAlpine *et al.*, 2013).

In budding yeast, Atg13 is repressed by hyper-phosphorylation under nutrient rich conditions (Kamada *et al.*, 2000). Upon starvation this is inhibited, resulting in Atg13 dephosphorylation which allows it to associate with Atg1 (Abeliovich *et al.*, 2000; Kamada *et al.*, 2000, 2010). Atg17 subsequently binds to Atg13, which contains two binding regions within its intrinsically disordered region (Yamamoto *et al.*, 2016), forming a multimeric complex (Kabeya *et al.*, 2005). Atg1 kinase activity is increased in an Atg13 and Atg17-dependent manner (Kamada *et al.*, 2000), and trans-phosphorylation of Atg1 occurs. In this respect, Atg1 has both kinase-dependent and independent functions during autophagy initiation (Cheong *et al.*, 2005).

In mammalian cells, the Atg1 complex composition and process of activation is slightly different. It contains Atg1 (Young *et al.*, 2006), Atg13 (Ganley *et al.*, 2009; Mercer *et al.*, 2009), Atg101 (Hosokawa *et al.*, 2009; Mercer *et al.*, 2009) and FIP200 (Hara *et al.*, 2008), and which are associated under basal conditions, but regulated by phosphorylations (Puente *et al.*, 2016). Under basal conditions both Atg1 and Atg13 are inhibited by phosphorylation. When nutrients become limited, inhibitory phosphorylations are blocked and Atg1 becomes activate. This permits phosphorylation of both Atg13 and FIP200 (Ganley *et al.*, 2009), in addition to autophosphorylation (Chan *et al.*, 2009). Atg13 was first characterised by (Chan *et al.*, 2009) and subsequently shown to be essential for Atg1-kinase function (Hosokawa *et al.*, 2009; Jung *et al.*, 2009).

The Atg1 complex in *Dictyostelium* is more similar to the mammalian ULK, than the yeast Atg1, complex. The complex contains the Atg1 kinase (Otto *et al.*, 2004), Atg13 (Mesquita *et al.*, 2015), Atg101 (Calvo-Garrido *et al.*, 2010; Mesquita *et al.*, 2015) and the current putative FIP200 homologue DDB_G0285767 (Figure 1.2; Mesquita *et al.*, 2015). Atg13 interacts with both Atg1 and Atg101, with the latter stabilising Atg13 (Mesquita *et al.*, 2015). It is unknown whether *Dictyostelium* Atg13 is hyper-phosphorylated under nutrient-rich conditions as observed in yeast. In higher eukaryotes, Atg1 is able to interact with Atg13 regardless of phosphorylation status (Hosokawa *et al.*, 2009; Jung *et al.*, 2009) although potential dephosphorylation may be masked by alternative, Atg1-mediated, phosphorylations (Chang and Neufeld, 2009).

Once active, the Atg1 complex can phosphorylate Atg6 (Beclin-1) which is part of the phosphatidylinositol 3-kinase (PI3K) complex and involved in the nucleation stage. The PI3K complex is comprised of Atg6, Atg14, Vacuolar Protein Sorting (Vps) 34 and Vps15; the latter which is membrane tethered. In yeast, Vps34, 15, 14 and 30 (Atg6) for the class III PI3K complex and all components are essential for autophagy (Kihara *et al.*, 2001). Class III PI3K activity has been reported as essential in several organisms (Lindmo and Stenmark, 2006), therefore it is expected orthologues will exist in *Dictyostelium* however not all have been identified. Generation of phosphatidylinositol-3-phosphate (PI3P), catalysed by Vps34, is essential for
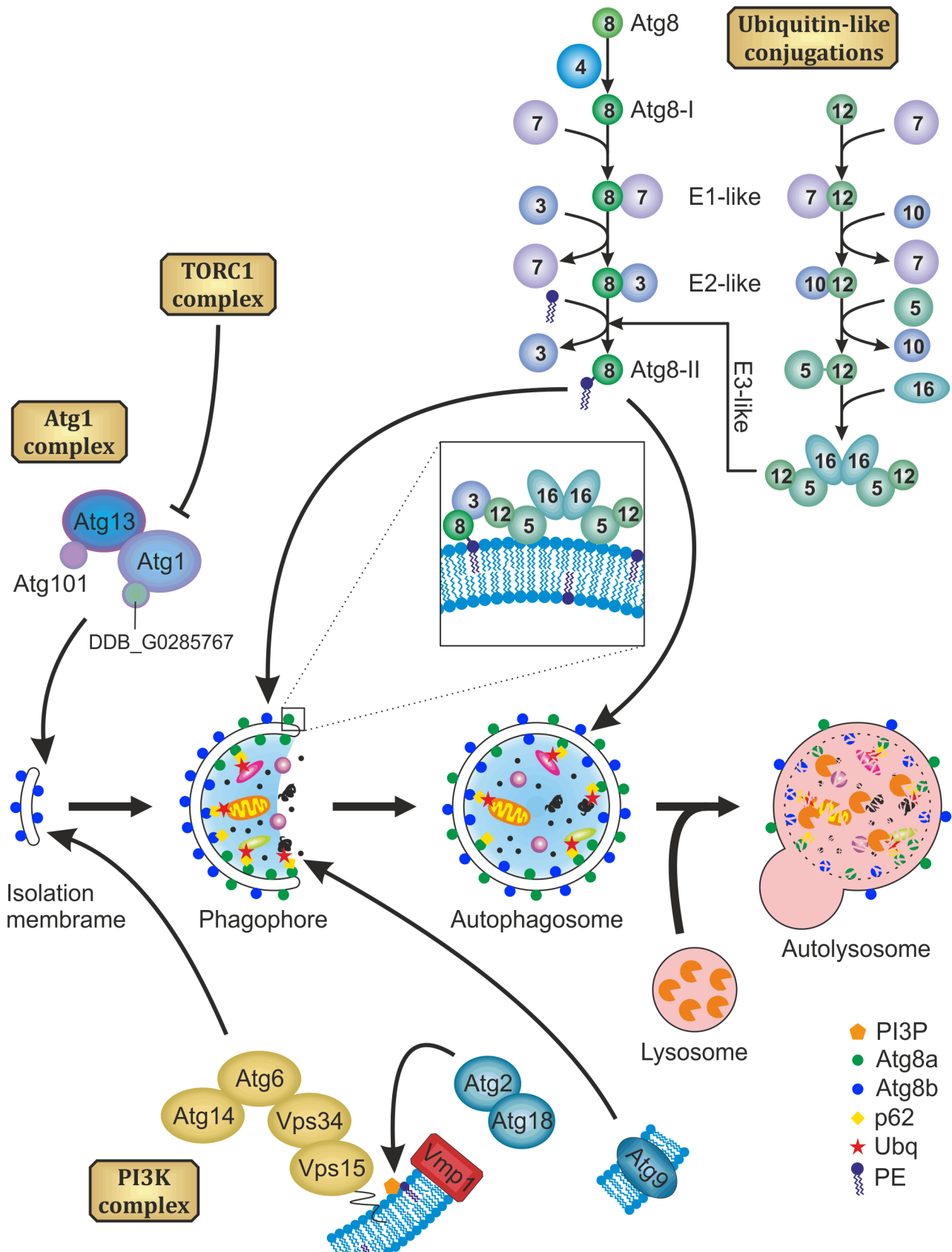
Figure 1.2 **Schematic depiction of autophagosome formation**. Once inactive, TORC1 no longer inhibits the Atg1 complex. Atg1 kinase activity drives initiation of autophagosome biogenesis, including phosphorylation of Atg6 (Beclin-1). Part of the Class III PI3K complex, Vps34 phosphorylates phosphatidylinositol generating PI3P. This recruits Atg2-Atg18 which, along with the PI3K complex and Vmp1, drives nucleation and expansion of the isolation membrane. Transmembrane Atg9 delivers membrane to facilitate elongation of the phagophore. The ubiquitin-like conjugation reactions form two branches: formation of the Atg12~5/12 complex, and conjugation of Atg8 to phosphatidylethanolamine (PE). Atg8-PE is embedded within the membrane of the phagophore. Upon lysosomal fusion, contents are degraded. External Atg8-PE is cleaved by Atg4, liberating the Atg8 protein.

recruitment of Atg2-Atg18, which are required for correct formation of the omegasome (Obara *et al.*, 2008). The only transmembrane protein, Atg9, and vacuole membrane protein 1 (Vmp1) are involved in membrane delivery and PI3P signalling (Calvo-Garrido *et al.*, 2008, 2010; Calvo-Garrido, King, Muñoz-Braceras, *et al.*, 2014; Tung *et al.*, 2010; Xie and Klionsky, 2007). Together, these elements drive elongation of the phagophore membrane until subsequent closure.

The elongation steps involve two highly conserved ubiquitin-like conjugation reactions, which have been assessed in great detail (Geng and Klionsky, 2008). The first involves binding of Atg12 to the ubiquitin activating enzyme E1-like protein Atg7. Atg7 is subsequently replaced by the ubiquitin conjugating enzyme E2-like Atg10, which facilitates the formation of a covalent linkage between Atg12 and Atg5 (hereafter referred to as Atg12~5). Atg5 possesses membrane binding ability, but this is suppressed after conjugation to Atg12 (Walczak and Martens, 2013). The Atg12~5 fusion protein then binds to Atg16 (Fujita *et al.*, 2008), and two of these multimers bind via Atg16 to form a tetramer comprising two Atg12~5/16 complexes. Association with Atg16 activates the membrane binding-capacity of Atg5, allowing the multimer to associate with the membrane of the expanding phagophore (Walczak and Martens, 2013). This complex functions as a scaffold for the subsequent Atg8 lipidation described below (Fujita *et al.*, 2008).

The second ubiquitin-like conjugation reaction functions to process the ubiquitin-like autophagy protein Atg8. Upon initial translation, pro-Atg8 is almost immediately cleaved by the cysteine protease Atg4, exposing a critical glycine residue at the C-terminus (Tanida *et al.*, 2004). The resulting Atg8-I is then sequentially processed by ubiquitin activating enzyme E1- and ubiquitin conjugating enzyme E2- like proteins Atg7 and Atg3 respectively. Atg8-I/Atg3 translocates to the expanding phagophore and binds to the Atg12~5/16 complex. Specifically, Atg3 binds Atg12, which brings Atg3 and Atg5 into close proximity, and Atg8-I adjacent to the membrane (Noda *et al.*, 2013). Atg12~5 binding to Atg3 enhances the E2-like activity of Atg3 (Sakoh-Nakatogawa *et al.*, 2013). Furthermore, the Atg12~5 conjugate exhibits ubiquitin ligase E3-like activity which drives the fusion of Atg8-I with phosphatidylethanolamine (PE; Hanada *et al.*, 2007), a phospholipid embedded in the phagophore membrane. This covalent linkage forms the membrane associated Atg8-II, which speculated to act as a scaffold for further protein binding and membrane expansion (Geng and Klionsky, 2008).

1.1.2 Physiological relevance of autophagy

Autophagy was initially attributed to the maintenance of homeostasis through degradation of long-lived proteins in the 1960's. More recently, however, it has been implicated in a host of roles and pathologies. Autophagy activation has been documented to increase lifespan in a variety of model organisms. In mice, absence of functional autophagy through knockout of core autophagy genes results in an embryonic lethal phenotype (Maria Fimia *et al.*, 2007). Disruption of autophagy has been linked to neurodegenerative disease, such as Huntingdon's and Alzheimer's, as well as heart disease (Chen *et al.*, 2014; Ochaba *et al.*, 2014; Salminen *et al.*, 2013). In Huntington's disease, it is thought that polyglutamine-expanded huntingtin (polyQ-htt) disrupts axonal transport, limiting fusion of autophagosomes and lysosomes, consequently

impairing autophagy generally which restricts the timely removal of dysfunctional mitochondria (Wong and Holzbaur, 2014). Over time, the defect progressively gets worse until neurodegeneration and cell death occurs.

In the context of cancer, autophagy is often described as a "double-edged sword" (White and DiPaola, 2009). This is due to the protective role autophagy plays in preventing initial cancer formation, and that it can be subverted by established cancer cells to aid their survival. Solid tumours are harsh environments and may lack a nutrient supply until angiogenesis occurs. Autophagy maintains cell survival under these nutrient limited, hypoxic conditions (Fujii *et al.*, 2008; Hu *et al.*, 2012; Zhao *et al.*, 2012); low oxygen triggers hypoxia-inducible-factor-1 (HIF-1) which has been shown to induce autophagy (Zhu *et al.*, 2014). Given the involvement of autophagy in so many biological processes and disease, a comprehensive understanding of this process and how it is regulated could provide novel opportunity for treatment of disease.

1.2 Studying autophagy in the model organism *Dictyostelium*

Model organisms are essential research tools that allow the study of complex processes and disease in controllable contexts. The key genes involved in autophagy were first identified in budding yeast. Subsequent studies identified such genes in a range of organisms including mammals, plants and amoeba, indicating an ancient lineage. However, with the advent of rapid genome sequencing and bioinformatics, there is growing evidence that yeast autophagy has become specialised and thus diverged from other species. Alternative model organisms, such as *Dictyostelium*, with autophagic machinery more similar to humans are therefore better suited for studying autophagy, including in context of disease.

There are several key advantages to using *Dictyostelium* to study autophagy. Firstly, *Dictyostelium* are genetically amenable as they are haploid during the vegetative cycle (one gene copy), meaning knockout and mutant lines can be produced relatively quickly. While autophagy has been studied extensively in yeast, the *Dictyostelium* Atg1 complex exhibits greater similarity to the mammalian ULK1-complex (Mesquita *et al.*, 2017). Yeast also lack Vmp1, present in both Dictyostelium and mammalian cells, which is essential for autophagy due to its role in modulating PI3P signalling (Calvo-Garrido, King, Munoz-Braceras, *et al.*, 2014; King, 2012). Both mammalian cells and *Dictyostelium* utilise lysosomes to degrade cargo, whereas yeast delivers cargo to a single vacuole (Reggiori and Klionsky, 2013). Additionally, it is suggested that yeast are an evolutionary outlier due to highly specialised variations of autophagy and the presence of multiple Atg proteins which cannot be identified in other organisms (King, 2012; Reggiori and Klionsky, 2013). Due to the many similarities between the *Dictyostelium* and mammalian autophagy machinery, coupled with the ease of genetic manipulation, *Dictyostelium* is an ideal model organism for the study of autophagy.
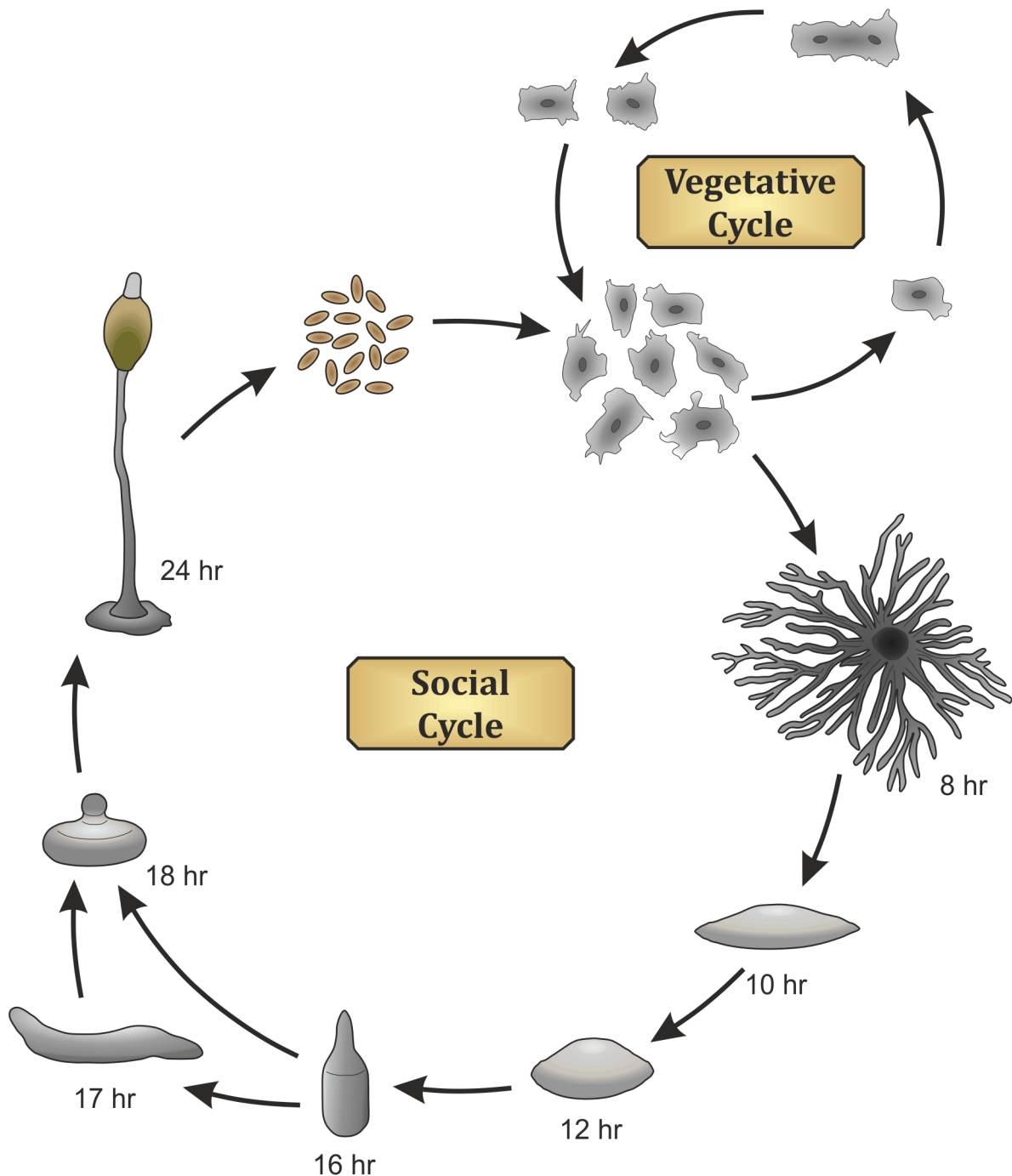
Figure 1.3 **Dictyostelium asexual lifecycle.** *Dictyostelium* populate leaf mould, soil and ponds as single cells, primarily surviving by predation and phagocytosis of bacteria. When food sources are abundant, cells exist individually within the vegetative cycle and divide by mitosis. Upon nutrient depletion, cells enter into the social cycle, comprising aggregation, migration and culmination stages. Starvation triggers production and secretion of the second messenger cAMP, which stimulates adjacent *Dictyostelium* to produce and secrete cAMP. This creates a chain-reaction resulting in generation of cAMP waves. At 5 hours, cells migrate up the cAMP concentration gradient towards the source of the chemoattractant. This aggregation continues until characteristic cell streaming occurs after around 8 hours. Aggregation areas can span 1 cm in diameter. At 10 hours, a multicellular, loose aggregate forms which then becomes a tight aggregate at 12 hours, and forms a finger at 16 hours. The finger may topple and form a slug, capable of migrating towards a site with available nutrients, or progress directly into the culmination stages. Cells form into a tipped mound structure after around 18 hours, followed by formation and elevation of the spore-containing sorus. The sorus is elevated by cells which undergo an autophagy-dependent programmed cell death process, coupled with secretion of cellulose to reinforce the structure. After 24 hours, the mature fruiting body is formed and spores are subsequently released to become independent cells.

Dictyostelium live in leaf litter, dirt and ponds, predating bacteria for food. Wild-type DH1 cells are more closely related to "wild" Dictyostelium, in that they require bacteria as a food source to survive. However there are several axenic strains, also referred to as wild-type, which are Ax2, Ax3 and Ax4. While referred to as wild-type, they are capable of surviving by macropinocytosis of liquid media due to a mutation in RasGAP NF1 (Bloomfield *et al.*, 2015). Additionally, Ax3 and Ax4 strains contain a large duplication in chromosome 2 not present in Ax2. Equally, duplications have been detected within the same strains from different labs (Bloomfield *et al.*, 2008). Both of these factors should be taken into consideration when making comparisons between results obtained from different axenic strains or wild-type stocks.

1.3 Autophagy and mechanical forces

Mechanical forces are physical motions which impact on molecules and structures. They are ubiquitous in life, affecting individual proteins through to tissues and whole organisms. The effect they cause varies, determined by multiple factors: frequency, magnitude, direction and mechanism of action. These characteristics determine whether the force is instructive, destructive or both. Regarding physiology, mechanical forces can be broadly categorised into 3 groups: compression, stretch, and fluid shear. Compression is the application of antiparallel forces which converge on a cell, reducing cell height. Stretch is the opposite of compression, with antiparallel force vectors radiating from a central cell. Fluid shear forces are borne of friction against the cell periphery, comprising the plasma membrane and extracellular matrix (ECM). How a force manifests depends on the environment and circumstance, but all have the capacity to disrupt homeostasis and prevent nominal cell function. Therefore cells must be able to detect and adapt to these physical cues to maintain viability.

In order to adapt to mechanical forces, cells need to be able to convert the strain into a chemical signal. To achieve this, a wide array of detectors can be employed, including stretch-activated ion channels, adhesion molecules, primary cilia, G-proteins and cytoskeletal tension to name a few (Ando and Yamamoto, 2013; Ingber, 1997). Cells can sense their physical environment through integrins which bind to the ECM, and act as the hub of focal adhesions (DeMali *et al.*, 2014; Geiger *et al.*, 2009; Pelham and Wang, 1997). Physical changes in integrin affect activity of signalling proteins within the focal adhesion complex, such as focal adhesion kinase, triggering signalling cascades (Katsumi *et al.*, 2004; Mitra *et al.*, 2005). Mechanical forces can be converted to biochemical signals via stretch-activated calcium ion-channels such as Piezo1 and 2 (Coste *et al.*, 2010; Maksimovic *et al.*, 2014), or deformation of cilia triggering calcium influx (Nguyen and Jacobs, 2013). Transmembrane G-protein coupled receptors (GPCRs) have also been implicated in detecting strain and initiating downstream signalling (Gudi *et al.*, 1996; Jo *et al.*, 1997). Mechanosensing is complex, capable of detecting tiny sound waves and changes in ECM tension, to the effects of mechanical strain during exercise.

Compression is the flattening of an object which reduces its height. The same is true for a cell or tissue, with internal pressures increasing as the force is applied. In large, terrestrial organisms gravity is a major contributor to compressive forces, particularly during locomotion where body weight is distributed down

the legs. This manifests a cyclic application and release of pressure. Compressive forces of this nature are essential for some biological processes, such as osteoclastogenesis mediated by periodontal ligament cells (Kanzaki *et al.*, 2002). Inflammation can generate compressive pressure which is utilised to combat infection. While beneficial, compression can also be damaging if sustained (Gawlitta *et al.*, 2007) such as with bedsores (Breuls *et al.*, 2003) or crush injuries. Detection and adaption to compression is essential for organisms which experience them. It has been shown that compression is capable of inducing autophagy in both *Dictyostelium* and mammalian cells (King *et al.*, 2011). Additional studies have confirmed a causal link between compression and autophagy in both skeletal muscle (Teng *et al.*, 2011) and nucleus pulposus cells (Ma *et al.*, 2013). Whether the underpinning signalling pathways are shared between *Dictyostelium* and mammalian cells remains unclear.

Shear forces are generated when friction occurs at a boundary or surface. Fluid shear occurs when the force is applied through a liquid medium against a solid surface. In nature various examples exist, with different forms eliciting different effects. Laminar shear force (LSS), or undisturbed flow, is a uniform flow rate where force is constant and evenly distributed across a surface. Examples include blood flow through veins accounting for around 1 Pa force (Kwak *et al.*, 2014). In lymph ducts and nephrons interstitial fluid flow generates extremely low-magnitude shear. Oscillatory shear force (OSS) involves disturbed fluid flow, where movement and subsequent force occurs in multiple directions and varying in magnitude. These arise in arches and bifurcations in the vasculature, the latter which was depicted clearly by modelling (Steinman, 2000). These variations of shear force have been shown to affect autophagy in different ways.

The literature available indicates an unclear, perhaps circumstantial, interaction between shear forces and autophagy. Earliest indications of shear regulating autophagy activity were by (Lee *et al.*, 2010) where increased phosphorylation was detected for both mechanistic Target Of Rapamycin (mTOR) and its substrate ribosomal S6 kinase (p70S6K) in osteoblast-like MG63 cells. Using a parallel plate flow chamber 0.5 ± 4 dynes/cm^2 OSS was applied and phosphorylation changes were detected between 5 min until 24 h. Published the same year similar, albeit less convincing, results were reported in vascular smooth muscle cells using an orbital shaking setup at 9.8 dynes/cm^2 (Rice *et al.*, 2010). In both instances autophagy was not explicitly mentioned however mTOR is an established negative regulator for autophagy via ULK1 phosphorylation, therefore it can be inferred autophagy was downregulated under both conditions by Lee *et al.* (2010) and Rice *et al.* (2010). On the other hand, LSS was shown to induce autophagy in a manner proportional to force applied (Lien *et al.*, 2013). They concluded the induction was mTOR1-independent, acting via Smad1/5 and p38 MAPK pathways instead of canonical pathways. Both shear forces induce differing outputs with respect to autophagy, indicating the magnitude, direction and frequency of shear forces are critical in determining the autophagic response in a cell.

Stretch forces occur when cells and tissues are pulled in opposing directions, and can occur in multiple planes. Typical examples include muscle tissues during exercise and vasculature where pulsating blood flow distort carrying vessels. One of the first papers covering stretch forces which mentioned autophagy was

published in 1971. Authors determined aged rat levator ani (LA) muscle cells contained autophagic vesicles not present in younger counterparts (Gutmann *et al.*, 1971), although a causative link between the two events was not determined. More recent studies have revealed a link between autophagy and stretch forces in both skeletal muscle during exercise (Grumati *et al.*, 2011) and trabecular meshwork cells under sustained 20% elongation (Porter *et al.*, 2014). The latter paper determined autophagy induction was mTORC1-independent and ruled out chaperone-assisted autophagy (CASA). Determining specific signalling pathways critical in autophagy induction might prove challenging given stretch has been shown to induce rapid activation of a plethora of second messenger pathways including MAP kinases, PKC and phospholipases (Sadoshima and Izumo, 1993). Unveiling these mechanisms would, however, provide promising new avenues for therapeutic interventions for a host of pathologies.

Mechanical forces manifest in different ways, although often can occur in conjunction. A cell subjected to lateral uniaxial stretch will reduce in height in a similar manner to compression. Elevated intraocular pressure described by (Porter *et al.*, 2014) will generate concurrent stretch and compressive forces. Heart cells must adapt to constantly changing shear and stretch forces as a result of muscle tissue contraction and blood flow. Despite similarities of action or coincidence, it is unclear whether all forces act through a single pathway/process or utilise multiple mechanisms. Further study is necessary to resolve the systems underpinning force detection and translation into a biological response.

1.4 Osmotic stress response

When a mechanical force is applied to a cell the immediate effect is membrane deformation. Compressive forces sandwich the cell and drive the cytoplasm and PM perpendicular to the applied force. Shear creates friction and pulls the membrane in the direction of the force. In a similar manner to shear, stretch forces apply tension parallel to the force but in multiple directions. Another external stimulus that can similarly alter cell morphology and result in global membrane tension change is osmotic stress (OS). Hyper-osmotic stress (Hyper-OS) is caused by increased external solute concentration, drawing water out of the cell and reducing cell volume. Conversely hypo-osmotic stress (hypo-OS) is the result of decreased external solute concentration causing with water to translocate into the cell and increasing cell volume. Changes in solute concentration, and the resulting translocation of water and altered cell volume, consequently affects the tension on the PM as cells shrink or swell. Given the similar physical effects of OS to mechanical forces on cell morphology and internal pressure, it provides an avenue worth pursuing.

Unlike for mechanical forces, the osmotic stress response (OSR) has been studied in detail using *Dictyostelium*. A complex network of proteins have been implicated in mediating the response to OSR. In some cases, components respond specifically to hyper- or hypo-OS only. Arrestin Domain-Containing protein A (AdcA) is a Fab1, YOTB, Vac1 and EEA1 (FYVE)-type zinc finger-containing protein. The histidine kinase DokA (*Dictyostelium* Osmosensing Kinase A). STAT (Signal transducer and activator of transcription) proteins are transcription factors which alter gene expression when activated. In response to hyper-OS *Dictyostelium* STAT protein C (DstC) becomes phosphorylated and translocates to the nucleus (Araki *et al.*,

2003), rapidly altering gene expression (Na, 2007; Na *et al.*, 2007). One up-regulated gene identified was KrsA (Kinase Responsive to Stress protein A), a putative S/T kinase belonging to the Mammalian Sterile20-like (MST) subfamily of protein kinases and similar to STE20-like kinases, named after the yeast Sterile20 kinase. One of these diverse OSR proteins could be involved in transducing mechanical forces.

Dictyostelium contain an osmo-regulatory organelle, the contractile vacuole complex (CVC) (Gerisch *et al.*, 2002) to survive in hypotonic environments (Allen and Naitoh, 2002). It is distinct from the endocytic system (Gabriel *et al.*, 1999), and composed of the contractile vacuole (CV; also called the "bladder") formed from fused vacuoles (Heuser *et al.*, 1993), radial arms and a smooth spongiform containing V-type H+-ATPase (Fok *et al.*, 1993; Heuser *et al.*, 1993; Nolta *et al.*, 1993) which creates a proton gradient (Grønlien *et al.*, 2002). Plasma membrane Ca2+-ATPase (PMCA-type pump) has also been reported at the CVC (Marchesini *et al.*, 2002). The CVC allows cells to sequester excess water and retain ions, such as calcium, and expel the contents when necessary (Allen and Naitoh, 2002). Loss of proteins involved in the CVC, such as LsvA, can sensitise cells to hypo-OS (Gerald *et al.*, 2002).

Another highly studied signalling pathways involved in OSR is the cyclic GMP pathway. Cyclic guanosine monophosphate, cGMP, is a small secondary messenger produced by the conversion of guanosine triphosphate (GTP) by guanylyl cyclase (GC) enzymes. *Dictyostelium* contain two GCs: the membrane-bound guanylyl cyclase GcA (Roelofs, Snippe, *et al.*, 2001) and the cytosolic soluble guanylyl cyclase (SgcA) (Roelofs, Meima, *et al.*, 2001). cGMP production can be stimulated by binding of external cyclic adenosine monophosphate (cAMP) to transmembrane cAMP receptor cAR1 during development, differentiation inducing factor (DIF-1), and hyper-OS. Additionally hyper-OS can stimulate intracellular cAMP production, peaking after 2 min (Ott *et al.*, 2000). The cGMP then binds to proteins containing a cyclic-nucleotide binding motif to exert its effect.

In *Dictyostelium* there are four proteins capable of binding cGMP. These were identified in a bioinformatics screen completed by Goldberg *et al.* (2002) and termed cGMP-binding proteins A-D (GbpA-D). GbpA and GbpB are cGMP-activated phosphodiesterases (PDEs). GbpD is highly similar to the C-terminal portion of GbpC, both containing RasGEF domains which regulate Ras proteins. Of the 4 candidates, only GbpC showed a high affinity to cGMP. GbpC is a large multi-domain protein, containing two cyclic-nucleotide binding domains (cNBD) and a kinase domain. Furthermore it also contains a Ras/GTPase domain which subsequently founded the Roc (Ras of complex) and COR (C-terminal of Roc) domains, and the Roco protein family where both domains were present (Bosgraaf and van Haastert, 2003). Upon cGMP binding to GbpC, a chain of intramolecular events occur which stimulate kinase activity (van Egmond *et al.*, 2008). Summarising their findings, the GEF domain becomes active and facilitates replacement of GDP with GTP at the Roc-COR domain. This activates the domain which in turn increases activity of the MAPKKKinase domain, promoting phosphorylation of substrates. GbpC, via the kinase or RasGEF domains, then regulates downstream processes.

In mammalian cells, cGMP signalling is most commonly associated with regulation of blood vessels. When stimulated nitric oxide synthase (NOS) produces nitric oxide (NO) (Shah *et al.*, 2013; Takizawa *et al.*, 2013) which diffuses to the smooth muscle where it stimulates guanylyl cyclase activity in adjacent cells (Roczniak and Burns, 1996). In turn cGMP is produced and binds to PKG, activating the kinase and downstream signalling pathways including ones involved in driving blood vessels vasodilation (Ignarro, Buga, *et al.*, 1987). cGMP signalling has been implicated in mechanotransduction of shear and stretch stimuli (Angelone *et al.*, 2015; Ohno *et al.*, 1993; Shah *et al.*, 2013). Shear forces have been implicated in autophagy induction (Liu *et al.*, 2015), as have stretch forces (Porter *et al.*, 2014), however the potential role of cGMP signalling has not been studied in this respect. Furthermore, hyper-OS, an established stimulus for cGMP production, has been shown to induce autophagy (Liu *et al.*, 2009; Nunes *et al.*, 2013) however cGMP, again, has not been implicated. Taken together, it could be speculated from these various observations that cGMP signalling provides a functional link between the mechanical and osmotic stimuli and autophagy induction.

The existence of a cGMP-binding protein with kinase function was speculated long before ultimately being uncovered through computational analysis which identified cGMP-binding proteins (Gbp) A-D (Goldberg *et al.*, 2002). GbpC was the largest and most complex of the 4 *Dictyostelium* Gbp's, composed of a diverse domains architecture. Due to their C-terminal domain homology GbpC is believed to have arisen from duplication of GbpD and subsequent fusion to a CG5483 KIAA1790-like gene (Goldberg *et al.*, 2002). The most noteworthy domains were the Ras in complex proteins domain (Roc) and domain C-terminal of Roc (COR), which together coined the Roco protein family which GbpC founded (Bosgraaf and van Haastert, 2003). *Dictyostelium* contain a further 10 Roco proteins, and Roco proteins were also identified in mammals, plants, prokaryotes and metazoa. GbpC also contain leucine-rich repeats (LRR), MAPKKK, N-GEF, DEP, RasGEF, cyclic nucleotide binding (cNB) and a GRAM domain (Goldberg *et al.*, 2002), where the latter domain facilitates GbpC translocation to the cortex (Kortholt *et al.*, 2012). Complex intramolecular interactions regulate GbpC function, where cGMP binding to cNB domains trigger a sequential chain reaction via the GEF, Roc-COR and finally MAPKKK domains (van Egmond *et al.*, 2008), which results in phosphorylation of target proteins. It is postulated the LRR domain directs protein-protein interactions which determines GbpC substrates (Kortholt *et al.*, 2012), which suggests GbpC might not have an explicit consensus target for phosphorylation. Despite this intricate understanding of GbpC's molecular mechanisms, knowledge of downstream targets is less refined.

The role of cGMP signalling, and consequently GbpC, has been predominantly studied in context of *Dictyostelium* chemotaxis and development. Starving cells secrete cAMP, triggering adjacent cells to secrete cAMP, generating cAMP waves. It has long been known cAMP signalling resulted in increased cGMP levels (Mato *et al.*, 1977). cGMP is produced from GTP by two guanylyl cyclase enzymes, soluble guanylyl cyclase A (SgcA; Roelofs, Meima, *et al.*, 2001) and a membrane associated guanylyl cyclase (GcA; Roelofs, Snippe, *et al.*, 2001). SgcA was later shown to be predominantly responsible for this (Roelofs and van Haastert, 2002) Furthermore, both folate and hyper-OS could stimulate cGMP production. Roelofs and van Haastert (2002)

also determined that ablation of both cGMP-producing enzymes blocked all detectable cGMP production, although this did not prevent aggregation or fruiting body formation.

GbpC is expressed in vegetative cells which increased upon starvation, peaking at 8 hr into development then decreasing until almost undetectable (Goldberg *et al.*, 2002). GbpC-null cells are capable of completing the developmental cycle, but aggregation was delayed by 3 hr (Goldberg *et al.*, 2002). Spatial orientation when migrating to chemoattractant cAMP was shown to be defective in GbpC-null cells (Bosgraaf *et al.*, 2002), with smaller aggregation territories resulting in smaller spores attributed to defective streaming as a result of unstable cell:cell contacts (Veltman and van Haastert, 2008). Chemotaxis is a critical process essential for migration towards nutrient and cAMP sources, which is dependent on the cytoskeleton.

The *Dictyostelium* cytoskeleton is a dynamic structure which provides movement machinery and protective mechanisms against environmental stresses. It is involved in chemotaxis towards cAMP during development (Chung *et al.*, 2000a), formation of phagocytic and macropinocytic cups (Hacker *et al.*, 1997), cortical reinforcement in response to OS (Khurana *et al.*, 2002) and transportation of intracellular organelles (Bush *et al.*, 1993). The cytoskeleton is predominantly composed of actin and myosin, both of which are regulated by a complex network of signalling pathways to facilitate the dynamic structure. Currently 29 myosin-related genes are known in *Dictyostelium* (Dictybase.org), including myosin II heavy (*mhcA*), essential/light (*mlcE*) and regulatory (*mlcR*) chains, heavy (*mhkA-D*, *pakB*) and light (*mlkA*, 4 putative genes) chain kinases, 12 unconventional myosins (*myoA-K*, *myoM*) and corresponding light chains (*mlcB-D*). Myosin kinases and phosphatases regulate myosin intra- and inter-molecular interactions, and consequently subcellular localisation, through the addition and removal of phosphate groups (Berlot *et al.*, 1985; Liu and Newell, 1994; Smith *et al.*, 1996). Phosphorylation of myosin II heavy, essential and regulatory chains has been shown to be regulated by cGMP signalling (Bosgraaf *et al.*, 2002).

The majority of research has focussed on myosin class II, a hexamer comprising heavy, essential and regulatory chains (Clarke and Spudich, 1974). Myosin II heavy chain (MhcA) is the largest component, with a globular head and extended C-terminal tail. Myosin II exists in various conformations: cytosolic monomers and dimers, antiparallel tetramers and multimeric filaments and bundles. Filament bundle formation is inhibited by phosphorylation (Kuczmarski and Spudich, 1980), which can be triggered by cAMP and was shown to increase myosin localisation to the cytoskeleton (Berlot *et al.*, 1985, 1987). Critical phosphorylations were mapped to threonine residues 1823, 1833, 2029 (Lück-Vielmetter *et al.*, 1990; Vaillancourt *et al.*, 1988), which were shown to regulate filament formation by replacing these MhcA loci with alanine (3XALA) or aspartate (3XASP) to generate non-phosphorylatable and phosphomimetic mutants respectively (Egelhoff *et al.*, 1993). These myosin mutants were later used to show dynamic phosphorylation and dephosphorylation events were essential for proper function in response to cAMP waves, and for both chemotaxis and streaming (Heid *et al.*, 2004).

MhcA phosphorylation has been shown to change in response to a variety of upstream stimuli in *Dictyostelium*. Cyclic GMP was reported to regulate MhcA phosphorylation and incorporation into the cytoskeleton (Liu *et al.*, 1993; Liu and Newell, 1991) although they incorrectly concluded cGMP signalling played a negative regulatory role in myosin chain phosphorylation and speculated that kinases were not involved in signal transduction. Using both 8Br-cGMP and hyper-OS to increase cGMP levels, (Kuwayama *et al.*, 1996) detected increased MhcA phosphorylation which blocked filament formation. They showed both MhcA-null and 3XALA mutant cells exhibited increased sensitivity to hyper-OS, highlighting the importance of functional cGMP signalling for adaptation to environmental cues. It is likely GbpC is responsible for mediating this response as ablation of the Roco protein reduces MhcA phosphorylation upon cAMP stimulation, and consequently less MhcA was found in the Triton-insoluble cytoskeletal fraction (Bosgraaf *et al.*, 2002). While there is no evidence suggesting GbpC directly phosphorylates MhcA, it is clear cGMP signalling does transiently contribute to myosin II regulation.

There are 4 myosin heavy chain kinases in *Dictyostelium* responsible for phosphorylation of myosin heavy chain and driving filament disassembly. Côté and Bukiejko (1987) first identified myosin heavy chain kinase A (*mhkA*). *mhkB* was discovered much later by Clancy *et al.* (1997), and *mhkC* was verified as a functional kinase by Luo *et al.* (2001), with Liang *et al.* (2002) validating the gene product phosphorylated MhcA. In a review of myosin II regulation, De La Roche *et al.* (2002) identified a putative fourth kinase *mhkD* on account of its similarity to the other myosin heavy chain kinases. Systematic knockout of MHCK genes showed MHCK A-C, but not putative MHCK D, were critical modulators of myosin II through phosphorylation of MhcA and assembly control (Yumura *et al.*, 2005). Another candidate heavy chain kinase initially believed to phosphorylate MhcA was MHC-PKC (Ravid and Spudich, 1989), which was phosphorylated in response to cAMP treatment in a cGMP-dependent manner (Dembinsky *et al.*, 1996). It was later determined to be an error arising from a "questionable" cDNA. It transpired the actual gene was a diacylglycerol kinase (*dgkA*) involved in phosphorylation of diacylglycerol to phosphatidic acid (de la Roche *et al.*, 2002). There does not appear to be any literature studying cGMP stimulation of cells lacking MHCK and the impact on MhcA phosphorylation. Given MhcA phosphorylation occurs exclusively through these kinases, it is reasonable to assume cGMP-stimulated MhcA phosphorylation will act through them.

Myosin regulatory light chain (*mlcR*) forms part of the myosin II hexamer and, as its name suggests, regulates myosin II. MlcR regulates the actin-activated Mg^{2+}-ATPase activity of myosin, which is increased when MlcR is phosphorylated by myosin light chain kinase A (*mlkA*) (Griffith *et al.*, 1987) at a serine-13 residue (Ostrow *et al.*, 1994). Using an unphosphorylatable S13A mutant it was shown the post-translational modification is not essential for critical cellular functions (Ostrow *et al.*, 1994), however fewer lateral pseudopodia were formed during chemotaxis and cell polarity was not lost in response to cAMP waves (Zhang *et al.*, 2002). MlcR phosphorylation might not be essential, but does contribute to proper myosin II filament function.

As described, MlcR is phosphorylated by myosin light chain kinase A (*mlkA*). MlkA activity is increased by phosphorylation of at least one threonine residue (Tan and Spudich, 1990), where one was resolved at threonine-166 within the activation loop (Smith *et al.*, 1996). Previously Griffith, Downs and Spudich (1987) determined both cAMP and cGMP did not activate purified MlkA, however it had been shown that cAMP did illicit an increase in both MlcR phosphorylation via MlkA and affiliation of MlcR with the Triton-insoluble cytoskeletal fraction *in vivo* (Berlot *et al.*, 1985, 1987). cGMP, too, was later shown to transiently regulate MlcR phosphorylation (Liu and Newell, 1994), with cGMP accumulation shown to increase MlkA activity in crude lysates (Silveira *et al.*, 1998). GbpC was shown to transiently mediate MlcR phosphorylation in response to cAMP through ablation of the cGMP-regulated kinase which reduced, but did not completely diminish, RLC phosphorylation (Bosgraaf *et al.*, 2002). Unsurprisingly, it was subsequently shown that MlkA could be activated by both cGMP-dependent and -independent pathways (Goldberg *et al.*, 2006). Therefore cGMP and GbpC can be partially attributed to phosphorylation of MlcR via MlkA, and further regulation of the myosin activity.

Dictyostelium undergo a complex developmental programme in response to prolonged starvation involving global signalling activation and gene expression change. As GbpC has already been implicated in development it is understandable that downstream transcription factors could be regulated by cGMP signalling. *Dictyostelium* Signal Transducer and Activator of Transcription protein C, referred to as both STATc and DstC, regulates expression of target genes when activated. DstC undergoes tyrosine phosphorylation in response to DIF-1, dimerises and then translocates to the nucleus (Fukuzawa *et al.*, 2001). This was later shown to also occur in response to hyper-OS, with nuclear translocation peaking at 3 min (Araki *et al.*, 2003). Na, (2007) and Na, Tunggal and Eichinger (2007) showed DstC stimulation by hyper-OS altered expression of 809 genes, peaking between 45-60 min. Up-regulation of many cytoskeletal genes was reported, including actobindin (*abnB*), dynacortin (*dct*), LIN-11, Isl-1 and MEC-3 (LIM) domain-containing protein D (*limD*), formin-A (*forA*) and myosin IA and IK heavy chains (*myoA* and *myoK*). Multiple metabolic genes were also up-regulated, which was speculated to facilitate synthesis of osmolytes in response to the OS (Na, 2007; Na *et al.*, 2007). Gene ontology (GO) analysis verified actin-filament based movement (chemotaxis, protrusions etc.) and ATP metabolism were significantly altered. Given cGMP production is drastically elevated by hyper-OS, the vast expression changes observed could, at least in part, be attributed to cGMP signalling.

In addition to DstC activation by hyper-OS, (Araki *et al.*, 2003) showed tyrosine phosphorylation of DstC could be triggered by 8Br-cGMP. Tyrosine phosphorylation of DstC was detectable after 1 min for both stimuli, which peaked at 3 and 5 min for hyper-OS and 8Br-cGMP respectively. Loss of both cGMP-producing guanylyl cyclase enzymes GcA and SgcA dampened DstC tyrosine phosphorylation in response to OS, implicating cGMP signalling in DstC activation (Araki *et al.*, 2003). As GbpC is a predicted serine/threonine kinase, it is unlikely to be responsible for directly phosphorylating tyrosine residues of DstC. It was subsequently verified that GbpC transiently mediated DstC phosphorylation (Araki *et al.*, 2010)

and acted via tyrosine kinase-like (TKL) enzymes Pyk2 and Pyk3 (Protein Tyrosine Kinase 2 and 3 respectively; Araki *et al.*, 2014). Like GbpC, Pyk3 was shown to translocate to cortex in response to hyper-OS, however definitive colocalisation was not verified (Araki *et al.*, 2014). With DstC phosphorylation and consequent translocation to the nucleus occurring rapidly, and in response to increased cGMP, it potentially provides a suitable indicator for GbpC activity.

Stress-activated protein kinase α (*spkA*) is a stress activated MEK-like kinase. Another TKL protein, it is composed of N-terminal ankyrin repeat motifs, a sterile-α motif (SAM domain) and a C-terminal dual-specificity kinase domains (Sun *et al.*, 2003). It is rapidly activated within 5 min by a host of stress stimuli including 30°C heat shock and hyper-OS by sorbitol, glycerol and NaCl treatment. Cells lacking SpkA exhibited increased sensitivity to hyper-OS. Furthermore cells treated with 8Br-cGMP show SpkA activation, with significant phosphorylation detected after 1 min. It was not shown whether GbpC mediated cGMP activation of SpkA, although interestingly expression of SpkA during development was strikingly similar to GbpC (Goldberg *et al.*, 2002). SpkA was present in vegetative cells and increased sequentially at 4 and 8 hr, peaking between 8-12 hr then falling below vegetative expression levels from 16-24 hr. SpkA-null cells completed development, although spores appeared smaller. No streaming defects were mentioned, so it is unclear if the developmental phenotype was similar to GbpC-null cells. Aside from the findings provided by (Sun *et al.*, 2003), no further literature is available regarding SpkA. Nevertheless, the rapid phosphorylation of SpkA induced by cGMP and its role as a stress activated kinase make it an interesting candidate for downstream GbpC targets.

At present there are no known direct substrates of GbpC, but several phosphorylations have been attributed to cGMP signalling. These known downstream effectors can be used to validate results obtained in phosphoproteomics analysis. In particular phosphorylations linked to myosin related proteins, including MlkA, MhcA (threonines 1823, 1833 and 2029), and MlcR (serine 13), actin and cytoskeletal proteins, along with Pyk3, DstC, SpkA and DgkA, will provide useful indicators of data reliability. These gene products might not be involved in autophagy signalling, but can provide a critical baseline.

1.5 Aims of thesis

This project aims to determine if mechanical force is a universal inducer of autophagy, and the signalling pathway(s) responsible using compression as an inducing force. This is covered in Chapters 3 and 4. Chapter 4 also covers the role of hyper-OS as an autophagy inducing stimulus, which is further investigated in chapter 5 which aims to identify candidates involved in mediating the response.

1.5.1 Identifying which mechanical forces induce autophagy

Compression has been shown to induce autophagy in both *Dictyostelium* and mammalian cells in a transient, and proportional manner (King *et al.*, 2011). In addition, both fluid shear and stretch forces have been implicated in autophagy by other groups, albeit with some conflicting results. The issue of comparing available research data is further complicated by both the different cell lines and methodologies being employed. Chapter 3 aims to trial and develop appropriate experimental protocols to establish a defined system to study the effects of different mechanical forces in the context of autophagy.

1.5.2 Identifying candidate signalling pathways which mediate mechanically-induced autophagy

Autophagy induction by compression occurs via a non-canonical signalling pathway which is yet to be determined. Chapter 4 aims to identify candidate signalling components using knockout *Dictyostelium* lines, and testing for ablated autophagy induction in response to compression.

1.5.3 Investigating the effect of osmotic stress on autophagy

While exploring for candidate proteins involved mediating the autophagic response to mechanical stimulation, it was determined that hyper-OS was a potent inducer of autophagy in *Dictyostelium*. The secondary messenger cGMP is known to play a role in responding to hyper-OS. This, like hyper-OS, was also found to elicit a potent and dose-dependent induction in autophagy. This part of the project investigated the effects of both hyper-OS and cGMP on autophagy, and aimed to determine if any overlap could be identified with mechanically-induced autophagy induction.

Chapter 2

Materials and Methods

2.1 Maintaining plasmid stocks

Competent bacteria and plasmid DNA were thawed on ice. 0.2µL plasmid DNA was added to 50µL competent bacteria suspension and incubated on ice for 10 min. Bacteria were heat-shocked at 42°C for 40 s, then incubated on ice for 2 min. 200µL sterile LB (Fisher Scientific, BP1426-2) was added and bacterial suspensions incubated for 1 hr at room temperature (ampicillin resistance selection only). SM agar (Formedium™, SMA0102) selection plates containing ampicillin (Fischer Scientific, BP1760-5) or kanamycin (Fischer Scientific, BP906-5) were warmed to room temperature. Under sterile technique, 5µL bacterial suspension was aliquoted per plate and evenly distributed using an L-shaped spreader (Starlab UK Ltd., E1412-1005). For lower plasmid concentrations higher volumes were used (≤100µL) although this typically resulted in a bacterial lawn. Plates were incubated overnight at 37°C.

LB supplemented with appropriate antibiotic was warmed to room temperature, then aliquoted into bacterial tubes (Scientific Laboratory Supplies Ltd., BSF2051). Five independent colonies were harvested per plate using a pipette tip under sterile technique and added to separate bacterial tubes. Tubes were incubated at 37°C with 200 rpm orbital shaking (IKA KS4000i control) overnight.

Bacterial suspensions were pelleted using a benchtop centrifuge at 3000 x g, room temperature, for 10 min. Supernatant was disposed of and bacterial pellets were retained. Plasmid DNA was liberated from the bacteria using either FastGene Plasmid Mini Kit (Nippon Genetics Ltd., FG-90502) or GeneJET Plasmid Miniprep Kit (Thermo Fisher Scientific, K0503) as per respective manufacturer instructions. Plasmid concentration was verified using a Nanodrop Lite. Plasmids were stored at -20°C until required.

2.2 Cell culture

2.2.1 *Dictyostelium*

Cells were cultured and expanded to create a large stock, which were subsequently frozen down into starter aliquots. A long-term lab stock was used to create new starter aliquots. This was to ensure cells used in all experiments were of a comparable passage number, with thawed stocks only retained for a maximum of one month. Ax2 and Ax3 axenic cell lines were used as wild-types. When a knockout cell line was tested, it was compared with the same axenic line it was created from, e.g. GbpC-null cells were derived from Ax3.

2.2.1.1 Solid culture

SM agar was prepared by mixing 41.7g SM agar (Formedium™, SMA0102) with 1L water and autoclaving. Once cooled, but agar still molten, 20mL was transferred to 9cm Petri dishes (Thermo Fisher, 100315Z) under sterile technique. SM agar plates were set overnight at room temperature, and then stored at 4°C until required.

Klebsiella aerogenes were harvested from a stock plate and homogenised in LB (Fisher Scientific, BP1426-2) under sterile technique. The bacterial suspension was evenly distributed across a room temperature SM agar plate using an L-shaped spreader (Starlab UK Ltd., E1412-1005) to create a bacterial lawn.

Dictyostelium were added to the centre of the plate, either as cells from frozen stocks or spores harvested using an inoculation loop (Starlab UK Ltd., E1412-0112). Plates were incubated at room temperature and protected from light for a minimum 24 hr until a leading edge or spores formed. These were harvested for further culture on SM agar plates, or transfer to liquid culture.

2.2.1.2 Liquid culture

Adherent

Axenic *Dictyostelium* cell lines were cultured in plastic Petri dishes in filter sterilised HL5 (Formedium, FM/0A213/004518R) supplemented with 13.5g/L D-glucose (Fisher Scientific, G/0500/61) and 50U/mL penicillin 50µg/mL Streptomycin (Thermo Fisher Scientific Inc., 15070-063), hereafter referred to as "complete HL5". Cell were suspended by pipetting using complete HL5 and transferred to new dishes, typically passaged 2-3 times per week for a maximum of 5 weeks. Cultures were incubated at 22°C in darkness.

Transferring from bacterial plates

Under sterile technique, *Dictyostelium* were harvested from an SM agar plate using an inoculation loop (Starlab UK Ltd., E1412-0112) from either the leading edge or from spores. The harvested cells were suspended in 200µL complete HL5, then added to a 9cm Petri dish (Thermo Fisher, 100315Z) containing 10mL complete HL5 supplemented with 10µg/mL doxycycline hydrochloride (Fisher Scientific, BP2653-1). Cells were incubated overnight at 22°C in darkness. After 24 hr, media was removed and dishes were washed with complete HL5. 10mL fresh complete HL5 was added and cells were cultured at 22°C until confluence had been reached.

Suspension

When large quantities of cells were required, *Dictyostelium* cells were cultured in 500mL glass conical flasks containing 100mL complete HL5. Flasks were incubated at 22°C in darkness with 180 rpm orbital shaking to maintain cells in suspension. This culture method was used primarily for proteomic and phosphoproteomic experiments.

2.2.2 Mammalian

MDA-MB-231 cells were cultured in DMEM (Thermo Fisher Scientific, 21969-035) supplemented with 10% foetal bovine serum (Thermo Fisher Scientific, 10270-106), 2mM L-glutamine (Thermo Fisher Scientific, 25030-024), 50U/mL penicillin and 50µg/mL streptomycin (Life Technologies, 15070-063); hereafter referred to as "complete DMEM". HUVECs were cultured in M199 (Sigma Aldrich, M0650) supplemented with 20% foetal bovine serum (Thermo Fisher Scientific, 10270-106), 0.1ng/mL EGF (Sigma Aldrich, C-39210), 1ng/mL heparin (Sigma Aldrich, C-39210), 2.5µg/mL Amphotericin B (Sigma Aldrich, A2942), 100U/mL penicillin and 100µg/mL streptomycin (Life Technologies, 15070-063), hereafter referred to as "complete M199".

All mammalian cells were maintained as adherent cultures using tissue culture treated T25 (Thermo Fisher Scientific, 156340) and T75 flasks (Thermo Fisher Scientific, 10538931) using aforementioned media. A 1% gelatine (Fisher Scientific, S25335) coating was included for HUVECs (see Substrate treatments). Cells were incubated at 37°C + 5% CO_2 in darkness and passaged 2-3 times per week. MDA-MB-231 cultures were maintained for a maximum of 5 weeks (15 passages), whereas HUVECs were maintained for <2 weeks (3 passages) to prevent differentiation. Cells expressing fluorescent proteins were protected from ambient light where possible, particularly when used for microscopy purposes.

2.3 *Dictyostelium* transformation

Dictyostelium were transformed by electroporation. *Dictyostelium* cells were cultured until 80% confluence was reached, suspended in complete HL5, then ⅓ cell suspension was centrifuged at 600 x g for 2 min. Supernatant was removed and the cell pellet was resuspended in 400µL ice-cold E-buffer (10mM KH_2PO_4 (Fisher, 10757214) pH 6.1 supplemented with 50mM sucrose (Thermo Fisher, 10386100)). Cell suspension was transferred to an ice-cold 2mm gap electroporation metal cuvette (Geneflow Ltd., E6-0062) containing 0.5µg plasmid DNA for extrachromosomal expression. Cells were electroporated using a Gene Pulser II (Bio-Rad) connected to a 5Ω resistor. Parameters used were: 1.2kV, 3µF capacitance, ∞ resistance. Time constant was displayed and noted, as higher values were inversely correlated with cell viability. A typical 0.2-0.4ms value was optimal; deviations above 0.8ms indicated sub-optimal transfection conditions and would be repeated using a new cuvette.

Electroporated cells were transferred to a Petri dish containing complete HL5 supplemented with 10µg/mL doxycycline hydrochloride (Fisher Scientific, BP2653-1) and incubated at 22°C for 24 hr. The appropriate selection antibiotic was added for final concentrations 10µg/mL G418 sulphate (Thermo Fisher Scientific Inc., 10131-035), 50µg/mL hygromycin B (Thermo Fisher Scientific Inc., 10687-010) or 10µg/mL blasticidin S HCl (Melford Laboratories, B1105) as required, and cells were incubated for 48-72 hr until colonies formed. For selection of *gbpC*⁻ cells, 30µg/mL G418 sulphate was used due to greater tolerance of the selection antibiotic. All transformations involved fluorescent-labelled proteins, therefore transformation efficiency was verified using a ZOE™ Fluorescent Cell Imager (Bio-Rad). From here, standard culturing technique was used with supplementation of appropriate selection antibiotics.

2.4 Freezing cells

Dictyostelium cells were cultured to 90% confluence as per standard culturing technique, suspended in complete HL5 then centrifuged at 2000 rpm for 2 min. Supernatant was removed and the cell pellet was suspended in 50:50 complete HL5:horse serum (Sigma, H1270-100ML) supplemented with 10% DMSO (AnalaR® BHD Laboratory Supplies, 103234L). For short-term storage, final cell density was approximately $1x10^7$ cells/mL with 200µL cell suspension aliquoted into 0.5mL Eppendorf tubes (Starlab UK Ltd., E1405-2600). For long-term storage, final cell density was approximately $1x10^8$ cells/mL with 1mL cell suspension aliquoted into cryotubes (Fischer Scientific, 11740573). Samples were frozen to -80°C in a cell freezer (VWR

International, 479-1181) for 24 hr, and either stored at -80°C (short-term) or transferred to liquid nitrogen storage (long-term).

Mammalian cells were cultured as previously described to 90% confluence. Cells were washed once with 1X PBS and detached from the flask using 1X trypsin (Fisher Scientific Ltd, 10584623) in 1X PBS, then suspended in complete medium to homogenise cells and inactivate trypsin enzymes. Suspensions from multiple flasks were pooled if applicable. The cell suspension was centrifuged at 1000 rpm for 5 min then supernatant aspirated. The cell pellet was resuspended in freezing medium (complete medium supplemented with 10% DMSO (AnalaR® BHD Laboratory Supplies, 103234L)) for 2×10^6 cells/mL, and 1mL aliquoted into cryotubes (Fischer Scientific, 11740573). Samples were frozen to -80°C in a cell freezer (VWR International, 479-1181) for 24 hr, and then transferred to liquid nitrogen storage.

2.5 Acid-washing coverglass

Acid-washing was used to improve *Dictyostelium* binding to coverglass. 13mm diameter borosilicate coverglasses (VWR International, 631–0149) were bathed in 50% nitric acid (Sigma-Aldrich Company Ltd., 438073-500ML-M) for 10 min with occasional agitation. Nitric acid was removed and coverglasses were washed thoroughly with water to remove residual acid. Coverglasses were dried and then sterilised either by autoclaving or UV treatment.

2.6 Plasma surface treatment

Surfaces were activated with plasma using a Zepto plasma machine (Diener) to facilitate chemical bonding. Surfaces were typically treated for 30s at 100W, 1psi, however for cell stretching, treatment was increased to 150s. The effect of plasma treatment on silicone surfaces is temporary (Dr. Cecile Perrault (TUoS), personal communication), therefore all subsequent steps were executed immediately afterwards.

2.7 Liquid PDMS preparation

Polydimethylsiloxane (PDMS) base and curing agent (Sylgard KIT Dow Corning Sylgard 184; Robnor Resins, 0002-01-000032) were combined to a ratio of 10g base with 1g curing agent, and then mixed vigorously. This ratio could be adjusted depending on the elasticity required. Mixture was degassed using a vacuum chamber and bubbles burst by application of force (slamming the mixing vessel onto a hard surface). These steps were repeated until the majority of bubbles were removed. PDMS mixture could then be poured into a mould. Any bubbles introduced were removed using a syringe needle. The PDMS was set for 1 week at room temperature on a flat surface and protected from dirt and atmosphere (e.g. a cupboard). For heat-resistant moulds, PDMS could be set at 80°C using an oven.

2.8 Substrate treatments

Various substrates were employed to aid cell adhesion to surfaces. Fibronectin (Invitrogen, 33010-018) was used for all mammalian cultures unless explicitly stated otherwise. Fibronectin was prepared and used as per manufacturer instructions ($5\mu g/cm^2$). Poly-L-lysine (Sigma, P4707) was used to coat larger surface areas

or improve adhesion of *Dictyostelium*, and was used as per manufacturer instructions. Collagen I (rat tail) substrate (Gibco Life Technologies, A10483-01) was only used during stretching experiments as per manufacturer instructions. For all HUVEC culture and seeding, and orbital shaking experiments, 1% gelatine (Fisher Scientific, S25335) dissolved in 1% PBS was used to coat surfaces for 30 min at 37°C + 5% CO_2. Liquid was aspirated and wells were then washed with 1X PBS 3 times prior to cell seeding.

2.9 Cloning cylinders

Glass cloning cylinders (Millipore, c1059-1EA) were used for some experimental setups to permit simultaneous treatment and image acquisition using the same microscope dish, to limit the use of expensive reagents that required high concentrations, or both. For first use, glass cloning cylinders could be used immediately. For repeated use, multiple steps were required to ensure they were sufficiently clean, sterile, and to attach them to a glass surface. Failure to do so resulted in contamination, cell stress and elevated basal autophagy, and leaking due to incomplete silicone seals. For first use, see below but skip all steps prior to attachment to glass surfaces.

Cloning cylinders were cleaned thoroughly and forcefully using 70% IMS and tissue to remove silicone, cells and debris; the cylinders are tough and silicone grease is difficult to remove. Cleaned cloning cylinders were incubated in a beaker containing deionised water and incubated overnight at room temperature with stirring to aid removal of contaminants (cells, debris, compounds etc.). Care was taken to ensure no bubbles were within the cloning ring which would prevent cleaning. Once complete, cloning cylinders were dried and washed again with 70% IMS and tissue, then autoclaved in a sealable container. Silicone vacuum grease (Beckman Instruments Inc., 335148) was added to a glass beaker which was covered with foil, then autoclaved. Within a Category 2 laminar flow hood, a thin layer of vacuum silicone grease was spread across a sterile 9cm Petri dish using a sterile spatula and retained for later use.

Within a Category 2 laminar flow hood, cloning cylinders were removed using forceps and placed onto the silicone sheet and twisted gently until the cylinder base was evenly coated. Care was taken to avoid strands of silicone which fall within the central region and obstruct cell adhesion within the well. The cloning cylinder was then placed onto the glass region of a 35mm microscopy dish with 20mm glass bottom (MatTek Corporation, P35G-1.5-20-C) then pressed down gently with the forceps to prevent detachment. The dish was inverted and the cloning cylinder carefully pressed down firmly and twisted slightly using a gloved finger until a complete seal of silicone had formed at the base. Inverting the dish made visualising this viable, and using a finger allowed for greatest control; any lateral movement smeared the grease, obstructing cell binding. This process was repeated for up to 3 cylinders per dish.

2.10 Cell seeding

2.10.1 *Dictyostelium*

Dictyostelium cells were washed with, and then suspended in, filter sterilised SIH (Formedium™, SIH0101) supplemented with 50U/mL penicillin and 50μg/mL streptomycin (Thermo Fisher Scientific Inc., 15070-

063); hereafter referred to as "complete SIH". Cells were counted using a haemocytometer and seeded at required densities for 16-24 hr prior to treatment or imaging. For live-cell microscopy, cells were seeded into 35mm Petri dishes containing a 20mm glass micro well (MatTek Corporation, P35G-1.5-20-C) directly, or into affixed cloning cylinders. For fixation and immunocytochemistry, cells were seeded into 6- or 24-well plates containing acid-washed 13mm borosilicate coverglass (VWR International, 631-0149). Cells were then carefully washed with fresh complete SIH to minimise starvation-induced autophagy, and incubated a further 1 hr at 22°C to offset any mechanically-induced autophagy incurred during washing.

2.10.2 Mammalian

Mammalian cells were washed with 1X PBS then detached using 1X trypsin (Fisher Scientific Ltd, 10584623) in 1X PBS for 5 min at 37°C + 5% CO_2. Trypsin was inactivated with FBS by addition of complete media. Cells were counted using a haemocytometer, diluted to required cell density, and seeded. Glass surfaces were pre-treated with appropriate substrate as previously described, applicable to both 35mm Petri dishes with 20mm glass micro wells (MatTek Corporation, P35G-1.5-20-C) and 13mm borosilicate coverglass (VWR International, 631-0149). No substrates were used for tissue-culture treated polystyrene plates unless they contained coverglass for immunocytochemistry. Cells were incubated at 37°C + 5% CO_2 for a minimum 16 hr prior to adhere. Cells were provided with fresh complete media 1 hr before addition of compounds or treatment.

2.11 Mechanical stimulation

2.11.1 Compression

Agarose (Fisher Scientific, BP1356-500) was added to the appropriate complete media (SIH or DMEM) for 1% (w/v). The 1% agarose media was dissolved using a microwave, with intermittent manual mixing. Mixtures were cooled briefly until receptacles could be safely handled without heat-resistant PPE to prevent melting plastic containers. To avoid incorporating bubbles with the agar, 16mL media was taken up and 15mL dispensed into a plastic 9cm diameter Petri dish (Thermo Fisher, 100315Z). Dishes were set at room temperature for 1 hr. Once set, discs were typically cut out using a bacterial tube (Scientific Laboratory Supplies Ltd., BSF2051) for a consistent diameter and suitable size for 35mm microscopy dish with 20mm glass bottom (MatTek Corporation, P35G-1.5-20-C). 5mL media was added to prevent desiccation of agar, as this resulted in gel ripping during removal.

Agarose discs were placed upon cells using a small spatula. Care was taken to avoid lateral movement of the disc, which detached and sheared cells. This was achieved by wedging the agarose disc into a suitable well edge and retracting the spatula, gently lower the agar gel onto cells. Where appropriate, a lid insert (Figure 2.1) and metal weights were placed onto the agarose for greater compressive force. Compressive force was calculated using the formula below, where total weight consists of agarose disc, lid and metal weights (where appropriate). Force in g/cm^2 was converted to kPa using the constant indicated.

$$Force \ (kPa) = \frac{total \ weight \ (g)}{agarose \ disc \ SA \ (cm^2)} \times 0.0980665000000027$$
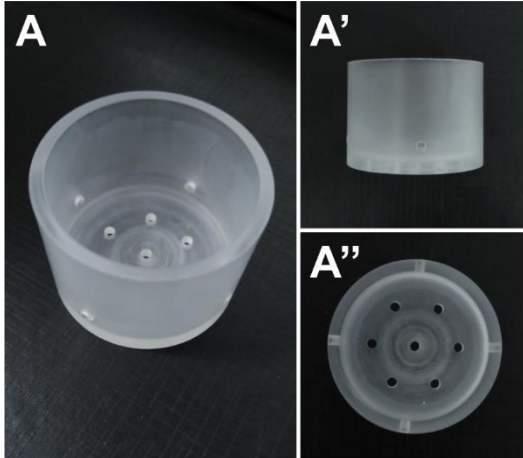
Figure 2.1 **Compression inserts**. The flat rim allows weights to be placed and evenly balanced, while the flat base evenly distributes the force. Holes in the base and side permit media through to prevent insert floating when weights not used. Views are (A) oblique, (A') from the side or (A'') base.

2.11.2 Fluid Shear

2.11.2.1 Orbital Shaking

Round 35mm borosilicate coverglass thickness 1.5 (ThermoFisher, CB00350RAC40MNT0) was fixed into wells of a 6-well plate using DPX (distyrene, a plasticizer, and xylene; Merck, 44581), a synthetic resin mounting media which partially degraded the plastic surface prior to setting. Three small volumes were added to the well base and the coverglass placed on top. This was pressed down firmly then set for 10 min at room temperature. Coverglasses were coated in 1% gelatine, and then 1mL complete media was added to wells. The plates were incubated at 37°C + 5% CO_2 while cell suspensions were prepared. MDA-MB-231 cell expressing enhanced green fluorescent protein tagged LC3B (EGFP-LC3B) and HUVECs were seeded as previously described for a final well volume of 3 mL, and incubated overnight at 37°C + 5% CO_2 aiming for ~80% confluence the following day.

Wells were washed with sterile 1X PBS 3 times, then provided with 3mL fresh, warm media. Plates were incubated for 1 hr at 37°C + 5% CO_2 for cells to acclimatise and reduce basal autophagy. The plates were placed onto an orbital shaker (Grant Instruments, PSU-10i), secured, and then subjected to 210 rpm shaking with a radial orbit of 10mm. The agitated media generated low intensity (~5dynes/cm^2) disturbed flow within the central region, and high intensity (~15dynes/cm^2) directional flow at the periphery (Dardik *et al.*, 2005; Warboys *et al.*, 2014). Cells were incubated under these conditions at 37°C + 5% CO_2 for up to 24 hr.

Once treatment times had elapsed, plates were removed and cells were fixed (see 2.18 Cell fixation) for immunocytochemistry (see 2.19 Immunocytochemistry) and counterstaining (see 2.20 Counterstaining).

26

Once complete, the coverglasses were removed using a wide-gauge syringe needle splayed to create a hook, and then broken in half prior to mounting on microscope slide. Breaks, conveniently, often occurred during removal and were necessary to accommodate size restrictions within microscope stage slide holders. Coverglass fragments containing central and peripheral regions were mounted using an appropriate volume of ProLong Gold Antifade mounting reagent (Life Technologies, P36934) to accommodate the greater surface area.

2.11.2.2 Laminar Flow

MDA-MB-231 cells expressing EGFP-LC3B were seeded in complete DMEM into μ-Slide VI $^{0.4}$ collagen IV-coated channels (6 x 10^4 cells in 30μL per channel; ibidi®, 80602), and then incubated at 37°C + 5% CO_2 for 1 hr. After this time a further 120μL complete media was added to each channel. Slides, along with 200mL complete DMEM in a bunged conical flask, were incubated at 37°C + 5% CO_2 overnight.

Prior to LSS and image acquisition, CO_2-infused complete DMEM was transferred into 60mL syringes (BD Plastipak™, 300866) which were each mounted into a syringe pump (New Era Pump Systems Inc., NE-1000 Multi-Phaser™) as required. Slides were tilted to remove any bubbles that formed within the channel. The syringe was connected to the slide via a single channel using tubing and appropriate luer-slip fixtures to bridge gaps. Additional tubing was attached to the opposing end of the channel connected to a waste receptacle. All devices and components were placed within an Oko-lab environmental control chamber (37°C + 5% CO_2) affixed to a Nikon Inverted Ti eclipse microscope. The slide was mounted to the motorised stage fitted with a 100μm Mad City Labs Z-Piezo.

Cells were subjected to LSS at 1 or 2 dynes/cm^2 for up to 60 min. Flow rates were used according to manufacturer instruction (ibidi®). Images were acquired from the central region of the channel every 10 min using an Apo 60x oil (NA 1.4) objective. Cells were illuminated with 470nm SpectraX LED excitation, with emission light passed through a GFP filter and captured on a Dual Andor Zyla sCMOS (2560 x 2160; 6.5μm pixels) camera. All components were controlled using NIS Elements software (Nikon). Acquisitions were exported and processed using ImageJ.

2.11.3 Stretch

The protocol below is the final version amalgamating findings and trails from several experiments detailed previously. Details and findings of these exploratory trials are presented in Chapter 3.

2.11.3.1 PDMS well production

In order to seed cells on silicone sheet a well was required which retained liquid media and remained static during stretch. To produce wells with consistent dimensions, liquid PDMS (Sylgard KIT Dow Corning Sylgard 184; Robnor Resins, 0002-01-000032) was cured using a mould. The mould consisted of a 9cm diameter Petri dish (Thermo Fisher, 100315Z) and Lego™ bricks, presented in Figures 2.2A-B. Bricks were affixed with Blu Tack® (Figure 2.2A), which additionally prevented PDMS leaking into the well region. Attachment of additional bricks fixed lower tier bricks in place and kept them equidistant from the central brick (Figure

2.2A'-A''). Liquid PDMS was prepared as previously described (see 2.7 Liquid PDMS preparation) and poured into the mould until ~4mm deep. Any bubbles were removed using a syringe needle. The PDMS was set on a flat, enclosed surface (e.g cupboard; prevents incorporation of dust) for 1 week at room temperature.

PDMS was detached at the periphery from the Petri dish using a scalpel. The upper tiers of Lego™ bricks were removed, and then both the PDMS and remaining bricks were removed from the mould. The Lego™ bricks were carefully removed, to avoid tearing PDMS, and the liberated PDMS placed upon a clean cutting board. PDMS which had leaked into the well region prior to setting was removed. The individual wells were excised, leaving a 4mm thick wall around the well space (noted by dotted lines in Figure 2.2A-A''). The wells were washed thoroughly with acetone, 70% EtOH and then distilled water. Residual water was removed using lint-free tissue and the wells were stored in a clean Petri dish and covered until later use.
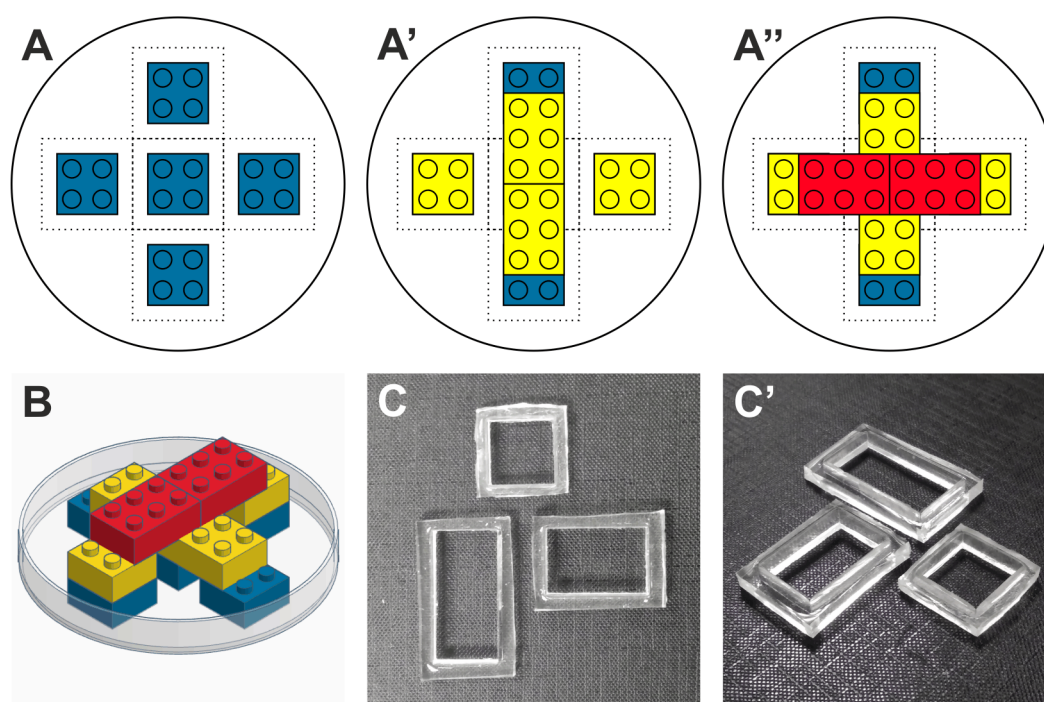
Figure 2.2 **PDMS well production using Lego™**. Schematics depicting sequential positioning of Lego™ bricks to create a defined, reproducible well. (A) Bricks affixed within petri dish using Blu Tack®, which define the well dimensions. Additional bricks added systematically in (A') and (A'') hold the bricks in (A) in place. (A-A'') Dotted lines denote cutting points and the well exterior. (B) Oblique view of well mould drawn in tinkercad. PDMS wells generated from different moulds viewed from (C) above and (C') oblique.

2.11.3.2 Silicone sheet preparation

A 65mm x 18mm rectangle was cut using a scalpel from ultra-thin 200µm silicone sheet (Wacker Chemie GmbH), retaining protective backing (Figure 2.3A). From both ends, 10mm x 18mm was cut from the protective backing (Figure 2.3B). The following steps were all completed under sterile conditions using a category 2 laminar flow cabinet. For each silicone strip prepared (one per condition), one sterile 9cm Petri dish (Thermo Fisher, 100315Z), one frosted glass microscope slide (VWR International, VWR 631-1550) and one PDMS well were placed into the hood. Tweezers, a small spatula and autoclaved vacuum silicone grease (Beckman Instruments Inc., 335148) were also placed into the hood. The following were cleaned

and sterilised with 70% EtOH then air dried: frosted glass microscope slides, PDMS wells, small spatula and tweezers.

The exposed surface of the silicone sheet was washed with acetone, 70% EtOH then sterile distilled water. Excess water was removed using sterilised lint-free tissue, and then sheets were left to air dry. Collagen I (rat tail) substrate (Gibco/Life Technologies, A10483-01) was prepared as per manufacturer instructions for each 2.56cm^2 well surface area, then stored at 4°C until required. All other items were subjected to UV treatment for 10 min within the biological cabinet. The silicone sheet was placed onto a frosted microscope slide, protective backing on the underside, and these were placed inside a Petri dish (Figure 2.3C). Using a small spatula, the 16mm x 16mm PDMS well base was coated with a thin but consistent layer of sterile vacuum silicone grease (Figure 2.3D). Coated wells were inverted and placed down with silicone greased surface facing upwards for later use.
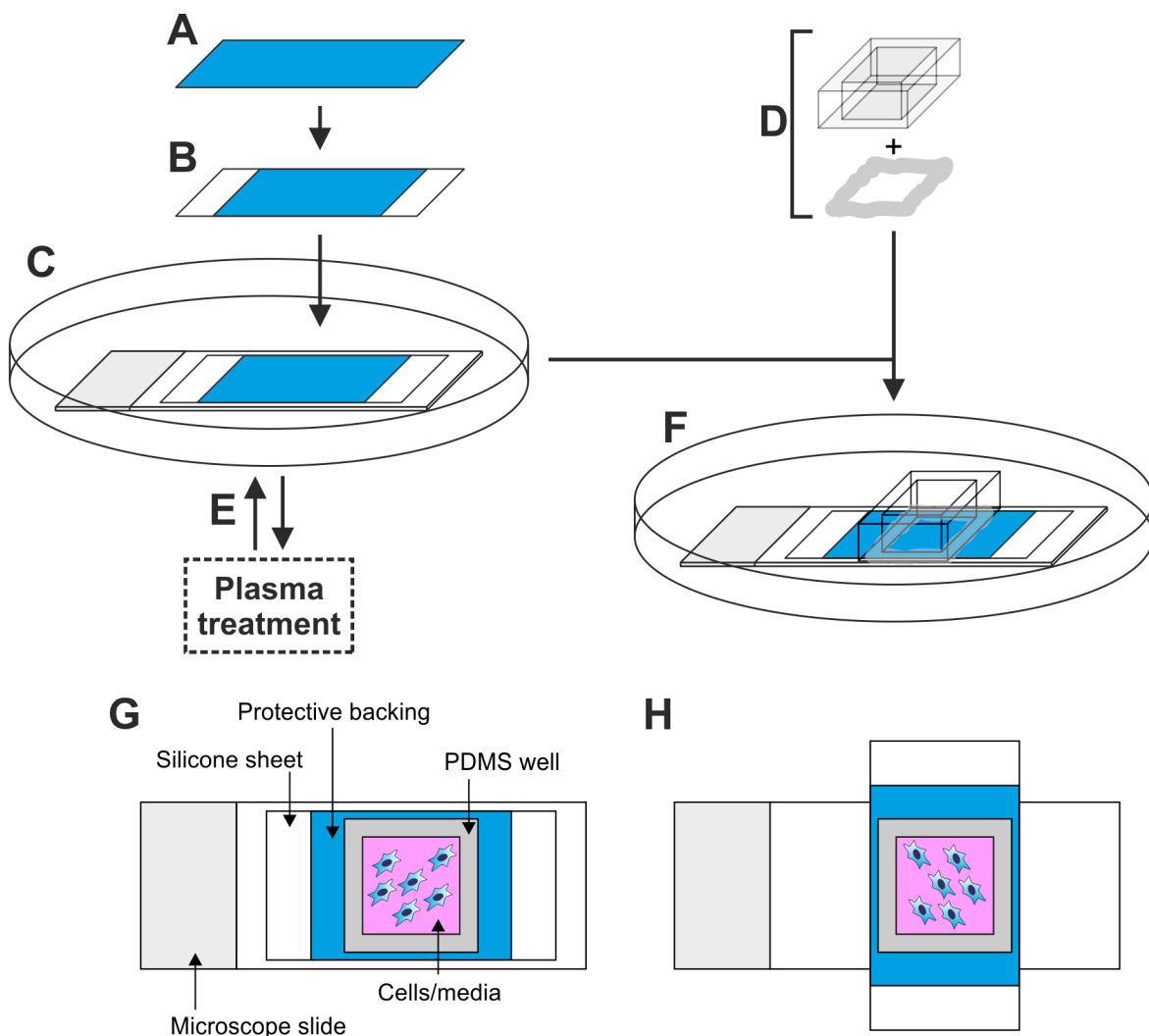
Figure 2.3 **Silicone sheet preparation.** Sequential process for preparing 200 µm silicone sheet for culturing cells. 65 mm x 18 mm silicone film cut out (A) with 10 mm x 18 mm protective backing removed from both ends (B), placed onto a frosted glass microscope slide within a petri dish (C). The PDMS well base was coated with silicone vacuum grease (D) prior to silicone sheet plasma treatment (E). (F) The PDMS well was attached to the sheet. (G) Stylised, aerial, depiction of silicone film with well containing cells. (H) 90° rotation facilitated easier attachment to stretching device, while the microscope slide supported and protected cells from stretch.

The Petri dishes containing the silicone sheets were removed from the biological cabinet and brought to the Zepto plasma machine (Diener). Note that immediately after plasma treatment, all subsequent steps were executed as quickly as possible as plasma treatment of silicone materials is temporary. The frosted microscope slides and silicone sheets were removed from the Petri dish and placed into the plasma machine, and subjected to plasma treatment at 100W, 1psi, for 150s (Figure 2.3E). Once complete, microscope slide mounted sheets were returned to Petri dishes and covered, and then returned to the biological safety cabinet. One silicone grease coated 16mm x 16mm PDMS well was firmly placed onto the silicone sheet creating a water-tight seal between the silicone and PDMS surfaces (Figure 2.3F). Collagen substrate, prepared previously, was added to the well, then Petri dishes were closed and incubated at 37°C + 5% CO_2 for 16-24 hr.

2.11.3.3 Cell seeding and handling

Collagen substrate was removed and washed as per manufacturer instructions, and then cells were seeded using the standard protocol for mammalian cells in appropriate complete media (Figure 2.3G). For 16mm x 16mm PDMS wells, the minimum and maximum volumes used were 1mL and 1.75mL respectively.

Despite substrate treatment and the presence of cells, the silicone sheet surface remained hydrophobic. Any activity involving large volume changes pre-fixation, e.g. 1X PBS washes, was undertaken using a dual pipetting technique to ensure the minimum well volume was maintained. This prevented liquid beading and subsequent cell lysis by desiccation. Two 1000µL pipettes were used simultaneously at opposing well corners; one to dispense and the other to aspirate an equal volume in parallel. Additional liquid was always added before aspiration began, so total well volume never decreased below the minimum 1mL. Well corners for dispensing and aspirating liquid were rotated to ensure complete washing of the sample. For addition of compounds, concentrated treatments were prepared which diluted to the desired final concentration upon addition.

2.11.3.4 Arduino setup

An Arduino microchip board (Figure 2.4A) was connected to a laptop via USB, then the motors (Figure 2.4B') of the stretching apparatus (Figure 2.4B) were connected to the Arduino microchip board. Arduino software (version 1.6.7, Arduino LLC©) was used to run codes which were written and calibrated to specific stretching distances e.g. 5mm stretch, 10mm stretch, as stretch was found to be non-linear during testing. The specific USB port connecting the laptop to the Arduino microchip board and stretching device was verified via Arduino software to confirm the microchip board was detected; the software anticipates connection to an exact USB port, and will not detect the equipment if connected to an alternative USB port. Once the connection was verified, the controller code was uploaded to the Arduino microchip board. Serial Monitor was opened (magnifying glass icon) where commands could be entered to control the stretching device motors.

2.11.3.5 Stretching

Moving components of stretching apparatus (Figure 2.4B'') were moved towards each other to remove any "play" in the motors. The smallest distance between the parts was measured using a calliper to ensure calibration was correct. The motors were instructed to decrease distance by 2mm. The silicone sheet was rotated 90° (Figure 2.3H) and then placed between the stretching device moving components (Figure 2.4B''; Figure 2.4C). The microscope slide was retained for support during this step. The silicone sheet ends lacking protective backing were carefully positioned using tweezers, ensuring the sheet length was parallel to the stretch force direction. Neodymium magnets were placed on top of the silicone sheet ends to fix them in place; opposing magnets were already fixed in place on the underside of moving components. The microscope slide was removed, as was remaining protective backing on the silicone sheet underside. The stretching device was instructed to increase distance by 2mm to render the sheet taut but not stretched.
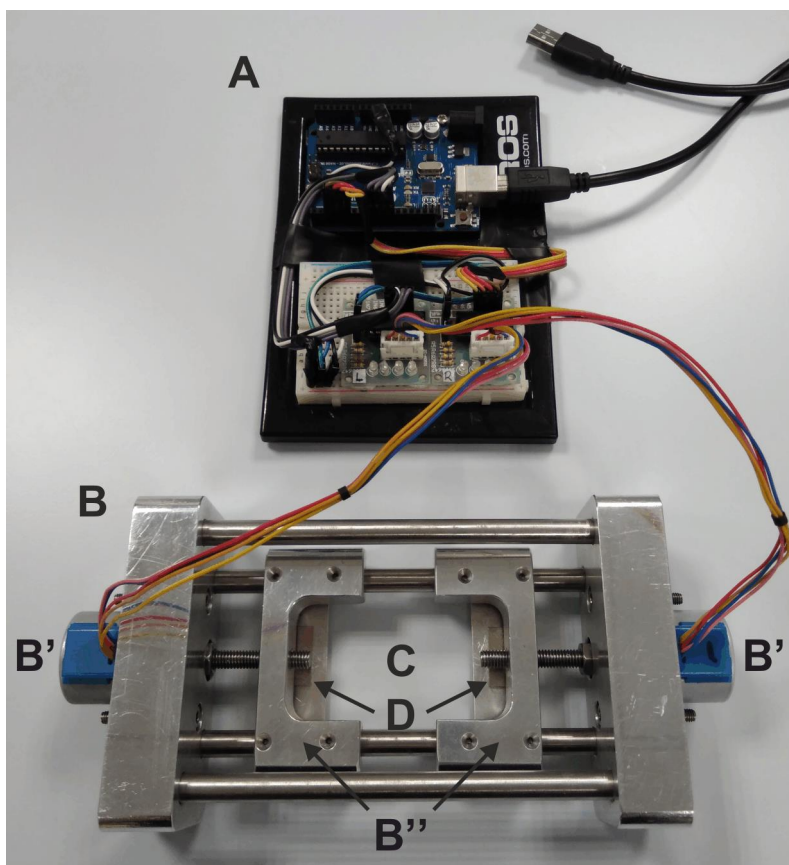
Figure 2.4 **Stretching device.** (A) The Arduino microchip board interface between the laptop and Arduino software, and the stretching device. (B) The stretching device was composed of a solid metal frame, 2 motors (B') and sliding parts (B'') connected to the motors. (C) Region where silicone sheet was affixed to the sliding parts using oblong neodymium magnets marked by (D).

From this point, the stretching device could either be mounted to a microscope stage for live-cell imaging, or used free-standing for immunocytochemistry/biochemical assays. Stretch force was applied using commands entered into the Arduino Serial Monitor window as required. Once stretch treatment was complete, the apparatus was instructed to return to resting position. After live-cell imaging, the silicone sheet was removed and disposed of. For immunocytochemistry, the silicone sheet was supported using a

microscope slide and released by cutting off the neodymium magnet fixed ends. The microscope slide was retained to protect the sample, as was the PDMS well to facilitate fixation, immunostaining, counterstaining, and/or biochemical assay steps.

For sample mounting, e.g. for microscopy, the region within the well was cut using a scalpel and retained; vacuum grease-contaminated silicone sheet and the PDMS well was removed. Approximately 20μL ProLong Gold Antifade reagent (Life Technologies, P36934) was added directly onto silicone and a 24mm x 24mm square borosilicate coverglass (Agar Scientific, L46S24-1) was placed on top sandwiching the sample between the microscope slide and coverglass. This was set for 24 hr at room temperature in darkness, then sealed with clear nail varnish prior to fluorescence microscopy.

Once the sheet was removed, the next silicone sheet could be mounted for treatment and the previous steps were repeated as required. If no further stretching was necessary, the stretching apparatus was checked to ensure the moving components were in resting position (23mm apart) using a calliper and adjusted if necessary. This was essential as the software assumed a starting position of 23mm, regardless of actual distance. Software was closed, and wired connections were detached.

2.11.4 Stretch method development

2.11.4.1 General

A variety of tests were undertaken to determine the viability of culturing cells on silicone-based surfaces, and optimisation of handling. Initial tests utilised 125μm (Shielding Solutions, SSP.M823.005) and 200μm (Shielding Solutions, SSP.M823.008) thick PDMS sheets. Circles were cut using an 8mm Harris Uni-Core borer. This PDMS sheet was subsequently abandoned due to striations which caused optical aberrations during microscope imaging. No alternative commercial PDMS sheet was available, therefore 200μm silicone sheet (Wacker Chemie GmbH) was used instead.

Low magnification brightfield imaging was undertaken using a standard inverted microscope with 4X and 10X air objectives. Images were acquired using the camera application (Android) on a tablet connected to the microscope.

2.11.4.2 Cell viability assay

PDMS was prepared as previously described (see 2.7 Liquid PDMS preparation). Approximately 200μL PDMS was added to all wells of a 24-well plate (Thermo Scientific Ltd, 142485) using a 1,000μL pipette tip with the end removed, then set for 1 week at room temperature. The plate was plasma surface treated (see 2.6 Plasma surface treatment) and PDMS-filled wells coated in substrate (see 2.8 Substrate treatment), both as previously described. Cells were seeded and cultured for 24-72 hr at 37°C + 5% CO_2.

Cells were detached from PDMS-filled wells at 24, 48 or 72 hr using 200μL 1X trypsin (Fisher Scientific Ltd, 10584623) in 1X PBS for 5 min at 37°C + 5% CO_2. Trypsin was inactivated using 800μL complete DMEM. From each well, 10μL cell suspension was combined with 10μL 0.4% trypan blue (Sigma Aldrich, T8154-

20ML) on parafilm. From each mixture, 10µl was transferred into single chamber of dual chamber counting slide (Bio-Rad, 1450011) and analysed using a TC20 Cell Counter (Bio-Rad) using the appropriate protocol for automated cell counting. Results were noted, and processed using Excel 2013.

2.11.4.3 Mounting PDMS/silicone samples

Samples were washed with deionised water and excess liquid was removed. Silicone sheet was cut within the PDMS well region using a scalpel; the well and cell-free silicone was removed. Silicone samples were mounted in two ways: directly to a glass microscope slide, or sandwiched between a microscope slide and a coverglass.

For direct attachment, the silicone was mounted in the same way as a coverglass using 5µL ProLong Gold Antifade mounting reagent (Life Technologies, P36934) per sample. Additional care to avoid bending, folding or stretch silicone during handling was essential. Mounting reagent was set overnight (≥16 hr) at room temperature and protected from light. The edges of the silicone were sealed using clear nail varnish, then the mounted silicone surface was gently cleaned using breath and lint-free tissue prior to imaging. Extra care was taken to avoid excessive force and prevent sample damage.

For sandwich mounting, the silicone was fixed to a glass microscope slide using 5µL ProLong Gold Antifade mounting reagent (Life Technologies, P36934) with the cell-coated surface exposed. A further 10µL mounting reagent was added to the silicone, and No.1 thickness 24mm x 24mm coverglass (Agar Scientific, L46S24-1) was placed on top. Coverglass corners were fixed in place using clear nail varnish. Mounting reagent was dried overnight (≥16 hr) in darkness at room temperature. The entire coverglass edge was sealed with clear nail varnish and dried for 30 min in darkness at room temperature. The mounted coverglass surface was cleaned using breath and lint-free tissue prior to imaging.

2.11.4.4 Ink dot imaging

The stretching device was connected and calibrated by measuring the distance between moving parts (Figure 2.4B'') using a calliper before and after movement of a defined distance. A 65mm x 18mm rectangle of 200µm silicone sheet (Wacker Chemie) was mounted to the stretching device using neodymium magnets, ensuring it was taut. Any protective backing was removed, and then black ink dots were added to the sheet using a 10µL pipette tip. The device was mounted to the stage of a Nikon Eclipse inverted microscope. Timelapses were acquired in brightfield using a 4X objective before, during and after stretch application at defined distances. Further images were acquired post-relaxation of tension. Distortion of silicone sheet was calculated by measuring distances in the x-axis between ink dot centres.

2.11.4.5 Cell stretch trial

A 65mm x 18mm rectangle of 200µm silicone sheet (Wacker Chemie GmbH) was prepared with protective backing retained (Figure 2.3A-B). Along with 9cm Petri dishes, glass microscope slides, tweezers, spatula, pre-made 16mm x 16mm PDMS wells and autoclaved silicone vacuum grease, all components were sterilised using UV. Both the silicone sheet and PDMS well were washed with 70% EtOH to remove any lint

and ensure sterility. The silicone sheet was placed on top of a glass microscope slide with the silicone side exposed, and these were placed inside a 9cm Petri dish (Figure 2.3C). The PDMS well base was coated with silicone vacuum grease (Figure 2.3D), and affixed to silicone sheet so the centres of both the PDMS well and silicone sheet were aligned (Figure 2.3F); plasma surface treatment was skipped. The well was coated using collagen I (Gibco Life Technologies, A10483-01) as per manufacturer instruction for 24 hr at 37°C + 5% CO_2.

The well was aspirated and washed 3 times with sterile 1X PBS. MDA-MB-231 cells expressing EGFP-LC3B were suspended and diluted as previously described, and 2 x 10^5 cells were seeded. Cells were left to adhere for 24 hr at 37°C + 5% CO_2 (Figure 2.3G). The silicone sheet was rotated (Figure 2.3H) and mounted to the stretching device with neodymium magnets, using the glass microscope slide to provide support during mounting. Once attached, the protective backing was removed. The stretching device was mounted to the stage of a Nikon Eclipse inverted microscope within an environment chamber at 37°C + 5% CO_2. Cells were subjected to 20% or 45% elongation, and timelapses were acquired in brightfield using a 10X and 20X air objective. Distortion was calculated by measuring cell length in the x-axis.

2.11.5 Ultrasound

MDA-MB-231 cells expressing EGFP-LC3B were cultured in tissue-culture treated 6-well plates (Thermo Scientific Ltd., 140675) or individual Biolite 35mm tissue culture treated dishes (Thermo Scientific Ltd., 130180) as standard. Individual dishes were used to accommodate multiple treatment times, allowing single dishes to be removed without disturbing other conditions. For microscopy, 13mm borosilicate coverglasses (VWR International bvba, 631-0149) were included and wells/dishes were coated with fibronectin as previously described.

Ultrasound emitting 2.5cm diameter transducers (Exogen; Bioventus LLC) were held in a 2 x 3 orientation optimised for 6-well cluster plates. Cluster plates and dishes were coupled to transducers using a water-based gel (Sonotech Inc., EX-SPINE0907). The samples and transducers were both placed into a 37°C + 5% CO_2 incubator for the duration of treatment and post-treatment rest phases. Cells were subjected to 30mW/cm^2 pulsed ultrasound, 1.5MHz wave frequency, pulsed at 1kHz for times indicated in figure legend. Individual dishes or coverglass was removed and samples were liberated for fixation, immunostaining and microscopy, or for biochemical analysis.

2.12 Compound treatments

Compound treatments used were prepared to 2X concentrations as required. Final concentrations of 8Br-cGMP (Santa Cruz Biotechnology Inc., sc-200316A) and 8Br-cAMP (Santa Cruz Biotechnology Inc., sc-201564A) varied and is stated in figure legends. Stocks for both compounds were prepared in deionised water. Final concentrations for rapamycin (Alfa Aesar, J62473) and bafilomycin A1 (Alfa Aesar, J61835) were 100nM and 200nM respectively. Rapamycin stock was prepared using 100% EtOH (Fisher Scientific, E/0650/08). Bafilomycin A1 stock was prepared using 100% DMSO (AnalaR® BHD Laboratory Supplies, 103234L). Treatment times are stated in figure legends.

2.13 Amino-acid starvation

Amino acid starvation of arginine and lysine residues was used to induce autophagy without initiation of development in *Dictyostelium* (King *et al.*, 2011). Media was removed from adherent cells and cells were washed once using SIH lacking arginine and lysine (SIH-R/L; Formedium™, SIH1001), before addition of additional SIH-R/L. SIH-R/L was always supplemented with 50U/mL penicillin and 50μg/mL streptomycin (Thermo Fisher Scientific Inc., 15070-063).

2.14 Osmotic shock

Osmotic shock was achieved using sorbitol (Fisher Scientific, BP439-500) dissolved in media for hyper-OS, and deionised water for hypo-OS. A range of sorbitol concentrations were used, detailed in figure legends. Verification of increased solute concentration using sorbitol was confirmed using an osmometer (protocol detailed in 2.24 Osmolality measurements). For results refer to Appendix 7.1 (Figure 7.1).

2.15 cGMP radio-immuno assay (RIA)

Wild-type Ax2 *Dictyostelium* cells were seeded into all wells of a 6-well plate (Thermo Scientific Ltd, 140675) in complete SIH for 4×10^6 cells in 3mL per well. Plates were centrifuged at 250 x g for 1 min to settle cells, then incubated at 22°C for a minimum 1 hr prior to use. 1% agarose (w/v; Fisher Scientific, BP1356-500) in complete SIH was prepared as previously described (see 2.2.1 *Dictyostelium* (Cell Culture)) for a final volume of 70mL. Once sufficiently cooled, 60mL was transferred to a 13.9cm diameter Sterilin™ Petri dish (Thermo Fisher, 501V) and set for 30 min. Agarose discs were cut using a modified 50mL falcon lid (Fisher Scientific UK Ltd., 11819650) which was sharpened using a scalpel to create a disc punch. The agarose discs generated covered the cluster plate well almost completely. Once discs were cut, 10mL complete SIH was added to prevent agarose desiccation, which increased the likelihood of disc tearing during removal.

For compression treated cells, agarose gel discs were added to all wells and excess media removed using a narrow-ended Pasteur pipette. In-house produced compression inserts (Figure 2.1A-A'') and weights were added to all wells for 2 min. Once complete, plate was placed on ice-slush. cGMP degrades rapidly so the following steps were undertaken one well at a time. The weight and compression insert was removed and, immediately afterwards, 150μL 7% (v/v) perchloric acid (SLS, 244252-100ML) was added at the well edge under the agarose disc to preserve cGMP; final concentration ~3.5% (v/v) perchloric acid. The agarose disc was carefully removed and discarded. Cells were detached from the well using a scraper. Cell suspension was transferred to a 2mL tube on ice. This process was repeated for all 6 wells, pooling all cell suspensions. Samples were stored at -20°C.

For control treatments, 2.85mL media was removed per well and 150μL 7% (v/v) perchloric acid (SLS, 244252-100ML) was added; final concentration ~3.5% (v/v) perchloric acid. Cells were detached from the well using a scraper. Cell suspension was transferred to a 2mL tube on ice. This process was repeated for 5 wells, pooling all cell suspensions. The cGMP assay requires 2×10^7 cells per condition and an additional

well was included for compression to account for sample loss (cells attached at agarose disc). Samples were stored at -20°C until shipping on dry ice to Peter van Haastert (University of Groningen, Netherlands) who completed the cGMP RIA protocol detailed below.

Samples were thawed and centrifuged at 15,000 x g for 3 min. Supernatant was transferred and split equally into 2 fresh tubes. The pellets were retained for protein determination to normalise cGMP levels to cell count. Perchloric acid in sample supernatants was neutralised using $KHCO_3$ (50% saturated at room temperature; 2.2375M) for 30 min at room temperature, allowing CO_2 to escape; $KHCO_3$ final concentration 559mM. Samples were pH tested to confirm neutralisation.

Neutralised samples were centrifuged at 15,000 x g for 3 min. Supernatant was transferred and split into fresh tubes containing at most 0.5mL liquid. Samples were dehydrated using a Speed-Vac at 45°C for 4 hr until ~40µL per tube remained. Separated sample aliquots were recombined, and residual sample rinsed using 120µL deionised water (~280µL per sample). This was further dehydrated for 1.5 hr until sample volumes were between 50-100µL, and then stored overnight at -20°C.

Samples were thawed and water was added to each tube as required for ~100µL final volume. Samples were centrifuged at 15,000 x g for 3 min. Supernatant was transferred to tubes of known weight to ensure exact volumes for each sample were identical.

Sample cGMP concentration was determined by displacement of radioactive [3H]cGMP from an anti-cGMP antibody (in-house production by P. van Haastert, R. van Driel and P. Jansen, 1982; personal communication) with unlabelled cGMP. Outputs were compared with a cGMP concentration standard to calculate the exact values. This was completed in quadruplicate: 2 x 20µL undiluted sample and 2 x 20µL 2-fold diluted sample. Radioactivity of the antibody was determined, and cGMP concentration (pmol/20µL) was converted to pmol/10^7 cells. Values were normalised using protein concentrations from sample pellets produced previously.

2.16 Western blotting

Plates containing cells were placed on ice-slush. Media was removed with care to avoid complete desiccation of samples. Samples were washed 3 times with ice-cold 1X PBS then aspirated, again avoiding complete desiccation. Samples were scrape lysed with 1X RIPA buffer (150mM NaCl, 5mM Tris pH 7.5, 1mM EGTA, 1mM EDTA, 1% Triton X100) supplemented with 1X HALT protease inhibitor (Thermo Fisher Scientific, 78430) and the lysis buffer dispensing pipette tip. Samples were incubated on ice-slush for 5 min. Lysates were transferred to 1.5mL Eppendorfs (Starlab UK Ltd., E1415-2600) and centrifuged at 16,863 x g, 4°C, for 6 min. Supernatant was transferred to a fresh 1.5mL tube and stored on ice-slush.

Lysate concentration was determined as per standard protocol using a spectrophotometer. In a cuvette (Fisher Scientific, 11602609), 10µL sample was mixed with 1mL precision red advanced protein assay (Cytoskeleton Inc., ADV02-A) and incubated for 5 min at room temperature. The spectrophotometer (SmartSpec™ Plus Spectrophotometer, Bio-Rad, Serial No.: 273 BR07533) was blanked using lysis buffer,

then optical density (OD) was measured at 600nm. Outputs were converted to protein concentrations using a BSA protein standard described previously. Samples were either used immediately, for stored at -20°C until required.

SDS gels were prepared using Bio-Rad casting equipment and prepared either the day of use or the day before. Gels comprised a 15% acrylamide main gel with a 5% acrylamide stacking gel containing wells for sample loading. High acrylamide concentrations were used for resolution for LC3 isoforms I and II (14 and 16kDa respectively).

Glass plates (Bio-Rad) were fixed in place using a plate holder (Bio-Rad) with sponge at the base to prevent leaking. The main gel was prepared, mixed by inverting, and 4.6mL was added between the glass plates. On top of this 0.5mL isopropanol (Fisher Scientific, 10674732) was slowly pipetted to flatten the gel top surface. The main gel was set for a minimum 30 min; unused gel mix was retained to verify gel polymerisation.

Gel cassettes were removed and the isopropanol was poured away. Residual alcohol would evaporate while preparing the stacking gel. Gel cassettes were returned to the cassette holder. The stacking gel was prepared as required and mixed by inverting. To each cassette, 1.5mL stacking gel mix was added then well combs (Bio-Rad) were added, ensuring no bubbles were incorporated. Overflow liquid was removed. The stacking gel was set for a minimum 30 min; unused gel mix was retained to verify gel polymerisation.

Cast gels were placed into the gel holder (Bio-Rad) using a plastic dummy well (Bio-Rad) when necessary. The gel-containing unit was placed into the gel tank (Bio-Rad). Fresh 1X SDS (Fisher, 10552785) running buffer was added to both the gel containing unit and the gel tank. Well combs were removed. Any bubbles that formed within wells were displaced by pipetting.

Samples were prepared using lysate, lysis buffer and 4X Laemelli sample buffer (0.5M Tris-HCl pH 8.0, 10% SDS, 10% glycerol, 5% β-mercaptoethanol and 0.05 % bromophenol blue) ensuring all protein concentrations were constant. Samples were boiled at 100°C for 5 min to break disulphide bonds. Samples were briefly centrifuged to pool all liquid.

The gel was loaded using a Precision Plus Protein™ Kaleidoscope™ ladder (Bio-Rad, 161-0375) in at least the 1st lane, and where possible a central or final lane. Samples were loaded into empty wells, using an appropriate volume for the well capacity. Once complete, the gel tank lid was placed and wires were attached to a power supply. Samples were subjected to electrophoresis at 150V for 45 min, then 200V for 15 min, or until the sample buffer reach the end of the gel. This maximised resolution of LC3 isoforms.

Fresh 1X transfer buffer was prepared containing 20% MeOH. Pre-cut hybond C 45μm nitrocellulose membrane (Amersham Biosciences), 4 x pre-cut filter pads, and 2 x sponge filter pads were soaked in 1X transfer buffer. The following were added sequentially into a transfer cassette (Bio-Rad): 1 x sponge pad, 2 x filter pads, the gel, nitrocellulose membrane, 2 x filter pads, 1 x sponge pad. Between addition of each

component, bubbles were removed used a roller moistened with 1X transfer buffer. Particular care was taken ensuring no bubbles were between the gel and the nitrocellulose membrane. The transfer cassette was closed and locked, and then placed into the transfer cassette holder in the correct orientation. This was placed into a gel tank along with an ice pack, and then the entire tank was filled with 1X transfer buffer. Protein was transferred for 90 min at 100V in the cold room (4°C).

Pre-cut hybond C 45µm nitrocellulose membrane (Amersham Biosciences) and 16 x pre-cut filter pads were soaked in 1X Trans-Blot transfer buffer (Bio-Rad, 1704271). The following were added sequentially into a Trans-Blot Turbo (Bio-Rad) transfer cassette: 8 x filter pads, hybond C 45µm nitrocellulose membrane, the gel, 8 x filter pads. Between addition of each component, bubbles were removed used a roller moistened with 1X Trans-Blot Turbo transfer buffer. Particular care was taken ensuring no bubbles were between the gel and the membrane. The transfer cassette lid was placed and locked, and the cassette inserted into the Trans-Blot Turbo. Protein was transferred for 7 min using the "Turbo" option.

Protein-bound membrane was removed from the transfer cassette and briefly rinsed in deionised water. The membrane was then blocked using 5% skimmed milk powder (Tesco) in 1X PBS at room temperature on a platform shaker (40 rpm) for 30 min.

Blocking solution was removed and the membrane was briefly rinsed in deionised water. Blocked membrane was washed 3 times with 1X PBS supplemented with 0.05% Tween-20 (hereafter PBS-T; Fisher Scientific, BP337-500) at room temperature on a platform shaker (40 rpm) for a minimum 5 min per wash. Primary antibody solutions were prepared as required (see 2.30 Table of Antibodies) and 5mL was dispensed into a 50mL falcon (Fisher Scientific UK Ltd, 11819650) per antibody probed. Where appropriate, membrane was cut into fragments flanking the region containing protein(s) of interest. For protein detection by fluorescence, 2 different proteins could be probed from the same membrane. Membrane fragments were placed into 50mL falcons and incubated overnight (≥16 hr) on a tube roller at 4°C.

Membrane fragments were removed and rinsed with deionised water. Membrane fragments were washed 3 times with 1X PBS-T at room temperature on a platform shaker (40 rpm) for a minimum 10 min per wash. Secondary antibody solutions were prepared as required (see 2.30 Table of Antibodies) and 5mL was dispensed into an appropriate container. Membrane fragments were transferred to secondary antibody solutions and incubated at room temperature on a platform shaker (40 rpm) for 1 hr in darkness (secondary antibodies used for protein detection by fluorescence are light-sensitive).

Secondary antibody solution was poured off and membrane fragments were briefly rinsed in deionised water. Fragments were washed 3 times with 1X PBS-T at room temperature on a platform shaker (40 rpm) for a minimum 10 min per wash. Once complete, membrane fragments were briefly rinsed in deionised water and excess liquid removed. Fragments were sandwiched between clean filter pads and a heavy, flat weight placed on top to blot remaining liquid.

Protein detection was completed using a LiCor Odyssey unit (machine info) running Image Studio software (LI-COR Biosciences). Detection parameters were optimised for maximal signal where no over-saturated pixels were within protein bands. All acquisitions used a linear pixel-value scale, where maximum and minimum values were adjusted to best visualise protein bands. Quantification of protein signal was completed using Image Studio Lite (version 5.2; LI-COR Biosciences) software. Band selection was completed manually, with automatic background detection from the immediate area surrounding the band (built-in function). Values were normalised to a loading control.

2.17 Proteomics and phosphoproteomics

This section describes the protocol employed for determining changes in both the proteome and phosphoproteome of untreated GbpC-null cells compared with untreated wild-type Ax3 parent cells, and the changes in the phosphoproteome in response to 8Br-cGMP treatment in wild-type Ax3.

2.17.1 Set-up

Confluent *Dictyostelium* cells from 2 standard 9cm Petri dishes were suspended using 10 mL complete HL5 per dish and transferred into 500mL conical flasks containing 80mL complete HL5 (100 mL final volume). Cells were incubated in darkness at 22°C with 180 rpm shaking for 24 hr.

For each sample, 5mL 10% trichloroacetic acid (TCA; SERVA Electrophoresis GmbH, 36913.01) was aliquoted into a 50mL falcon (Fisher Scientific UK Ltd., 11819650) and placed on ice. A bottle of 100% acetone (VWR International, 20066.330) was prepared and placed on ice, containing sufficient volume for 40mL per sample. The ice-box and reagents within were stored in a 4°C cold room until later use.

The cell density of each flask was calculated using a haemocytometer and resuspension volumes were calculated for a final concentration of 1×10^7 cells/mL (untreated Ax3 and GbpC-null) or 5×10^6 cells/mL (8Br-cGMP and vehicle treated Ax3). Cell suspensions were transferred from 500mL flasks into 50mL falcons (2 falcons per flask) and pelleted at 1500 rpm for 3 min. Liquid was aspirated and cells were washed with 5mL complete SIH. If the pellet was disturbed, the samples were centrifuged again as described above. Liquid was aspirated, and the wash step was repeated once more. Cell pellets were resuspended in the required volume of complete SIH, with separated cultures pooled together again. For each condition, 5mL cell suspension was transferred into a 50mL glass conical flask. Cells were incubated in darkness at 22°C with 180 rpm shaking for 1 hr.

2.17.2 8Br-cGMP treatment

This section only applies to phosphoproteomic analysis of Ax3 cells treated with 8Br-cGMP. Prior to addition of treatments the ice box, containing acetone and 10% TCA aliquots, was brought from the cold room to cell suspensions due to the brief treatment period.

Cell were treated 8Br-cGMP (Santa Cruz Biotechnology Inc., sc-200316A) for a final concentration of 5 mM, or a vehicle control (deionised water), for 2 min. Incubation remained at 22°C with 180 rpm shaking where possible.

2.17.3 Protein sample preparation

The ice box containing the acetone and 10% TCA aliquots was brought to the cell suspensions to facilitate rapid transfer. After removal from the orbital shaker flasks were be briefly vortexed by hand to resuspend any sedimented cells. Cell suspensions were decanted into separate 10% TCA aliquots, giving a final concentration of 5% TCA. Samples were kept on ice and stored in a 4°C cold room for 1 hr to lyse cells and precipitate protein.

Lysates were pelleted using a benchtop centrifuge at 3000 x g, 4°C, for 10 min. Liquid was aspirated and each pellet was washed twice with 20 mL ice-cold acetone. Addition of acetone was completed very slowly and with minimal force to prevent pellet fragmentation. If fragmentation occurred, prior to aspiration samples were centrifuged again to reconstitute the pellet (3000g, 4°C for 10 min). After the final wash step the pellet was air dried until excess acetone evaporated (~15 min). Sample pellets were not allowed to desiccate completely as they became impossible to completely resolubilise. Samples were stored at -80°C.

2.17.4 Sample solubilisation

From this point onwards, all subsequent buffers and reagents for proteomic and phosphoproteomic analysis were prepared using HPLC water (VWR International, 23595.328).

Protein pellets were transferred to individual 2mL Eppendorfs using a sterile standard pipette tip. Remaining protein pellet was washed out using 500µL solubilisation buffer (8M urea; Sigma, U0631-500G), 0.1M ammonium bicarbonate (ABC; Sigma, A6141-25G) and transferred to the 2mL Eppendorfs. Samples were solubilised for 1 hr at room temperature. If necessary, a D160 Homogenizer (Scilogex, 850101019999) was used to disrupt the pellet (1 s bursts, speed 3, 5 times) followed by a further 15 min incubation at room temperature. If unsuccessful the process was repeated at maximum speed followed by a further 15 min incubation at room temperature. The sonicator probe was washed between uses with 70% EtOH (Fisher Scientific, E/0600DF/17).

2.17.5 Sample reduction and alkylation

To solubilised protein, 10µL 0.5M Tris(2-carboxyethyl)phosphine (TCEP) hydrochloride solution (Sigma, 646547-10X1ML) was added for a final concentration of 10mM. Samples were mixed by inverting, then incubated on a heated shaker at 37°C with 550 rpm shaking for 20 min. 20 µL 0.5 M iodoacetamide (Sigma, I6125-10G) was added for a final concentration of 20mM. Samples were protected from light and incubated at 37°C with 550 rpm shaking for 20 min. Samples were diluted using 1.5 mL 0.1 M ABC then split equally across 2 x 2mL Eppendorfs (1mL each). A further 1mL 0.1M ABC was added to each tube, totalling 3.5mL per sample, to dilute urea to 1M.

2.17.6 Trypsin digestion

Preliminary tests had been undertaken to determine the protein yield for samples produced using the above protocol. Samples containing 5×10^7 cells yielded approximately 2mg protein, and samples using 2.5×10^7 cells yielded approximately 1mg. Protein concentrations were calculated as previously described using a BSA (Fisher Scientific, BP-1600-100) protein standard (see 2.23 Protein standard curve).

Mass-spectrometry grade lyophilised trypsin aliquots (Fisher Scientific Ltd, 90058) were resuspended using 100μL 0.1% trifluoroacetic acid (TFA; Sigma, T6508-25ML) per aliquot and stored on ice (final concentration 1μg/μL trypsin). Trypsin was added to samples at a weight ratio of 1:40 trypsin:protein sample. For 2mg untreated Ax3 and GbpC-null samples, 50μL 1μg trypsin/μL was added per sample (25μL per 2mL tube). For 1mg 5mM 8Br-cGMP or vehicle treated Ax3 samples, 25μL 1μg trypsin/μL was added per sample (12.5μL per 2mL tube). Samples were digested for 16 hr at 37°C with 550 rpm shaking and protected from light.

2.17.7 Desalting and protein fragment purification

Samples were run through reverse-phase tC18 SepPAK solid-phase extraction cartridges (Waters, WAT023501) to remove urea and salts prior to strong cation exchange (SCX) analysis. One cartridge was used per sample. Extraction cartridges were sequentially washed and conditioned by slowly flowing through 10mL 100% HPLC gradient grade acetonitrile (ACN; Sigma, 34851-2.5L-M) followed by 5mL 50% ACN, 0.1% TFA (Sigma, T6508-25ML). Extraction cartridges were then equilibrated using 10mL 0.1% TFA.

Trypsin enzyme in the digested protein sample was inactivated after 16 hr using 8μL 100% TFA per 2mL sample; final concentration 0.4% TFA, pH 3. Samples were mixed by inverting, then centrifuged at 16,863 x g, room temperature, for 20 min to pellet insoluble material. Sample supernatant was loaded to extraction cartridges, pooling previously separated sample aliquots. Sample supernatants were very slowly run through the extraction cartridges, and the run-through was collected. This was re-loaded to extraction cartridges and run through twice more to ensure all peptide was bound to the cartridge. After the third loading step, the sample run-through was retained and stored at -80°C as a precaution. Each extraction cartridge was washed with 10mL 0.1% TFA. Finally, the peptide fragments were eluted from the extraction cartridge using 2mL 50% ACN, 0.1% TFA and collected in a fresh 2mL Eppendorf. Eluted peptides were stored at -20°C prior to desiccation using a SpeedVac.

2.17.7.1 Preppy™ vacuum manifold

A Preppy™ vacuum manifold (Supelco, 57160-U) was used to facilitate processing of multiple samples in parallel during desalting and protein fragment purification steps detailed above. The device included a chemical-resistant cover and gasket, glass basin, vacuum release vent and 12 individual flow control valves with stainless steel solvent guide needles. Additional components included 15mL collection vessel racks (Supelco, 57162-U), 4mL collection vessel racks (Supelco, 57159-U), vacuum gauge/bleed valve assembly (Supelco, 57161-U), 10mL luer-slip syringes (BD Emerald™, 307736) and both 4mL and 15mL glass vials.

Glass vials (15mL) were placed into the appropriate collection rack within the glass basin of the device, then the cover/gasket was placed on top. Extraction columns were fixed into the control valves, and the syringe barrel only (no plunger) was fixed into the extraction column. All control valves were closed tightly, and appropriate buffer was added to syringe barrels. The vacuum gauge/bleed valve was opened to vent the glass basin and prevent vacuum, and then the air pump was switched on. Individual flow control valves with extraction columns attached were opened slightly. The vacuum gauge/bleed valve was slowly closed to apply vacuum to the glass basin, which was monitored by the gauge needle. Individual flow control valves were manipulated independently to regulate liquid flow rate across all samples. Individual flow control valves were closed before all liquid was drawn through. Once liquid for all samples had passed through and all flow controls were closed, the vacuum gauge/bleed valve was opened to vent the glass basin. The manifold was removed and collection vials emptied or retained as necessary. The above steps were repeated for all washing, loading and eluting stages. Note that 4mL glass vials were used for the final eluting step.

2.17.8 IMAC purification

Ion-metal affinity chromatography (IMAC) purification uses positively charged metal ions to bond negatively charged phosphorylated peptides for phosphoproteomic analysis. This section only applies to phosphoproteomic analysis.

Desiccated samples were resuspended in 400μL 50% ACN, 0.1% TFA, and then vortexed for 1 min. Samples were then incubated at 25°C with 700 rpm orbital shaking for 30 min while preparing IMAC purification.

PHOS-Select™ Iron Affinity Gel (Sigma, P9740), hereafter referred to as "resin", was warmed to room temperature and shaken vigorously prior to pipetting. Using a standard 200μL pipette tip with the end removed, 110μL resin was transferred to a 2mL Eppendorf. This was to accommodate the viscous resin and yield the required minimum 100μL. One tube containing resin was prepared for each sample. Resin was washed 3 times: 1mL 50% ACN, 0.1% TFA added to resin, resin centrifuged at 1000 rpm for 1 min, and then wash buffer was removed using a 200μL gel-loading pipette tip in contact with the tube base to prevent resin aspiration. Peptide samples were centrifuged at 16,863 x g, room temperature, for 5 min to remove insoluble material. Sample supernatant was transferred to resin-containing tubes to bind phosphopeptides to resin, incubated at 25°C with 700 rpm orbital shaking for 45 min. Original sample-containing tubes were retained.

Approximately 1.5cm was cut off from the tapered end of a 1000μL pipette tip. The larger fragment was forced into the open end of a 200μL TopTip pipette tip (Glygen, TT2EMT.96), and then the excess plastic cut away. This created a tight fixture to attach a 5mL syringe; hereafter referred to as TopTip[+] (Figure 2.5). One TopTip[+] was prepared per sample, and placed into a tip-holder mounted within the original sample-containing tubes. Phosphopeptide-bound resins were transferred to TopTip[+], and supernatant was pushed through into the sample tubes using a 5mL syringe. From this point onwards the resin was never desiccated

otherwise bubbles would get trapped within and prevent elution of phosphopeptides. The residual phosphopeptide-bound resin was washed out using 100μL 50% ACN, 0.1% TFA and transferred to the TopTip⁺. Excess liquid was pushed through. Supernatant was retained and stored at -20°C as a precaution.
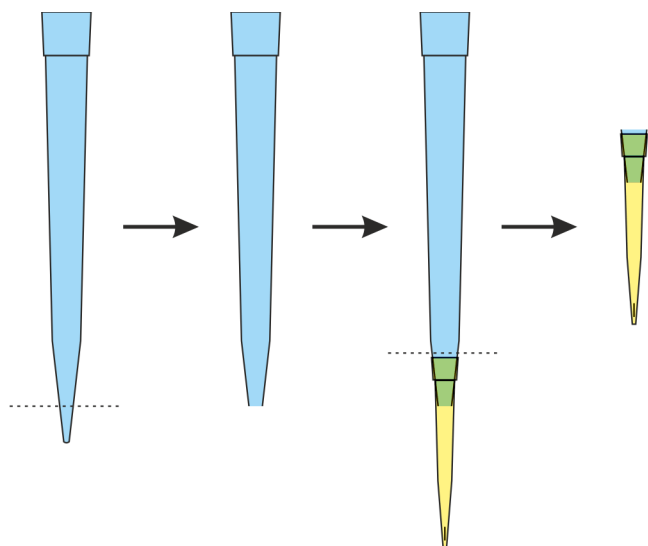
Figure 2.5 **TopTip⁺ preparation.** Standard 1000 μL pipette tip (blue) cut with scalpel at dotted line approximately 1.5 cm from open end. Larger fragment retained and inserted with force into 200 μL TopTip pipette tip (yellow; Glygen, TT2EMT.96). Scalpel used to remove excess plastic from 1000 μL pipette tip at dotted line. Resulting TopTip⁺ allowed attachment of 5 mL syringes for subsequent steps.

Resins were washed 3 times with 100μL 50% ACN, 0.1% TFA, once with 100μL 1% acetic acid and once with 100μL HPLC water (VWR International, 23595.328). Waste run-through liquid was disposed of. Phosphopeptides were then eluted using 75μL 0.5% ammonia (Merck, 1.05428.0250) pH 11.3 elution buffer. Elution buffer was added to TopTip⁺ and a small volume of liquid was pushed through to bathe resin in elution buffer. Run-through was collected in a new 2mL tube. Samples were incubated for 5 min at room temperature to dissociate phosphopeptides from resin. A small volume was pushed through again, collected in the same receptacle. Samples were incubated for a further 5 min at room temperature. These 2 steps were repeated until all liquid had been removed from the resin. Eluted samples were neutralised with 9μL formic acid (Fisher, A117-50) and dried down using a speedvac.

2.17.9 LC-MS/MS analysis

Samples were re-suspended in 40 μl of 0.5% formic acid and 18ul was analysed by nanoflow LC-MS/MS using an Orbitrap Elite (Thermo Fisher) hybrid mass spectrometer equipped with a nanospray source, coupled to an Ultimate RSLCnano LC System (Dionex). The system was controlled by Xcalibur 3.0.63 (Thermo Fisher) and DCMSLink (Dionex). Peptides were desalted on-line using an Acclaim PepMap 100 C18 nano/capillary BioLC, 100A nanoViper 20 mm x 75 μm I.D. particle size 3 μm (Fisher Scientific) at a flow rate of 5 μl/min and then separated using a 125-min gradient from 5 to 35% buffer B (0.5% formic acid in 80% acetonitrile) on an EASY-Spray column, 50 cm × 50 μm ID, PepMap C18, 2 μm particles, 100 Å pore size (Fisher Scientific) at a flow rate of 0.25 μl/min. The Orbitrap Elite was operated with a cycle of one MS (in

the Orbitrap) acquired at a resolution of 60,000 at m/z 400, with the top 20 most abundant multiply charged (2+ and higher) ions in a given chromatographic window subjected to MS/MS fragmentation in the linear ion trap. An FTMS target value of 1e6 and an ion trap MSn target value of 1e4 were used with the lock mass (445.120025) enabled. Maximum FTMS scan accumulation time of 500 ms and maximum ion trap MSn scan accumulation time of 100 ms were used. Dynamic exclusion was enabled with a repeat duration of 45 s with an exclusion list of 500 and an exclusion duration of 30 s.

2.17.10 Mass-spectrometry analysis

2.17.10.1 General

Raw data from MS was processed by Dr. Mark Collins (TUoS). All raw mass spectrometry data were analysed with MaxQuant version 1.6.2.6. Data were searched against a *Dictyostelium discoideum* UniProt sequence database (June 2018) using the following search parameters: digestion set to Trypsin/P with a maximum of 2 missed cleavages, oxidation (M), phosphorylation (STY) and N-terminal protein acetylation as variable modifications, cysteine carbamidomethylation as a fixed modification, match between runs enabled with a match time window of 0.7 min and a 20-min alignment time window, label-free quantification enabled with a minimum ratio count of 2, minimum number of neighbours of 3 and an average number of neighbours of 6. A first search precursor tolerance of 20ppm and a main search precursor tolerance of 4.5 ppm was used for FTMS scans and a 0.5 Da tolerance for ITMS scans. A protein FDR of 0.01 and a peptide FDR of 0.01 were used for identification level cut-offs.

Protein group and Phospho STY output files generated by MaxQuant were loaded into Perseus version 1.5.6 (25). The matrix was filtered to remove all proteins that were potential contaminants, only identified by site and reverse sequences. The LFQ intensities/phosphorylation site intensities were then transformed by $\log_2(x)$, normalised by subtraction of the median value and individual intensity columns were grouped by experiment. Proteins/phosphorylation sites were filtered to keep only those that had a minimum of 3 valid values in at least one group. The distribution of intensities of was checked to ensure standard distribution for each individual replicate. Missing values were randomly imputed with a width of 0.3 and downshift of 1.8 from the standard deviation. In order to identify significant differences in protein expression or phosphorylation, two-sided Student's t- tests were performed with a permutation-based FDR calculation (FDR = 0.05).

Processed data output from Perseus was handled using Microsoft Excel. Proteomic and phosphoproteomic datasets were cross-referenced for comparison, and significant and/or interesting results were further investigated using available literature and online databases.

2.17.10.2 Basic Local Alignment Search Tool (BLAST)

Dictyostelium genes with altered phosphorylation status in response to 8Br-cGMP treatment were compared with reference databases, particularly mammalian organisms, to identify conversed phosphosites. This was completed using the UniProt BLAST tool (Bateman, 2019).

2.17.10.3 Gene Ontology analysis

Gene ontology (GO) was completed using PANTHER 14.1 (Mi *et al.*, 2019). Lists of genes exhibiting increased or decreased expression, or phosphorylation status, were compared against the *Dictyostelium discoideum* reference list for GO enrichment analysis for biological processes, cellular compartment and molecular function. Enrichment was determined using the Fishers exact test with False Discovery Rate correction within the PANTHER online platform.

2.17.10.4 Consensus sequence alignment

Protein sequences flanking sites of phosphorylation status change in response to 8Br-cGMP treatment were analysed to identify consensus sequences. Sequences extending beyond the N- or C-termini were omitted as alignments could only run using sequences of identical length. For genes with 2 viable sequences e.g. genetic redundancy, both were included.

Alignments were completed using online pLogo (O'Shea *et al.*, 2013) using complete or refined sequence lists e.g. phosphoserine only, increased phosphorylation only etc. Recommended settings were used which are described briefly. Parameters used included removal of duplicate sequences in both foreground and background, and the subtraction of foreground sequences from background. All outputs were exported as 300dpi PNGs. The background was generated using the complete list of FASTA format protein sequences from DictyBase.org (Eichinger *et al.*, 2005).

2.18 Cell fixation for immunostaining

2.18.1 Ultra-cold methanol fixation

This protocol was used for *Dictyostelium* fixation. A 100mL glass beaker and coverglass holder were chilled using dry ice within a deep polystyrene box. Immediately prior to cell fixation, the beaker was placed on top of the dry ice, supported by a Petri dish lid and the coverglass holder placed within. The beaker was filled with approximately 60mL ultra cold (-80°C) methanol (Fisher Scientific, M/4058/PB17). Cell-coated coverglass was removed from media using inverted forceps (SLS, Z168769-1EA) and excess liquid was blotted. The coverglass was plunged into the methanol at a slight angle, cell-side up. The submerged coverglass was placed into the coverglass rack. Tweezers were rinsed in 1X PBS to remove residual methanol, and the process was repeated for all coverglasses. Cells were simultaneously fixed and permeabilised for 30 min. Coverglasses were removed using inverted forceps and washed 4 times by vertical submersion in 1X PBS, with excess liquid removed by blotting between wash steps. This wash process was repeated twice more using 2 new beakers of 1X PBS. Samples were placed into a 6-well plate containing 1X PBS and observed under a microscope to confirm samples remained attached, then placed onto blocking solution for immunostaining.

2.18.2 Paraformaldehyde fixation

This protocol was used for mammalian cell fixation. Cells were prepared and treated as required. The majority of liquid media was removed leaving a known remaining volume. A volume of 1X PBS equal to the

remaining media volume was added to samples, mixed briefly, and then an equal volume was removed. 2X 8% paraformaldehyde (PFA; Fisher Scientific, P/0840/53) in 1X PBS was added to samples; final concentration 4% PFA. Samples were fixed for 15 min at room temperature in darkness (primarily for protection of GFP-tagged proteins). Once elapsed, all liquid was aspirated and samples were washed 3 times with 1X PBS. Residual fixative was quenched using 0.1M glycine (Fisher Scientific, G/0800/60) in 1X PBS in darkness for 15 min at room temperature. Wells were aspirated and samples were washed 3 times with 1X PBS.

2.19 Immunocytochemistry

2.19.1 Permeabilisation

Mammalian cells were permeabilised using 1mL 0.1% Triton-X100 (Fisher Scientific, BP151-100) in 1X PBS in darkness for 15 min at room temperature. Once elapsed, all liquid was aspirated and samples were washed 3 times with 1X PBS.

2.19.2 Blocking

Both *Dictyostelium* and mammalian samples were blocked using 2% (w/v) BSA (Fisher Scientific, BP-1600-100) in 1X PBS for a minimum of 30 min at room temperature in darkness.

2.19.3 Antibody staining

Antibody vials were vortexed several times, and then briefly centrifuged. This ensured a homogenous suspension and sedimented any antibody aggregates. Primary antibody staining solutions were prepared to the required concentration in 2% BSA in PBS (see 2.30 Table of Antibodies). Immunostaining was completed under static conditions at room temperature for 1 hr in darkness. Samples were washed 3 times in 1X PBS.

Secondary antibody stains were prepared to the required concentration in 2% BSA in PBS (see 2.30 Table of Antibodies) for binding the primary antibody epitope. Secondary antibodies were linked to a fluorophore for protein detection by fluorescence microscopy. Samples were incubated for 1 hr under static conditions, room temperature, in darkness. Samples were washed 3 times in 1X PBS.

2.20 Counterstaining

Nuclei were visualised using either 4',6-diamidino-2-phenylindole (DAPI) or 1X Hoechst 33342 at 1.5µg/mL in 1X PBS for 5 min in darkness. DAPI-containing mounting reagents were avoided due to inconsistent staining across samples, and within the same sample. For live-cell staining (mammalian only) cells were incubated for 30 min in complete media containing DAPI or Hoechst prior to treatment or imaging, particularly for compression which physically obstructs staining. Cells were washed with 1X PBS then fresh media added.

Phalloidin CruzFluor™ 594 Conjugate (Santa Cruz Biotechnology Inc., sc-363795) was used to visualise F-actin in mammalian cells and prepared as per manufacturer instruction, however working solutions of 0.1X

were found to be effective. Samples were incubated on a rocking platform for 45 min in darkness at room temperature. Sample permeabilisation was essential.

2.21 Sample mounting for microscopy

Samples were washed with deionised water and excess liquid was removed. Coverglasses were mounted to glass microscope slides using 5µL ProLong Gold Antifade mounting reagent (Life Technologies, P36934) per sample. Mounting reagent was dried overnight (≥16 hr) in darkness at room temperature. Once dry, the entire coverglass edge was sealed with clear nail varnish and dried for 30 min in darkness at room temperature. The mounted coverglass surface was cleaned using breath and lint-free tissue prior to imaging.

2.22 Fluorescence microscopy

Imaging was predominantly undertaken using a Perkin-Elmer Ultraview VoX spinning disk confocal microscope, comprising an Olympus Ix81 body. All imaging of mammalian cells, except for LSS, was completed using this microscope with the UplanSApo 60x (NA 1.4) oil immersion objective. This objective was used for most *Dictyostelium* image acquisition, except timelapses of GFP-atg8/RFP-lifeAct expressing cells which used the UplanSApo 100x (NA 1.4) oil immersion objective. Cells were illuminated using 405nm, 488nm, and 561nm laser lines as required with appropriate filters. Images were captured on a Hamamatsu C9100-50 EM-CCD camera using Volocity software. Image processing was completed using ImageJ prior to analysis.

The *Dictyostelium* autophagosome formation timelapse was acquired using a Zeiss Axiovert LSM 880 Airyscan confocal microscope with a 63x Plan Apochromat oil objective (NA 1.4). Cells were illuminated using a 488nm argon laser. Images were initially processed using Zen software (Zeiss) followed by standard processing using ImageJ.

2.23 Protein standard curve

BSA (Fisher Scientific, BP-1600-100) was dissolved in appropriate buffer, e.g. RIPA lysis buffer, and serially diluted to concentrations ranging from 0-8mg/mL. In a cuvette (Fisher Scientific, 11602609), 10µL standard preparation was mixed with 1mL precision red advanced protein assay (Cytoskeleton Inc., ADV02-A) and incubated for 5 min at room temperature. The spectrophotometer (Bio-Rad) was blanked using appropriate buffer, then optical density (OD) was measured at 600nm. The gradient was calculated using only linear OD readings and used to determine protein concentrations of samples e.g. western blotting.

2.24 Osmolality measurements

Osmolality was quantified using a Vapor Pressure Osmometer (Wescor® Biomedical Systems, Model 5600) to determine the concentration of solute in liquid media. Due to device sensitivity, changes in ambient temperature affected readings; measurements were only taken when the on-screen indicator fell within functional range. Thorough cleaning was essential before use and between sample measurements to

prevent contamination. The device was calibrated using Reagecon Diagnostics Ltd osmolality standards of defined osmolality; 100 (RE-OSM-100), 290 (RE-OSM-290) and 1000 (RE-OSM-1000) mOsm/Kg. Osmolality standards were used within one month of opening. A tolerance of ±5 mmol/Kg was applied during calibration.

A sample disc (Wescor® Biomedical Systems, SS-033) was placed into the sample chamber using forceps. A 2-step pipette was used to transfer 10µL sample onto the sample disc and then measured. The measurement was displayed on screen and recorded, then the used sample disc removed. The sample chamber was cleaned thoroughly, and the above process repeated for all samples. If multiple readings of a single sample were taken, the stored memory was erased prior to measurement as the device would calculate mean and standard deviations (up to 15 measurements).

The device has an automated cleaning protocol which was used after all measurements were taken. For samples with extremely high concentrations of protein and/or solute the likelihood of sensor contamination increased. Where outputs varied substantially from previous results the auto-clean protocol was run prior to further measurements.

2.25 Analysis and statistical testing

For manual quantification of microscopy images, files within a dataset were automatically randomised to an indistinguishable filename (range: Image001-Image999) using a modified Excel spreadsheet (MS Excel 2013). Quantification was then cross-referenced against a table containing original and randomised filenames.

For automated quantification, scripts were written and run using ImageJ (version 1.49i-1.52n). Scripts used are provided in Appendix 7.6.

Data handling was completed using Microsoft Excel (version 2013). All statistical tests were completed using GraphPad Prism (versions 6.05, 7.02, 8.0.1, 8.1.1), except for mass-spectrometry analysis (see 2.17 Proteomics and phosphoproteomics). Unpaired two-tailed T-tests were employed without post-hoc correction unless otherwise indicated. The only exception to this was for 24 hr 8Br-cGMP time-course data which employed Welch's correction due to highly inconsistent standard deviation.

2.25.1 *De novo* puncta tracking

Timelapse images of *Dictyostelium* cells expressing GFP-atg8 treated with 8Br-cGMP or vehicle controls were acquired between 5-15 min post-treatment. Individual cells which remained within the field of view (FOV) for the duration of the acquisition were tracked and XY coordinates noted. A script used these coordinates to generate a cropped timelapse for each tracked cell, facilitating easier puncta tracking Appendix 7.7. *De novo* puncta formation was completed manually using the Manual Tracking plugin in ImageJ. Results were processed in MS Excel.

2.26 Graphs and figures

All figures and diagrams were prepared using CorelDRAW® X7 (versions 17.1.0.572 and 17.5.0.907). Final versions of graphical data were generated using GraphPad Prism (version 8.1.1). Microscope images were processed post-acquisition using ImageJ (version 1.49i-1.52n). Any adjustments to brightness and contrast all used linear scales.

2.27 Table of *Dictyostelium* cell lines

Name	Parent	Genotype	Resistances	Source/creator	Dictybase Strain ID	Clone No.	Notes
Ax2	Ax1 (DBS0237979)	*axeA2, axeB2, axeC2*			DBS0235521		
Ax3		*axeA1, axeB1, axeC1*					
Ax3	NC4	*axeA1, axeB1, axeC1*		Peter van Haastert (University of Groningen, Netherlands)	DBS0237700		
adcA⁻	Ax3	*axeA1, axeB1, axeC1, adcA-, bsR*	Blasticidin	DictyBase Stock Center	DBS0349906		
dokA⁻	Ax2	*axeA2, axeB2, axeC2, neoR, dokA-*	Neomycin	DictyBase Stock Center	DBS0235920		Neomycin (G418) antibiotic
dstC⁻	Ax2	*axeA2, axeB2, axeC2, dstC-, hygR*	Hygromycin	DictyBase Stock Center	DBS0238125		
krsA⁻	Ax2 (DBS0350762)	*axeA2, axeB2, axeC2, krsA-, [bsRcas], bsR*	Blasticidin	DictyBase Stock Center	DBS0350759		
pzoA⁻	Ax2 (DBS0235521)	*axeA2, axeB2, axeC2, pzoA-, [bsR-loxP], bsR*	Blasticidin	Robert Kay (Medical Research Council Laboratory of Molecular Biology)	DBS0351499	1812	
pzoA⁻	Ax2			Robert Kay (Medical Research Council Laboratory of Molecular Biology)		1813	Unpublished piezoA- clone 1813
gcA⁻	Ax3 (DBS0237700)	*axeA1, axeB1, axeC1, gcA-, bsR*	Blasticidin	Peter van Haastert (University of Groningen, Netherlands)	DBS0350119		
sgcA⁻	Ax3 (DBS0237700)	*axeA1, axeB1, axeC1, sgcA, [pUCBΔBam], bsR*	Blasticidin	Peter van Haastert (University of Groningen, Netherlands)	DBS0350888		
gcA⁻ /sgcA⁻	gcA⁻ (DBS0350119)	*axeA1, axeB1, axeC1, gcA-, sgcA-, bsR, hygR*	Blasticidin, hygromycin	Peter van Haastert (University of Groningen, Netherlands)	DBS0302679		
gbpC⁻	Ax3 (DBS0237700)	*axeA1, axeB1, axeC1, gbpC-, bsR*	Blasticidin	Peter van Haastert (University of Groningen, Netherlands)	DBS0302680		
atg1⁻	Ax2 (DBS0235525)	*axeA2, axeB2, axeC2, atg1-, bsR*	Blasticidin	Jason King (University of Sheffield, UK)	DBS0350450		

Table 2.1. *Dictyostelium* cell lines used with supporting information.

2.28 Table of Mammalian cell lines

Cell Line	Expression Vector	Source	Info	Media	Supplements
MDA-MB-231	n/a	K. Ryan	Breast cancer epithelia cells	DMEM (Thermo Fisher Scientific Inc., 21969-035)	10% FBS (Thermo Fisher Scientific Inc., 10270-106)
					2mM L-glutamine (Thermo Fisher Scientific Inc., 25030-024)
					1X 50U/mL penicillin, 50μg/mL Streptomycin (Thermo Fisher Scientific Inc., 15070-063)
MDA-MB-231 (GFP-LC3B)	EGFP-LC3B	K. Ryan	Breast cancer epithelia cells	DMEM (Thermo Fisher Scientific Inc., 21969-035)	10% FBS (Thermo Fisher Scientific Inc., 10270-106)
					2mM L-glutamine (Thermo Fisher Scientific Inc., 25030-024)
					1X 50U/mL penicillin, 50μg/mL Streptomycin (Thermo Fisher Scientific Inc., 15070-063)
HUVEC	n/a	Paul Evans lab (University of Sheffield, UK)	Human umbilical vein endothelial cells	M199 (Sigma Aldrich, M0650)	20% FBS (Thermo Fisher Scientific Inc., 10270-106)
					0.1ng/mL EGF (Sigma Aldrich, C-39210)
					90μg/mL Heparin (Sigma Aldrich, C-39210)
					2.5μg/mL Amphotericin B (Sigma Aldrich, A2942)
					50U/mL penicillin, 50μg/mL Streptomycin (Thermo Fisher Scientific Inc., 15070-063)

Table 2.2 Mammalian cell lines used with supporting information.

2.29 Table of Plasmids

Plasmid ID	Description	Gene ID	Resistance
pDM430	GFP-atg8		G418
pJSK500	GFP-atg8		Hygromycin
pJSK622	GFP-atg8, RFP-lifeAct		G418

Table 2.3 Plasmids used for *Dictyostelium* transformation

2.30 Table of Antibodies

Primary Antibody	Source	Immunocytochemistry		Western blot		Ordering
		Liquid	Dilution	Liquid	Dilution	
αLC3B (2G6)	Mouse	1X PBS, 2% BSA	1:500 (HUVEC) 1:1,000 (MDA-MB-231)			Nanotools, 0260-100/LC3-2G6
αLC3B	Rabbit			1X PBS, 3% BSA	1:1,000	Cell Signalling, 2775S
αTubulin mAb Rat YL1/2	Rat			1X PBS, 3% BSA	1:1,000	Gift from Ralph Graf

Table 2.4 Primary antibodies

Secondary Antibody	Source	Immunocytochemistry		Western blot		Ordering
		Liquid	Dilution	Liquid	Dilution	
Alexa Fluor® 594 goat anti-mouse IgG (H+L)	Goat	1X PBS, 2% BSA	1:500 (HUVEC) 1:1,000 (MDA-MB-231)			Invitrogen, A11032
Goat anti-Rabbit IgG (H+L), DyLight 800	Goat			5% milk in 1X PBS-T	1:10,000	Thermo Fisher Scientific, SA5-35571
Goat anti-Rat IgG (H+L), DyLight 680	Goat			5% milk in 1X PBS-T	1:10,000	Insight Biotechnology Ltd, 072-06-16-06

Table 2.5 Secondary antibodies

2.31 Table of Microscopes

Microscope	Objective lenses	Excitation source	Emission filters	Detectors	Body/Stage Type	Add ons	Software
Perkin-Elmer Ultraview VoX spinning disk confocal	UplanApo 60x oil immersion (NA 1.4) UplanSApo 100x oil immersion (NA 1.4)	405nm, 488nm, 561nm laser lines	DAPI, GFP, TxRed	Hamamatsu C9100-50 EM-CCD camera	Olympus IX81 Prior rotary encoded XY stage; Prior 200μm z-piezo		Volocity
Zeiss Axiovert LSM 880 Airyscan confocal	63x Plan Apochromat oil immersion (NA 1.4)	488mm argon laser, 561nm diode laser	n/a	AiryScan, GaAsP detector and galvo scanner	Zeiss LSM 880 invert based on Axio Imager.Z	Environmental control chamber	Zen
Nikon Widefield (LMF)	Apo 60x oil (NA 1.4)	SpectraX LED excitation (470nm)	Single filter for GFP	Dual Andor Zyla sCMOS; 2560 x 2160; 6.5μm pixels	Mad City Labs Z-Piezo 100μm; Nikon motorised stage	Environmental control chamber	NIS Elements
Zeiss Axiovert 100 widefield	Plan Apochromat 63x oil immersion (NA 1.4)			Hamamatsu Orca ER	Axiovert 100		μManager (Edelstein et al., 2010, 2014)
Nikon Eclipse Widefield	4X, 10X, 20X and 40X air objectives	Bright-field	n/a	Unknown	Nikon motorised stage	Environmental control chamber	MetaMorph
TC microscope	4X, 10X and 20X air objectives	Bright-field	n/a	Tablet camera application			Android

Table 2.6 Microscopes used with supporting information

Chapter 3

Investigating the mechanical stimulation of autophagy

3.1 Introduction

Mechanical forces are physical motions which impact on molecules and structures. They are ubiquitous in life, affecting individual proteins through to tissues and whole organisms. The effect they cause varies, determined by multiple factors: frequency, magnitude, direction and mechanism of action. These characteristics determine whether the force is instructive, destructive or both. Regarding physiology, mechanical forces can be broadly categorised into 3 groups. Compression is the application of antiparallel forces which converge on a cell, reducing cell height. Stretch is the opposite of compression, with antiparallel force vectors radiating from a central cell. Fluid shear forces are borne of friction against the cell periphery, comprising the plasma membrane and ECM. Depictions of these forces, and their impact on cells, are shown in Figure 3.1. How a force manifests depends on the environment and circumstance, but all have the capacity to disrupt homeostasis and prevent nominal cell function. Therefore cells must be able to detect and adapt to these physical cues to maintain viability.
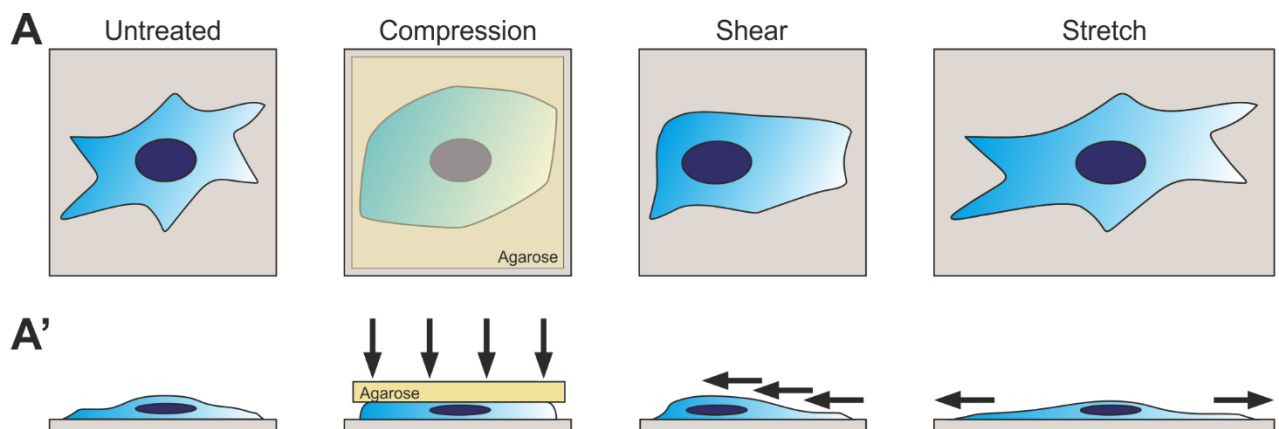
Figure 3.1 **Stylised schematic of mechanical forces.** Changes in environment impact cell architechture. Examples of mechanical forces affecting the cell structure are shown from (A) an aerial perspective and (A') a lateral cross-section. (A') Arrows indicate the force direction impacting the cell. During compression, the surface beneath the cell resists the applied force in an opposing, anti-parallel, manner (not indicated) which compresses the cell between.

A direct link between compression and autophagy was first described by (King *et al.*, 2011) in both *Dictyostelium* and a mammalian cell line. Following this, several studies have been published evidencing links between autophagy and compression (Ma *et al.*, 2013; Teng *et al.*, 2011), shear (Das *et al.*, 2018; Dong *et al.*, 2017; Liu *et al.*, 2015) and stretch (Inaba *et al.*, 2017; Porter *et al.*, 2014) forces. This suggests autophagy may be a general response to mechanical stress, however at present no study has tested multiple mechanical forces in parallel. A diverse range of stimuli have been shown to induce autophagy. This, along with the various publications described above, suggest it is plausible that mechanical forces, in all their manifestations, are part of this array of stimuli. Furthermore, it raises the question of whether a universal signalling pathways is responsible for mediating mechanically-induced autophagy. Several signalling pathways have been put forward as mediators of this induction, however each appears to be unique to the mechanical force. Studying each of these forces in unison could address both these questions simultaneously.

In this chapter, it was aimed to directly test whether induction of autophagy is a general response to mechanical force. To achieve this, a variety of methods for application of different mechanical forces were employed. Specifically regarding stretch forces, a system was developed to image live-cells under strain at high resolution. Additionally, the effect of ultrasound was tested as, while not a physiological force *per se*, soundwaves are a physical force and have been shown to promote wound healing (Roper *et al.*, 2015). The results will provide the foundation for further study aiming to determine the signalling responsible for autophagy induction by mechanical stimuli.

3.2 Results

3.2.1 Compression

Under compression cell height is reduced, internal pressure increases and autophagy is induced (King *et al.*, 2011). To visualise this in greater detail, *Dictyostelium* wild-type Ax2 cells were transfected to express RFP-lifeAct and resolve the actin cytoskeleton. The autophagy marker, GFP-atg8, was co-expressed to reveal both cytosol and autophagic structures. Cell shape and structure of uncompressed cells was heterogeneous, with projections and uneven upper surfaces (Figure 3.2A-A''). Upon addition of compression apparatus, the cell top surface became flattened and cell height reduced (Figure 3.2B-B''). Cortical actin (red) revealed membrane blebs arising from increased intracellular pressure (Figure 3.2B, B''; arrows). After 10 min of continuous compression cell surface area greatly increased, cell height was approximately halved, and GFP-atg8 puncta were more abundant (Figure 3.2C-C''). Compression causes rapid changes in cell structure, which demand cellular adaptation.

The initial discovery that compression induced autophagy in *Dictyostelium* utilised wild-type Ax3 (King *et al.*, 2011). Our standard wild-type lab strain is Ax2, which lacks a large genome duplication found in Ax3 (www.Dictybase.org). Consequently, I wanted to verify whether the response observed in Ax3 also occurred in Ax2. Rapid image acquisition allowed individual puncta to be tracked during compression, verifying structures were genuine autophagosomes with a characteristic lumen (Figure 3.2D; arrowhead). The autophagic response to compression was shown to be proportional to the force applied in Ax3 (King *et al.*, 2011), and this was confirmed in Ax2. Application of low (0.36 kPa) and high (1.3 kPa) compressive force elicited a proportional autophagic response (Figure 3.2E-F). Furthermore, the autophagic response to mechanical induction was greater than to amino acid starvation (Figure 3.2E-G) which, again, corroborated findings in Ax3 (King *et al.*, 2011). The maximal response in Ax2 was at least 2-fold greater for both mechanical and starvation stimuli relative to Ax3. These results confirmed our Ax2 lab strain was responsive to mechanical stimulation in the context of autophagy, comparable to Ax3, and suitable for use here.
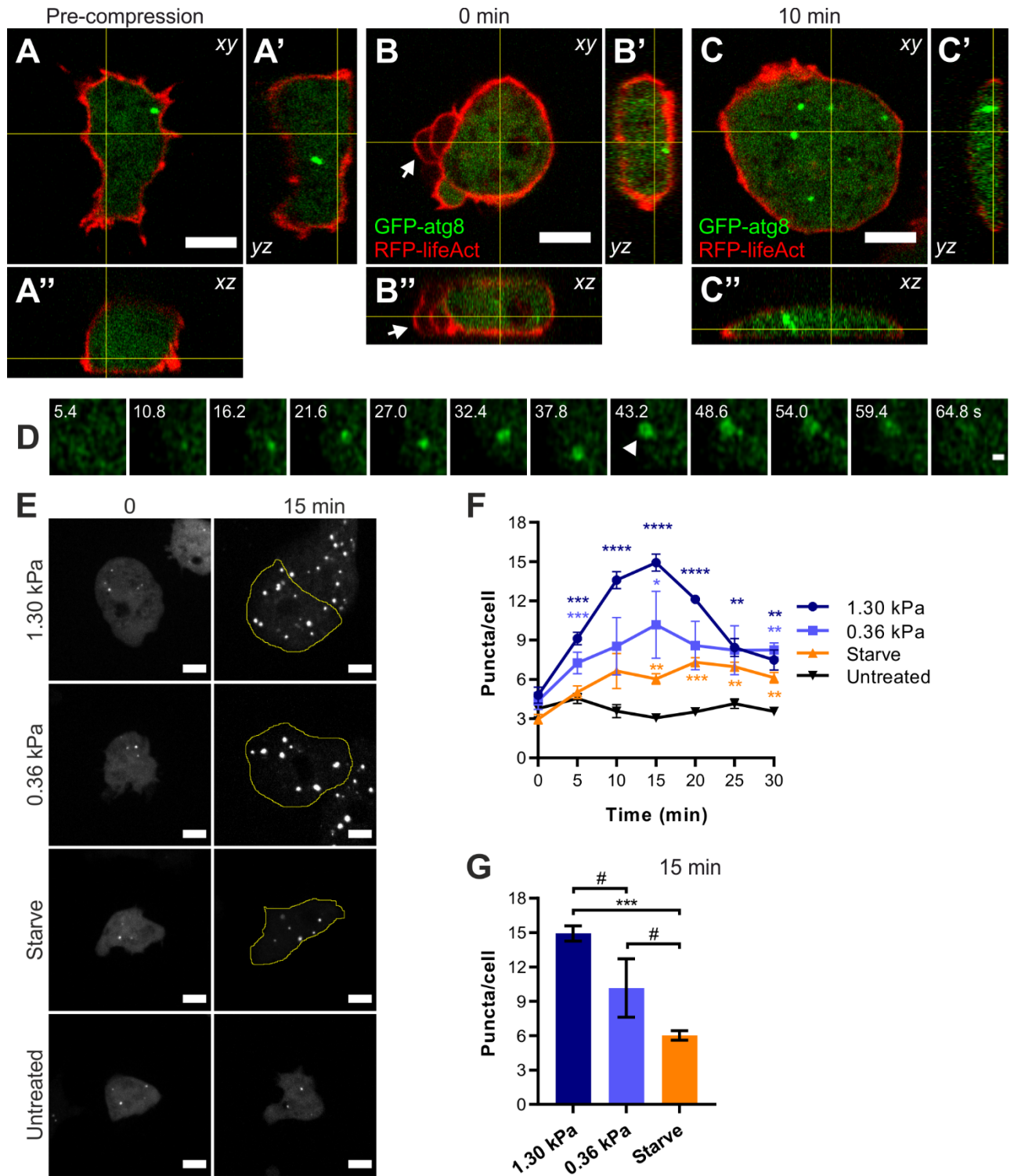
Figure 3.2 **Mechanically induced autophagy in *Dictyostelium*.** Wild-type Ax2 expressing the autophagy marker GFP-atg8 subjected sustained compression. (A-C) Single Ax2 cell co-expressing GFP-atg8 and RFP-lifeAct, indicating autophagic structures and actin cytoskeleton respectively, subjected to 0.83 kPa compression. (A-A") Pre-compression cell. (B-B") Cell immediately after addition compression apparatus and (C-C") after 10 min compression. (A-C) Yellow lines indicate cross sections used for generating orthogonal projections in *xz* (A"-C") and *yz* (A'-C'). Scale bars = 5 µm. (B, B") White arrows denote membrane blebs. (D) Formation and lifetime of an autophagosome indicated using GFP-atg8 in Ax2. White arrowhead denotes completed autophagosome with a lumen. Scale bar = 1 µm. (E) Representative images of GFP-atg8 expression in Ax2 under compression. Arginine/lysine amino acid starvation included as positive control; untreated as negative control. Scale bars = 5 µm. (F) Quantification of mean average puncta per cell (74-147 cells quantified per data point). Error bars denote SEM (n = 4 independent repeats for 1.30 kPa, n = 3 for other conditions). Significance determined using unpaired 2-tailed t-test (# $P \geq 0.05$, * $P < 0.05$, ** $P < 0.01$, *** $P < 0.001$, **** $P < 0.0001$) comparing compression or starvation to untreated control. (G) Data from (F) at 15 min comparing stimuli using same statistical method.

3.2.2 Shear

The effect of shear force on autophagy was unclear, with literature indicating different variations of force yielding different results. MDA-MB-231 cells were shown to be mechano-responsive to compression which induced autophagy (King *et al.*, 2011), however it was unknown if shear force would also affect autophagy. Using a syringe pump system, cells expressing the autophagy marker EGFP-LC3B were subjected to different levels of LSS for up to 1 hr (Figure 3.3A). Cells adopted a rounder morphology in response to LSS, indicating a response to the stress, although the cause is unclear (Figure 3.3B). Quantification of puncta showed a decrease for both 1 and 2 dynes/cm^2, with the larger force inducing a more rapid reduction (Figure 3.3C). As a single experimental repeat, statistical testing was no appropriate. It was plausible the reduction in puncta arose from provision of fresh nutrients as chambers contained minimal media. This would have been tested by subjecting cells to extended periods of LSS, however the experimental setup was limited by the syringe volume which, in turn, restricted maximal treatment time. Attempts to replicate the protocol with *Dictyostelium* were unsuccessful due to their low adhesion, causing the majority of cells to detach upon force application (data not shown). Preliminary results indicate LSS could prevent autophagy initiation but further study is required.
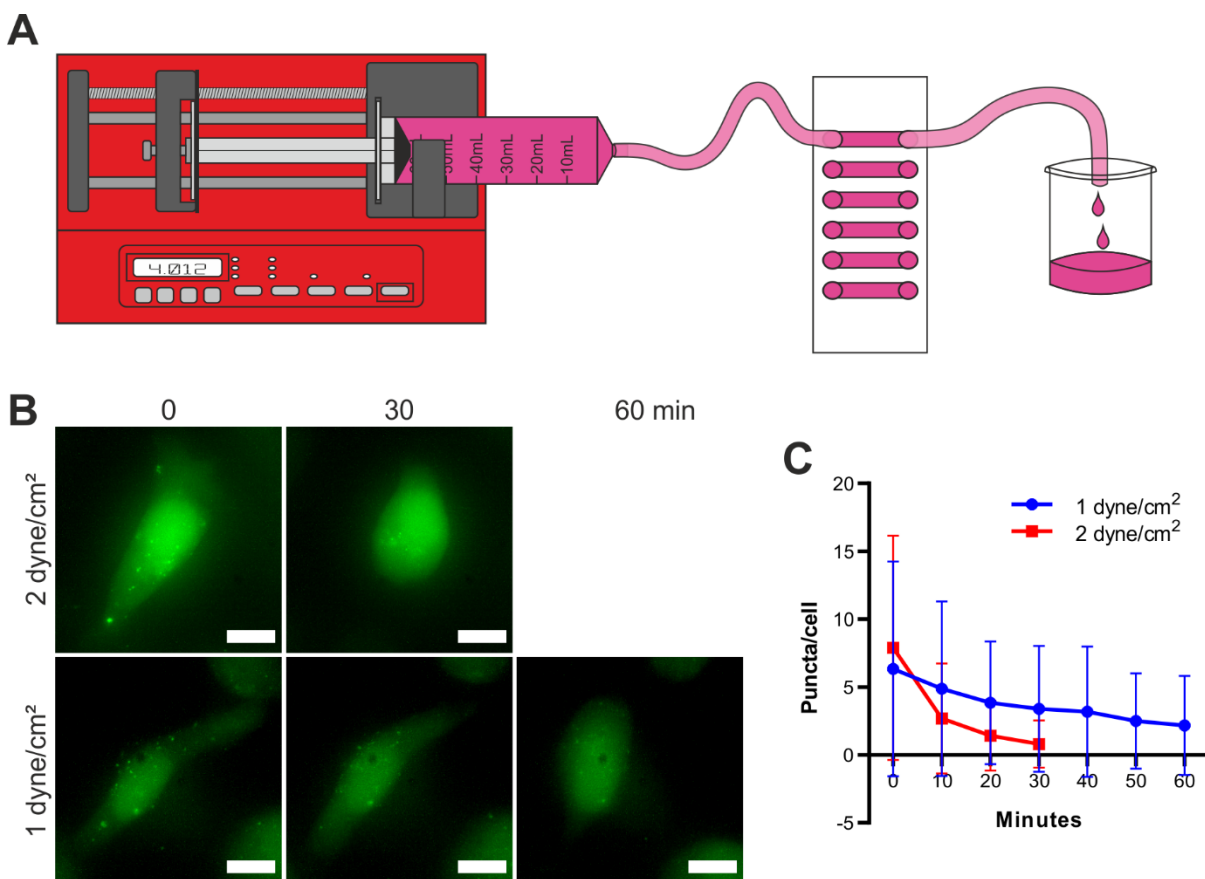
Figure 3.3 **Effect of laminar shear force on autophagy.** MDA-MB-231 cells expressing EGFP-LC3B subjected to laminar shear force up to 1 hr using syringe pump system. (A) Stylised depiction of experimental setup using NE-1000 syringe pump (New Era Pump Systems Inc.) to apply laminar shear stress (LSS) to cells seeded in tissue culture treated ibidi™ micro-channel slides. Live-cell imaging through slide base using inverted microscope. (B) Representative images shown for 1 and 2 dyne/cm^2. Scale bars = 10 μm. (C) Quantification of puncta per cell, where error bars denote SD (single experiment).

An alternative established method of studying shear forces utilises a plate shaking system which allows testing of both high intensity unidirectional oscillatory, and low-intensity multidirectional shear forces, simultaneously (Figure 3.4A). This was first described by Tsao *et al.*, (1995) as an alternative to the cone-plate viscometer devices established by (Dewey *et al.*, 1981) developed to study LSS. Shear forces are not uniform using the plate-shaking method, and vary depending of the proximal location of cultured cells within the well (Figure 3.4B); this has been computationally modelled and is included within the aforementioned figure (Warboys *et al.*, 2014). Therefore, the orbital shaking method described by Warboys *et al.* (2014) was utilised given the computational analyses of the force throughout the well. Human umbilical vein endothelial cells (HUVECs) are well established as shear-sensitive and commonly used for studying the effects of shear stress (Sigurdson *et al.*, 1993), and were therefore tested in parallel. Again, *Dictyostelium* were deemed unsuitable as cells detached readily even at reduced rpm rates.
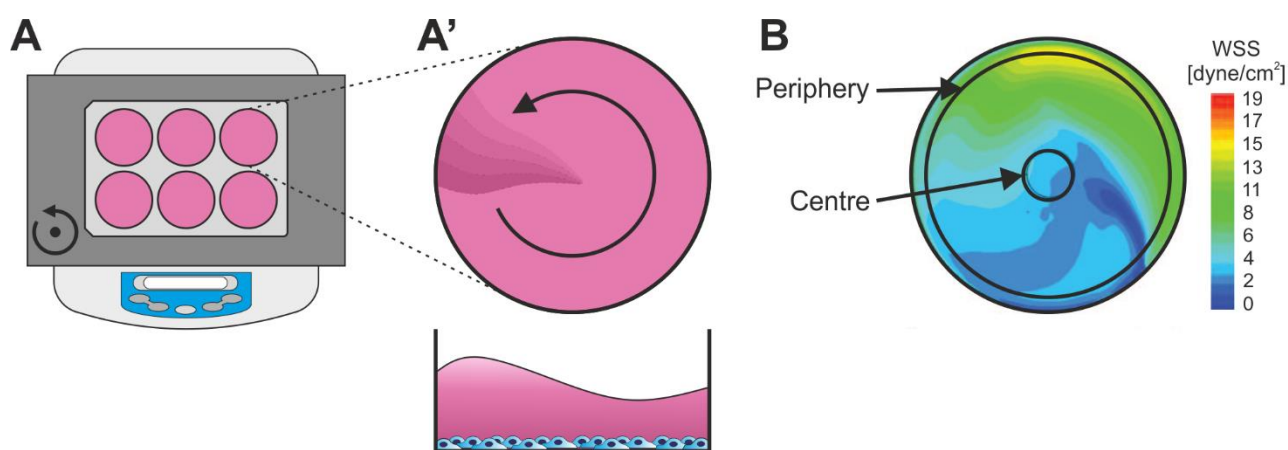
Figure 3.4 **Schematic of orbital shaking protocol.** (A) Cells were cultured in a standard 6-well plate which was fixed in place upon an orbital shaker platform. When switched on, the constant rotation generated a wave within each well which subjected the cells below to shear stress. (A') A magnified view from above depicting a single well, where wave direction is indicated. A lateral perspective highlights the wave more clearly. (B) Adapted figure from Warboys CM *et al.* (2014) who, using computational analysis, quantified the wall shear stress (WSS) affecting the cells below. The centre region of the well exhibits low shear (~2 dyne/cm^2), whereas at the periphery, where the wave manifests, the shear stress is much greater (~15 dyne/cm^2) and pulsatile.

MDA-MB-231 and HUVEC cells were subjected to orbital shaking to determine the effect on autophagy. Figure 3.5A shows representative images of both lines. Acquisitions were taken at the centre and peripheral regions of the well for low-intensity multidirectional and high-intensity unidirectional shear stress respectively. Although not clearly visible by LC3B immunostaining, during image acquisition under brightfield there were obvious differences in HUVEC morphology between central or peripheral locations. At the well boundary cells were oriented longitudinally parallel to the force, whereas in the central region cell shape was not uniform or directional. This was consistent with previous findings by (Dong *et al.*, 2017). Additionally, the sporadic perinuclear structures observed in HUVECs (Figure 3.5A) were detected in 1° antibody-free controls (Figure 3.5E) suggesting they were not genuine autophagic structures or due to suboptimal immunostaining (marked with arrowheads). MDA-MB-231 cells did not exhibit any morphological changes in any proximal location at any timepoint. This discrepancy suggests detection and response to shear varies between mechanosensitive cell lines.
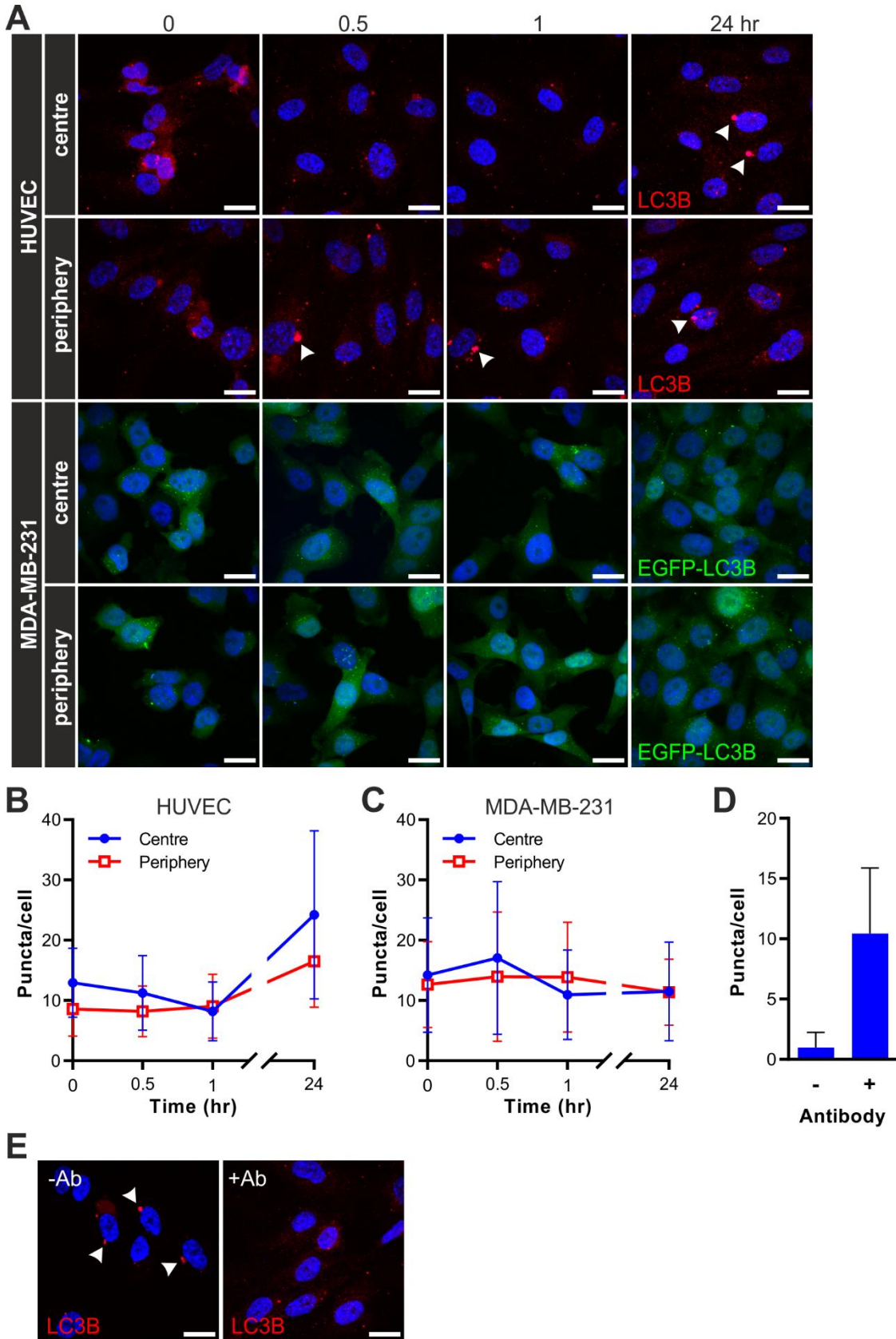
Figure 3.5 **Autophagy induction in shear-force specific mechano-sensitive cells.** MDA-MB-231 cells expressing EGFP-LC3B and HUVECs were subjected to shear forces by orbital shaking. (A) Representative images showing LC3B visualised by immunocytochemistry (HUVECs; red) or GFP-labelling (MDA-MB-231; green). Quantification of LC3B puncta for (B) HUVECs and (C) MDA-MB-231, where error bars denote standard deviation. (D) Primary antibody-free control in HUVECs, where error bars denote standard deviation. (E) Representative images for controls. (A, E) Scale bars = 20 μm. Arrowheads indicate autofluorescent aggregates identified in HUVECs, with signal detected in all channels.

Visual observations showed no obvious change in puncta counts in either cell line. However, upon quantification, while this was verified in MDA-MB-231 (Figure 3.5C), at 24 hr an increase was detected in HUVECs in both central and peripheral regions (Figure 3.5B). These preliminary findings in HUVECs are consistent with literature which showed shear force induced autophagy in HUVECs/endothelial cells. LC3B detection differed between cell lines and consequently alternative means of quantification were employed. GFP-LC3B puncta in MDA-MB-231 were counted manually, whereas immunostained LC3B in HUVECs were analysed using ImageJ. No statistical tests were completed as this was a single experimental repeat. Quantification of an antibody-free control is shown in Figure 3.5D, with representatives in Figure 3.5E. Together these results suggest MDA-MB-231 cells are not shear-responsive, unlike HUVECs, and shear stress can induce autophagy in specialised, responsive cells.

3.2.3 Ultrasound

Ultrasound is a sound wave with a frequency above audible range (>20 kHz) for human beings. Sound occurs through physical vibrations and is a mechanical forces in its own right. The application of ultrasound has garnered interest as a means of promoting wound healing although the mechanisms are largely unknown. It was initially shown that ultrasound at 1.35 W/cm^2 could induce autophagy in nasopharyngeal carcinoma CNE2 cells (Wang *et al.*, 2011), however observations were made 24 hr afterwards. The earliest indication of a causal link between ultrasound and autophagy was in 2013 where the conversion of LC3-I to LC3-II occurred 30 min after ultrasound treatment, with increased stimuli magnitude generating a greater conversion (Wang *et al.*, 2013). We therefore performed several exploratory tests attempting to reproduce these results with our cell line. This was completed in collaboration with Dr. Mark Bass (University of Sheffield, UK), whose laboratory specialised in the development of therapeutic ultrasound.

A standard medical ultrasound device was employed, repurposed to apply treatment to 6-well cluster plates. MDA-MB-231 cells expressing the autophagy marker EGFP-LC3B were subjected to ultrasound for a typical treatment period of 20 min (Figure 3.6A). After ultrasound treatment and a 40 min rest period, no substantial change was detected in puncta counts (Figure 3.6B). Western blots probing for LC3B under the same conditions indicated a minor reduction in both isoforms after 20 min (Figure 3.6C-D), but no striking changes were observed. Conversion of LC3B-I to LC3B-II and subsequent PE conjugation is indicative of autophagic flux. The ratio between LC3B isoforms remained largely unchanged under all conditions tested (Figure 3.6E). These preliminary results suggested autophagy was not affected immediately after ultrasound treatment using our experimental setup.

As positive controls, the protocol was repeated and modified to include autophagy manipulating treatments, and both extended treatment and acquisition times. Ultrasound stimulation was applied for 60 min with samples fixed during and after treatment. Ultrasound is known to affect the cytoskeleton therefore samples were stained with Alexa Fluor™ 594 Phalloidin to visualise any change. After 30 min actin staining intensity at the cell periphery was reduced (Figure 3.7A). Additionally, no obvious change in GFP$^+$ puncta was detected. Representative images at 60 and 120 min are shown in Figures 3.7B and
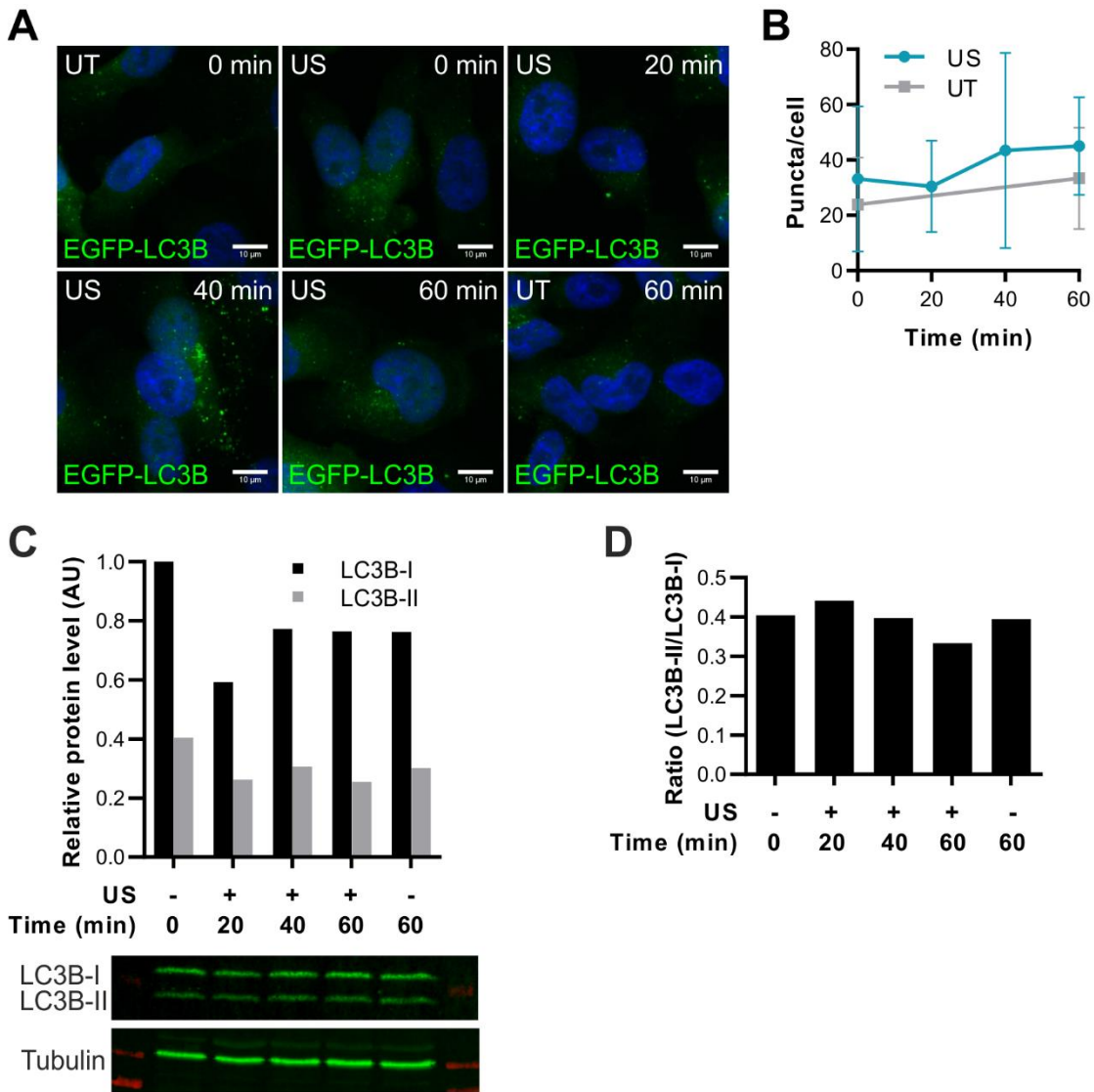
Figure 3.6 **Preliminary data suggests short-term ultrasound has no effect on autophagy.** MDA-MB-231 cells expressing EGFP-LC3B stimulated with ultrasound (US) or untreated (UT). (A) Representative images showing cells subjected to 20 min ultrasound stimulation followed by recovery, where samples were taken at the timepoints indicated. Untreated controls at 0 and 60 min. Scale bars = 10μm. Nuclei counterstained using DAPI. (B) Quantification of images in (A), where data points represent mean average puncta per cell under the conditions indicated. Bars denote SD (n = 21-32 cells per condition). (C) Densitometry measurements of LC3B-I and -II bands normalised to the tubulin loading control determined by Western blot. Protein bands below graph aligned with the measurements above. (D) Ratio of LC3B-II/LC3B-I bands shown calculated from results in (C). All data from single experiment.

3.7C respectively. Quantification of puncta per cell confirmed no difference after 30 min ultrasound treatment irrespective of bafilomycin A_1 co-treatment (Figure 3.7D). At both 60 and 120 min, ultrasound and untreated conditions were comparable. Rapamycin only induced a minor increase, although this was less than expected. When ultrasound was combined with bafilomycin A_1 treatment, the puncta count was greater than bafilomycin A_1 alone, and more similar to the rapamycin/bafilomycin A_1 positive control. This suggested ultrasound could, in fact, could be inducing autophagy, although replication is required for statistical analyses.
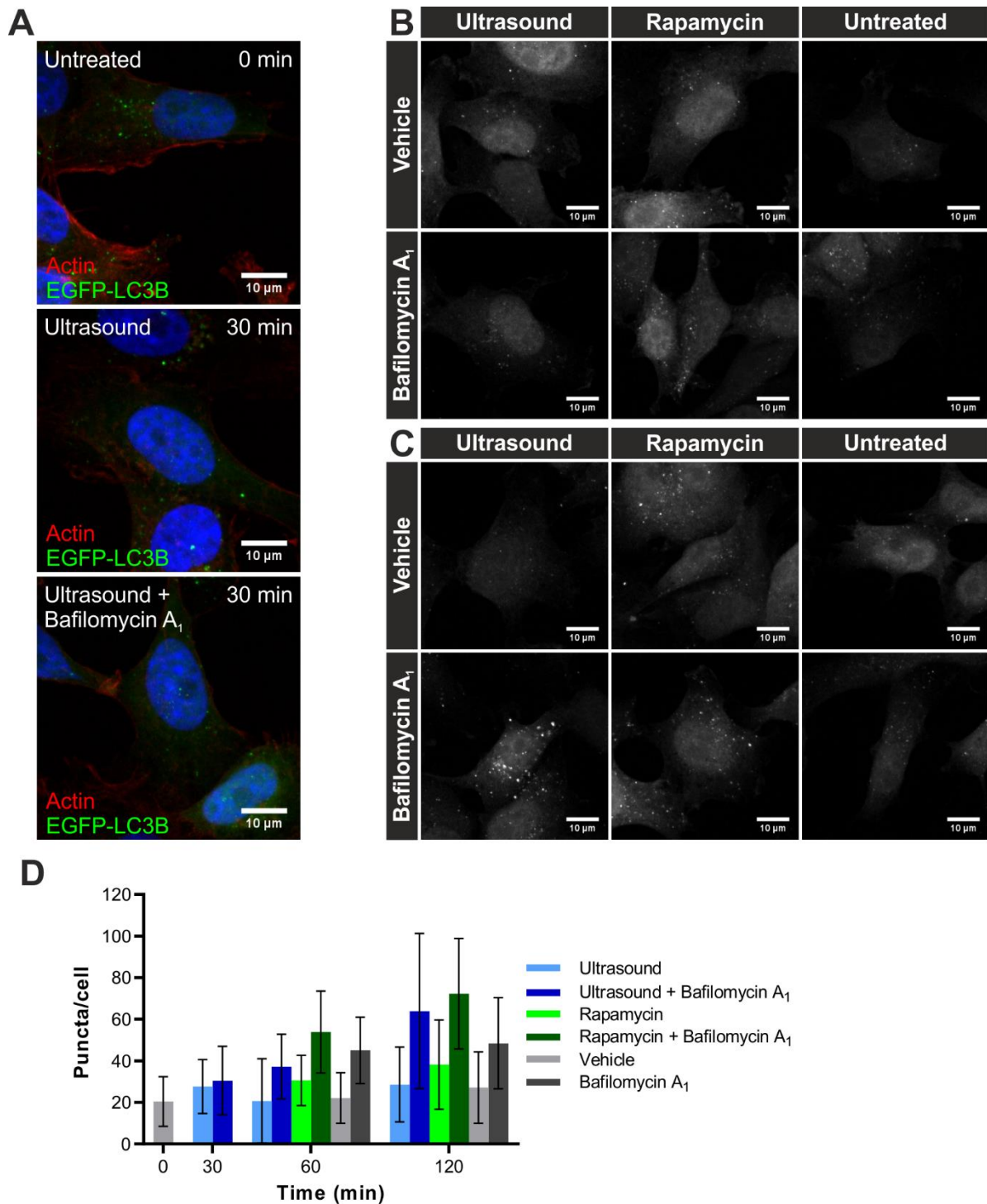
Figure 3.7 **Ultrasound and autophagy.** MDA-MB-231 cells expressing EGFP-LC3B stimulated using ultrasound, rapamycin, Bafilomycin A₁, dual-treatments or vehicle. Ultrasound stimulation was maintained for up to 60 min, followed by 60 min recovery. All other treatments were maintained for the durations indicated. (A) Representative images under conditions indicated. The nuclei and actin cytoskeletons were counterstained with DAPI (blue) and Phalloidin CruzFluor™ 594 Conjugate (red) respectively. Representative images showing EGFP-LC3B fluorescence in cells under conditions indicated after 1 hr (B) and 2 hr (C). Scale bars = 10 μm (A-C). (D) Quantification of images in (A-C) showing average puncta per cell under conditions indicated. Bars denote SD (n = 40-68 cells per condition; one bar extends beyond axis). All data from single experiment.

3.2.4 Stretch

To study the effects of stretch forces cells need to be cultured either on an elastic surface which permits distortion, or in a manner allowing direct application of force. Several studies have achieved this, however the methods employed vary substantially and each have limitations. Live-cell imaging techniques were

64

typically small-scale involving a minimal number of cells and consequently prevented biochemical assays, such as western blotting, to be undertaken. Systems which utilised larger samples did allow for biochemical testing however live-cell microscopy was not possible. Furthermore imaging was completed using relaxed samples which were subsequently fixed, losing structural changes arising from stretch. Using elements from different methodologies it was aimed to develop a novel system capable of live-cell imaging, which also used sufficient cellular material to permit biochemical analyses.

Polydimethylsiloxane (PDMS) is a silicon-based substance used in a variety of applications as it is optically clear, elastic and mouldable. Microfluidic devices had been produced using PDMS to study the effects of shear forces (Queval *et al.*, 2010) or generate organ-on-chip style systems (Beaurivage *et al.*, 2019; Fetah *et al.*, 2019; Sontheimer-Phelps *et al.*, 2020). Additionally, cells had previously been cultured on PDMS and subjected to stretch (Hecht *et al.*, 2012). Together, these show cells can be cultured on this material. Seemingly trivial changes to external environment, such as binding to different molecules on the surface, can have drastic effects on a cell. As a stress response, autophagy is prone to activation by a range of stimuli. It was therefore critical to optimise conditions for PDMS-based cell culture to minimise stress and maintain low basal autophagy.

Initial tests indicated MDA-MB-231 cells were able to bind untreated PDMS, although much less efficiently compared with tissue-culture treated (plasma treated) polystyrene cluster plates. We therefore attempted to optimise cell binding using different PDMS types, and pre-treating with different adhesion ligands. Two forms of PDMS were used during testing: in-house cured PDMS and commercially available thin sheets. The first attempt to culture cells involved cured PDMS which had been aliquoted into a 24-well plate. This produced a smooth, flat and highly hydrophobic surface which cells bound to poorly (data not shown). The PDMS sheets were striated (see Figures 3.8A-C) and yielded a marked improvement in adhesion and morphology. However, cells preferentially bound polystyrene despite substrate coating of both surfaces (Figure 3.8A). When provided with only a PDMS surface to bind, cells did adhere, albeit with differing morphology compared to polystyrene-bound cells (Figure 3.8B). Comparison of several common adhesion substrates indicated fibronectin improved cell adhesion most based upon similar morphology to polystyrene-cultured cells, although cells still preferred polystyrene (Figure 3.8C). It was concluded the substrate treatments were not binding the PDMS efficiently due to its hydrophobicity, and that pre-treatment with plasma would improve this.

Plasma treatment bombards surfaces with high energy ions to disrupt chemical bonds. It generates hydrophilic surfaces for cell adhesion and is commonly used for the tissue-culture treating of standard polystyrene consumables. Plasma treatment is also used to temporarily activate PDMS surfaces allowing bonding for microfluidic device production. PDMS was plasma treated prior to addition of substrates to determine if cell adhesion and morphology improved, and whether proliferation was affected. After 24 hr no major differences were detected in proliferation or viability (Figure 3.8D). Morphology, however, was

improved with substrate coated surfaces, and more so when pre-treated with plasma; plasma treatment alone had no effect. A similar trial experiment with reduced seeding density, to accommodate
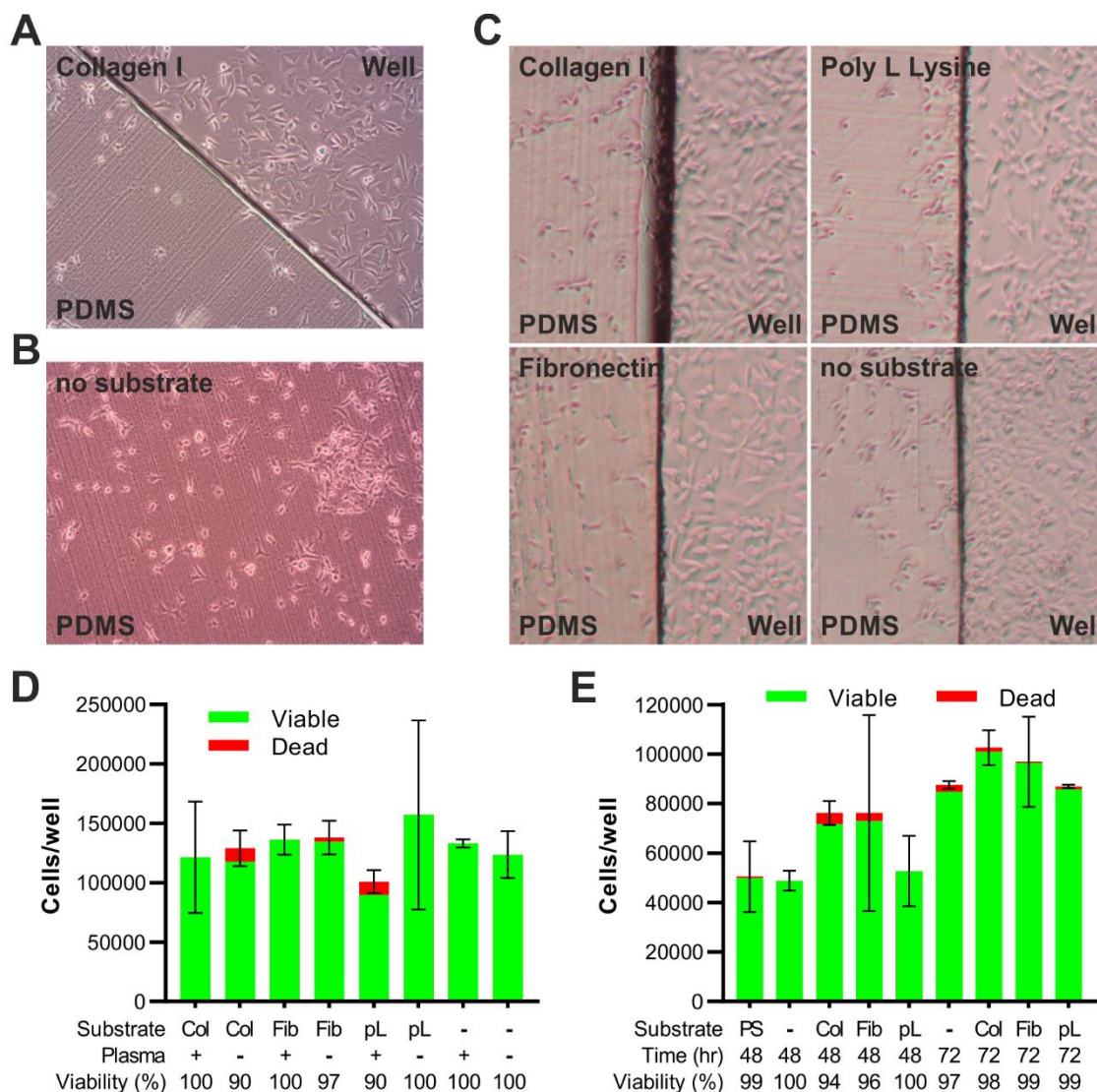
Figure 3.8 **Culturing cells on silicone surfaces.** Multiple conditions tested to determine optimal parameters for culturing mammalian cells on hydrophobic silicone-based surfaces. (A) Cell attachment after 24 hr on PDMS film placed within polystyrene well, where both surfaces were coated with Collagen I. (B) Cell attachment after 48 hr on untreated PDMS film. (C) Cell attachment after 24 hr on PDMS film placed within polystyrene well. Both surfaces coated using substrate indicated. (D) Cell proliferation and viability after 24 hr in PDMS wells coated with collagen I (Col), fibronectin (Fib), poly-L-lysine (pL) or uncoated (-), with or without plasma pre-treatment. (E) Cell proliferation and viability after 48-72 hr in plasma-treated PDMS wells coated with substrates indicated as described for (D). PS denotes TC-treated polystyrene well control. (D-E) Error bars denote SD of total cell counts (single experiment). Cell count and viability calculated using trypan blue staining, where samples were loaded into dual chamber slides and analysed using a TC20 Cell Counter (Bio-Rad).

longer incubation times and global plasma treatment, showed increased cell density for both fibronectin and collagen I coated PDMS after 48 hr (Figure 3.8E). By 72 hr the variation between conditions was less pronounced. Visual observation using a standard brightfield inverted microscope indicated cell morphology was improved by substrate treatment at both timepoints. PDMS surfaces were therefore treated with plasma followed by surface coating, using either collagen I or fibronectin, to ensure optimal culture conditions in all future experiments.

To identify the effect of stretch on autophagy in live-cells, it needed to be determined if: A) high resolution images could be acquired through silicone-based sheet, and B) culturing cells on silicone surfaces had any impact on basal autophagy. Cells were cultured on substrate-treated PDMS prior to fixation and mounting as depicted in the schematic Figure 3.9A-A'. Images were acquired through both glass and silicone (Figure 3.9B). Cells could be visualised through either medium, however the striations of the PDMS caused optical aberrations and reduced image quality. No alternative commercial PDMS sheet was available, therefore ultra-clear silicone sheet was used in subsequent experiments. As with PDMS sheet, dual-treatment of ultra-clear silicone sheet, with both plasma and substrates, allowed effective cell adhesion and comparable morphology to polystyrene cultured cells. Additionally, basal autophagy did not appear to be negatively affected (Figure 3.9C). The cells appeared slightly elongated but similar to standard culture conditions (Figure 3.9D). Immunostaining of LC3B was unaffected by the silicone and high-resolution images were acquired with no unexpected fluorescence (Figure 3.9E). Together these findings indicated silicone sheet could be used to culture cells without inducing stress, was compatible with immunostaining, and permitted high-resolution image acquisition.

With the cell culture system finalised, we next tested the stretching device. The precursor device was designed and manufactured by Dr Simmons' lab (University of Florida, USA) to fit on a standard microscope stage. They also provided code to run the device. The device was constructed of 3D printed components held together with metal cylinders, and driven by motors at either end. During preliminary testing the plastic elements developed hairline fractures which, through continued use, deteriorated until the device underwent catastrophic failure. A replacement device composed entirely of metal was designed by Dr. Cecile Perrault and manufactured in-house (Medical School Workshop, in house; Figures 2.4B). All other components remained unchanged. Due to different dimensions from the precursor device, the controlling code was adapted and calibrated by undergraduate engineering student Hira Nayyar. The calibration was validated using ink dots on silicone sheet mounted to the device (Figure 3.10A). Images were acquired before and after application of stretch at varying magnitudes, and at relaxation once the force was removed (Figure 3.10B). Lateral distortion of ink dots was calculated (Figure 3.10C) showing high correlation between input and output elongation. Additionally, images were acquired live and through the silicone sheet (Figure 3.10A). The replacement device functioned correctly, with image live image acquisition possible.

Once the initial testing was completed and protocol finalised, all that remained was to subject cells to stretch. MDA-MB-231 cells were cultured on collagen I coated silicone sheet within a PDMS well, then mounted to the device (Figure 3.11A). The sample was subjected to 20 and 45% elongation and timelapses were acquired. Representative images at specific stages are shown in Figure 3.11A. Calculation of actual distortion plotted against input stretch indicated less efficient elongation of cells (Figure 3.11B) compared with ink dots (Figure 3.10C). The additional weight of the PDMS well and media caused the silicone sheet to bow, which also resulted in cells moving out of focus once stretch was applied. The variance in applied and
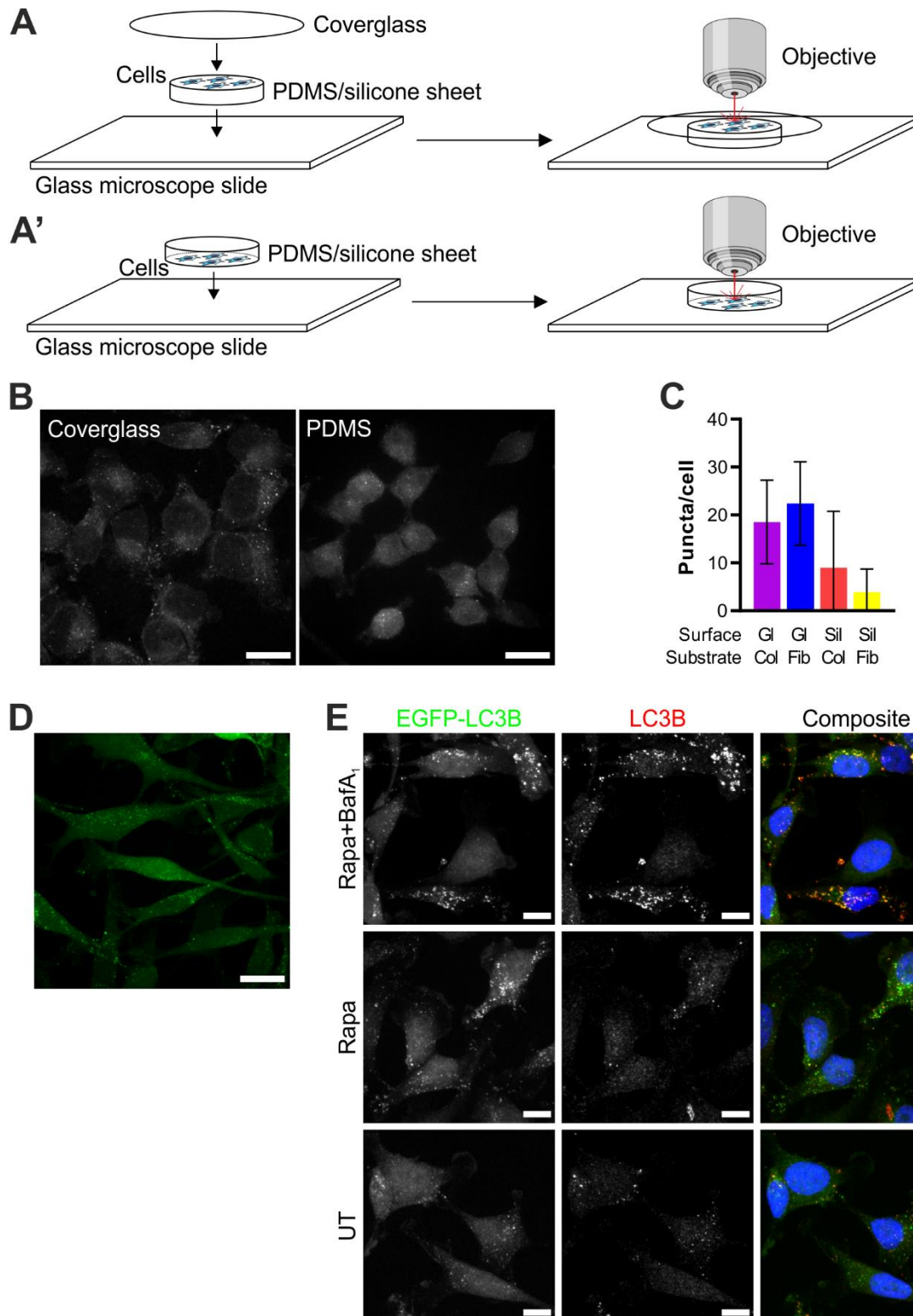
Figure 3.9 **High-resolution imaging of autophagy in cells cultured on silicone.** MDA-MB-231 cells expressing EGFP-LC3B cultured on substrate-coated silicone-based films. Schematic of microscope slide setup for imaging cells through coverglass (A) or PDMS film (A') shown. Objective shown for reference, however both upright and inverted microscopes were used; microscope slide inverted for use with inverted microscopes. (B) Representatives of initial PDMS film trial imaging through coverglass or PDMS. (C) Quantification of EGFP-LC3B puncta in untreated cells cultured on ultra-clear 200 μm thick silicone film (Sil) or standard borosilicate coverglass (Gl) coated with collagen I (Col) or fibronectin (Fib). Bars denote SD (17-40 cells per condition, single experiment; two bars extend beyond axis). (D) Representative image of cells cultured on fibronectin coated silicone imaged through coverglass. (E) LC3B immunostaining of EGFP-LC3B expressing cells cultured on fibronectin coated silicone film. Counterstained using DAPI. Untreated (UT), rapamycin only (Rapa), or both rapamycin and Bafilomycin A$_1$ (Rapa+BafA$_1$). Scale bars = (B,D) 20 μm or (E) 10 μm.

output stretch was likely due to pre-existing tension caused by the additional weight. Further modifications are required to improve the protocol, however the goal of live-cell imaging under stretch was achieved. The next step was to attempt high resolution, live-cell fluorescence imaging, to determine if stretch induced autophagy in MDA-MB-231 cells; this awaits testing.
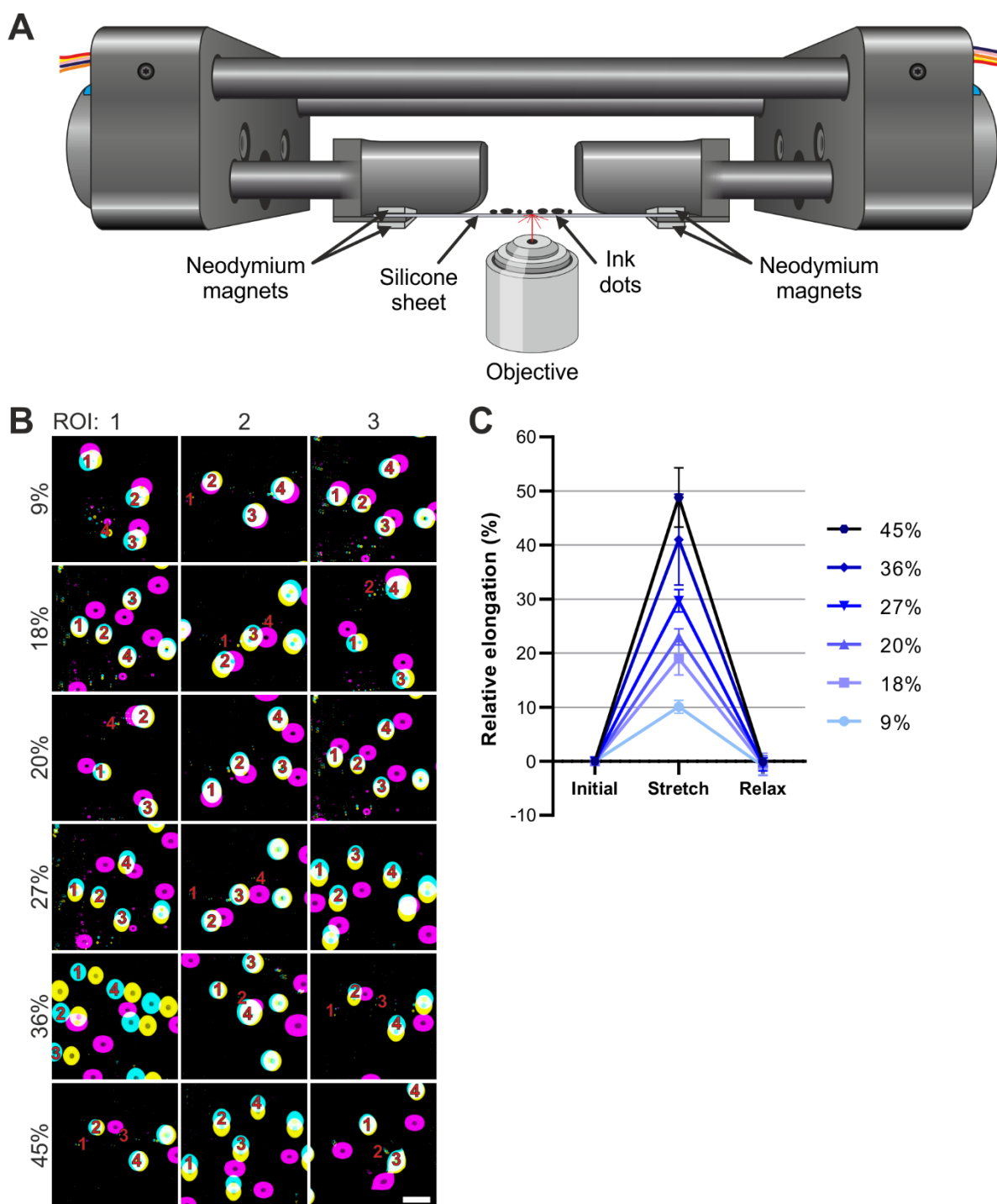
Figure 3.10 **Quantification of stretch.** Ink dots were placed onto silicone sheet as reference points to quantify stretch. (A) Stylised depiction of stretching device with mounted with silicone sheet mounted with neodymium magnets and ink dots; labelled. The central sliding components and the anterior bar are partially removed for clear view of silicone sheet. (B) Composite images where initial, stretched and post-stretch (Relax) images are false coloured cyan, magenta and yellow respectively and LUTs inverted. All 3 FOVs per stretch are shown. Numbers indicate the ink dots used as points of reference pre-stretch. Scale bar = 500 μm. (C) X co-ordinates for ink dots were determined and used to calculate relative distances between them. This was completed for before, during and after stretch, then normalised to the initial distance and presented as percentage relative elongation in x, where bars denote SD.
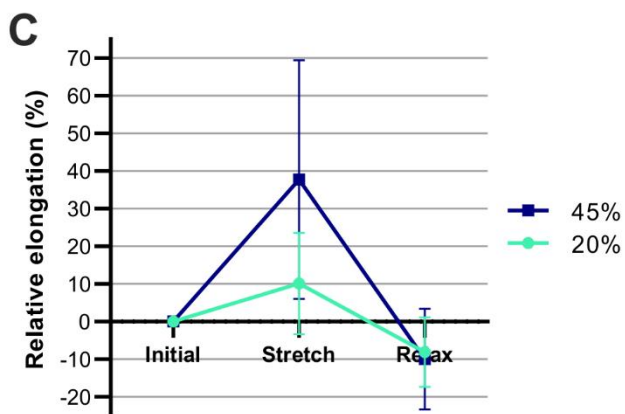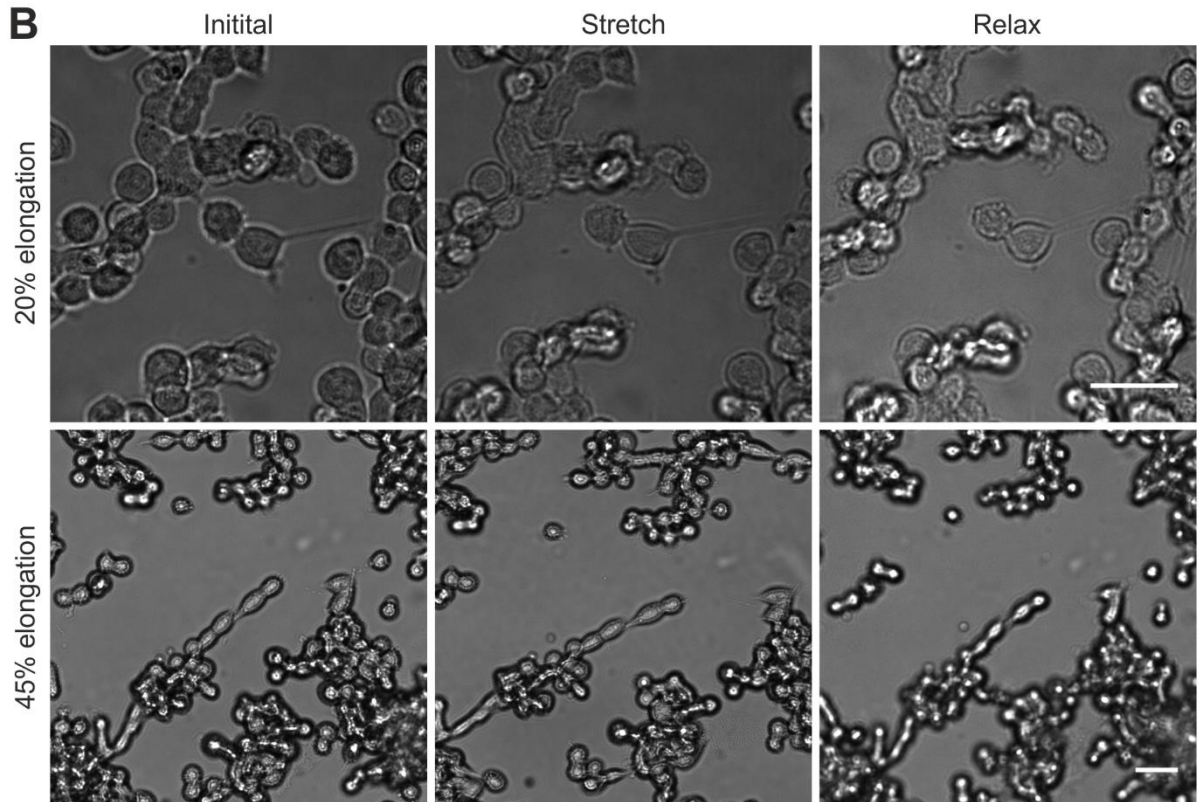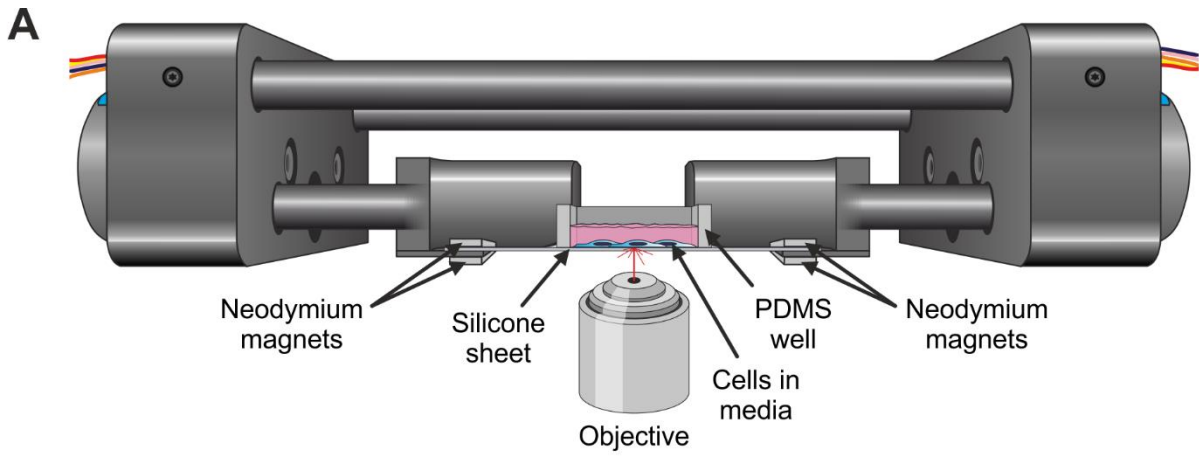
Figure 3.11 **Cell stretching testing.** MDA-MB-231 cells expressing EGFP-LC3B cultured on collagen I coated silicone film and subjected to unidirectional stretch. (A) Stylised depiction of stretching device with silicone sheet mounted with neodymium magnets, affixed PDMS well, cells and media; labelled. The central sliding components and the anterior bar are partially removed for clear view of silicone sheet and cells. (B) Cropped FOV showing cells before (Initital) and after (Stretch) force applied, then after the force was removed (Relax) at 20% and 45% elongation. Scale bars = 25 μm. (C) Quantification of cell lengths at each stage, normalised to initial length for relative elongation. Bars denote SD (n = 6 cells per condition; single experiment).

3.3 Discussion

The aim of this chapter was to determine if all mechanical forces were capable of inducing autophagy. This included fluid shear, ultrasound, and stretch stimuli, which would be compared with the effects of compression (Figure 3.2) for comparison where appropriate. To achieve this a host of existing and, where appropriate, novel systems were employed to address this question and each force. The results obtained were largely preliminary and require repetition for rigour, however some conclusions can be drawn from the findings.

Findings from previous publications regarding fluid shear force and autophagy yield mixed results and conclusions. Under all conditions tested *Dictyostelium* were unsuited to such experiments as low intensity shear forces were sufficient to dislodge cells from surfaces. However, short-term treatment with LSS resulted in a decrease in autophagic puncta in MDA-MB-231 cells (Figure 3.3). LSS has been previously shown to induce autophagy however the earliest timepoint tested was 12 hr (Lien *et al.*, 2013) making comparison difficult. The reduction we observed could have been due to provision of fresh media and not the LSS. Additionally, to test LSS for extended periods would require appropriate equipment to facilitate this. OSS has been shown to activate mTOR, with phosphorylation of p70S6K detected as early as 5 min (Lee *et al.*, 2010; Rice *et al.*, 2010). This is in stark contrast with findings from Lien *et al.*, (2013), who reported LSS-activated autophagy was mTORC1-independent. My results suggest OSS was capable of inducing autophagy in HUVECs, but not MDA-MB-231 cells, indicating a cell-line specific response, possibly due to specialisation (Figure 3.5A-C). LC3B expression in HUVECs appeared low, and immunostaining trials were undertaken in parallel with MDA-MB-231 which verified the antibody was functioning (data not shown). Given the poor dynamic range of HUVECs, an alternative endothelial line should be tested under both LSS and OSS to verify any change in autophagy.

The use of ultrasound has garnered wide interest in several fields as a mechanism for treatment of various pathologies. Sonodynamic therapy (SDT) utilises ultrasound to stimulate a sonosensitiser which generates reactive oxygen species (ROS), causing intracellular damage and triggering apoptosis. This procedure has been shown to induce autophagy in murine sarcoma 180 cells (Wang *et al.*, 2010) and paclitaxel-resistant pancreatic cancer cells (Wu *et al.*, 2018), with the latter indicating autophagy is cytoprotective against chemotherapy sensitisation. Other applications of ultrasound include global treatment of mice brains with tauopathies where upregulated autophagy was detected (Pandit *et al.*, 2019), and promotion of mesenchymal stem cell (MSC) differentiation which acted via autophagy inhibition (Wang *et al.*, 2019). Combined with preliminary findings in this thesis, which suggest autophagy may be stimulated by ultrasound (Figure 3.7), it indicates a link between the two. However, the varied autophagic response highlights the importance of determining specific outputs under differing conditions. Nevertheless, the prospect of autophagy manipulation for therapeutic intervention is promising and should be studied further.

In order to study the effect of stretch forces in a manner permitting live-cell imaging substantial preliminary work was necessary to develop a suitable methodology. A host of trials culminated with a method whereby cultured cells exhibited standard physiology and basal autophagy levels (Figures 3.8-3.9) on an optically clear elastic surface permitting live-cell imaging during stretch (Figure 3.10-3.11). Optimisations to overcome the additional weight of the PDMS well and media are still required. Despite this, it is still possible to study the effect of stretch and calculating the actual distortion applied. What remains to be determined is whether stretch induces autophagy in MDA-MB-231 cells. Whether stretch would affect *Dictyostelium* also remains unclear. Due to their low adhesion and tactic nature, it is anticipated a single application of sustained stretch would be rapidly overcome, unlike in mammalian cells where disassembly and reassembly of adhesion complexes might be necessary. Instead, the application of cyclic stretch could prove more efficacious for studying stretch-induced autophagy in *Dictyostelium*, by continuously distorting the surface substrates and maintaining the mechanical stimulus.

Summarising the work in this chapter, the results obtained and conclusions drawn were largely preliminary. Shear stress appears to induce autophagy in shear-sensitive HUVECs but not compression-sensitive MDA-MB-231. The effect of stretch on autophagy induction was unfortunately not determined as development of the method proved more complex than anticipated. However it is readily available to be utilised for this purpose along with alternative study requiring high resolution imaging of cells subjected to stretch. Ultrasound stimulation, in line with other mechanical forces, proved less straightforward than expected however an induction was detected. Many aims this chapter hoped to address were ultimately not completed, yet some conclusions can still be drawn. It is unlikely a single pathway is responsible for mediating an autophagic response to all mechanical stimuli, and where induction does occur it depends on the cell line and stimulus. Further study is necessary to resolve the precise interactions between the two.

Chapter 4

The role of cyclic GMP in autophagy induction

4.1 Introduction

In the previous chapter, the effects of various mechanical forces and, where possible, their effects on autophagy were studied. What remained unclear are the signalling pathway(s) involved in mediating the autophagic response to compression. Several publications have alluded to different signalling pathways in specific mammalian cell lines for different forces (Ando and Yamamoto, 2013; Lien *et al.*, 2013; Porter *et al.*, 2014; Rice *et al.*, 2010), whereas no literature is available for *Dictyostelium*. Consequently it is unknown if these mammalian signalling pathways are conserved in *Dictyostelium*. Our original hypothesis was that mechanotransduction in *Dictyostelium* for various stimuli (compression, shear, stretch etc.) would eventually act through a single pathway, however the multiple pathways identified in mammalian cells imply this might not be the case.

When a mechanical force is applied to a cell the immediate effect is membrane deformation. Compressive forces sandwich the cell and drive the cytoplasm and PM perpendicular to the applied force. Shear creates friction and pulls the membrane in the direction of the force. In a similar manner to shear, stretch forces apply tension parallel to the force but in multiple directions. Depictions of these forces are shown in Figure 4.1A-A'. Another external stimulus that can similarly alter cell morphology and result in global membrane tension change is OS (Figure 4.1B-B'). Hyper-OS is caused by increased external solute concentration, drawing water out of the cell and reducing cell volume. Conversely hypo-OS is the result of decreased external solute concentration causing with water to translocate into the cell and increasing cell volume. Changes in solute concentration, and the resulting translocation of water and altered cell volume, consequently affects the tension on the PM as cells shrink or swell. Given the similar physical effects of OS to mechanical forces on cell morphology and internal pressure, it provides an avenue worth pursuing.
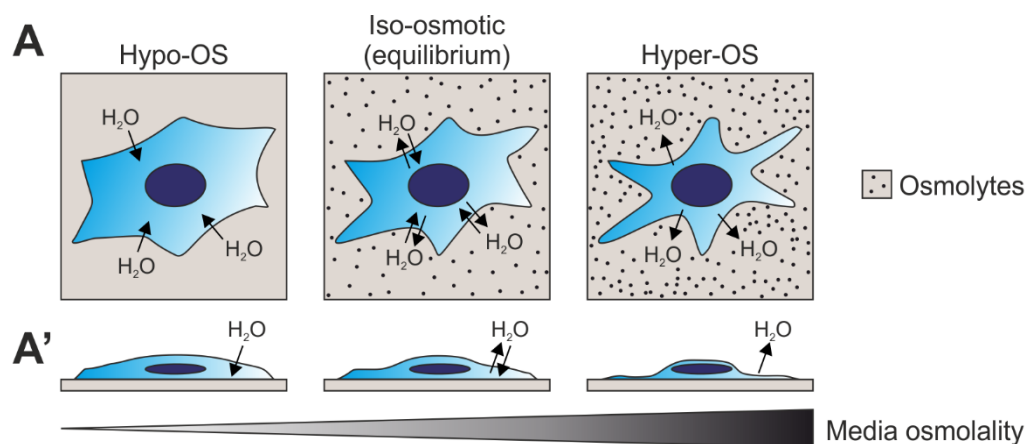
Figure 4.1 **Stylised schematic of osmotic stress.** Changes in environment impact cell architechture. Osmotic stress (OS) causes global morphological change by altering equilibrium and driving water translocation across the plasma membrane. Increasing or decreasing solute concentration (osmolytes) causes hyper- and hypo-OS respectively. Examples of hypo- and hyper-OS affecting the cell structure are shown from (A) an aerial perspective and (A') a lateral cross-section. Movement of water with respect to the cell is indicated. For comparison to mechanical forces, refer to Figure 3.1.

Unlike for mechanical forces, the OSR has been studied in detail using *Dictyostelium*. A complex network of proteins have been implicated in mediating the OSR, predominantly in context of hyper-OS. Arrestin

domain-containing protein A (AdcA) is a FYVE-type zinc finger-containing protein which associates with membrane, primarily early endosomes (Guetta *et al.*, 2010) and becomes phosphorylated at multiple sites in response to hyper-OS; hypo-OS has no effect (Habourdin *et al.*, 2013). The histidine kinase DokA (*Dictyostelium* Osmosensing Kinase A) is a negative regulator of the RdeA-RegA phosphorelay, acting as a phosphatase for RdeA and inhibiting the cAMP phosphodiesterase activity of RegA (Ott *et al.*, 2000). Arising from lateral gene transfer from prokaryotes (Glöckner *et al.*, 2016), DokA expression is increased during development and loss of the protein severely reduces cell survival after hyper-OS (Schuster *et al.*, 1996). STAT (Signal transducer and activator of transcription) proteins are transcription factors which alter gene expression when activated. In response to hyper-OS *Dictyostelium* STAT protein C (DstC) becomes phosphorylated and translocates to the nucleus during hyper-OS (Araki *et al.*, 2003), rapidly altering gene expression (Na, 2007; Na *et al.*, 2007). One up-regulated gene identified was KrsA (Kinase Responsive to Stress protein A), a putative S/T kinase belonging to the MST subfamily of protein kinases and similar to STE20-like kinases. KrsA acts as a cAMP relay, activating adenylyl cyclase in response to hyper-OS (Muramoto *et al.*, 2007). One of these diverse OSR proteins could be involved in transducing mechanical forces.

Another highly studied signalling pathway involved in OSR is the cyclic GMP pathway. An overview of the pathway is provided in Figure 4.2. Cyclic guanosine monophosphate, cGMP, is a small secondary messenger produced by the conversion of guanosine triphosphosphate (GTP) by guanylyl cyclase (GC) enzymes. *Dictyostelium* contain two GCs: the membrane-bound GcA (Roelofs, Snippe, *et al.*, 2001) and the cytosolic, soluble, SgcA (Roelofs, Meima, *et al.*, 2001).These two enzymes are solely responsible for cGMP production (Roelofs and van Haastert, 2002). cGMP production can be stimulated through binding of extracellular cAMP to transmembrane receptors cAR1 and cAR3 (Insall *et al.*, 1994), as well as folate and hyper-OS (Oyama, 1996). Additionally hyper-OS can stimulate intracellular cAMP production, peaking after 2 min (Ott *et al.*, 2000). While both cyclase enzymes can convert GTP to cGMP, SgcA mediates ~90% conversion under cAMP stimulation (Roelofs and van Haastert, 2002). The cGMP then binds to proteins containing a cyclic-nucleotide binding motif to exert its effect.

In *Dictyostelium* there are 4 proteins capable of binding cGMP. These were identified in a bioinformatics screen completed by (Goldberg *et al.*, 2002) and termed cGMP-binding proteins A-D (GbpA-D). GbpA and GbpB are cGMP phosphodiesterases (PDEs). GbpD is highly similar to the C-terminal portion of GbpC, both containing RasGEF domains which regulate Ras proteins. Of the 4 candidates, only GbpC showed a high affinity to cGMP. GbpC is a large multi-domain protein, containing two cyclic-nucleotide binding domains (cNBD) and a kinase domain. Furthermore it also contains a Ras/GTPase domain which subsequently founded the Roc (Ras of complex) and COR (C-terminal of Roc) domains, and the Roco protein family where both domains were present (Bosgraaf and van Haastert, 2003). Upon cGMP binding to GbpC, a chain of intramolecular events occur which stimulate kinase activity (van Egmond *et al.*, 2008). Summarising their findings, the GEF domain becomes active and facilitates replacement of GDP with GTP at the Roc-COR

domain. This activates the domain which in turn increases activity of the MAPKKKinase domain, promoting phosphorylation of substrates. GbpC, via the kinase or RasGEF domains, then regulates downstream processes.

Figure 4.2 **Summary of cGMP stimuli and signalling.** In *Dictyostelium*, production of cGMP is mediated by two enzymes: membrane-associated guanylyl cyclase A (GcA) and cytoplasmic soluble guanylyl cyclase A (SgcA). cGMP production can be stimualted by hyper-OS, and extracellular cAMP signalling during aggregation. cAMP stimulation via cAR1 and cAR3 transiently exert their effect primarily through SgcA. cGMP binds to GbpC, triggering a complex intramolecular cascade which actives the kinase domain and drives downstream phosphorylation of substrates. cGMP signalling is negatively regulated by several phosphodiesterases (PDEs) which degrade the second messenger to GMP to terminate the signalling pathway.

In mammalian cells, cGMP signalling is most commonly associated with regulation of blood vessels. When stimulated, nitric oxide synthase drives production of nitric oxide (NO), which diffuses to the smooth muscle where it stimulates guanylyl cyclase activity in adjacent cells (Roczniak and Burns, 1996). In turn cGMP is produced and binds to Protein Kinase G (PKG), activating the kinase and downstream signalling pathways including ones involved in driving blood vessels vasodilation. cGMP signalling has also been implicated in mechanotransduction of shear (Ohno *et al.*, 1993) and stretch (Shah *et al.*, 2013) stimuli. Shear forces have been implicated in autophagy induction (Liu *et al.*, 2015), as have stretch (Porter *et al.*, 2014), however the potential role of cGMP signalling in mediating this response has not been investigated. Interestingly, hyper-OS has been shown to induce autophagy (Nunes *et al.*, 2013) however cGMP, again, has not been studied in this context. Together this suggests a potential link between the mechanical and osmotic stimuli, cGMP signalling, and autophagy induction.

In this chapter, the effect of OS and its activation of autophagy in *Dictyostelium* was investigated. Using knock-out cell lines lacking OSR signalling proteins, and both canonical and non-canonical mechanisms of autophagy induction, this activation was partially attributed to cGMP signalling. Subsequently, cGMP

signalling was determined to be a potent autophagy inducer, and was generated in response to compression. These results provide insight into potential candidates for mechanotransduction and autophagy initiation.

4.2 Results

4.2.1 Osmotic stress-induced autophagy

In order to maintain optimal function and viability, cells detect and adapt to changes in environment, such as disruption to the equilibrium of osmolytes. Changes to concentrations of soluble material in the extracellular space will drive diffusion of water through the membrane (Figure 4.1B). Through manipulation of media composition, OS was induced. For hypo-OS, osmolytes are washed away and cells are bathed in distilled water. For hyper-OS, osmolyte concentration was increased through addition of sorbitol, an inert soluble compound commonly used for this purpose. The effect of hyper-OS is shown in Figures 4.3A-C'' where cross-sections of 3D images provide a multi-faceted view of the cell volume. Cells were bathed in 100mM sorbitol resulting in water moving out of the cell, visibly reducing cell volume after 1 min (Figure 4.3B) and to a greater extent by 5 min (Figure 4.3C). Hypo-OS would result in dilution of external osmolytes causing water to move into the cell, increasing the cell volume. However, whether these events would induce autophagy in *Dictyostelium* was unknown.

The aldose reductase enzyme converts glucose and NADPH, to sorbitol and $NADP^+$ (Lee, 1998). In *Dictyostelium*, this reaction is facilitated by aldose reductase A (*alrA*), which is regulated by secreted counting factor during development (Ehrenman *et al.*, 2004). In humans, the zinc-containing homo-tetramer sorbitol dehydrogenase (SDH) converts sorbitol to fructose using the coenzyme NAD^+ (Iwata *et al.*, 1995; Pauly *et al.*, 2003). Both conversion reactions described are reversible and catalysed by the same enzymes. Currently, no sorbitol dehydrogenase orthologue has been identified in *Dictyostelium*, however there are two zinc-containing alcohol dehydrogenase genes (*ahd5* and *DDB_G0272628*) which could facilitate this reaction. Due to the partial duplication of chromosome 2 in Ax3 and Ax4, there is a second copy of the *DDB_G0272628* gene; *DDB_G0274085*. However while sorbitol could be metabolised, it is unlikely to provide a nutrient source. It was reported that use of an isotonic starvation buffer supplemented with 100 mM sorbitol still yielded a starvation response and induced multicellular development (Smith *et al.*, 2010). Instead, sorbitol more likely plays a role in osmo-regulation.

To determine the effect of OS on autophagy, wild-type Ax2 cells were subjected to hyper- and hypo-OS using 400mM sorbitol and distilled water respectively. Representative examples of cells under these conditions, with arginine/lysine starvation and compression used as positive controls, are shown in Figure 4.3D. Hyper-OS treated cells showed reduced volume and, consequently, surface area was reduced. The number of detectable puncta decreased to approximately 1 puncta per cell which remained significantly reduced relative to untreated control cells (Figure 4.3E). Time-lapses of cells under the same conditions with more frequent image acquisition showed motile puncta slowed until static, then the GFP-signal faded away. This loss of signal did not occur globally and thus was not the result of photobleaching, suggesting
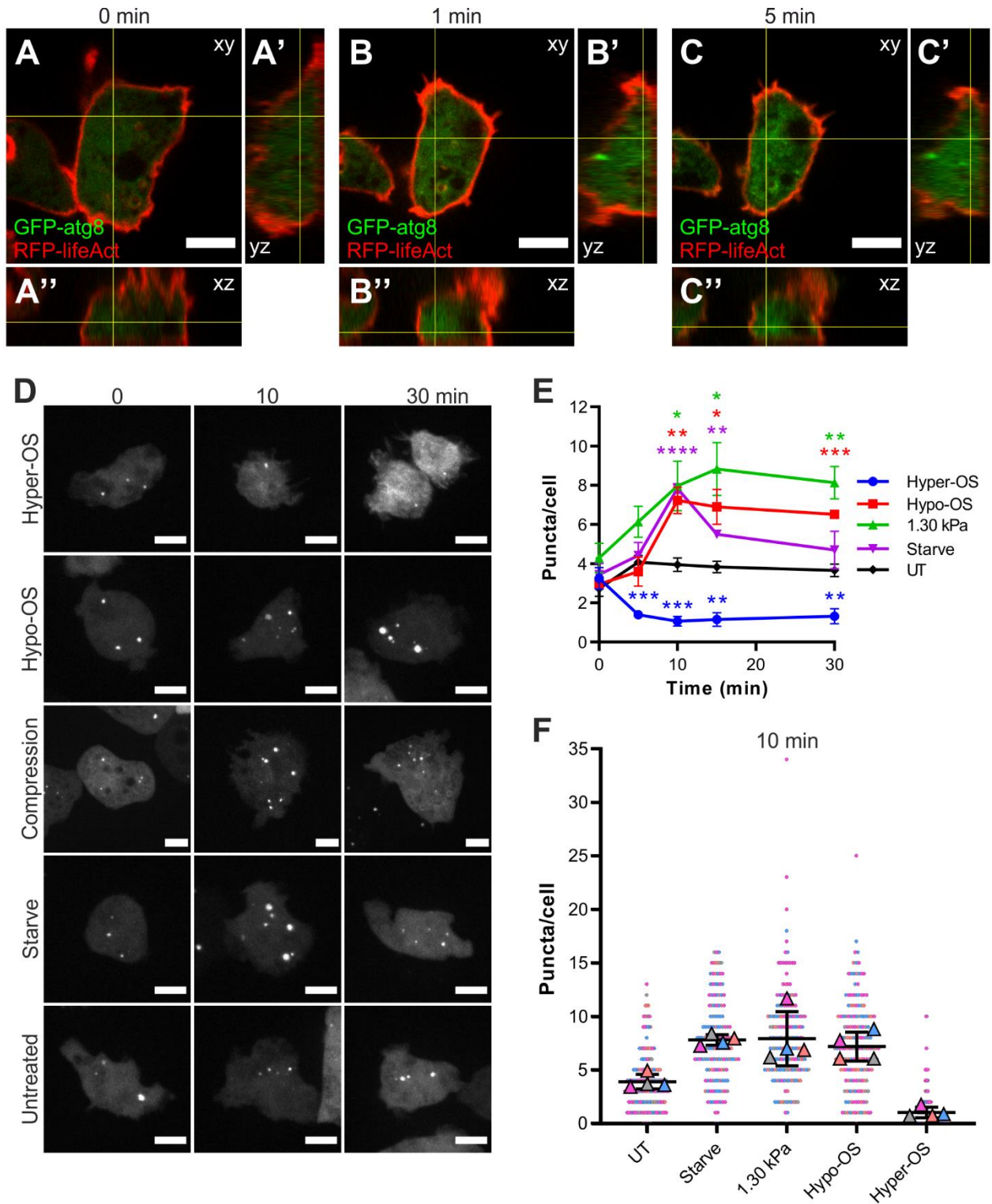
Figure 4.3 **Osmotic stress induces and impairs autophagy.** Ax2 wild-type cells co-expressing GFP-atg8 (green) and RFP-lifeAct (red) subjected to hyper-osmotic stress (100 mM sorbitol). Representative cell at 0 (A-A''), 1 (B-B'') and 5 (C-C'') min. Cross-sections and orthogonal projections from a 3D image for XY (A-C), YZ (A'-B') and XZ (A''-B'') axes are shown, where yellow lines indicate intersections.(D) Representative images of Ax2 wild-type cells expressing GFP-atg8 subjected to sustained compression (1.30 kPa), hyper- and hypo-osmotic stress (Hyper-OS, 400 mM sorbitol; Hypo-OS, distilled water), arginine/lysine amino acid starvation (Starve) or untreated (UT) control. (A-D) Scale bars = 5 μm. (E) Quantification of mean puncta per cell ± SEM across 4 independent experiments (3 independent experiments for 30 min only; 91-227 cells quantified per data-point). Significance determined using unpaired 2-tailed t-test (* $P < 0.05$, ** $P < 0.01$, *** $P < 0.001$, **** $P < 0.0001$) comparing each treatment and time-point to untreated control. (F) Data from (E) at 10 min presented as a SuperPlot (Lord JS *et al.* (2020)). Independent repeats (n = 4; 138-174 cells per condition) are colour coordinated, where puncta counts per individual cell (circle) and mean average per independent repeat (triangle) are shown. Mean average and SD overlayed with bar and whiskers.

autophagic structures were being dismantled (data not shown). Cell volume under hypo-OS did not change as strikingly however fewer projections and a more rounded morphology were visible, suggesting water had moved into the cells (Figure 4.3D). Due to the absence of nutrients in distilled water, it was anticipated that hypo-OS would induce autophagy in at least a similar manner to starvation. This was found to be the case with both conditions showing similar maximal responses at 10 min, although hypo-OS maintained a more elevated puncta count at 15 and 30 min (Figure 4.3E). Figure 4.3F highlights the distribution of data at 10 min between each treatment using the SuperPlot format (Lord *et al.*, 2020). It was concluded that both hyper- and hypo-OS impacted autophagy, however it was not obvious whether the stimuli were regulating it specifically.

As described above, sorbitol is used to induce hyper-OS, and has been in various research articles with concentrations typically ranging from 100-400mM. Given the severe cell volume decrease observed in our experiments, it was speculated that the stimulus could be too aggressive and consequently inhibit basic cellular function. To test this and verify that hyper-OS was indeed preventing autophagy, a sorbitol titration was undertaken. Sorbitol-supplemented media osmolality measurements were quantified and compared with calculated (expected) osmolarity (Figure 4.4A). The osmolar gap describes the variance which can arise in complex liquids composed of concentrated soluble material. We observed a minimal discrepancy, and concluded our treatments were within a linear range. These treatments were then added to Ax2 cells and autophagic structures quantified (Figure 4.4B). Quantification of the puncta per cell revealed that hyper-OS induced, rather than impaired, autophagy as sorbitol concentration increased, up to 200mM where the puncta count remained largely unchanged. This was more clearly visualised as a dose-response at 5 min (Figure 4.4C). Representatives for this are shown in Figure 4.4D, where the increasing magnitude of hyper-OS causes a progressive increase in puncta and decrease in cell volume. Hyper-OS data from Figure 4.3E (indicated in red) was included for comparison in Figures 4.4B-C. In contrast to initial findings, hyper-OS induced autophagy until a threshold was reached where, presumably, cellular function was so greatly impaired that autophagosome formation appeared to be inhibited.

4.2.2 Loss of established osmotic-stress response proteins does not impair autophagy

Several proteins are known to play key roles in coordinating the response to OS. Known proteins include the histidine kinase DokA, the STAT transcription factor DstC, the stress-responsive kinase KrsA and the arrestin-domain containing protein AdcA. To test whether these proteins were responsible for autophagy induction, we subjected knockout cells lacking these response elements to starvation and compression to determine if autophagy induction was impaired. PiezoA (PzoA; *DDB_G0282801*), a putative mechanosensitive piezo homologue in *Dictyostelium* (Srivastava *et al.*, 2020) was included as a candidate for its role in mechanotransduction. Both *pzoA*- clones (HM1812 and HM1813) were provided by Rob Kay (MRC-LMB, Cambridge). Representative images for all knockout cell lines under either stimulus is shown in Figure 4.5A. Quantification for compression and starvation is shown in Figures 4.5B and Figure 4.5C respectively, with outputs separated depending on the parent cell line from which the mutant was

generated. No significant differences relative to the wild-type parent were detected under any condition. Of the genes tested, none appear to affect the induction of autophagy in response to either compression or starvation.
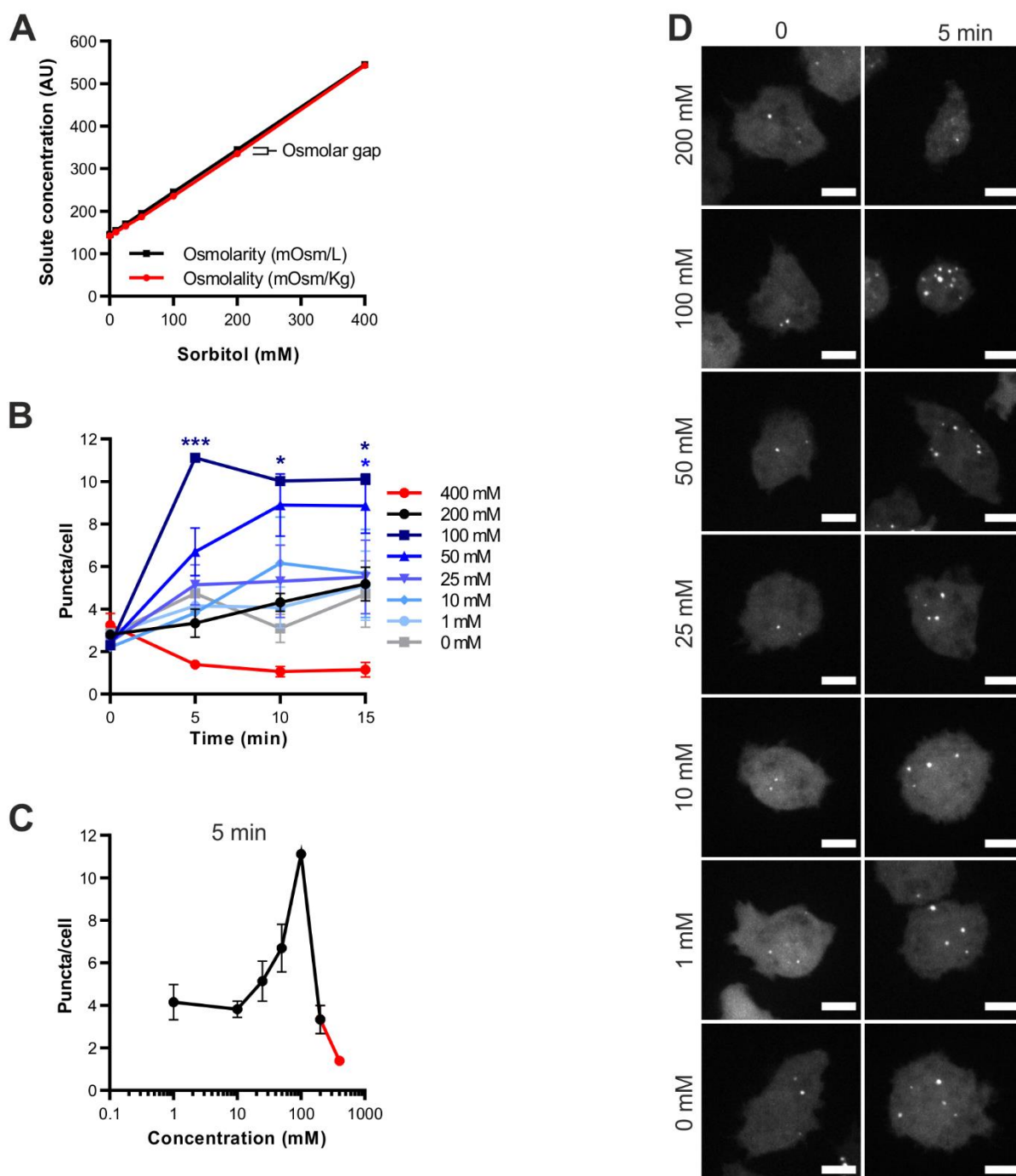
Figure 4.4 **Hyper-osmotic stress induces autophagy in a dose-dependent manner.** Ax2 cells expressing GFP-atg8 subjected to hyper-osmotic stress using titrated sorbitol concentrations. (A) Calculated osmolarity (mOsm/L) and measured osmolality (mOsm/Kg) of cSIH supplemented with sorbitol for hyper-osmotic shock treatment. The variance between calculated osmolarity and measured osmolality is the "osmolar gap", indicated. Error bars denote SD (3 independent experiments; osmolality only). (B) Data-points represent mean puncta per cell ± SEM across 3 independent experiments (minimum 144 cells per data-point) for all time-points and sorbitol concentrations indicated. Unpaired 2-tailed t-test (* $P < 0.05$, *** $P < 0.001$) comparing untreated control (0 mM sorbitol) to hyper-osmotic shock (1-200 mM) conditions. (C) Dose-reponse at 5 min using data in (B). (B-C) Data for 400 mM sorbitol treatment from previous experiment shown in red, included for reference (from Figure 4.3E). (D) Representative images for quantification in (B-C). Sorbitol concentrations indicated. Scale bars = 5 μm.
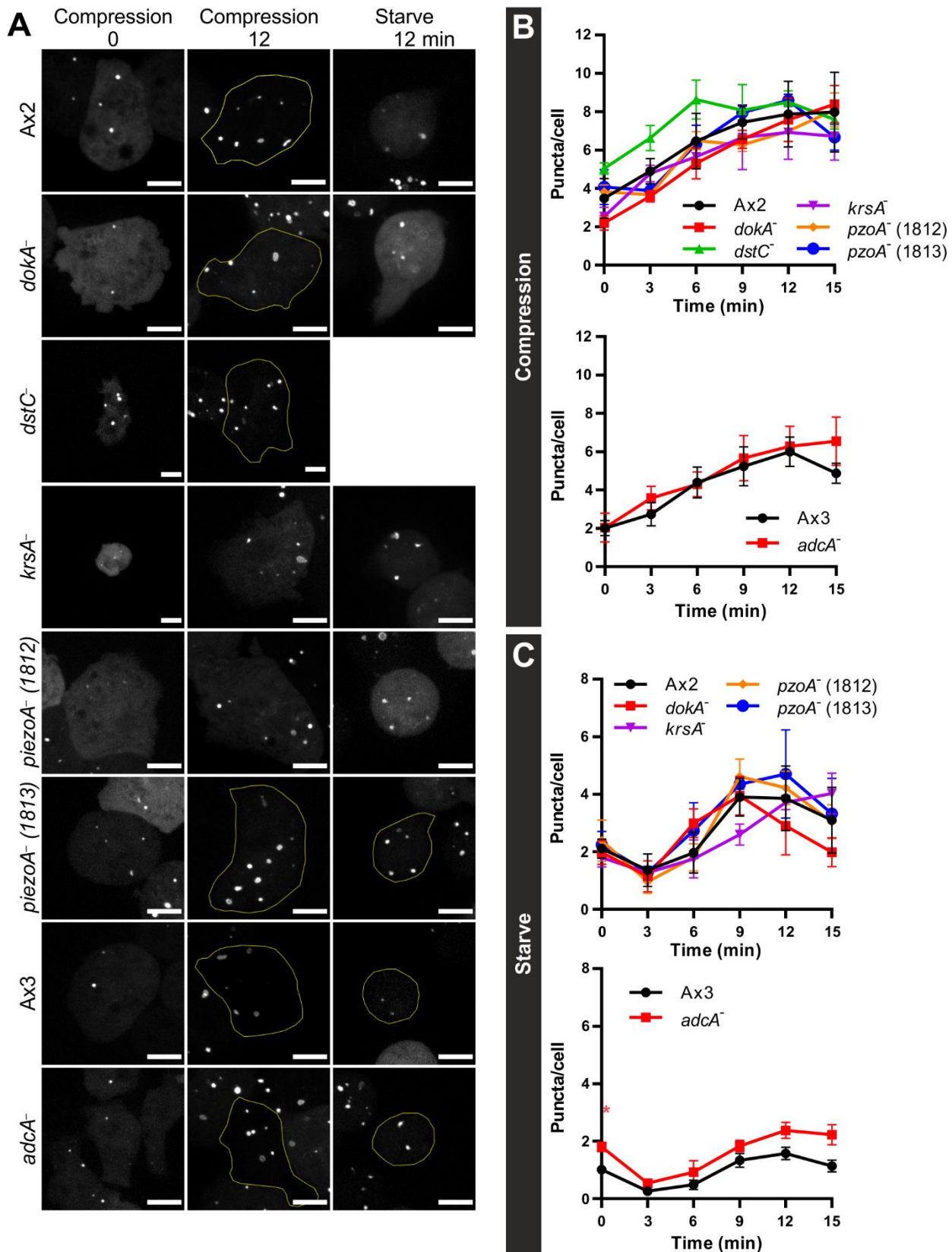
Figure 4.5 **Osmo-regulatory protein loss does not impair compression or starvation induced autophagy.** *Dictyostelium* expressing GFP-atg8, and lacking functional genes for osmo-regulatory signalling proteins, were subjected to 1.31 kPa compression or arginine/lysine starvation. (A) Representative cells shown for each cell line and condition. Cell boundaries are highlighted in yellow where GFP-atg8 expression is low. Scale bars = 5 µm. Quantification of puncta per cell presented for compression (B) and starvation (C), grouped according to wild-type parent (Ax2 or Ax3). Error bars indicate SEM across 3-4* independent repeats (n = 28-132 cells per data point. *piezoA⁻ (1812) T = 0min compression only consists of 2 independent repeats). Unpaired 2-tailed t-test (* *P* < 0.05) comparing knock-out line to appropriate Ax2 or Ax3 parent line.

4.2.3 Autophagy is induced by cGMP via the cGMP-regulated kinase GbpC

Hyper-OS is global stimulus which impacts a range of biological processes, including cGMP signalling. Simultaneous activation of multiple signalling pathways could mask the effect of knocking-out cGMP signalling proteins. To negate the effect of any compensatory mechanisms, a more precise technique was employed which activated cGMP signalling alone. Wild-type Ax2 were treated with a non-hydrolysable membrane-permeant cGMP analogue, 8-bromo-cGMP (8Br-cGMP). 8-bromo-cAMP (8Br-cAMP) was used as a control for its similar role as a cyclic nucleotide second messenger to determine any overlap. Figure 4.6A shows representative images for both treatments, and quantification is presented in Figures 4.6B and 4.6C for 8Br-cGMP and 8Br-cAMP respectively. 8Br-cAMP induced a minimal increase in puncta per cell, whereas 8Br-cGMP stimulated a clear response in a dose-dependent manner. This is visualised more clearly in Figure 4.6D, where a clear correlation between 8Br-cGMP concentration and puncta per cell is observed at 10 min. This time-point was selected as most maximal responses for 8Br-cGMP treatments were detected then. The minor induction by 20 mM 8Br-cAMP could be an off-target effect, where concentration was sufficiently high to bind cGMP motifs despite weaker affinity, or an alternative pathway may have been activated. The data provided clearly shows that cGMP is capable of inducing autophagy in *Dictyostelium*.

An increase in GFP-atg8 puncta, or an accumulation of lipidated atg8-II, indicates autophagic flux is affected, but fails to resolve if a compound is stimulating autophagy or blocking fusion with the lysosome and degradation. To study the effect of 8Br-cGMP on autophagic flux, traditional techniques are not suitable. In mammalian cells bafilomycin A_1 is frequently used to inhibit V^+-ATPase activity, blocking lysosomal acidification and subsequently fusion with autophagosomes (Yamamoto *et al.*, 1998). In combination with autophagy inducers such as rapamycin or Torin compounds, these controls allow for comparison to resolve how a treatment affects autophagy. Due to their dependence of both macropinocytic and phagocytic processes as a nutrient source, bafilomycin A_1 treatment proves fatal for *Dictyostelium* and is unsuitable. Instead, the rate of *de novo* puncta formation and lifetime was tracked by microscopy to determine if 8Br-cGMP induced autophagy or blocked autophagosome degradation.

Wild-type Ax2 cells were treated with 8Br-cGMP for 5 min before time-lapses were acquired for 10 min. Atg1-null cells were used as a negative control. It was verified that the acquisition parameters used did not induce phototoxicity until after 13-14 min of image acquisition, therefore any changes detected within the 10 min time-lapse were due to 8Br-cGMP. Figure 4.7A shows 8Br-cGMP treatment of Ax2 cells significantly increased the rate of new puncta formation compared to vehicle treatment across the full 10 min treatment window. Atg1-null cells often form aggregates of GFP-atg8 due to lack of protein turnover. Consequently, some Atg1-null cells are noted as having new puncta due to *de novo* formation of aggregates which could not be resolved from genuine puncta at the magnification used. Results were further broken down into min-long windows, demonstrating new puncta formation over the 10 min for Ax2 treated with 8Br-cGMP or vehicle control (Figure 4.7B). The puncta formation is consistently, but not always significantly, increased between 5-13 min for 8Br-cGMP treatment. It appears to decline after this time
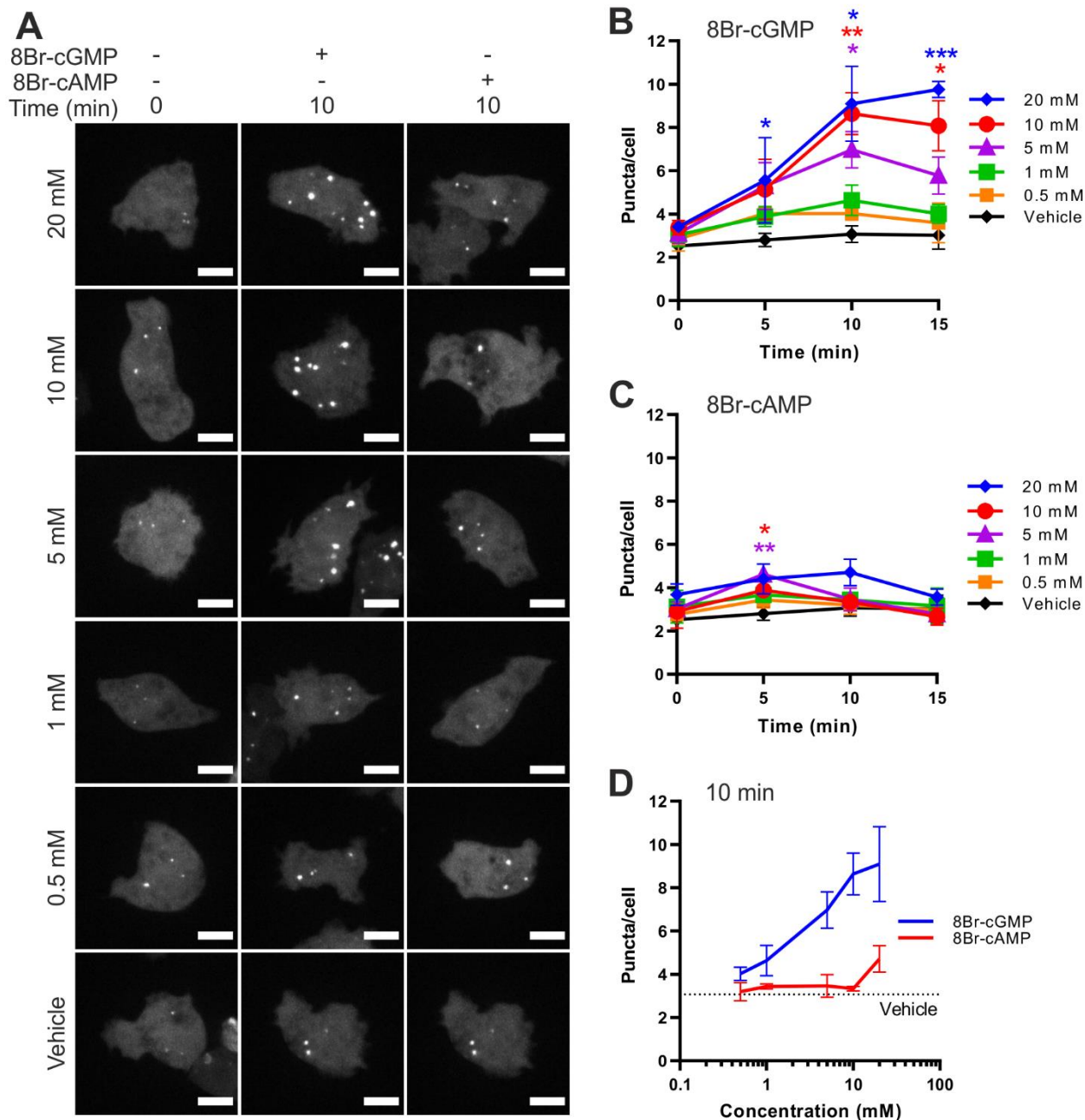
Figure 4.6 **8Br-cGMP induces autophagy in a dose-responsive manner.** Ax2 expressing GFP-atg8 treated with titrated 8Br-cGMP or 8Br-cAMP. Representative images shown in (A). Scale bars = 5 μm. Quantification shown in (B-D), where data-points represent mean puncta per cell ± SEM across 3 independent experiments (58-111 cells per data-point). (B) 8Br-cGMP titration. (C) 8Br-cAMP titration. (B-C) Unpaired 2-tailed t-test (* $P < 0.05$, ** $P < 0.01$, *** $P < 0.001$) comparing treatments to vehicle control at each time-point. (D) Dose-reponse at 10 min using data from (B-C).

potentially to basal levels, which is consistent with the plateau observed between 10-15 min (Figure 4.6B). This raised the question of whether autophagy initiation was stimulated as a result of the transient restructuring of the cortex, instead of being mediated by other signalling proteins downstream of cGMP. Nevertheless, the results clearly showed 8Br-cGMP treatment induced autophagy.

To quantify the rate of puncta formation in Figures 4.6A-B, puncta were tracked across the timelapse. Typically, this protocol combines high magnification (100X), and compression under agarose to limit cell migration while inducing autophagy. Consequently, compression under agarose was not appropriate and lower magnification was essential to accommodate the highly motile cells. This reduced resolution meant it
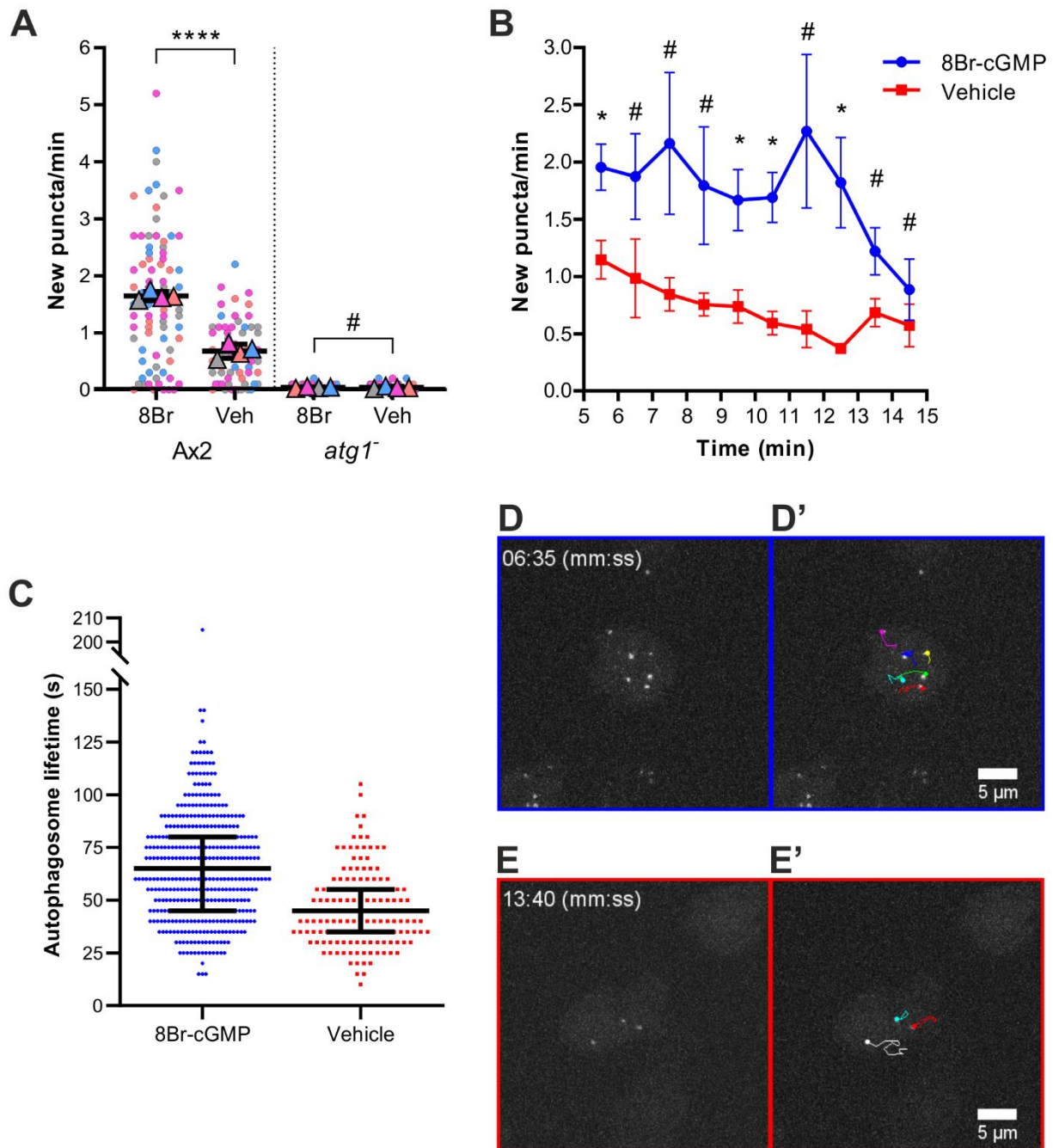
Figure 4.7. **8Br-cGMP induces formation of new autophagosomes.** Wild-type Ax2 and *atg1⁻* cells expressing GFP-atg8 treated with 8Br-cGMP for 5 min then imaged every 5 s for 10 min. The number of newly forming phagophores and autophagosome lifetime was quantified. (A) The rate of phagophore formation presented as a SuperPlot (Lord JS *et al.* (2020)). Independent repeats (n = 4; minimum 50 cells per condition) are colour coordinated, where puncta counts per individual cell (circle) and mean average per independent repeat (triangle) are shown. Mean average and SD overlayed with bar and whiskers. Unpaired 2-tailed t-test (# $P \geq 0.05$, **** $P < 0.0001$) comparing treated and untreated conditions. (B) New puncta per cell within 1 min time-frames across 3 independent repeats, where error bars denote SEM. Unpaired 2-tailed t-test (# $P \geq 0.05$, * $P < 0.05$) comparing treated and untreated conditions. (C) Lifetime of autophagosomes in Ax2, from phagophore inception to formation of autolysosome collated from 3 independent repeats. (D-E) Examples of autophagosome tracking in Ax2 under (D) 8Br-cGMP and (E) vehicle treatments respectively. (D) and (E) show GFP-atg8 localisation and (D') and (E') are overlayed with traces following the puncta.

was not possible to define each stage of autophagosome formation and degradation, particularly after

lysosomal fusion where fluorescence diminished rapidly. However overall lifetime was calculated and

shown to be increased in 8Br-cGMP treated cells with median life-time was 65 s, compared with 45 s for

vehicle control (Figure 4.7C). 8Br-cGMP treatment yielded a comparable average lifetime to previous

descriptions of 60 s from initiation to completion under compression, although a further 60 s was necessary for the acidification/degradation stage (Mesquita *et al.*, 2017) which we were unable to quantify. Example images for 8Br-cGMP (Figure 4.7D) and vehicle control (Figure 4.7E) are shown, with traces overlaid in Figures 4.7D'-E'. The results presented here suggest several possibilities: autophagosomes produced by basal activity are turned over more rapidly compared with stimulated activity, or that cGMP affects maturation and inhibits lysosomal fusion.

As described above, cGMP induces the generation of new autophagosomes, leading to the question: what propagates this response? In *Dictyostelium* there are four genes encoding proteins with cGMP binding motifs but only one, *gbpC*, contains a protein kinase domain (Goldberg *et al.*, 2002). To determine if GbpC was responsible for propagating the cGMP signal to induce autophagy, mutants lacking a functional copy of this gene were treated with 8Br-cGMP and the induction of autophagy observed. It was determined that cells lacking GbpC were unable to induce autophagy compared with Ax3 wild-type parent cells (Figure 4.8A), with vehicle controls shown in Figure 4.8B, and representative images in Figure 4.8C under conditions described. GbpC is therefore essential for 8Br-cGMP induced autophagy.

4.2.4 Hyper-osmotic stress induces autophagy via multiple mechanisms

Hyper-OS induces both cGMP formation as well as autophagy, but likely activates multiple signalling pathways. Whether these additional pathways contribute to autophagy initiation, alongside cGMP signalling, is unknown. To determine if this was the case cells lacking both guanylyl cyclases (GcA and SgcA) or the cGMP-regulated kinase GbpC were subjected to hyper-OS. Ax3 cells exhibited a greater sensitivity to 100mM sorbitol treatment, with morphology and lack of puncta similar to observations made in Ax2 at 200-400mM sorbitol (data not shown), therefore lower concentrations were used. Quantification of puncta per cell is presented for all cell lines indicated (Figure 4.9A). Treatment with 50mM sorbitol caused a significant increase in autophagic structures in all lines tested, whereas 10mM was generally not significantly increased relative to untreated control. The peak response occurred after 10 min, and comparison of cell lines at this time-point is provided in Figure 4.9B with representatives in Figure 4.9C. Only *gbpC*⁻ cells showed a significant reduction in puncta at 10mM sorbitol, however the result was also significantly lower than the vehicle control and as such should be interpreted with caution. Ultimately the conclusion drawn was that autophagy induction by hyper-OS was not solely dependent on cGMP signalling, although cGMP signalling could contribute to induction.

4.2.5 Compression induces cGMP production, but is not essential for autophagy induction

We hypothesised that hyper-OS and compression may function in a similar manner to induce autophagy. Hyper-OS results in cGMP production (Oyama, 1996), and it has been shown that both hyper-OS (Figure 4.4B-C) and the cGMP analogue, 8Br-cGMP (Figures 4.6-4.7), induce autophagy. Compression induced autophagy acts via a non-canonical mechanism (King *et al.*, 2011). Together, this raised the question of whether cGMP was responsible for mediating this response. Wild type Ax2 cells were compressed for 2 min then lysed in perchloric acid to preserve cGMP. Lysates were sent to, and assayed by, Peter van Haastert
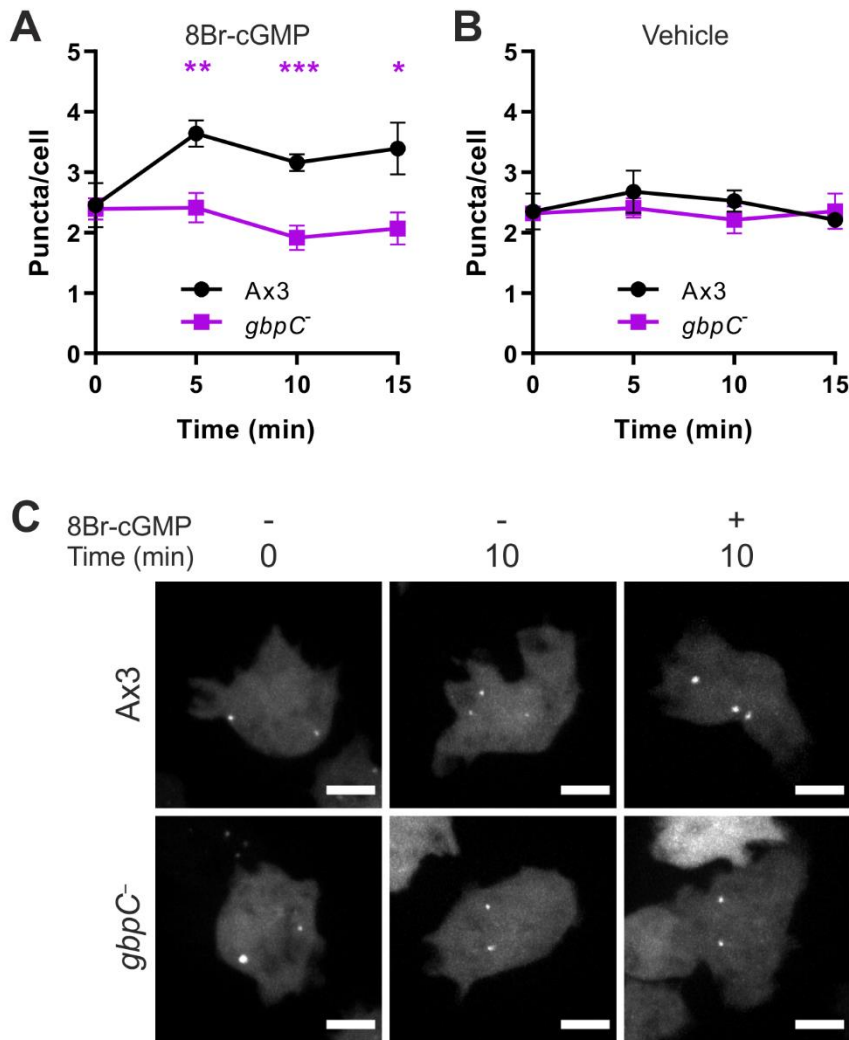
Figure 4.8 **GbpC is essential for autophagy induction in response to 8Br-cGMP.** Ax3 and *gbpC⁻* cells treated with 10 mM 8Br-cGMP (A) or vehicle control (B). (A-B) Mean average GFP+ puncta per cell shown ± SEM (n = 5 independent experiments except gbpC- at 15 min for both treatment conditions, n = 4. 170-343 cells per data point). Unpaired 2-tailed t-test (* P < 0.05, ** P < 0.01, *** P < 0.001) comparing wild-type Ax3 to *gbpC⁻* for 8Br-cGMP (A) or vehicle control (B) treatments. Any data points lacking annotation were non-significant (P > 0.05). (C) Representative images for (A-B). Scale bars = 5 µm.

(University of Groningen, Netherlands), who quantified intracellular cGMP levels by RIA (see Chapter 2.15 for details). A moderate, but significant, increase of approximately 20% was detected in Ax2 cells subjected to compression (Figure 4.10A). Production and degradation of cGMP can be rapid: cAMP stimulation causes cGMP levels to increase 10-fold, peaking after 30 s and returning to basal levels by 60 s (Oyama, 1996). Disassembling the compression apparatus prior to cell lysis takes time. Consequently, the majority of cGMP produced may already have been degraded prior to lysis and preservation, meaning the peak cGMP concentration is potentially greater than observed.

Next, we wanted to verify whether cGMP was responsible for mediating compression-induced autophagy. To test this, cells lines lacking either, or both, guanylyl cyclase enzymes, or the cGMP regulated kinase GbpC were compressed and puncta quantified. All cell lines tested produced comparable responses (Figure 4.10B); representatives in Figure 4.10C. Therefore loss of cGMP production capability, or the kinase which responds to it, does not prevent autophagy initiation. Unpublished data presented by Tsuyoshi Araki
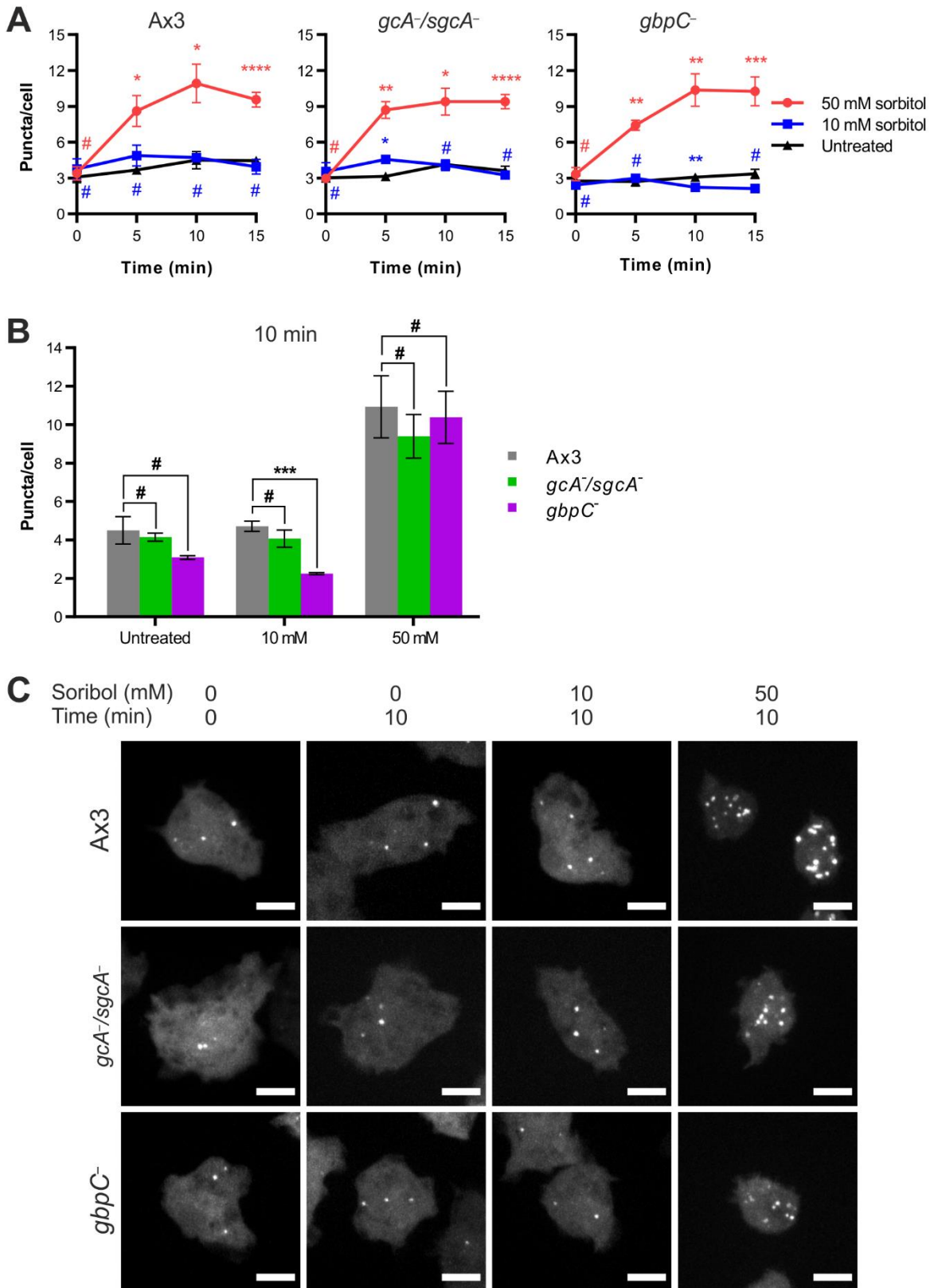
Figure 4.9 **Hyper-osmotic stress induces autophagy via multiple signalling pathways.** (A) Ax3 wild-type parent, *gcA⁻/sgcA⁻* and *gbpC⁻* cells expressing GFP-atg8 subjected to hyper-osmotic stress or untreated. Data points represent mean puncta per cell. (B) Comparison of cell lines at 10 min only. (A-B) Error bars denote SEM of 3 independent repeats (6 independent repeats for untreated at 0 and 15 min), where at least 132 cells were quantified per condition across all repeats. Unpaired 2-tailed t-test (# $P \geq 0.05$, * $P < 0.05$, ** $P < 0.01$, *** $P < 0.001$, **** $P < 0.0001$) comparing (A) 50 mM or 10 mM sorbitol treatment to untreated cells or (B) Ax3 parent line to KO mutants under conditions indicated. (C) Representative images for (A-B). Scale bars = 5 μm.

(Sophia University, Japan) at the UK *Dictyostelium* Christmas Meeting (December 2019) showed GFP-DstC translocated to the nucleus under compression. As compression elevates intracellular cGMP levels (Figure

4.10A), and cGMP has previously been shown to promote GFP-DstC translocation (Araki *et al.*, 2003), it can be inferred that compression stimulates sufficient cGMP production to observe a physiological response. Therefore, cGMP signalling might contribute to compression-induced autophagy, but cGMP is not the primary mechanism driving this.
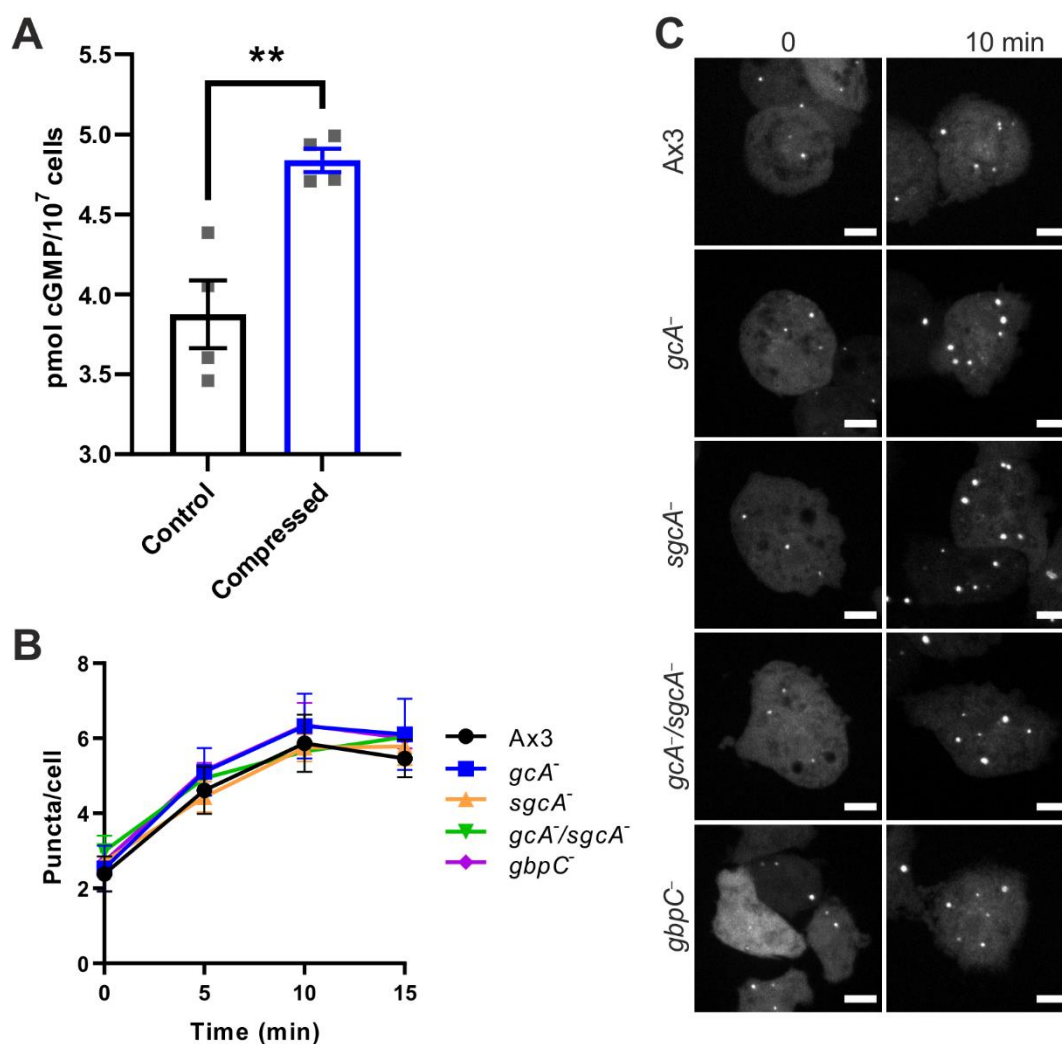
Figure 4.10 **Compression induces cGMP production but is not essential for autophagy.** (A) Ax2 cells subjected to sustained compression for 2 min then lysed in perchloric acid to liberate cGMP for analysis. Bars denote mean average cGMP concentration, where error bars indicate SEM of 4 independent experiments. Each data-point represents an independent biological repeat (mean average of 4 technical repeats). Unpaired 2-tailed t-test, no correction (** $P < 0.01$). (B) Ax3 wild-type parent, *gcA⁻*, *sgcA⁻*, *gcA⁻/sgcA⁻* double knock-out and *gbpC⁻* cells expressing GFP-atg8 subjected to 1.296 kPa sustained compression. Quantification of mean average puncta per cell. Error bars denote SEM of 3 independent experiments (117-271 cells per data-point). Unpaired 2-tailed t-test comparing wild-type Ax3 to knock-out cell lines. No annotation as no significant differences detected. (C) Representative images for each cell line. Scale bar = 5 μm.

4.2.6 Loss of GbpC causes minor impairment to starvation-induced autophagy

Nutrient starvation induces autophagy through canonical signalling pathways and is the driving force behind *Dictyostelium* development. Prolonged nutrient deprivation induces autophagy in a host of organisms (Furuya *et al.*, 2005; Otto *et al.*, 2003; Tanida *et al.*, 2001). In *Dictyostelium* this is primarily mediated through the Tor protein complex. cGMP signalling has been shown to play key roles during development, which occurs in response to starvation, and cGMP has been shown to induce autophagy as a non-canonical signalling pathway (Figure 4.6B, D). As it had not been studied, we wanted to determine if

88

cGMP signalling played a role in autophagy initiation in response to starvation. The effect of starvation is shown in representative images (Figure 4.11A), with quantification for starvation and untreated controls in Figure 4.11B and Figure 4.11C respectively. GbpC-null cells showed a slightly reduced response but loss of both guanylyl cyclase enzymes had no significant effect. This suggests cGMP signalling could contribute to the starvation response, but doesn't play a major role.
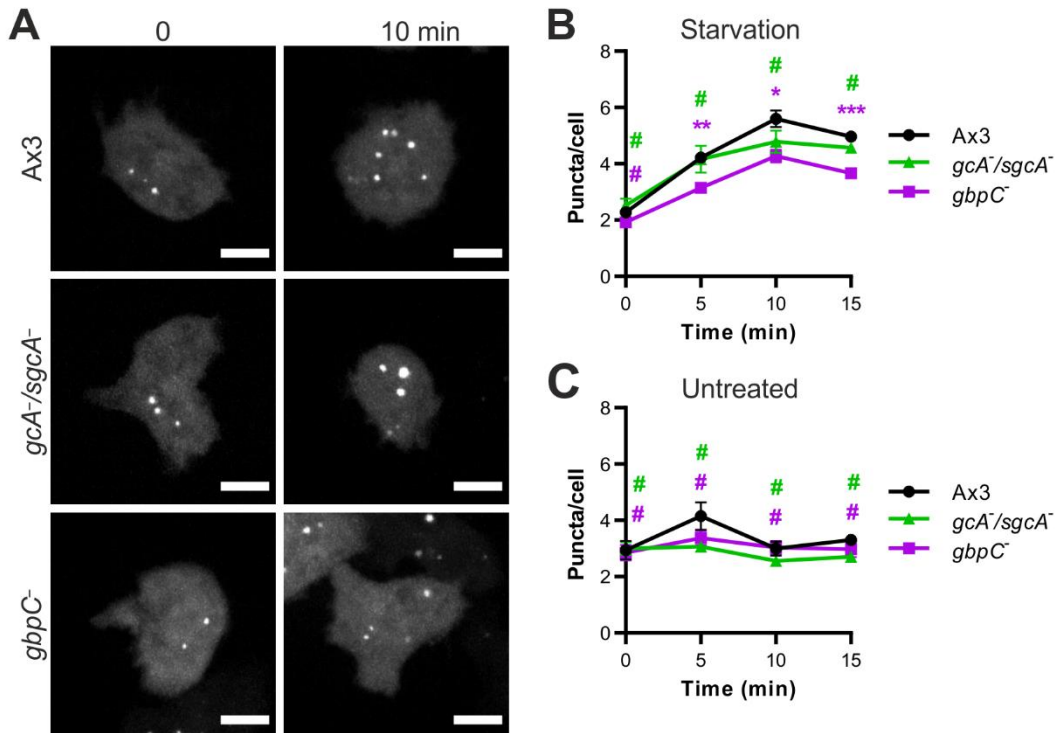
Figure 4.11 **Loss of GbpC reduces autophagic response to nutrient starvation.** Ax3 wild-type parent, *gcA⁻/sgcA⁻* double knock-out and *gbpC⁻* cells expressing GFP-atg8 subjected to arginine and lysine amino acid starvation. (A) Representative images for each condition. Scale bars = 5 μm. Quantification of mean average puncta per cell for (B) starvation and (C) untreated control. Error bars denote SEM of 3 independent experiments (6 independent repeats for *gbpC⁻*) where 160-289 cells were quantified per data-point. Unpaired 2-tailed t-test comparing knock-out cell lines to Ax3 for (B) starvation and (C) untreated control (# $P \geq 0.05$, * $P < 0.05$, ** $P < 0.01$).

4.2.7 Conservation of cGMP-induced autophagy in mammalian cells remains unclear

The autophagic machinery between *Dictyostelium* and mammalian cells is conserved. As a stress-response, autophagy can be induced by multiple stimuli in both *Dictyostelium* and mammalian cell cultures, including nutrient starvation and compression (King *et al.*, 2011). Using *Dictyostelium*, I have shown that compression induces cGMP production (Figure 4.10A) and cGMP induces autophagy (Figures 4.6A-D, 4.7A-B). No literature exists linking cGMP signalling with autophagy in mammalian cells, therefore it was unknown if the response observed in *Dictyostelium* was conserved. In an experimental setup similar to that used with *Dictyostelium*, 8Br-cGMP was titrated and added to MDA-MB-231 cells expressing the autophagy marker GFP-LC3B (Figure 4.12A), alongside relevant control treatments (Figure 4.12B). Quantification of puncta for all treatments shows no clear dose-response after 45 min (Figure 4.12C). Equally the control treatments did not yield a clear increase, and no significant differences were observed under any condition. We concluded that 45 min might have been insufficient to allow accumulation of puncta, and to determine the effect of 8Br-cGMP on autophagy in mammalian cells.
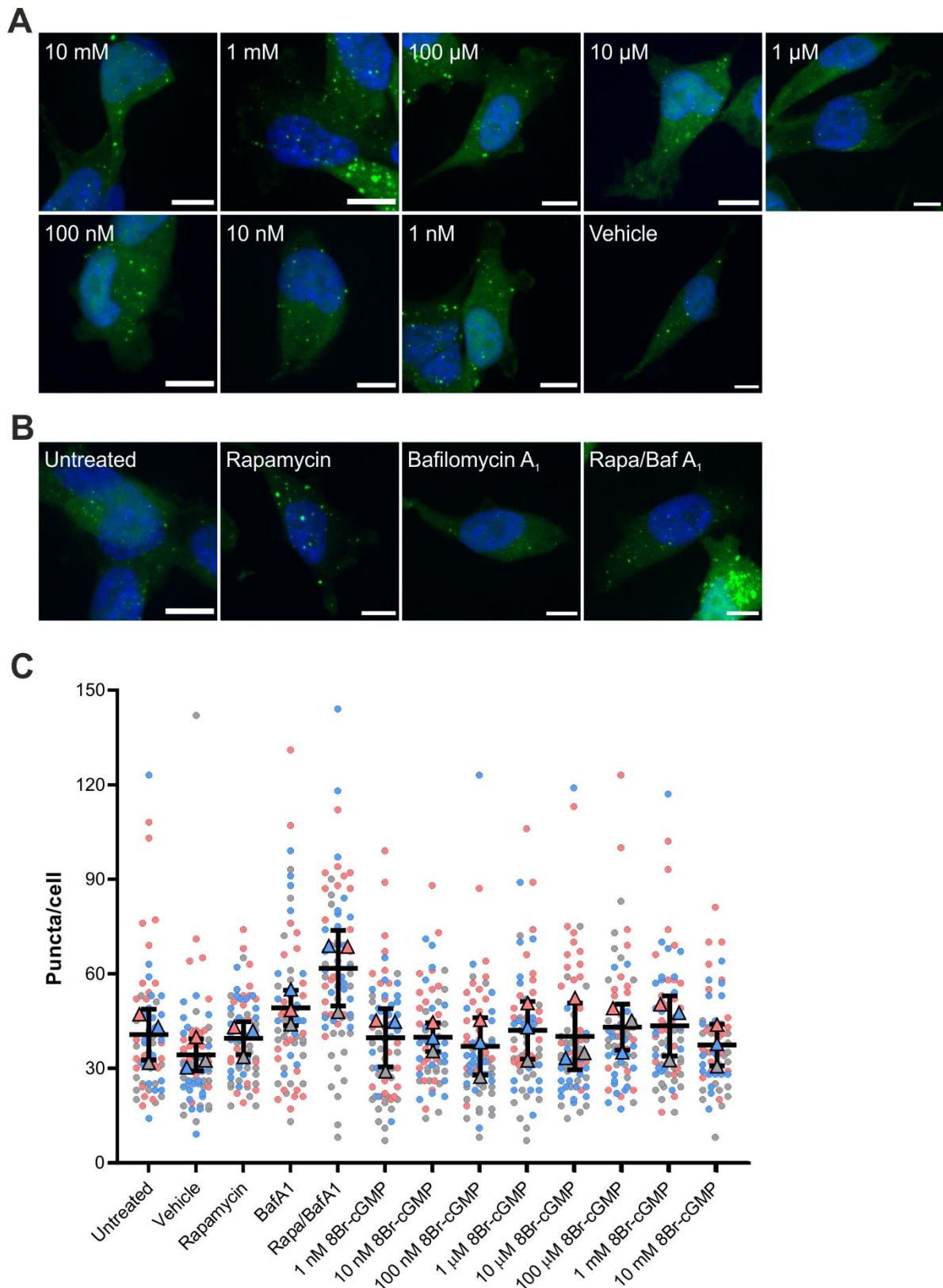
Figure 4.12 **The effect of 8Br-cGMP on autophagy induction in mammalian cells.** MDA-MB-231 cells expressing EGFP-LC3B treated with serially diluted 8Br-cGMP for 45 min. Representative cells for (A) 8Br-cGMP serial dilution, vehicle (10% water) control, and (B) additional control treatments; untreated, rapamycin, and/or Bafilomycin A$_1$. (A-B) Scale bars = 10 μm. (C) Quantification of EGFP-LC3B puncta per cell presented as a SuperPlot (Lord JS *et al.* (2020)). Independent repeats (n = 3; 62-72 cells per condition) are colour coordinated, where puncta counts per individual cell (circle) and mean average per independent repeat (triangle) are shown. Mean average and SD overlayed with bar and whiskers. No significant differences detected using unpaired 2-tailed t-test (# $P \geq 0.05$) comparing controls or treatments.

In light of the previous findings, the protocol was modified to exaggerate any autophagy induction. To ensure no degradation of autophagosomes occurred all conditions were treated in combination with bafilomycin A_1. This would ensure any increase in basal activity could be detected. Additionally treatment time was increased to 2 hr to allow sufficient time for autophagy initiation. Representative images of all conditions tested are shown in Figure 4.13A, with quantification shown in Figure 4.13B. A dose-response was not observed for the 8Br-cGMP titration, however several concentrations were significantly increased compared with vehicle control (Figure 4.13B). No concentration was significantly different to rapamycin treatment (Figure 4.13B). To clarify, "Untreated" was a negative control for all treatments (rapamycin, 8Br-cGMP or vehicle) but contained bafilomycin A_1 which was present in all conditions except "None". "None" was the negative control for bafilomycin A_1 activity. Bafilomycin A_1 was sufficient to significantly increase puncta counts, and addition of the vehicle control had no significant effect (Figure 4.13C). Rapamycin in conjunction with bafilomycin A_1 yielded a significantly greater puncta count than bafilomycin A_1 alone (Figure 4.13C). Violin plots were used to present spread of data across all conditions (Figure 4.13D). There appears to be a small upward trend as 8Br-cGMP concentration increases, but the correlation is not as striking as observed in *Dictyostelium* (Figure 4.6D). Therefore 8Br-cGMP might be capable of inducing autophagy in mammalian cells albeit not as effectively as in *Dictyostelium*.
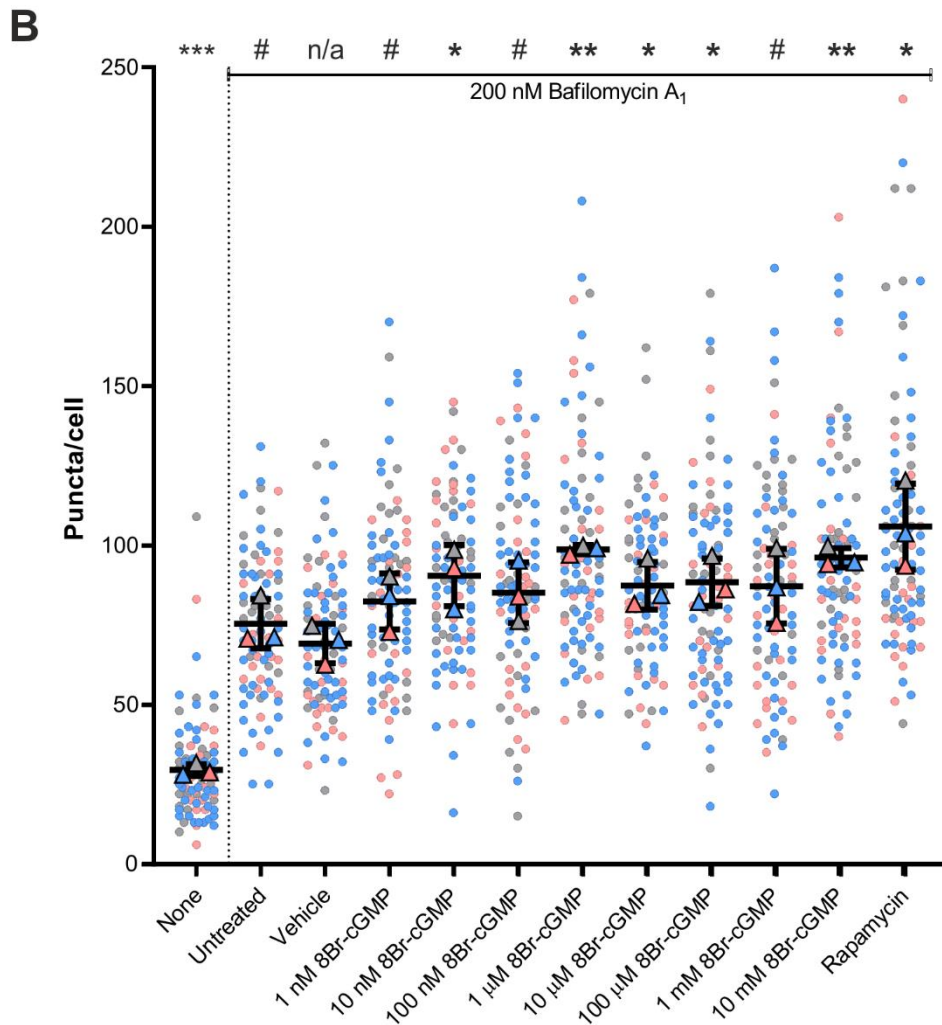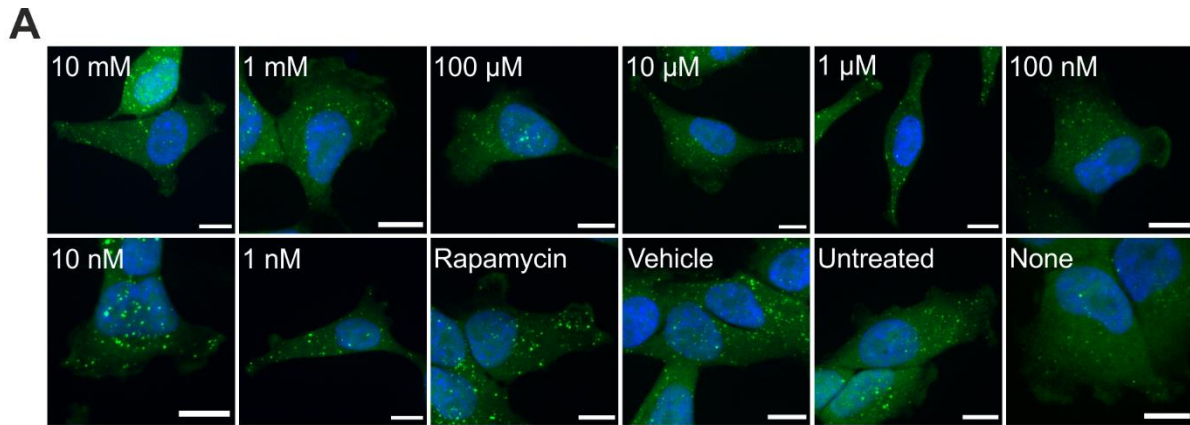
Figure 4.13 **Potential autophagy induction by 8Br-cGMP in mammalian cells.** MDA-MB-231 cells expressing EGFP-LC3B treated with serially diluted 8Br-cGMP, or control treatments, in combination with 200 nM Bafilomycin A_1 for 120 min. (A) Representative cells labelled with either 8Br-cGMP concentrations or relevant control (rapamycin, vehicle (10% water), or untreated). All conditions included Bafilomycin A_1 except "None". Scale bars = 10 μm. (B) Quantification of EGFP-LC3B puncta per cell presented as a SuperPlot (Lord JS *et al.* (2020)). Independent repeats (n = 3; 81-92 cells per condition) are colour coordinated, where puncta counts per individual cell (circle) and mean average per independent repeat (triangle) are shown. Mean average and SD overlayed with bar and whiskers. Unpaired 2-tailed t-test (# $P \geq 0.05$, * $P < 0.05$, ** $P < 0.01$, *** $P < 0.001$) comparing all conditions to vehicle control.

4.3 Discussion

4.3.1 The novel role of cyclic GMP in autophagy

The aim of this chapter was to identify candidates involved in mediating the autophagic response to mechanical stress. Based upon the similar effects on cellular morphology, our hypothesis was that OS and mechanical forces could both act through a common signalling pathway, which, in turn, could induce autophagy. After testing various knock-out cell lines lacking OS effectors, we identified cGMP had a significant and dose-dependent effect on autophagy, causing an accumulation of GFP-atg8$^+$ puncta (Figure 4.6D). Next, we verified whether 8Br-cGMP treatment was increasing autophagy initiation, or blocking degradation. Standard techniques employed in mammalian cultures to quantify autophagic flux were not suitable, as rapamycin does not induce autophagy in *Dictyostelium* and bafilomycin A$_1$ is cytotoxic (data not shown); an alternative approach was required.

Tracking and quantification of *de novo* puncta formation indicated that 8Br-cGMP treatment caused a significant increase in puncta formation (Figure 4.7A). This elevated rate remained reasonably constant from 5-12 min post-treatment addition, then appears to diminish (Figure 4.7B). Furthermore, it was concurrent with increased puncta lifetime, suggesting maturation was slowed (Figure 4.7C). Together, this explains the rapid accumulation of puncta detected in the titration timelapse, followed by the response plateauing by 15 min (Figure 4.6B). Initially, I had attempted to measure autophagic flux directly using the method described by Cardenal-Muñoz *et al.* (2017). This method is optimised for cells growing in HL5 complex medium, however I observed that 8Br-cGMP-induced autophagy was greatly diminished in this media compared with SIH (Appendix 7.2; Figure 7.2). We speculated the complex proteins and/or lipids present in HL5, but not SIH, sequester the 8Br-cGMP. We therefore adapted the protocol to use SIH, however cells exhibited hyper-sensitivity to protease inhibition. Direct measurement of autophagic flux would be useful to resolve the effects of cGMP on autophagy, and a suitable approach needs to be devised.

There are 4 *Dictyostelium* genes containing cGMP binding domains. Of these, only one product exhibits high cGMP affinity and a kinase domain: GbpC (Goldberg *et al.*, 2002). There is currently no evidence that another cGMP-regulated kinase exists in *Dictyostelium*, as loss of GbpC has been show to impair myosin phosphorylation (Bosgraaf *et al.*, 2002). When GbpC was knocked-out, the ability to induce autophagy in response to 8Br-cGMP treatment was lost completely (Figure 4.8A). GbpC is therefore essential for mediating cGMP-induced autophagy. It would be interesting to determine the effect of manipulating specific domains in GbpC, e.g. kinase-dead variant, rather than completely removing the protein. Additionally, the maximal autophagic response in Ax3 to starvation, compression and 8Br-cGMP treatment is markedly lower than observations in Ax2. Validating the role of GbpC in an Ax2 background would further support the conclusion that GbpC is critical for this process.

Both *Dictyostelium* and mammalian cells use cGMP as a secondary messenger. Given the strong dose-response observed in *Dictyostelium*, we expected a similar response would occur within our mammalian cell line. While there were significant increases after 2 hr at several concentrations, a clear correlation was

not detected. The MDA-MB-231 cells used are breast cancer epithelial cells. As cGMP signalling is largely studied in endothelial cells (Angelone *et al.*, 2015; Bredt and Snyder, 1990; Ohno *et al.*, 1993) regarding its role in smooth muscle relaxation and subsequent vasodilation (Ignarro, Byrns, *et al.*, 1987), it raised the question of whether our cell line was capable of responding effectively to cGMP. However the capacity for cGMP production has been shown in response to 10nM dopamine or fenoldopam after 60 min (Borcherding *et al.*, 2016). Additionally, PKG appears to ubiquitously expressed in most human tissues (Papatheodorou *et al.*, 2020), although isoform-specific expression been observed in some tissues (Ørstavik *et al.*, 1997). HUVECs were considered, and while autophagy has been reported to occur in this cell line the induction was minimal; a finding shared by results in the previous chapter (Figure 3.5A-B). Instead an endothelial or smooth muscle cell line amenable to autophagy stimulation, and exhibiting a greater dynamic range between basal and induced conditions, would be more suitable to test cGMP signalling in mammalian cells.

4.3.2 The autophagic response to hyper osmotic stress

Hyper-OS causes water to translocate out of the cell. We showed this induced autophagy with a similar dose-response effect as observed with cGMP (Figure 4.4C). We are confident the data shows a causal link, however best practice is to test multiple osmolytes to verify the response is due to hyper-OS, and not the presumably inert soluble compound; replacing sorbitol with mannitol or NaCl would achieve this. It was established that hyper-OS exerts its effect by stimulating production of cGMP (Oyama, 1996), therefore we explored the role of cGMP signalling machinery in context of autophagy induction. We anticipated that loss of cGMP producing enzymes or the cGMP-regulated kinase GbpC would diminish the response, however loss of cGMP signalling had little effect (Figure 4.9C). We concluded that cGMP was not the primary mechanism responsible, however cGMP could still contribute to the autophagy induction observed. In *Dictyostelium* 809 genes exhibited altered expression in response to hyper-OS (Na, 2007; Na *et al.*, 2007), highlighting the rapid and expansive impact of this stress. It suggests compensatory mechanisms may mitigate the loss of cGMP signalling.

In addition to studying hyper-OS, we looked at hypo-OS and determined it, too, affected autophagy. During hypo-OS, water to move into the cell causing it to swell. This was achieved using distilled water which, by virtue of lacking any soluble material, will elicit a starvation response. The puncta counts were similar to amino acid starvation, although slightly elevated (Figure 4.3E). Whether this is attributed to a starvation response of greater magnitude, or hypo-OS, is hard to resolve. Assuming the latter, it suggests a common pathway may be underpinning all OS. OS disrupts ion homeostasis across the PM, exacerbated by translocation of water, which requires rapid resolution to maintain cellular function. Transmembrane ATPase pumps achieve this, hydrolysing ATP in the process. In mammalian cells, accumulation of AMP or ADP, or the depletion of ATP, activates the AMPK complex (Hardie and Hawley, 2001), which can regulate autophagy through mTORC inhibition (Shaw, 2009) or ULK1 phosphorylation (Egan *et al.*, 2011; Kim *et al.*, 2011). Recently it was shown that *Dictyostelium* AMPKα, the catalytic subunit of the AMPK complex, was

required for basal autophagy and contributed to the starvation response (Ranjana *et al.*, 2019). Assuming *Dictyostelium* respond to disrupted ion gradients in a similar manner to mammalian cells, it is plausible AMPK may mediate the autophagic response. Subjecting cells lacking SnfA (*Dictyostelium* AMPKα) cells to autophagy stimuli, such as OS and 8Br-cGMP, would provide insight into the specific mechanisms response under each circumstance.

4.3.3 The role of cGMP signalling in mechanically induced autophagy

We aimed to identify new candidate signalling pathways which regulate autophagy in order to uncover the mechanism by which mechanical forces induce autophagy. Our discovery that compression activated cGMP signalling is novel, and was particularly promising as a candidate pathway for mechanically induced autophagy, which acts via an unknown, non-canonical mechanism (King *et al.*, 2011). The magnitude of compression-induced cGMP production is substantially lower than reported maximal responses to other stimuli. Aggregating Ax2, Ax3 and DH1 respond to cAMP stimulation, with reports of at least 4-fold increase in cGMP concentration peaking within 10-15 s and diminishing after 60 s (Bosgraaf *et al.*, 2002; Insall *et al.*, 1994; Oyama, 1996). The response to hyper-OS is markedly slower, with a 2.5 min delay before increases are detected, however the response magnitude is much greater: ~16-fold increase at 15 min (Oyama, 1996). It is unclear if compression-induced cGMP production occurs in a manner more similar to the cAMP or hyper-OS responses. Quantifying cGMP concentrations at later time points after sustained compression would resolve this.

Another limitation is the time-consuming process of dismantling the compression apparatus, as cGMP is rapidly degraded by PDEs. Consequently, the true cGMP levels may be greater than we observed. Eliminating the ability to degrade cGMP would circumvent this. PDE inhibition in combination with mechanical stimulation is possible, however there are 3 cGMP-degrading PDEs in *Dictyostelium*: Pde3, Pde5 (PdeD/GbpA) and Pde6 (PdeE/GbpB). In context of Pde5, inhibitors such as sildenafil or SCH 51866 are not suitable as they fail to inhibit cGMP hydrolysis in *Dictyostelium* (Lusche *et al.*, 2005). An alternative approach would be compression of knockout lines. Pde3 and 5 are primarily responsible for regulation of basal cGMP levels (0.01-2μM *in vivo*), whereas Pde6 activity is greatest at higher cGMP concentrations (≥100μM) and speculated to degrade cGMP produced by hyper-OS (Bader *et al.*, 2007). If mechanically-induced cGMP production kinetics mimics that of cAMP stimulation (rapid produced and degraded), compressing Pde3/Pde5 dual-null would be appropriate. However, if compression stimulates a response in a manner akin to hyper-OS with a delayed, but greater induction (Oyama, 1996), Pde6-nulls should be used. This would limit cGMP degradation, and more clearly reveal the extent to which mechanical force induces cGMP production.

The purpose of cGMP production in response to a mechanical stimulus is unclear. The induction is sufficient to elicit a physiological response (unpublished data on GFP-DstC translocation; Tsuyoshi Araki, Sophia University, Japan), but is not responsible for mechanically-induced autophagy (Figure 4.10B). Given the potent effect of 8Br-cGMP on autophagy induction, cGMP signalling may well contribute to autophagy

under compression but was compensated for by currently unknown, redundant pathways. cGMP signalling drives downstream phosphorylation of myosins (Bosgraaf *et al.*, 2002) and can influence cytoskeletal gene expression via DstC (Na, 2007; Na *et al.*, 2007), processes which can modulate cytoskeletal remodelling in response to hyper-OS (Kuwayama *et al.*, 1996). As compression, too, demands cytoskeletal remodelling, it is plausible that the stimulation of cGMP production serves the same purpose as with hyper-OS. This could be tested by probing for myosin phosphorylation post-compression, or compressing myosin-null cells and quantifying cell shape recovery.

4.3.4 Conclusion

We have shown the cGMP is a potent inducer of autophagy and facilitates *de* novo formation of autophagosomes. We have shown that compression elevates intracellular cGMP levels, but this induction is not essential for the autophagic response. Additionally, we have shown the hyper-OS induces autophagy in a proportional manner, and, like compression, does not depend on cGMP signalling. Furthermore, when subjected to amino acid starvation, cells lacking cGMP signalling machinery were generally unperturbed (Figure 4.11B). Currently, it is unclear under what scenario is required for cGMP signalling to induce autophagy. For both compression and hyper-OS, loss of cGMP signalling had no effect on autophagy indicating cGMP signalling isn't required or is being compensated for. It may be that cGMP signalling is itself the compensatory mechanism for other signalling pathways. Further study is needed to resolve the physiological relevance of cGMP in context of autophagy.

The findings in this chapter provide new insights into the many stimuli which can activate autophagy, but also raise further questions about their mechanisms and purpose. cGMP is a novel non-canonical signalling molecule capable of stimulating a strong autophagic response. Figure 4.14 summarises the established and novel findings for cGMP mediated responses to compression, hyper-OS and starvation, highlighting their differences and similarities. In *Dictyostelium* cGMP exerts its function exclusively via the kinase GbpC. At present no explicit GbpC substrate has been reported. Identifying these proteins could uncover downstream components, which would provide candidates to test with respect to autophagy induction. In the event the signalling pathway is found to be conserved in mammalian cells, these substrates would also guide future study to further validate pathway conservation. Potentially they could also provide novel therapeutic targets for treatments manipulating the autophagic process. While largely speculative at present, this research provides a starting point for future studies aiming to uncover the broader implications of cGMP signalling in context of autophagy.
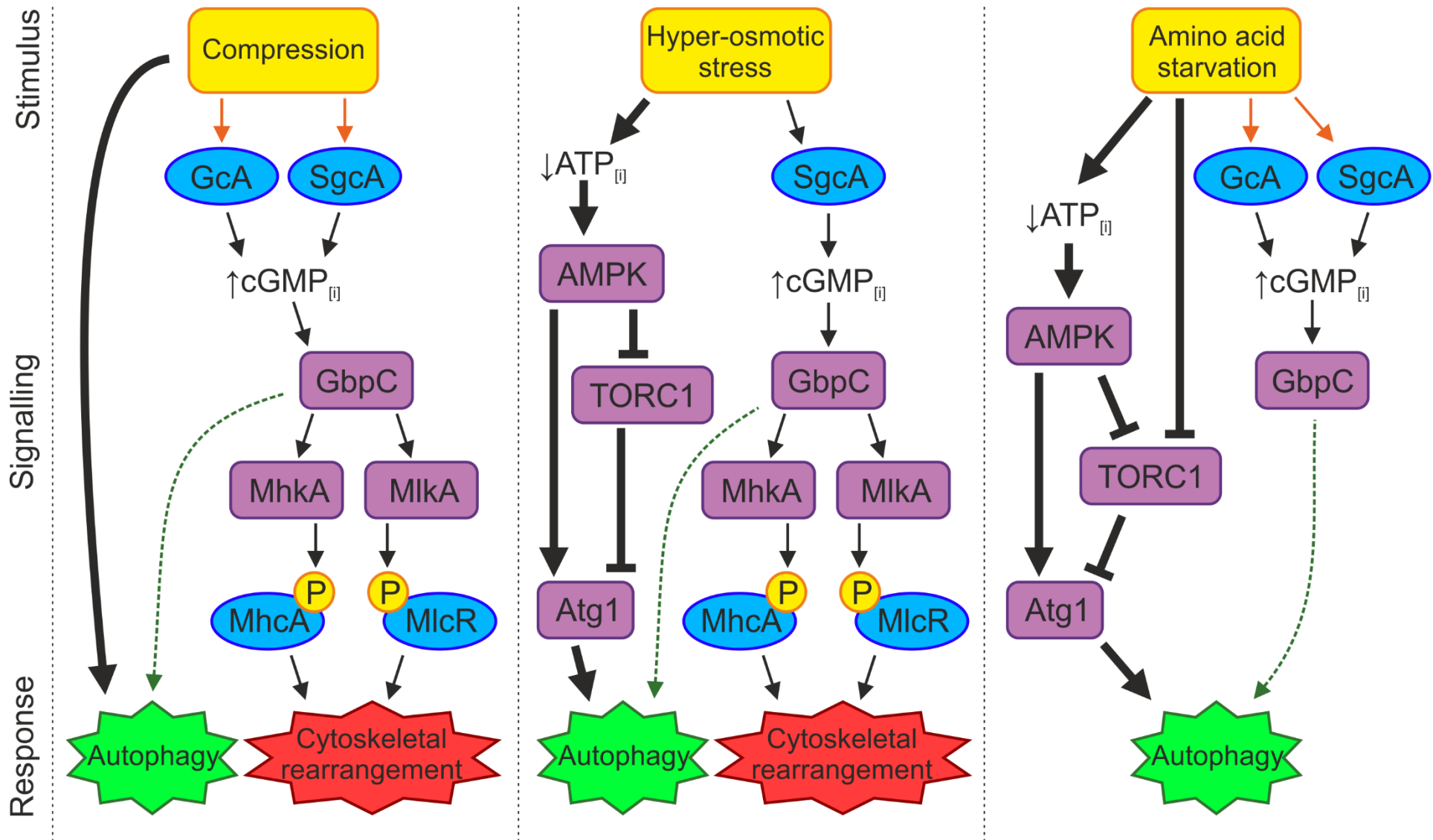
Figure 4.14 **Summary of cGMP roles under stimuli tested.** A schematic depicting the signalling proteins and molecules involved in context of the stimuli utilised in this chapter. Components and connections are based upon available literature and results obtained. Connections are colour co-ordinated based upon whether they are established in literature (black), obtained from data in this chapter (green), or preliminary/inferred (orange). Bold arrows indicate the dominant pathway that contributes the greatest effect in context of autophagy induction deduced from KO experiments ablating components of the secondary pathways.

Chapter 5

Identification of GbpC substrates and candidates for autophagy induction

5.1 Introduction

In the previous chapter, it has been shown that GbpC was essential for autophagy initiation in response to cGMP, however signalling downstream of GbpC remains poorly understood. The existence of a cGMP-binding protein with kinase function was speculated long before ultimately being uncovered through computational analysis almost 20 years ago (Goldberg *et al.*, 2002). GbpC was, and remains, the only *Dictyostelium* gene product containing both cyclic-nucleotide binding and kinase capability. Despite this, no direct substrates have been identified. It is postulated the LRR domain directs protein-protein interactions which determines GbpC substrates (Kortholt *et al.*, 2012), suggesting GbpC might not have an explicit consensus target for phosphorylation.

Although no explicit GbpC substrates are known, several downstream effectors of cGMP signalling have been identified. These include myosin II heavy chain A (MhcA; Kuwayama *et al.*, 1996) and myosin regulatory light chain (MlcR; Liu and Newell, 1994), OSR elements *Dictyostelium* signal transducer and activator of transcription protein C (STATc/DstC; Araki *et al.*, 2003, 2010) and stress-activated protein kinase α (SpkA; Sun, Hui and Firtel, 2003), and diacylglycerol kinase (DgkA; de la Roche *et al.*, 2002). While not involved in autophagy, these known effectors will provide critical validation of phosphoproteomic analyses.

The aim of this chapter is to determine GbpC substrates, specifically those that transduce cGMP signalling to regulate autophagy. This would primarily be achieved by studying the phosphoproteome of wild-type cells treated with 8Br-cGMP to specifically activate GbpC, and identifying upregulated phosphorylations. This will be supported by quantifying changes in the GbpC-null phosphoproteome. Cross-referencing 8Br-cGMP upregulated, and GbpC-null downregulated, phosphosites will uncover candidate substrates for further study. In addition to this, the GbpC-null proteome will be determined, and gene ontology (GO) analysis and/or consensus sequence alignments will be undertaken, where appropriate, to further our understanding of the role and function of GbpC within *Dictyostelium*. This is outlined in Figure 5.1.

5.2 Results

5.2.1 Loss of GbpC alters the proteome

The signalling pathways involving GbpC are poorly understood. GbpC is encoded by a large gene, yielding a 2631 amino acid protein. Consequently cloning GbpC has proven challenging, however null cells were successfully generated from Ax3 parent cells in the van-Haastert lab (University of Groningen, Netherlands; Veltman and van Haastert, 2008). Expression of GFP-tagged GbpC is low, observed in both literature and my own experiments, making it difficult to determining interacting partners and kinase substrates. To better understand the global impact of GbpC loss, changes in the proteome were determined. While it was unclear whether loss of GbpC would have any impact, one known GbpC effector is the transcriptional regulator DstC suggesting minor changes in the proteome were plausible.
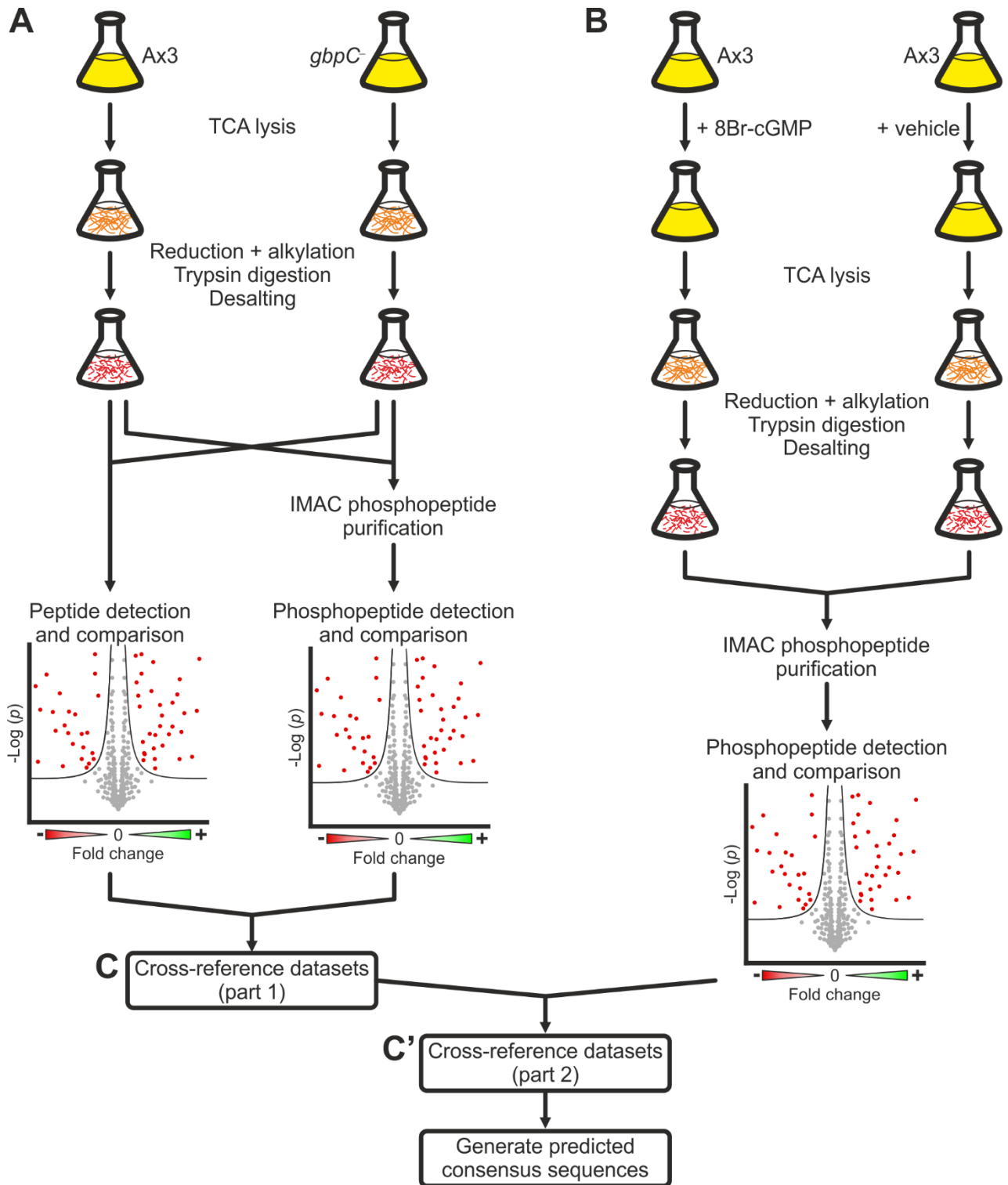
Figure 5.1 **Experimental design for identifying GbpC-mediated phosphorylations**. To identify changes in the phosphoproteome mediated by GbpC, the experiment was broken down into 3 main stages: (A) comparison of wild-type Ax3 and *gbpC⁻* cells in both the proteome and phosphoproteome, (B) identification of phosphorylation changes in response to the GbpC activating compound 8Br-cGMP, and (C-C') systematic cross-referencing datasets to identify candidate GbpC substrates, downstream proteins involved in signalling and prediction of consensus sequences. (A-B) Cells were cultured and, where appropriate, treated with 5 mM 8Br-cGMP or vehicle (water) control. Signalling was halted using TCA which lysed cells and precipitated proteins. Protein pellets were solubilised, reduced and alkylated, then digested overnight with trypsin. Digested samples were desalted using reverse-phase tC18 SepPAK solid-phase extraction cartridges. Where necessary, a small sample of purified peptides were used for proteome analysis. Remaining samples were enriched for phosphopeptides by IMAC and phosphopeptides were detected by gas-phase mass spectrometry. Results were processed and analysed using MaxQuant and Perseus to detect changes in peptide or phosphopeptide abundance between samples, presented as a volcano plot to identify both fold-change and signficance. Data points above the threshold and considered significant are red.

Protein samples for both vegetative GbpC-null and wild-type Ax3 cells were prepared and subjected to gas-phase mass-spectrometry to determine changes in protein levels. Peptides were detected and matched to 2820 individual genes, of which 152 showed altered expression (Figure 5.2A); 68 genes were increased, and 84 were decreased. A refined selection of gene products with altered abundance are shown in Table 5.1, containing known GbpC effectors, stress-response and cytoskeletal proteins, as well as genes with the greatest fold-change (greater than 3-fold change). A complete list of all genes can be found in Appendix 7.3 (Table 7.1). Whilst GbpC itself did not initially appear on the list of significantly reduced proteins, review of the raw data confirmed no peptides were aligned to GbpC in any of the 4 GbpC-null samples (Figure 5.2B). Low numbers of peptides detected in the control samples prevented this from being statistically significant, but the data confirm that the GbpC-null cell line was definitively a knock-out. The genes that were identified with altered expression were found to have diverse roles, however similar functions were identified.

To visualise all genes and their corresponding fold-change in GbpC-null cells, data points were presented as a volcano plot. Figure 5.2C shows all 2820 genes plotted by fold-change and the inverse log of significance (determined by T-Test). To determine significance, a non-linear threshold was applied which combined a minimum significance of $p < 0.05$ which was proportional to the fold-change. As the fold-change magnitude decreased the p-value required for significance also decreased. Genes which failed to meet this criteria are highlighted in grey, whereas significant increased or decreased expression are shown in green and red respectively. Larger data-points denote genes of interest and are categorised in the legend, which will be discussed further below.

Cyclic-nucleotide monophosphate (cNMP) interactors are involved in the generation of, and/or binding to, cyclic-nucleotides. cAMP and cGMP are both second messengers with individual and overlapping roles, therefore it is important to consider both. cAMP-interacting proteins CapB (cAMP-binding protein 2) and PrtB (cAMP-regulated M3R protein) were both less abundant in GbpC-null cells. Beyond GbpC no other proteins explicitly involved in cGMP signalling were identified. Consequently loss of GbpC affects genes involved in both cAMP and cGMP signalling.

Several cytoskeletal proteins were identified with altered abundance. Myosin kinases were unchanged, however both myosin heavy chain IB (MyoB) and IK (MyoK) were more abundant. Loss of GbpC altered expression of several actin-binding proteins. Ponticulin A (PonA) and ponticulin-like protein C2 (PonC2) both exhibited increased expression. Levels of actobindin-A (AbnA), which sequesters G-actin and stabilises actin dimers, was reduced.

Interestingly a variety of proteins involved in guanine nucleotide signalling were identified. Guanine Exchange Factors (GEFs) facilitate dissociation of GDP from a protein and subsequent binding of GTP to replace it, often resulting in activation. GTPase activating proteins (GAPs) stimulate hydrolysis of GTP which typically halts further activity. Together these proteins control which guanine nucleotide is bound, creating

a binary system for modulating signalling cascades. Several GAPs (GacG, RsmM, Rab2A and RasG) were determined to have increased expression, while the uncharacterised protein DDB0204568, a predicted Arf

Gene name	Protein name	Fold-change	-log(p)	Category
3B	Prespore-specific protein 3B	1.212	3.699	Development
abnA	Actobindin-A	-0.683	2.424	Cytoskeletal
amdA	AMP deaminase	0.421	5.551	Development, metabolism
capB	cAMP-binding protein 2	-0.832	4.483	cNMP-interactor
cshA	Citrate synthase, peroxisomal	-0.512	5.675	Metabolism
cupC	Calcium up-regulated protein C	2.097	1.863	Development, Stress response
cupF	Calcium up-regulated protein F	1.281	5.906	Development, Stress response
cupG	Calcium up-regulated protein G	2.225	1.668	Development, Stress response
DDB_G0268948	Putative methyltransferase DDB_G0268948	-1.144	5.088	Metabolism
DDB_G0274223	Glutathione S-transferase domain-containing protein DDB_G0274223	-4.209	4.844	Metabolism
DDB_G0279347	Uncharacterised protein	-3.756	1.629	Unknown
DDB_G0280445	Glutathione-dependent formaldehyde-activating, GFA family protein	-1.079	5.576	Metabolism
DDB0168017	Uncharacterised protein	-0.977	5.479	Unknown
DDB0188011	Uncharacterised protein	-1.468	5.867	Unknown
DDB0191869	Uncharacterised protein	3.210	2.796	Unknown
DDB0217648	Uncharacterised protein	3.206	4.871	Unknown
DDB0219383	Uncharacterised protein	-2.927	3.443	Unknown
DG1091	Developmental protein DG1091	-2.591	2.825	Development
ech1	Delta(3,5)-Delta(2,4)-dienoyl-CoA isomerase, mitochondrial	-4.552	4.285	Metabolism
gacG	Rho GTPase-activating protein gacG	2.229	2.324	G-protein
gcvT	Aminomethyltransferase, mitochondrial	0.506	2.39	Metabolism, Mitochondrial
gpaI	Guanine nucleotide-binding protein alpha-9 subunit	0.500	3.309	G-protein
gxcJJ	Rac guanine nucleotide exchange factor JJ	-2.099	1.643	G-protein
hspI	Small heat shock protein hspI, mitochondrial	-1.911	5.263	Mitochondrial
krsA	Serine/threonine-protein kinase 4 homologue A	0.550	2.458	Osmo-regulation
lmpB	Lysosome membrane protein 2-B	0.570	3.282	Lysosomal
metap1	Methionine aminopeptidase 1	-1.033	5.876	Proteolysis
metE	5-methyltetrahydropteroyltriglutamate-homocysteine methyltransferase	7.280	6.372	Metabolism
mob2	MOB kinase activator-like 2	3.005	2.530	Unknown
myoB	Myosin IB heavy chain	0.441	3.058	Cytoskeletal
myoK	Myosin-K heavy chain	0.585	3.946	Cytoskeletal
prtB	cAMP-regulated M3R protein	-0.716	3.717	cNMP-interactor
rab2A	Ras-related protein Rab-2A	0.526	3.003	G-protein, Osmo-regulation
rasG	Ras-like protein rasG	0.438	3.26	G-protein
rsmM	Small GTPase	0.669	2.764	G-protein

Table 5.1. Significant expression changes in vegetative *gbpC⁻* cells. Exhaustive table of results in Appendix 7.3 (Table 7.1).
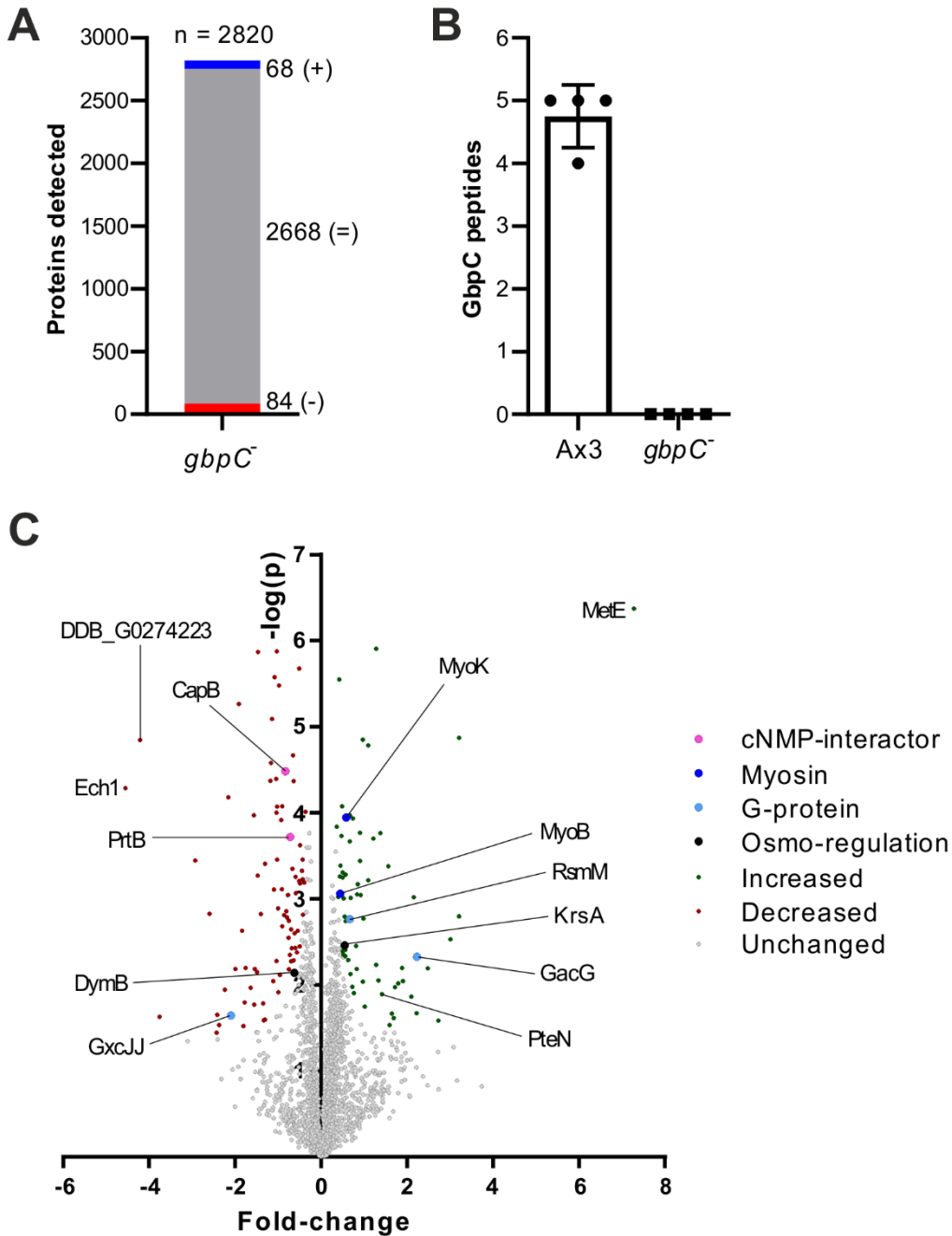
Figure 5.2 **GbpC loss alters proteome.** Protein expression profile of GbpC-null cells. (A) Total peptides identified as increased (+), decreased (-) or unchanged (=) in GbpC-null cells relative to wild-type Ax3. (B) Number of GbpC peptides detected in each sample subjected to mass-spec analysis. Error bar shows standard deviation (n = 4). (C) Volcano plot where all significant changes in proteome are shown. Grey data-points fell below the significance threshold ($P < 0.05$), with smaller fold-changes subjected to greater stringency and lower thresholds. Larger data-points denote genes of interest and are categorised as indicated, with key nodes are labelled.

GAP, was decreased. GxcJJ (Rac GEF factor JJ) was substantially reduced, while GpaI (guanine nucleotide-binding protein alpha-9 subunit) was more abundant. Given the various genes affected, downstream signalling of GbpC appears to have a significant impact on signalling machinery.

Two proteins involved in osmo-regulation were found to have altered expression. KrsA, a serine/threonine-protein kinase 4 homologue and member of the STE20 family, was found to have slightly increased expression. Dynamin B (DymB), which interacts with components of the actin cytoskeleton and is

103

implicated in cell motility, adhesion, fatty acid metabolism, and resistance to hypotonic osmotic shock (Rai *et al.*, 2011), was slightly less abundant (reduced 0.624-fold, p = 0.0072, q = 0.047). Altered expression of osmo-regulatory genes is likely to compensate GbpC loss.

In addition to the aforementioned genes, some exhibited drastic expression changes. MetE (5-methyltetrahydropteroyltriglutamate-homocysteine S-methyltransferase) is a cobalamin-independent methionine synthase involved in the terminal stage of methionine synthesis (Pejchal and Ludwig, 2005). This protein was 7.28-fold more abundant in cells lacking GbpC. The greatest protein level reduction was in Ech1, a mitochondrial Delta(3,5)-Delta(2,4)-dienoyl-CoA isomerase, reduced 4.552-fold. Additionally, several uncharacterised proteins were also found to have >3-fold altered expression. The cause and functional significance of these changes in GbpC-null cells is unclear.

Alongside the array of altered gene groups, several miscellaneous genes were differentially expressed in GbpC, highlighting the diverse range of pathways GbpC is involved with. Levels of LmpB, a lysosomal membrane protein, moderately increased in GbpC-null, while mitochondrial proteins heat shock 70kDa (Mhsp70) and small heat shock protein (HspI) were decreased. Calcium up-regulated proteins C, F and G all exhibited increased expression.

Gene ontology (GO) analysis identifies over- or under-represented terms affiliated with genes/proteins relative to a background dataset. GO terms are allocated to genes depending on their function, involvement with pathways and process and subcellular localisation. These terms are broadly categorised into three groups: biological process, cellular compartment and molecular function. This allows global changes to be more easily identified than through analysis of individual components alone.

GO analysis of proteomic changes in GbpC-null cells is shown in Figures 5.3A-C for biological process, cellular compartment and molecular function categories. The results were largely uninformative, relating to several different processes or compartments, however stress-related genes were 2.88-fold over-represented (Figure 5.3A). It is clear GbpC is involved in a multitude of biological pathways and processes, although no terms relating to autophagy were identified. While no autophagy terms were identified, the analysis supports previous findings that GbpC signalling and has a wide range of implications downstream.

The abolition of GbpC affects a plethora of biological processes throughout the cell. GbpC has been shown to be involved in cytoskeletal dynamics (Kortholt *et al.*, 2012; Veltman and van Haastert, 2008), myosin phosphorylation (Bosgraaf *et al.*, 2002), and the OSR (Araki *et al.*, 2003, 2010; Van Haastert and Kuwayama, 1997). The results presented have identified genes with altered expression in all these categories, further supporting the role of GbpC in their regulation. GbpC itself is not a transcription factor thus does not directly affect another genes abundance, but downstream signalling to known transcription factors such as DstC will impact target genes. As expected, no autophagy candidates were found, however several genes identified are potentially suitable for follow-up experimentation to validate both their existence and function.

Figure 5.3 **GO enrichment analysis of GbpC-null proteome.** Proteins identified as having altered expression in GbpC-null cells were compared with the complete GO annotation datasets for *D. discoideum* to identify over-representation of terms for (A) biological processes, (B) cellular compartment and (C) molecular function. GO over-representation was determined using the Fishers exact test with False Discovery Rate correction, using the PANTHER14.1.

5.2.2 GbpC loss causes minimal changes to phosphoproteome

GbpC contains a kinase domain essential for propagation of signalling, thus it was anticipated that ablation of the protein would result in substantial changes to the phosphoproteome. However, unlike in the proteome, the difference between wild-type Ax3 and GbpC-null cell phosphoproteomes was minimal. A total 4278 phosphorylation sites were detected but only 42 were significantly altered (Figure 5.4A). A selection of these modifications are shown in Table 5.2. An exhaustive list can be found in Appendix 7.4 (Table 7.2). Serine accounted for almost 75% of modifications, with threonine accounting for the remainder (Figure 5.4B). As expected, the majority of detected phosphosites were significantly phosphorylated.

As previously described for Figure 5.2C, all identified phosphosites were plotted as a scatter-graph to visualise changes. Figure 5.4C shows all 4278 phosphosites plotted by fold-change and the inverse log of significance (determined by T-Test). The non-linear significance threshold required a minimum of p<0.05, with increased stringency as the fold-change decreased. Data-points below the threshold are shown in grey, with significant increased and decreased phosphorylations shown in green and red respectively.

Larger data-points are proteins of interest, with similar genes grouped upon their function. Despite only a handful of proteins with altered phosphorylation status, several interesting hits were identified.

As expected, the majority of detected changes were negative. Unlike in the proteomics data where a decrease in GbpC peptide abundance was not detect, there was a significant decrease in a GbpC phosphopeptide. As with the proteomic results, the absence of GbpC peptides in GbpC-null cells was again verified using the raw data. The specific downregulated phosphorylation occurred at S2322 (Table 5.2). The phosphosite is not located within a domain, but is proximal to the GRAM domain (van Egmond *et al.*, 2008; Goldberg *et al.*, 2002). The function of this modification is unknown, and is only mentioned once in the literature. Nichols *et al.* (2019) detected increased phosphorylation in response to both cAMP (10, 45 and 360 s) and folate (45 s) stimulation, and concluded the modification was not within a known consensus motif. Given GbpC is absent in the null cells used in my experiment, it suggests the pool of available GbpC may be partially phosphorylated at S2322 at basal levels, and phosphorylation increases upon GbpC activation.

The most striking decrease was in the actin-interacting protein Carmil. Originally called p116 until renamed by Jung G *et al*. (2001) to Carmil (Capping protein, Arp2/3, and Myosin I Linker), this protein is a key component in actin regulation. Carmil is distributed throughout the cell, often concentrated at the leading edge and peripheral protrusions. As implied in its name, Carmil interacts with F-actin capping proteins AcpA and AcpB, Arp2/3, and type I myosins (specifically MyoB and MyoC), acting as a scaffold to these and other key proteins. This creates a complex capable of both initiating actin filament formation and terminating further assembly. Loss of GbpC resulted in a 6.270-fold decrease in phosphorylation of the T970 residue, occurring within one of the 2 PxxP domains with which myosins IB and IC bind via their Src homology 3 (SH3) domains (Jung *et al.*, 2001). This suggests a potentially novel mechanism for Carmil and actin cytoskeleton regulation by cGMP signalling via GbpC.

Several other genes were noted as having reduced phosphorylation. The probable polyketide synthase 16 (Pks16), a fatty acid synthase (FAS) gene expressed predominantly in vegetative cells (Narita *et al.*, 2014), showed reduced T1374 phosphorylation. MkcC, a probable serine/threonine-protein kinase similar to MAP kinase cascade C, was also less phosphorylated at S493. Several uncharacterised proteins also exhibited reduced phosphorylation, of which two (DDB0205685 and DDB0167384) contained multiple sites. The relevance of these modifications downstream of cGMP signalling will remain unclear until they are characterised.

The only gene identified with both altered expression and phosphorylation status was MetE, however there were similarities regarding the functions of affected proteins. Cytoskeletal proteins Phg2 and LimD, which interact with actin, showed increased phosphorylation. G-protein interactors were also modified, including the RhoGAP proteins GacF and GacH, and the RhoGTPase domain, vps9 domain containing protein, DDB0216929.

Gene name	Protein name	Phospho-site	Phosphoproteome Fold-change	-log(p)	Proteome Fold-change	-log(p)	Category
carmil	Protein CARMIL	T970	-6.270	6.757			Cytoskeletal
DDB0168507	Uncharacterised protein	T517	4.285	5.237			Unknown
DDB0169506	Uncharacterised protein	S315	-6.125	5.718			Unknown
DDB0184357	Uncharacterised protein	S20	4.172	5.816			Unknown
gacF	Rho GTPase-activating protein gacF	S9	-2.194	4.789			G-protein
gacH	Rho GTPase-activating protein gacH	S43	4.142	5.221			G-protein
gbpC	Cyclic GMP-binding protein C	S2322	-5.135	5.183			cNMP-interactor, Roco
limD	LIM domain protein	S501	2.964	3.549			Cytoskeletal
metE	5-methyltetrahydropteroyltriglutamate-homocysteine methyltransferase	S762	3.709	3.502	7.280	6.372	Metabolism
mkcC	Probable serine/threonine-protein kinase mkcC	S493	-3.255	4.049			Signalling
phg2	Serine/threonine-protein kinase phg2	S705	4.870	3.509			Osmo-regulation
pks16	Probable polyketide synthase 16	T1374	-4.691	5.819			Metabolism
prlA	Proliferation-associated protein A	S2	4.558	2.940			Vegetative
rpl18a	60S ribosomal protein L18a	S118	3.853	4.620			Ribosomal

Table 5.2. Significant phosphorylation status changes in vegetative *gbpC*⁻ cells with significant changes in proteome included. Refined list of potentially relevant and greatest fold-change entries. Exhaustive table of results in Appendix 7.4 (Table 7.2).
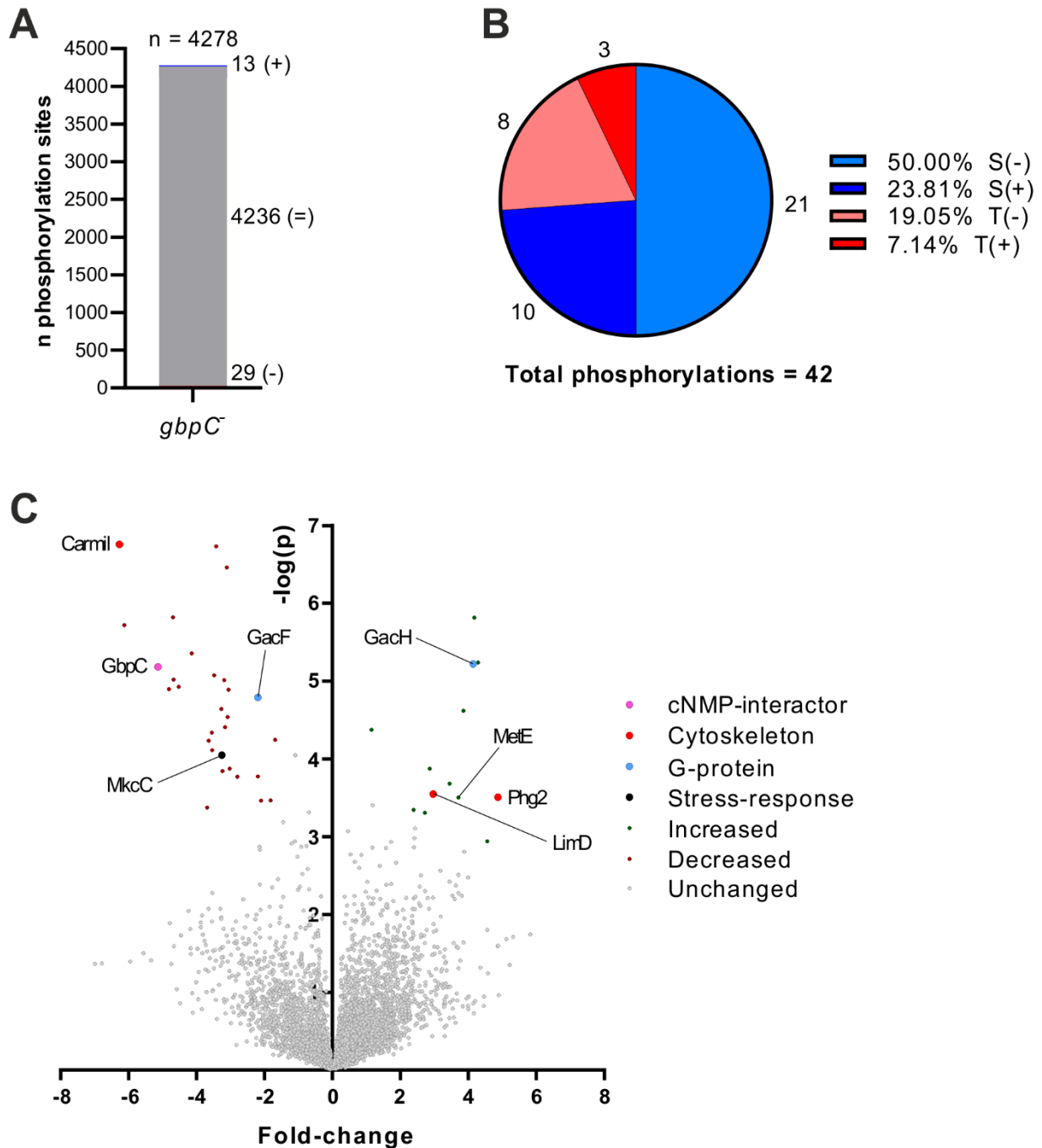
Figure 5.4 **GbpC loss causes minor changes to phosphoproteome.** Phosphoproteome of GbpC-null cells. (A) Phosphopeptides identified as increased (+), decreased (-) or unchanged (=) in GbpC-null cells relative to wild-type Ax3. (B) The proportion of significantly altered phosphosites broken down by phosphosite (serine or threonine) and whether the modification was increased (+) or decreased (-). (C) Volcano plot where all significant changes in phosphorylation status are shown. Grey data-points fell below the significance threshold ($P < 0.05$), with smaller fold-changes subjected to greater stringency and lower thresholds. Larger data-points denote genes of interest and are categorised as indicated, with key nodes are labelled.

As previously shown with proteome data, genes with significant changes in phosphorylation status were analysed for over- or under-represented gene ontology terms. All analysis procedures were identical, utilising the same background dataset, platform and statistical analyses. Due to the small sample size of 42, only a handful of GO terms were significantly over-represented for biological process (Figure 5.5A), cell compartment (Figure 5.5B) and molecular function (Figure 5.5C) terms. Across all groups, over-representation fold-change ranged from 2.01 to 4.02. Of the few gene ontology terms that arose from the

analysis, the definitions are broad; little can be concluded beyond that the loss of GbpC-mediated phosphorylation causes some changes to the cell.
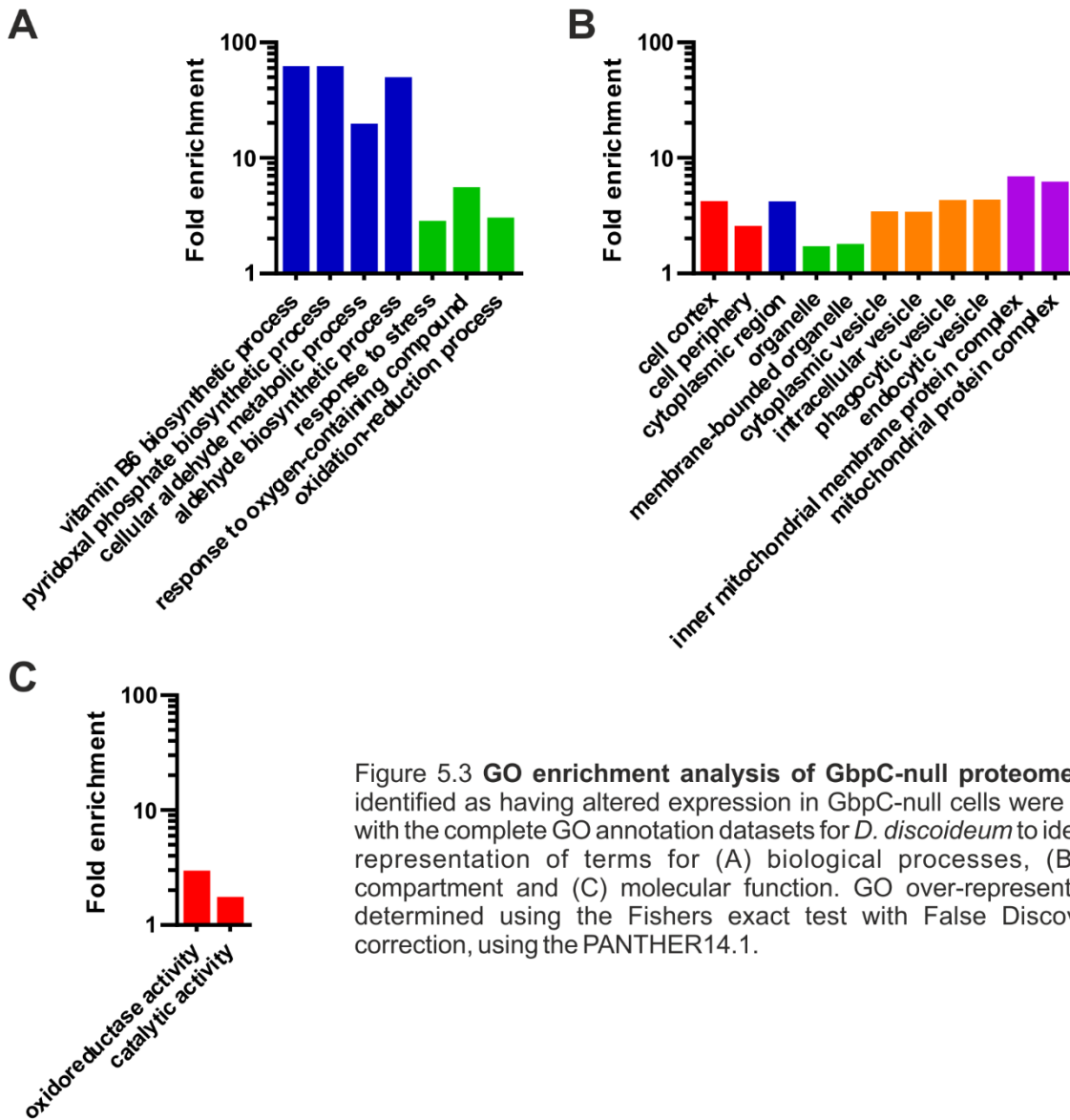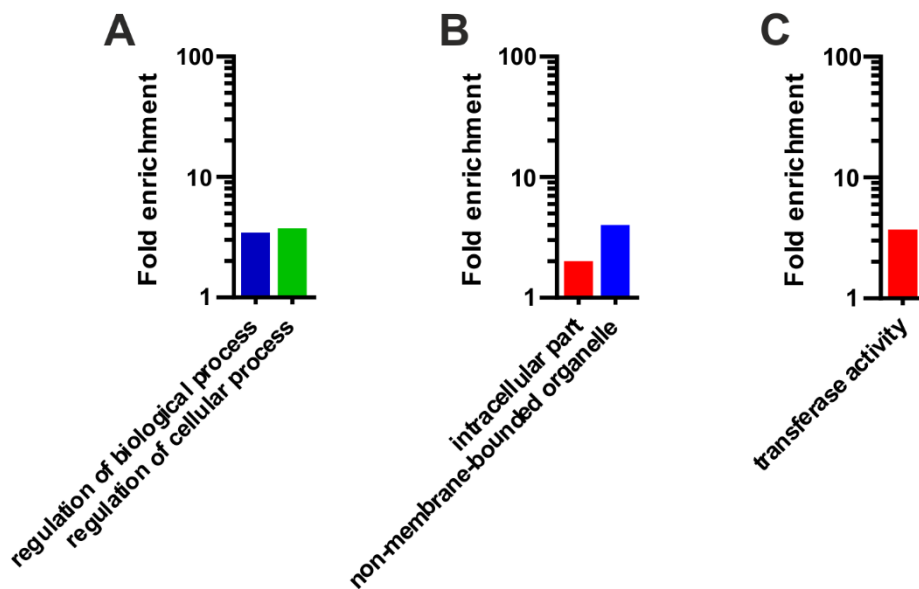

Figure 5.5 **GO enrichment analysis of GbpC-null phosphoproteome.** Proteins identified as having altered phosphorylation in GbpC-null cells were compared with the complete GO annotation datasets for *D. discoideum* to identify over-representation of terms for (A) biological processes, (B) cellular compartment and (C) molecular function. GO over-representation was determined using the Fishers exact test with False Discovery Rate correction, using the PANTHER14.1.

Ablation of a kinase will inevitably affect the phosphoproteome as target substrates are no longer phosphorylated by it. This was the case for GbpC, although global changes were less ground-breaking than anticipated. Despite this, the genes with altered phosphorylation largely fall within the same groupings as identified in the GbpC-null proteome; actin/cytoskeletal proteins, stress-response elements and GAPs/GEFs. Activation of the GbpC kinase domain requires cGMP production and subsequent binding. Given the minimal change in the phosphoproteome of cells lacking GbpC, and apparent lack of functional redundancy, it is likely that GbpC basal activity is minimal; it predominantly exerts its effect when stimulated. Unfortunately, no autophagy genes were identified, however the majority of significant changes were in uncharacterised proteins meaning their involvement cannot be ruled out until further characterisation has been completed. Despite not successfully elucidating genes involved in autophagy induction, both proteome and phosphoproteome data have provided further evidence of, or implicated for the first time, the role of GbpC in a variety of cellular processes.

5.2.3 GbpC stimulation causes rapid and diverse modification of the phosphoproteome

Upon stimulation, guanylyl cyclases convert GTP to cGMP which binds GbpC and activates its kinase domain, resulting in phosphorylation of substrate proteins. In chapter 4, I showed that autophagy was up-regulated upon 8Br-cGMP stimulation of cells, for which GbpC was essential. To further investigate the signalling pathways activated by this treatment, I performed phosphoproteomic analysis of cells stimulated with 8Br-cGMP. 8Br-cGMP, a plasma-membrane permeable analogue of cGMP, allowed for GbpC to be activated without interference from other pathways. Wild-type Ax3 cells were stimulated with 8Br-cGMP or

vehicle control for 2 min then, as previously described, protein samples were prepared, digested and enriched for phosphopeptides prior to mass-spectrometry. Na (2007) showed expression of 38 genes occurred after 15 min of hyper-OS, therefore given the short treatment time it was decided that proteome analysis was not necessary. Using the methods described, a plethora of phosphorylation changes facilitated by GbpC were identified.

In stark contrast to GbpC-null phosphoproteome data, the number of modified phosphosites identified was substantially greater. The number of sites was approximately half compared with GbpC-null phosphoproteome data, as half the protein sample was prepared (~1mg) per condition (Figure 5.6A). A total of 375 sites exhibited modified phosphorylation, with 310 increased and 65 decreased. A complete list of all modifications can be found in Appendix 7.5 (Table 7.3). Phospho-serine accounted for the greatest proportion of modified sites (84.96%) followed by phospho-threonine (14.51%), where the majority were increased (Figure 5.6B). Only 2 tyrosine residues were detected, both with increased phosphorylation. As previously described for Figures 5.2C and 5.4C, Figure 5.6C presents all identified phosphosites as a scatter-graph to visualise the impact of GbpC activation.

5.2.3.1 Known GbpC effector proteins were modified

Cyclic-nucleotide interacting proteins were anticipated as being modified and several were identified as phosphorylated in response to treatment. Phosphorylation of the T2480 residue of GbpC was increased (Table 5.3), however the role of this modification is unclear. Nichols JME (2019) noted that GbpC S2322 was phosphorylated after cAMP or folate stimulation, however no mention of T2480 was made. Phospho-S2322 was identified as significantly decreased in GbpC-null cells (Table 5.2), and while an increase was detected in 8Br-cGMP treated Ax3 this was not significant (p=0.389, q=0.485, 1.093-fold increase). It is unknown whether the modification was from another protein, or intramolecular. LRRK2, the mammalian GbpC homologue, contains a ROC-COR domain and has been shown to autophosphorylate itself both *in vitro* (West *et al.*, 2005) and *in vivo* (Sheng *et al.*, 2012), suggesting GbpC autophosphorylation is possible.

Phosphorylations occurred in several genes involved in cGMP metabolism. Soluble guanylyl cyclase, SgcA, is solely responsible for conversion of GTP to cGMP in response to hyper-OS (Roelofs and van Haastert, 2002), and was found to have reduced phosphorylation at the S2752 residue (Table 5.3). PdeD, the cGMP-dependent 3',5'-cGMP phosphodiesterase A, halts cGMP signalling by breaking the second messenger down to GMP. Binding of cGMP to PdeD enhances its catalytic activity (Bosgraaf *et al.*, 2002). An increase in PdeD S149 residue phosphorylation was detected (Table 5.3). The glutamine-hydrolysing GMP synthase, GuaA, also showed greater phosphorylation at the S5 residue. Modification of these genes likely functions as a feedback mechanism which would prevents unperturbed cGMP signalling once the stimulus has ceased. Furthermore, the detection of phosphorylation changes in known cGMP signal transduction proteins increases our confidence in the reliability of the phosphoproteomic data.
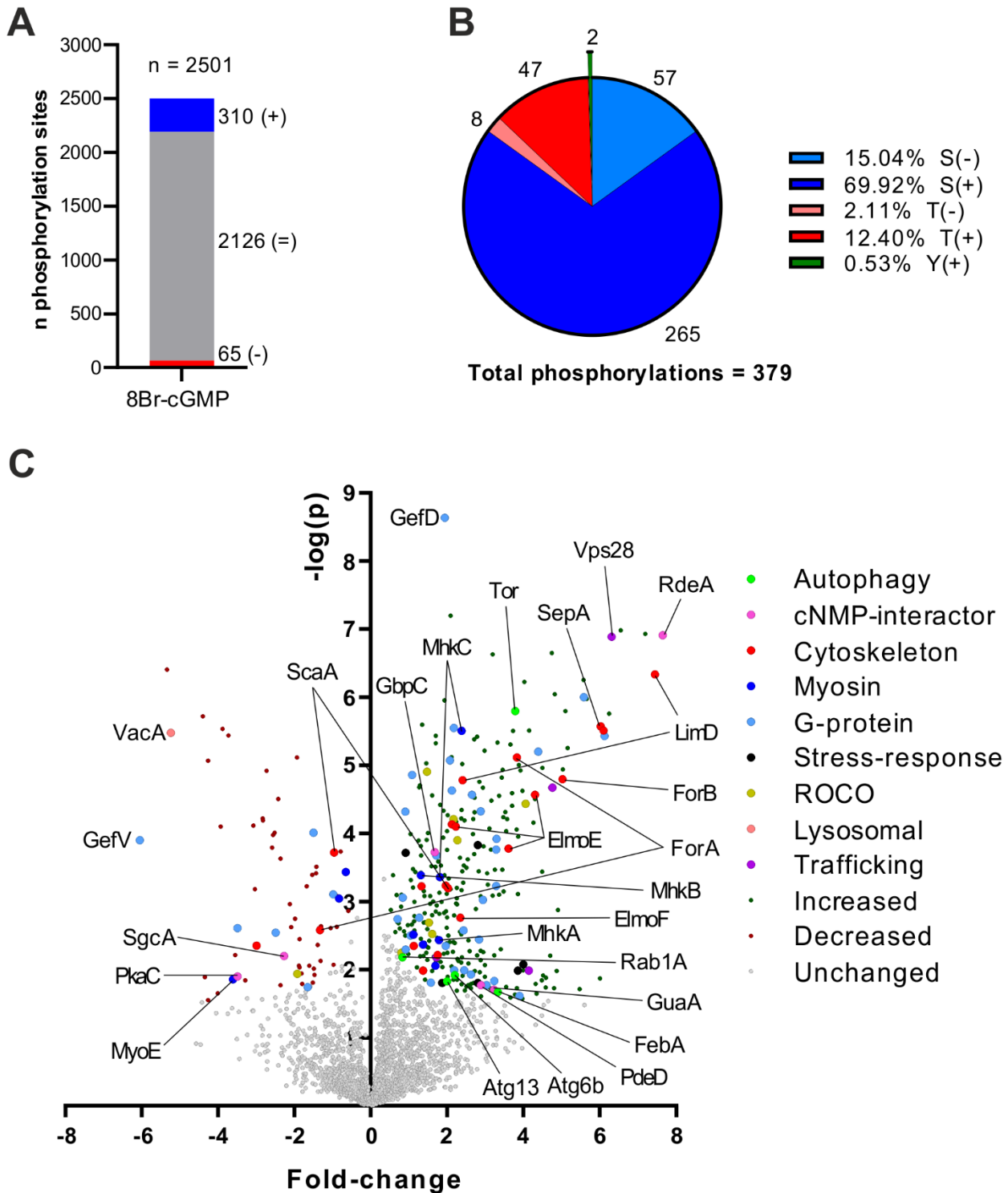
Figure 5.6 **Activation of GbpC yields substantial changes to phosphoproteome.** Wild-type Ax3 cells stimulated with 8Br-cGMP to activate cGMP-regulated kinase GbpC. (A) Phosphopeptides identified as increased (+), decreased (-) or unchanged (=) in 8Br-cGMP treated cells relative to vehicle control. (B) The proportion of significantly altered phosphosites broken down by phosphosite (serine, threonine or tyrosine) and whether the modification was increased (+) or decreased (-). (C) Volcano plot where all significant changes in phosphoproteome are shown. Grey data-points fell below the significance threshold ($P < 0.05$), with smaller fold-changes subjected to greater stringency and lower thresholds. Larger data-points denote genes of interest and are categorised as indicated, with key nodes are labelled.

Gene name	Protein name	Phospho-site	Fold-change	-log(p)
gbpC	Cyclic GMP-binding protein C	T2480	1.674	3.722
guaA	GMP synthase [glutamine-hydrolyzing]	S5	3.229	1.704
pdeD	cGMP-dependent 3',5'-cGMP phosphodiesterase A	S149	2.890	1.770
pkaC	cAMP-dependent protein kinase catalytic subunit	S434	-3.491	1.901
rdeA	Phosphorelay intermediate protein RdeA	S187	7.651	6.911
sgcA	Soluble guanylyl cyclase A	S2752	-2.267	2.199

Table 5.3. Cyclic-nucleotide-interacting proteins with altered phosphorylation status in response to 8Br-cGMP treatment in Ax3 cells.

Two proteins involved in cAMP signalling were identified as modified. RdeA, rapid development protein A, is a phosphorelay intermediate protein which regulates *Dictyostelium* development and fruiting body maturation in conjunction with the cAMP phosphodiesterase RegA (Thomason *et al.*, 1999). Phosphorylation of residue S187 was increased 7.651-fold, the greatest increase detected in the dataset (Table 5.3). cAMP-activated protein kinase catalytic subunit, PkaC, was less phosphorylated at S434. The modification did not align to any phosphosites of human *PKAC*, therefore its role is unknown. While cAMP signalling can stimulate cGMP production in *Dictyostelium* (Van Haastert, 1995), there is no evidence that cGMP can stimulate cAMP production. Activation of adenylyl cyclases and subsequently PkaC does not induce autophagy as loss of GbpC alone was sufficient to block this Figure 4.7. Nonetheless, sufficient proteins involved in cAMP/cGMP signalling exhibited altered phosphorylation to be detected by GO analysis (Figure 5.7; "response to organic cyclic compound"). Given overlap between cAMP and cGMP signalling reported in the literature, these results are expected.

At present, no known GbpC substrates exist, however some downstream effectors are known which are typically involved in stress-responses. The hippo-related severin kinase SvkA is stress-responsive and phosphorylates severin, a critical step for cell separation during cytokinesis (Rohlfs *et al.*, 2007). It is capable of binding actin, and its expression increased in response to hyper-OS (Na, 2007; Na *et al.*, 2007). In response to 8Br-cGMP, we detected an increase in phosphorylation at the S318 residue (Table 5.4). Signal transducer and activator of transcription (STAT) family protein DstD residue S102 also showed increased phosphorylation (Table 5.4). DstC, another STAT, known to be activated downstream of GbpC, was not detected. This was anticipated as Araki *et al.* (2003) showed by Western Blot that DstC phosphorylation both increased moderately using 5mM 8Br-cGMP after 3 min in a titration, and maximally at 5 min using 20mm in a time-course; our treatment time was 2 min. Two proteins involved in osmo-regulation also showed increased phosphorylation. The RabGAP/TBC domain-containing protein, CnrF, and hybrid signal transduction histidine kinase I, Dhkl-1, both exhibited increased phosphorylation. Details of these, and other stress-responsive proteins not mentioned, are shown in Table 5.4. These modifications provide further evidence of the role of GbpC in stress-responses and, again, increase confidence in the dataset.

Gene name	Protein name	Phospho-site	Fold-change	-log(p)
cnrF	RabGAP/TBC domain-containing protein	S66	4.142	1.986
dhkI-1	Hybrid signal transduction histidine kinase I	S1482	3.857	1.986
dst2	Serine/threonine-protein kinase Dst2	S170	1.872	1.801
		S1128	2.807	1.805
dstD	Signal transducer and activator of transcription	S102	0.915	3.716
fray2	Serine/threonine-protein kinase Fray2	T587	3.999	2.074
pakF	Serine/threonine-protein kinase PakF	S242	2.807	3.827
svkA	Serine/threonine-protein kinase SvkA	S318	1.369	1.985

Table 5.4. Stress-response proteins with altered phosphorylation status in response to 8Br-cGMP treatment in Ax3 cells.

Myosin and their respective kinases are critical components of the cell and several were modified in response to 8Br-cGMP. Myosins modulate a host of cellular processes, and their activity is regulated by kinases. Three heavy chain kinases, MhkA, MhkB and MhkC, showed increased phosphorylation (Table 5.5). MhkA was shown by Vaillancourt, Lyons and Côté (1988) and Lück-Vielmetter *et al.* (1990) to phosphorylate myosin heavy chain A, MhcA, at three threonine residues (1823, 1833 and 2029), although it was later determined MhkA, MhkB and MhkC all contributed to these modifications (Yumura *et al.*, 2005). The probable myosin light chain kinase, DDB_G0279831, showed decreased phosphorylation (Table 5.5). The modification of several myosin kinases highlights the multitude of regulatory elements in cytoskeletal dynamics.

Gene name	Protein name	Phospho-site	Fold-change	-log(p)
DDB_G0279831	Probable myosin light chain kinase DDB_G0279831	S143	-0.653	3.432
mhcA	Myosin-2 heavy chain	S1636	1.698	2.054
		T1835	1.373	2.365
mhkA	Myosin heavy chain kinase A	S517	1.789	2.433
mhkB	Myosin heavy chain kinase B	S335	1.312	3.387
mhkC	Myosin heavy chain kinase C	S367	2.383	5.507
		S373	1.810	3.355
mlcR	Myosin regulatory light chain	S13	1.119	2.511
		S14	1.119	2.511
myoC	Myosin IC heavy chain	T341	-0.834	3.042
myoE	Myosin IE heavy chain	S334	-3.608	1.858

Table 5.5. Myosin proteins and their kinases with altered phosphorylation status in response to 8Br-cGMP treatment in Ax3 cells.

As with myosin kinases, multiple myosin proteins were also found to be modified. Myosin complexes are formed of heavy, light and regulatory chains which form filaments, and regulate cell architecture and trafficking. Three myosin heavy chains exhibited altered phosphorylation: MhcA, MyoC and MyoE (Table 5.5). MhcA residues S1636 and T1835 showed increased phosphorylation. Neither modification is described in the literature, however for the latter phosphosite (T1835) after a review of raw data both T1833 and T1835 are indicated as equally statically likely to have been modified. This suggests a previously described phosphorylation critical for myosin function was identified (Lück-Vielmetter *et al.*, 1990; Vaillancourt *et al.*, 1988). Phosphosites T1823 and T2029 were not detected.
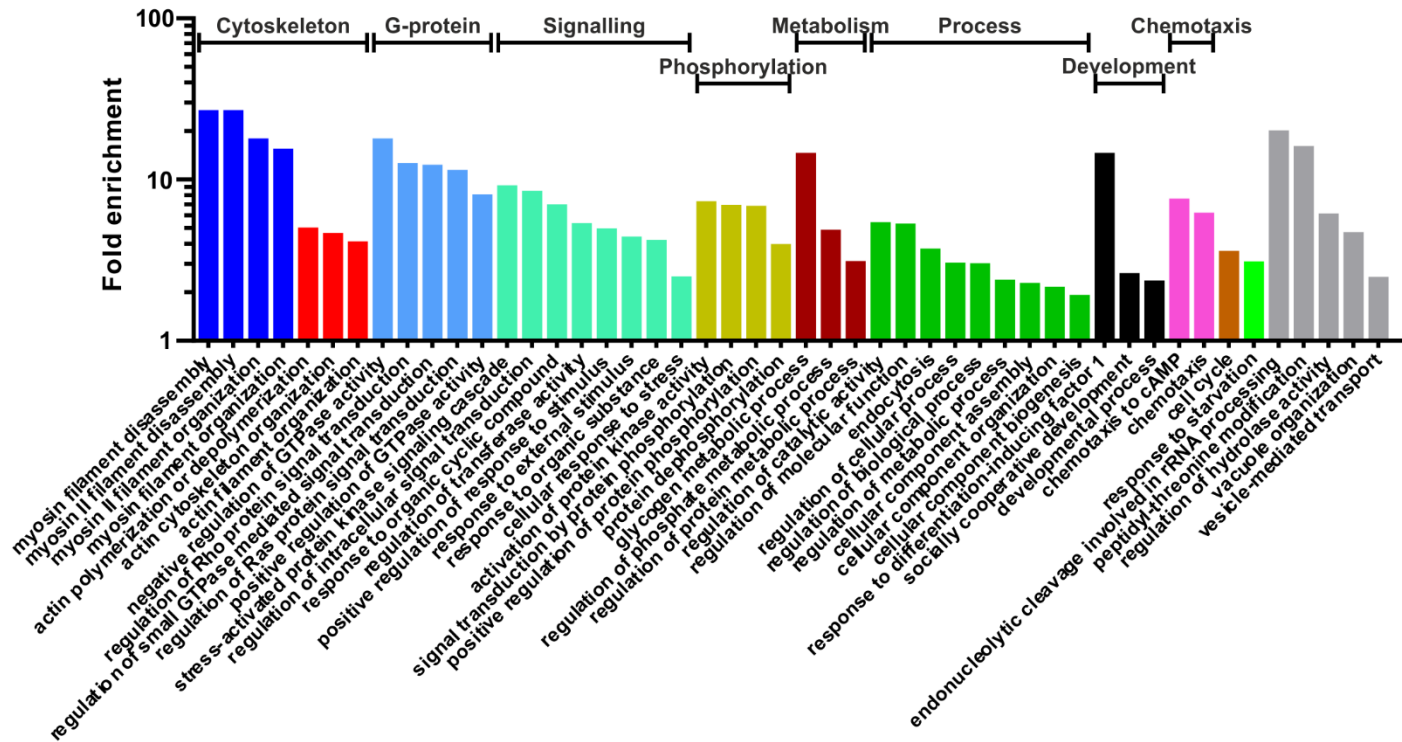
Figure 5.7 **GbpC stimulation stimulates signalling cascades affecting broad range of biological processes.** Wild-type Ax3 treated with 8Br-cGMP to activate GbpC kinase. Proteins identified as having altered phosphorylation in response to treatment were compared with the complete GO annotation datasets for *D. discoideum* to identify over-representation of terms for biological processes. GO over-representation was determined using the Fishers exact test with False Discovery Rate correction, using the PANTHER14.1. Total over-represented terms = 174.

114
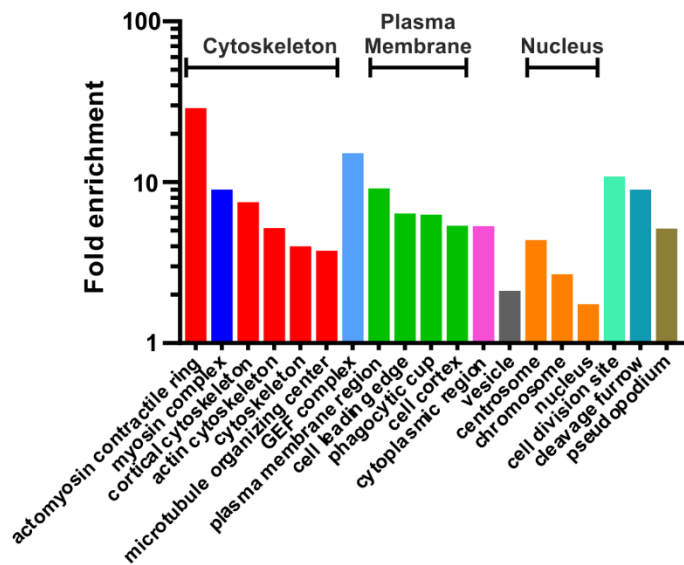
Figure 5.8 **GbpC stimulation stimulates signalling cascades affecting broad range of cellular compartment.** Wild-type Ax3 treated with 8Br-cGMP to activate GbpC kinase. Proteins identified as having altered phosphorylation in response to treatment were compared with the complete GO annotation datasets for *D. discoideum* to identify over-representation of terms for cellular compartment. GO over-representation was determined using the Fishers exact test with False Discovery Rate correction, using the PANTHER14.1. Total over-represented terms = 49.

Unconventional class I myosin heavy chain IC (MyoC) and IE (MyoE) both showed decreased phosphorylation (Table 5.5). MyoC is an actin regulator which limits the extension of protrusions (Jung and Iii, 1994; Titus *et al.*, 1989), whereas MyoE is unable to bind actin (Urrutia *et al.*, 1993) but can bind PIP$_3$ (Chen *et al.*, 2012).

The only myosin light chain found to be modified was MlcR, a regulatory light chain myosin and component of the actin-based molecular motor (Chen *et al.*, 1994). Phosphorylation of serine residues 13 and 14 were both increased. Previous studies mutated S13 to a non-phosphorylatable alanine residue, and determined that while it was not critical for cellular function (Ostrow *et al.*, 1994), loss resulted in fewer lateral pseudopods and loss of polarity in response to cAMP waves (Zhang *et al.*, 2002). It is clear that activation of GbpC is responsible for regulation of myosin activity and function.

The identification of several myosins and myosin kinases, as well as proteins involved in the stress-response is encouraging. These findings were also reflected in GO analysis, with myosin-related terms arising in all 3 categories (Figures 5.7-5.9) and the "stress-activated protein kinase signalling cascade" term for biological functions (Figure 5.7). These proteins and pathways are some of the limited few that are known to be downstream of GbpC signalling. That they are modified within this dataset provides validation of the reliability of the findings. In addition, this gives us confidence that the newly identified proteins not yet described, too, are genuine.
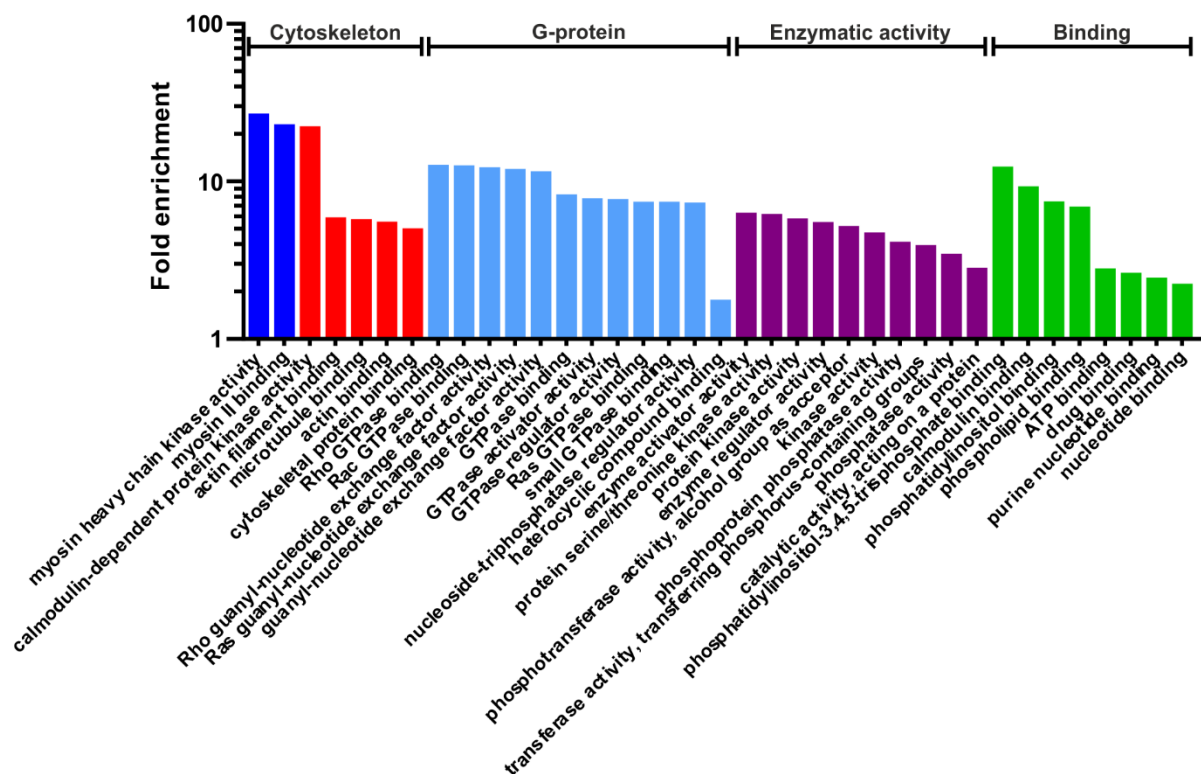
Figure 5.9 **GbpC stimulation stimulates signalling cascades affecting broad range of molecular function.** Wild-type Ax3 treated with 8Br-cGMP to activate GbpC kinase. Proteins identified as having altered phosphorylation in response to treatment were compared with the complete GO annotation datasets for *D. discoideum* to identify over-representation of terms for molecular function. GO over-representation was determined using the Fishers exact test with False Discovery Rate correction, using the PANTHER14.1. Total over-represented terms = 60.

5.2.3.2 Autophagy proteins are modified downstream of active GbpC

Several autophagy and autophagy-implicated genes were identified as phosphorylated in response to 8Br-cGMP. The *Dictyostelium* Tor acts as a master regulator of protein expression, stress responses and cellular homeostasis. When active it forms complexes with a host of other proteins to phosphorylate targets, including to block autophagy initiation. After 8Br-cGMP treatment, TOR was phosphorylated at residue S2282 (Table 5.6). This amino acid falls within the kinase domain C-loop (Yang *et al.*, 2013). *Dictyostelium* TOR was aligned against other TOR proteins in different organisms using Clustal Omega (EMBL-EBI), which showed the S2282 phosphosite resides within an unconserved region (Figure 5.10). It is, however, proximal to phosphosites in Human mTOR identified by kinome analysis (Gnad *et al.*, 2007).

Gene name	Protein name	Phospho-site	Fold-change	-log(p)
atg6B	Beclin-1-like protein B	S89	2.201	1.918
atg13	Autophagy-related protein 13	T514	2.000	1.827
febA	Eukaryotic translation initiation factor 4E-1A-binding protein homologue	S22	3.329	1.670
rab1A	Ras-related protein Rab-1A	T74	0.832	2.178
tor	Serine/threonine-protein kinase Tor	S2282	3.782	5.798

Table 5.6. Autophagy-related proteins with altered phosphorylation status in response to 8Br-cGMP treatment in Ax3 cells.

116

```
MTOR_HUMAN    2420  AFVYDPLLNWRLMDTNTKGNKRSRTRTDSYSAGQSV--E---------------------  2456
MTOR_MOUSE    2420  AFVYDPLLNWRLMDTNTKGNKRSRTRTDSYSAGQSV--E---------------------  2456
B0UX67_DANRE  2410  AFVYDPLLNWRLMDTNTKGNKRSRTRTDSYTAGQSV--EFPSKLTFLEID----TFLWY   2462
TOR_DROME     2341  AFVYDPLLNWRLLDVDKKGNDAVAGAGAPGGRGGSG--MQD-SLSN--------------  2383
TOR1_YEAST    2357  AFALDPLIHWGFDLPPQKLTEQTGIPLPLIN------------------------PSELL  2392
TOR_DICDI     2228  AFVHDPLINWRLLTPNENNTKHKATNIASNNSTSNSTTKIEGDLNTIDNPINKESPDHEA  2287
                    **. ***::* :        :  ..
```

Figure 5.10 *Dictyostelium* **Tor phosphorylation occurs within unconserved region of the kinase domain.** Alignment of Target Of Rapamycin proteins across multiple organisms using Clustal Omega (EMBL-EBI). The phosphorylation identified in *D. discoideum* Tor at residue S2282 in response to 8Br-cGMP is highlighted in red. Phosphosites identified in kinome analysis of Human mTOR are highlighted in blue (Gnad *et al.*, (2007)). The arrowhead denotes the residue with highest statistical significance. Sequence similarity is shown in greys, and annotated for degree of conservation below the sequences.

To further complicate matters, TOR forms 2 distinct complexes which regulate different pathways in *Dictyostelium*. During prolonged starvation and the beginning of the developmental cycle, *Dictyostelium* cells produce cAMP which stimulates adjacent cells to produce cAMP too. Ultimately this generates cAMP waves which propagate outwards, directing cells to stream towards the focal point. A complex array of proteins are involved in this process. Scaffold protein, ScaA, is an armadillo-like helical domain-containing protein which complexes with RasGEFs GefA and GefH, and phosphatase PppA, to form the Sca1 complex. This complex regulates RasC-TORC2-Akt/PKB pathway and facilitates chemotaxis towards cAMP (Charest *et al.*, 2010). We found altered phosphorylation states of ScaA residues S359 and S920, as well as a large increase in phosphorylation of the Sca1 complex protein, Phr (Table 5.7). GefH, another complex protein, showed decreased phosphorylation at T12 although this modification did not pass the threshold for significance (p=0.0378, q=0.077, 2.206-fold decrease). This suggests the TOR phosphorylation might be specific to protein in TORC2 complexes, rather than autophagy-regulating TORC1.

As previously described, active TOR phosphorylates substrate proteins. In mammals, one established target is Eukaryotic translation initiation factor 4E-binding protein 1 (4E-BP1) which is regulated by inhibitory phosphorylation of threonines 37 and 46 (Lekmine *et al.*, 2004). In *Dictyostelium*, TOR phosphorylates the 4E-BP1 homologue FebA (Four e-binding protein A). It was determined only 3 of the 5 phosphorylation sites were conserved in FebA: 4E-BP1 residues T82 aligned with L68 in FebA, which cannot be phosphorylated, and T37 aligned with S22 in but lacked a proline immediately afterwards (Morio *et al.*, 2001). However, in response to 8Br-cGMP treatment an increase in S22 phosphorylation was observed (Table 5.6; Figure 5.11), suggesting the site may not require the proximal proline and be conserved within *Dictyostelium*, assuming the modification functions in the same way as 4E-BP1. Phosphorylation of FebA suggests TOR is active, which would suggest autophagy initiation should be inhibited, however this was known not to be true.

Autophagy protein Atg6B, a Beclin-1 homologue, exhibited elevated phosphorylation at residue S89 (Table 5.6), however the modification occurred in the long N-terminal extension. This region is unique to *Dictyostelium*, and consequently not conserved in mammalian homologues. Interestingly, this phosphosite was detected in response to cAMP stimulation, but not folate, which induced a 45-fold increase after 45 s (Nichols *et al.*, 2019). This suggests the site is functional although the exact purpose of this modification requires further investigation. Additionally, all other detected phosphosites, regardless of

Gene name	Protein name	Phospho-site (multiplicity)	Fold-change	-log(p)
arpC	Actin-related protein 3	S268	1.969	3.234
dct	Dynacortin	S31	-2.989	2.352
DDB_G0279831	Probable myosin light chain kinase DDB_G0279831	S143	-0.653	3.432
DDB_G0295683	LIM-type zinc finger-containing protein	S94	2.125	4.132
		S1226	1.328	3.221
elmoE	ELMO domain-containing protein E	S1655	4.307	4.565
		S1664 (1)	2.225	4.100
		S1664 (2)	3.605	3.774
elmoF	ELMO domain-containing protein F	S1094	2.346	2.760
forA	Formin-A	S220	-1.329	2.581
		S222	3.827	5.114
forB	Formin-B	S15	5.024	4.795
forE	Formin-E	S303	1.751	2.211
limD	LIM domain protein	S496	7.449	6.333
		S507	2.407	4.783
mhcA	Myosin-2 heavy chain	S1636	1.698	2.054
		T1835	1.373	2.365
mhkA	Myosin heavy chain kinase A	S517	1.789	2.433
mhkB	Myosin heavy chain kinase B	S335	1.312	3.387
mhkC	Myosin heavy chain kinase C	S367	2.383	5.507
		S373	1.810	3.355
mlcR	Myosin regulatory light chain	S13	1.119	2.511
		S14	1.119	2.511
myoC	Myosin IC heavy chain	T341	-0.834	3.042
myoE	Myosin IE heavy chain	S334	-3.608	1.858
phr	Sca1 complex protein Phr	S50	5.578	5.999
scaA	Sca1 complex scaffold protein ScaA	S359	-0.956	3.721
		S920	2.026	3.194
svkA	Serine/threonine-protein kinase SvkA	S318	1.369	1.985
vilA	Villidin	S648	1.128	2.345

Table 5.7. Cytoskeletal proteins with altered phosphorylation status in response to 8Br-cGMP treatment in Ax3 cells.
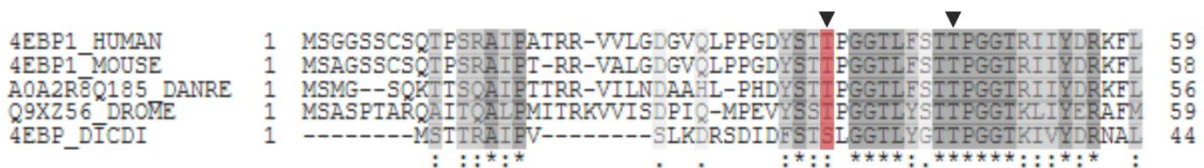
Figure 5.11 ***Dictyostelium* FebA phosphorylation occurs at a conserved regulatory site.** Alignment of eukaryotic initiation factor 4E binding protein 1 (4E-BP1) homologues across multiple organisms using Clustal Omega (EMBL-EBI). The phosphorylation identified in *D. discoideum* FebA at residue S22 in response to 8Br-cGMP is highlighted in red. Arrowheads denote conserved regulatory phosphosites which inhibit 4E-BP1. Sequence similarity is shown in greys, and annotated for degree of conservation below the sequences.

significance, from both phosphoproteomic datasets were located in this unconversed region (GbpC-null and 8Br-cGMP treated WT Ax3).

Dictyostelium Atg13, formerly U81000, showed elevated phosphorylation at T514 (Table 5.6). This site was not detected in GbpC-null phosphoproteome, although a phosphosite was identified at S515 with almost indistinguishable modification to WT Ax3. Due to substantial divergence of the *Atg13* gene across organisms, bioinformatics approaches such as sequence alignment show little similarity (Mesquita *et al.*, 2015). Perhaps unsurprisingly, the pT514 falls within an unconserved region (Figure 5.12). In mammals,

ATG13 is phosphorylated by mTOR at S224 (Puente *et al.*, 2016), and in budding yeast Tor protein hyper-phosphorylates Atg13 (Kamada *et al.*, 2000); in both organisms phosphorylation is inhibitory, disrupting the ULK1/Atg1 complex and thus preventing autophagy initiation. *Dictyostelium* Atg13 forms part of the Atg1 complex through interactions with both Atg1 and Atg101, and is essential for autophagy initiation (Mesquita *et al.*, 2015). Whether the phosphorylation detected here functions in the same way as in Humans and yeast remains unclear, given 8Br-cGMP induces autophagy and the post-translational modification is not conserved.

```
ATG13_HUMAN   350   -EIVS---NSSEGR-ASPHDVLETIFVRKVGAFVNKPI------------------NQV   385
ATG13_MOUSE   349   -EIVS---NSSEGR-ASPHDILETIFVRKVGAFVNKPI------------------NQV   384
ATG13_BOVIN   313   -EIVS---NSSEGR-ASPHDVLETIFVRKVGAFVNKPI------------------NQV   348
Q55BY0_DICDI  459   TTITSNNINTSGGININNHPSSNPLPIRQVSFTIPNQTTGISPTSYNNQQSKTRAISAPI  518
                    *.*     *:*  *   . * :  : :*:*.  : :                      :
```

Figure 5.12 ***Dictyostelium* Atg13 phosphorylation occurs at an unconserved locus.** Alignment Atg13 homologues across multiple organisms using Clustal Omega (EMBL-EBI). The phosphorylation identified in *D. discoideum* Atg13 at residue T514 in response to 8Br-cGMP is highlighted in red. Sequence similarity is shown in greys, and annotated for degree of conservation below the sequences.

The last protein modified and implicated in autophagy was Rab1A. Rab proteins are ras-related, and key components in regulation of endocytic trafficking, playing specific roles at defined stages in the pathway. In mammalian cells, RAB1A has been implicated in early autophagosome biogenesis through interaction with ATG9 (Winslow *et al.*, 2010). Phosphorylation of *Dictyostelium* Rab1A occurred at T74 with a 0.832-fold increase. Human RAB1A is reportedly phosphorylated at T75, which is attributed to induction of activity, intracellular localisation and regulation of molecular associations (Phosphosite.org). Evidence suggests T77 is also phosphorylatable (Zhou *et al.*, 2013). Alignment of Rab1A protein sequences across organisms suggests the *Dictyostelium* T74 phosphosite aligns with Human T77.

These modified proteins are promising leads for identifying the signalling components linking cGMP and autophagy. As only 4 candidates were detected, GO analysis detected no significant over-representation of autophagy terms. There was, however, one potentially relevant term: "response to starvation" (Figure 5.7). This does come with the caveat that GbpC, and downstream signalling, is involved in *Dictyostelium* development which is initiated by starvation. Terms relating to development, such as "response to DIF-1" and "chemotaxis to cAMP", were enriched, suggesting development might be the stronger influence on the GO result. Validating the roles of the above phosphosites will help to resolve this, but more importantly will provide a clearer picture of the complex interactions underpinning both *Dictyostelium* development and autophagy induction.

5.2.3.3 GbpC activation dynamically regulates multiple cytoskeletal proteins

GbpC has been implicated in regulation of the cytoskeleton in literature, and previously, regarding myosin and myosin kinase phosphorylations. In addition to our myosin-related findings, a plethora of components of the actin regulatory network were also altered regarding phosphorylations. These findings were supported by significant over-representation of "Cytoskeletal" terms in GO analysis (Figures 5.7-5.9). ArpC, also known as Arp3, forms a complex with Arp2, Carmil and myosin IB and IC which interacts with and

regulates actin filament formation at pseudopodia (Jung *et al.*, 2001). Phosphorylation of ArpC S268 was increased (Table 5.7). This amino acid is conserved and phosphorylated in humans and mice, however its function is unknown (Mertins *et al.*, 2014, 2016). Arp2, MyoB and Carmil were not found to be modified however MyoC, described previously, did show altered phosphorylation. Increased phosphorylation of several residues in Carmil were detected, however none were significant (T970: p=0.326, q=0.402, 1.262-fold; T976: p=0.278, q=0.348, 1.431-fold; T998: p=0.082, q=0.116, 2.440-fold). Activation of GbpC appears to modulate activity of a key regulatory complex of the actin cytoskeleton.

Engulfment and cell motility domain containing proteins, ELMOs, are found in most eukaryotes and transduce G-protein receptor signalling to the cytoskeletal network. The ELMOD superfamily is broadly separated into 2 groups; ELMOD, which arose from an ancient ancestor, and ELMO, a sub-family which arose from a more recent gene duplication event (East *et al.*, 2012). *Dictyostelium* contain 6 Elmo proteins (A-F; (Brzostowski *et al.*, 2009)) which, despite their nomenclature, fall into the ELMOD group. Elmo's E and F were both found to have increased phosphorylation (Table 5.7). ElmoE is a Gβγ effector which activates the small GTPase RacB upon GPCR activation, which regulates the cytoskeleton (Yan *et al.*, 2012). ElmoF shows high sequence similarity to ElmoE (Brzostowski *et al.*, 2009) but no further study has been undertaken into its function. Phosphorylation of ElmoE residue S1664 shows two outputs for multiplicity 1 and 2, which relates to the number of phosphorylations detected within the peptide. This suggests a double phosphorylation, of which pS1664 is one, was more abundant that a single phosphorylation.

Regulation of cortical actin is essential for cells to modulate rigidity and migration in response to environmental changes such as osmotic shock. Formin proteins are actin assembly factors involved in formation of cortical actin at rear of cell. Modified phosphosites were identified in Formins A, B and E (Table 5.7). Both ForA and ForE are regulated by the Rho GTPase RacE (Litschko *et al.*, 2019). RacE has also been shown to regulate dynacortin (Dct), involved in actin bundling (Robinson *et al.*, 2002), which was altered in response to 8Br-cGMP (Table 5.7). Another actin bundling protein, LimD, maintains cortical strength essential for resistance to OS (Khurana *et al.*, 2002). This protein was modified at two loci (Table 5.7), which included the 2nd highest increase in relative phosphorylation.

G-protein signalling plays a diverse role in a host of regulatory pathways. Guanine exchange factors (GEFs) facilitate replacement of GDP with GTP to activate proteins, whereas GTPase activating proteins (GAPs) stimulate the innate GTPase activity of GTP-bound proteins catabolise GTP into GDP. These combined activities of both GEFs and GAPs create a regulatory system which controls activity by modulating GTP binding to effector proteins. A large portion of modified proteins identified were GEFs and GAPs, with over 30 modifications detected across both groups. GO analysis also identified a range of G-protein, GEF and GAP related terms (Figure 5.7-5.9).

A summary of these phosphorylation changes are provided in Tables 5.8 (GEFs) and 5.9 (GAPs). Some examples include Racgef1, which upon activation stimulates RacB to promote F-actin polymerisation (Mun and Jeon, 2012), and the RacB kinase and exchange factor KxcB (Table 5.8). A GefV phosphosite showed the

greatest decrease in the dataset. The GAP, GacG, was one of the few proteins found to overlap GbpC-null and 8Br-cGMP treated Ax3 datasets (Table 5.9). XacA contains both GEF and GAP domains, and when knocked-out causes increased F-actin assembly at the cell periphery (Chung *et al.*, 2000b). One phosphosite, S538, falls within a proline-rich region which could provide SH3 binding motifs, or target sequences for proline directed S/T kinases (Ludbrook *et al.*, 1997).

Gene name	Protein name	Phospho-site	Fold-change	-log(p)
docA	Putative guanine nucleotide exchange factor DocA	S762	2.941	3.024
gefD	Ras guanine nucleotide exchange factor D	S374	1.943	8.634
gefE	Ras guanine nucleotide exchange factor E	T237	2.450	1.989
gefF	Ras guanine nucleotide exchange factor F	S92	-3.486	2.610
gefP	Ras guanine nucleotide exchange factor P	S519	3.897	1.614
gefQ	Ras guanine nucleotide exchange factor Q	S390	0.903	4.320
gefQ	Ras guanine nucleotide exchange factor Q	S460	0.911	2.295
gefR	Ras guanine nucleotide exchange factor R	S858	1.723	3.676
gefS	Ras guanine nucleotide exchange factor S	S370	-2.493	2.542
gefV	Ras guanine nucleotide exchange factor V	S518	-6.046	3.898
gxcDD	Guanine exchange factor for Rac 30	S373	1.267	2.760
gxcZ	RhoGEF domain-containing protein	T806	3.285	3.760
kxcB	Kinase and exchange factor for Rac B	S26	6.120	5.429
		S280	1.574	1.809
		S307	1.046	2.498
racgef1	Rac guanyl-nucleotide exchange factor	S620	3.296	3.918
		S1030	-1.503	4.010
		S1200	2.122	4.627
xacA	eXchange and Activating factor for raC	S538	3.235	1.831
		S1346	2.189	1.990

Table 5.8. Guanine exchange factor (GEF) proteins with altered phosphorylation status in response to 8Br-cGMP treatment in Ax3 cells.

		Phosphoproteome			Proteome	
Gene name	Protein name	Phospho-site	Fold-change	-log(p)	Fold-change	-log(p)
cnrF	RabGAP/TBC domain-containing protein	S66	4.142	1.986		
DDB_G0271806	PH and Rap-GAP domain-containing protein DDB_G0271806	S648	2.075	5.070		
		S648	1.963	2.345		
DDB_G0281809	Rap-GAP domain-containing protein DDB_G0281809	S1540	2.177	5.549		
DDB0230013	Rho GTPase	S365	-1.652	1.743		
gacG	Rho GTPase-activating protein GacG	S430	2.878	4.322	2.229	2.324
		T515	2.840	2.444		
gacI	Rho GTPase-activating protein GacI	S473	2.427	2.574		
gacJ	Rho GTPase-activating protein GacJ	S743	3.283	3.228		
gacL	Rho GTPase-activating protein GacL	S100	2.648	4.566		
gacP	Rho GTPase-activating protein GacP	S487	1.083	4.855		
gacU	Rho GTPase-activating protein GacU	S421	3.034	1.770		
gacX	Rho GTPase-activating protein GacX	S9	-0.979	3.102		
gxcGG	Uncharacterised protein	S771	2.625	1.925		
gxcM	Uncharacterised protein	S257	0.839	3.055		
xacA	eXchange and Activating factor for raC	S538	3.235	1.831		
		S1346	2.189	1.990		

Table 5.9. GTPase activating proteins (GAPs) with altered phosphorylation status in response to 8Br-cGMP treatment in Ax3 cells. Genes with significant changes in GbpC-null proteome included for reference.

GbpC is known to play a role in the mediating cell migration, chemotaxis, and to a degree development. Specific activation of GbpC using 8Br-cGMP stimulated the modification of multiple regulators of the cytoskeleton after just 2 min. The experimental findings presented here do not provide definitive roles for individual regulatory elements, but they do highlight avenues for further investigation which would provide greater understanding of this complex process. Critically, they cement GbpC as a key player in the dynamic regulation of cytoskeleton.

5.2.3.4 GbpC activation causes diverse changes in the phosphoproteome

cGMP signalling, and subsequent GbpC activity, has been linked to various biological processes in *Dictyostelium*. In addition to the processes already described, clusters of proteins with defined roles were also noted as modified. Phosphosites were detected in proteins involved in *Dictyostelium* development (Table 5.10) and transcriptional regulation (Table 5.11), as well as lysosomal proteins (Table 5.12) and other ROCOs (Table 5.13) which includes GbpC. The specific function of these individual modifications remains unclear. The detection of these protein clusters suggest GbpC may be involved in additional pathways which, as yet, have not been explored.

Gene name	Protein name	Phospho-site	Fold-change	-log(p)
DG1122	Development protein	T143	2.676	3.989
pspC	Prespore-specific protein	S1023	-1.816	1.942
		S1026	-1.431	3.413
scaA	Sca1 complex scaffold protein ScaA	S359	-0.956	3.721
		S920	2.026	3.194
vilA	Villidin	S648	1.128	2.345

Table 5.10. *Dictyostelium* development proteins with altered phosphorylation status in response to 8Br-cGMP treatment in Ax3 cells.

Gene name	Protein name	Phospho-site	Fold-change	-log(p)
DDB0220518	Myb domain-containing protein	S288	3.324	5.332
dstD	Signal transducer and activator of transcription	S102	0.915	3.716
gtf2f1	General transcription factor IIF subunit 1	S470	2.730	1.979
		S470	3.976	1.577
H1	Histone H1	T127	1.479	2.593
hdaA	Type-1 histone deacetylase 1	S415	3.149	3.762
hdaC	Type-2 histone deacetylase 2	T669	2.378	4.344
mybZ	Myb-like protein Z	S662	2.826	3.441
trfA	General transcriptional corepressor TrfA	S852	4.872	1.979
		T1239	2.561	2.089
		S1294	1.113	2.360
tupA	General transcriptional corepressor TupA	S87	1.706	5.436

Table 5.11. Transcription-related proteins with altered phosphorylation status in response to 8Br-cGMP treatment in Ax3 cells.

Gene name	Protein name	Phospho-site	Fold-change	-log(p)
vacA	Vacuolin-A	T9	-5.236	5.475
vps13F	Putative vacuolar protein sorting-associated protein 13F	S3313	4.761	4.670
vps28	Vacuolar protein sorting-associated protein 28	S78	6.306	6.889
vps51	Vacuolar protein sorting-associated protein 51 homologue	S795	1.716	2.179

Table 5.12. Lysosomal proteins with altered phosphorylation status in response to 8Br-cGMP treatment in Ax3 cells.

Gene name	Protein name	Phospho-site	Fold-change	-log(p)
gbpC	Cyclic GMP-binding protein C	T2480	1.674	3.722
roco5	Probable serine/threonine-protein kinase Roco5	S190	4.055	4.432
roco6	Probable serine/threonine-protein kinase Roco6	S954	1.476	4.907
		S977	0.802	2.245
		S1302	2.268	3.902
roco7	Probable serine/threonine-protein kinase Roco7	S2609	1.525	2.690
roco9	Probable serine/threonine-protein kinase Roco9	S764	2.165	4.207
		T3295	1.612	2.525
roco10	Probable inactive serine/threonine-protein kinase Roco10	S232	-1.921	1.937

Table 5.13. ROCO proteins with altered phosphorylation status in response to 8Br-cGMP treatment in Ax3 cells.

5.2.4 Identifying consensus sequences of GbpC substrates

The characteristics of a protein is primarily attributed to the arrangement of amino acids within it, forming complex 3D structures capable of catalysing reactions to determining binding partners. Kinases have conserved domains composed of critical amino acid side chains that catalyse transfer of a phosphate group to a substrate. Often substrates, too, have conserved domains which are essential for interaction with the kinase to facilitate phosphorylation. While the domains of GbpC are clear, the preferential target sequence(s) of potential substrates is not; currently no known proteins are directly phosphorylated by GbpC. Using sequence windows from phosphoproteome datasets for both GbpC-null and 8Br-cGMP treated Ax3 cells, I aimed to identify putative consensus sequences using alignment software pLogo (O'Shea *et al.*, 2013) to identify over-represented amino acids flanking phosphorylation sites. Datasets from both conditions were processed separately, then combined and compared to resolve candidate consensus sequences. The limited number of phosphorylation changes detected in GbpC-null cells meant only a few potential sequences were determined. For this dataset, the primary focus was to identify sequence similarities where phosphorylation was significantly decreased as a result of loss of GbpC. Alignment of all applicable sequence windows are shown in Figure 5.13A, showing no significant amino acid concomitance. As no significant residues were identified, the sequence windows were analysed separately to determine if any alignments could be resolved based upon specific phosphosite. Phospho-serine sequences (Figure 5.13B) showed no significant over-representation, while phospho-threonine (Figure 5.13C) did. The

significance threshold in all alignments is depicted by a bold red line with the calculated value indicated on the left y-axis.
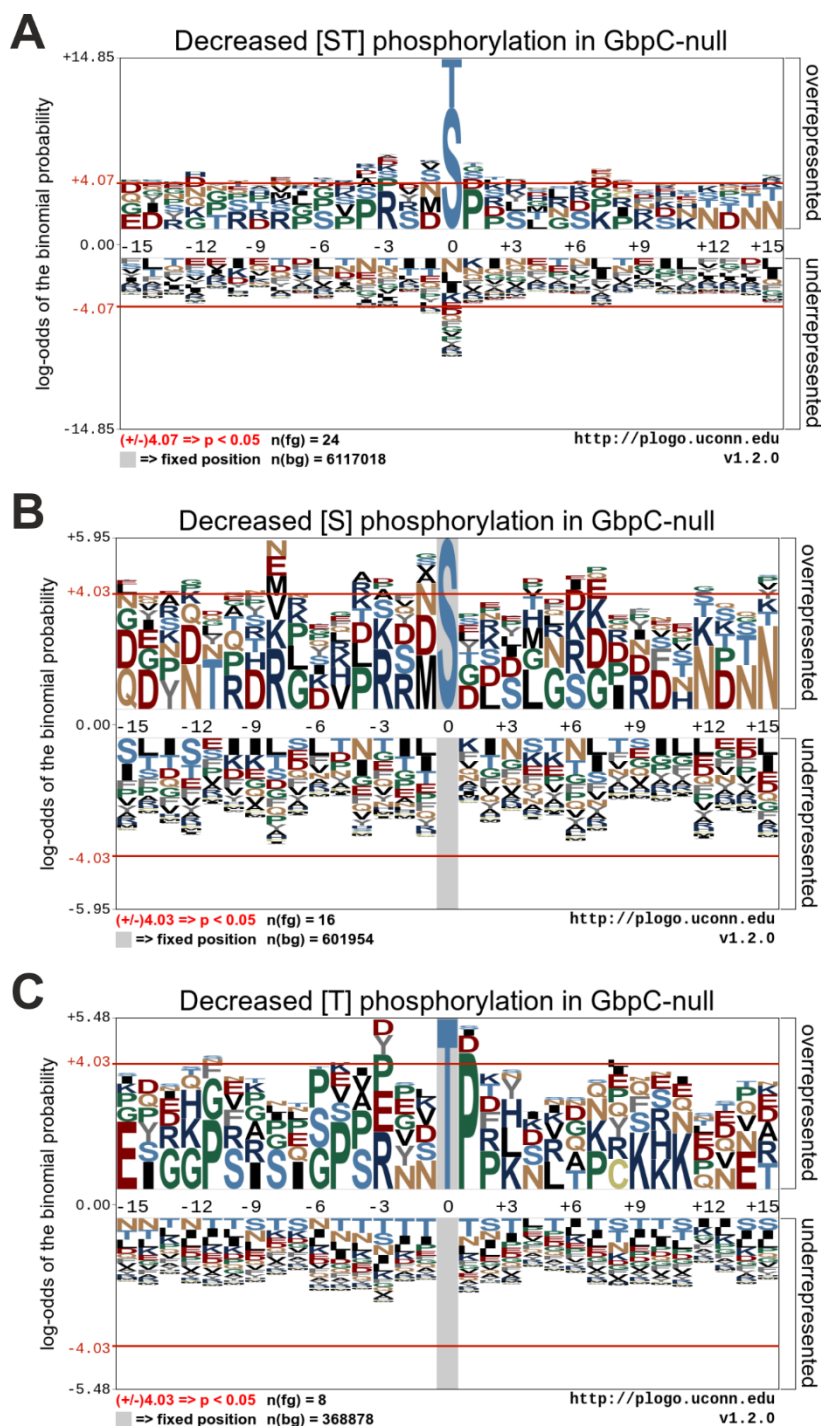
Figure 5.13 **Consensus sequences with decreased serine/threonine phosphorylation in GbpC-null**. Over-representation analysis of amino acids in sequence windows of significantly modified peptides in GbpC-null cells. Sequences were compared with a *D. discoideum* background derived from Dictybase. Letter size is proportional to probability and the red lines indicate significance thresholds. Decreased phosphorylation of any residue (A), serine only (B) or threonine only (C) shown, where fixed positions are shaded in grey.

When considering all sequence windows centred on a site of reduced phosphorylation, no significantly over- or under-represented amino acids were found (Figure 5.10A). Position -3 does appear to have more

basic residues, particularly arginine (R) and lysine (K), while position +1 seems to be mostly occupied by proline (P). The abundance of basic residues, particularly at position -3, is also seen in phospho-serine sequences (Figure 5.13B), while adjacent proline at position +1 is significantly over-represented in phospho-threonine sequences (Figure 5.13C). Due to the small sample size it is difficult to deduce anything definitive from these alignments. Interestingly, however, was the frequency of proline residues, particularly flanking phospho-threonine (Figure 5.13C). As previously mentioned, Carmil T970 phosphorylation was greatly diminished (Table 5.2). This lies within a PxxP motif previously described as a binding site for myosins IB and IC via their Src homology 3 (SH3) domains (Jung *et al.*, 2001). No other down-regulated phosphorylations were found within PxxP motifs, although 2 more PxxP motifs were found adjacent within the flanking sequence. The only conclusion that can be drawn is there are inherent differences between the adjacent amino acids flanking either phosphorylatable serine or threonine, which could implicate 2 potential target sequences.

Treatment with 8Br-cGMP had a greater impact on the phosphoproteome than loss of GbpC. Consequently, the combination of potential consensus sequences dwarfed those found in GbpC-null cells. GbpC is suspected of being an orthologue of mammalian PKG as both are regulated by cGMP and possess kinase activity. In a review by Francis, Busch and Corbin, (2010) summarising the roles of cGMP and PKG, a variety of PKG substrates were discussed. In particular they highlighted that PKG modifies substrates with different adjacent amino acids, implicating multiple consensus sequences which PKG can modify. It was also speculated that modification was largely dependent upon the sub-cellular location of PKG and prevalence of substrates in the vicinity. Considering these findings, and assuming GbpC and PKG are evolutionarily related, it likely no single consensus sequence exists and instead GbpC can modify a variety of substrates.

The modifications of greatest interest were significantly increased phosphorylations of serine and threonine residues. GbpC is a predicted serine/threonine kinase, therefore the 2 tyrosine modifications were unlikely a result of direct GbpC phosphorylation. When all sequences with increased phosphorylation were aligned, two striking co-localisations were observed (Figure 5.14A). Firstly, position -3 was dominated by basic residues arginine (23.3%) and lysine (21.0%). Including histidine, basic residues accounted for 47.8% of amino acids at this position. Position +1 was most frequently proline, accounting for 24.2% abundance. Although not as striking, several other amino acids were significantly over-represented at various positions (Figure 5.14A'). This consensus sequence suggests a coincidence with specific amino acids at given positions. As previously undertaken, sequences were separated based upon phosphosite to reveal differences between candidate consensus sequences.

Alignment of increased phospho-serine yielded similar results to the complete alignment previously described. Figure 5.14B shows the consensus when serine is fixed at position 0. Position -3 was predominantly basic with 51.7% amino acids being either arginine, lysine or histidine. Basic residues were over-represented at several other loci too. Proline was significantly increased at positions 1 and occurred at additional loci too. Sequence windows flanking a phospho-threonine (Figure 5.14C) showed some

similarities to phospho-serine, with over-representation of arginine (position -3) and proline (+1). Over-representation of lysine at position -3 was not apparent, and no strong consensus was observed. Nonetheless, the over-represented amino acids identified here seem to reflect the sequence alignments generated from GbpC-null phosphoproteome data, and therefore warranted further study.
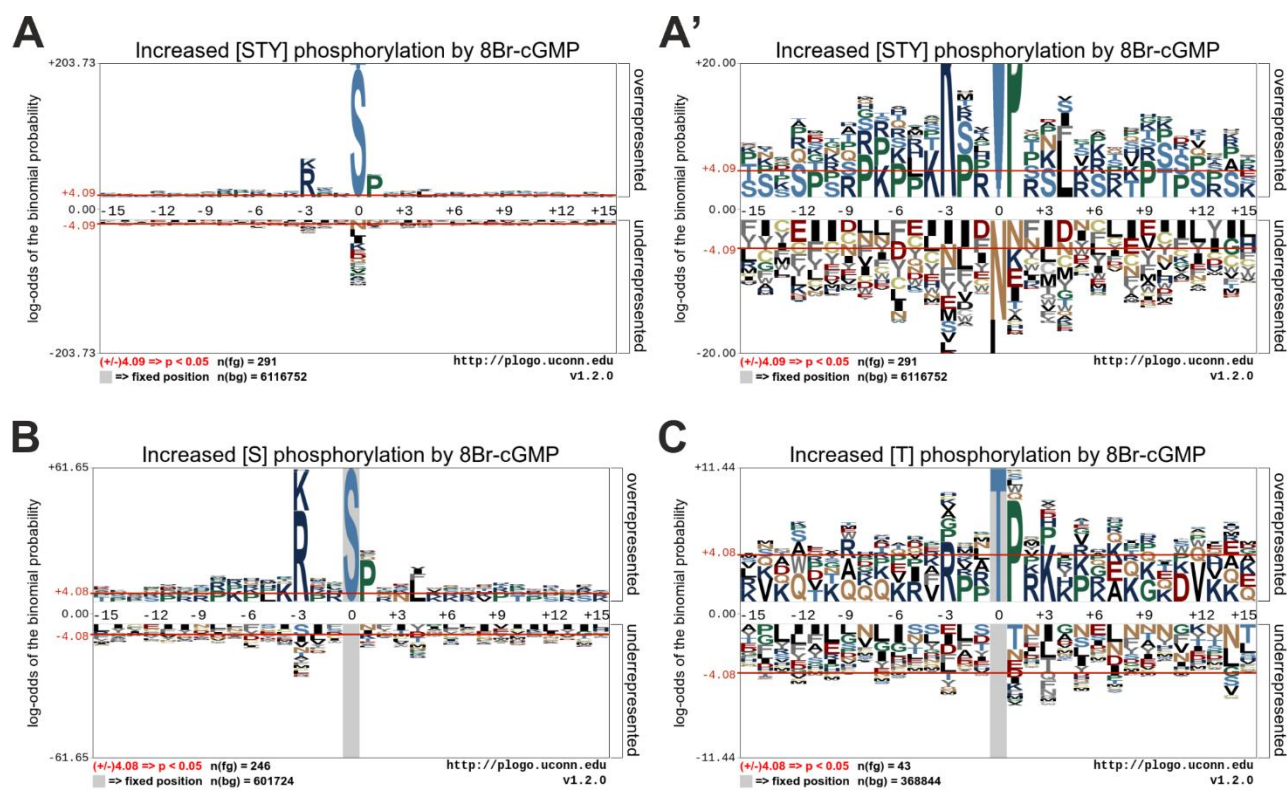
Figure 5.14 **Consensus sequences with increased phosphorylation in response to 8Br-cGMP.** Over-representation analysis of amino acids in sequence windows of significantly modified peptides in response to 8Br-cGMP treatment. Sequences were compared with a *D. discoideum* background derived from Dictybase. Letter size is proportional to probability and the red lines indicate significance thresholds. Increased phosphorylation of any residue (A), serine only (B) or threonine only (C) shown, where fixed positions are shaded in grey. For clarity, zoomed in alignment of (A) shown in (A') to resolve residues with lower probabilities.

The consensus sequences for phospho-serine and threonine both exhibited similar concomitant amino acids: basic arginine/lysine, and proline residues. Using only sequences containing arginine (Figure 5.15A), lysine (Figure 5.15B) or proline (Figure 5.15C) residues at specified positions, consensus sequences were generated to resolve additional information regarding possible motifs. Magnified views are provided (Figures 5.15A'-C') to resolve residues clearly. Proline and leucine were over-represented when arginine was fixed at position -3 (Figure 5.15A-A'), whereas fixing lysine at this locus did not reveal any over-representation. Fixing proline at position +1 showed a strong concomitance with basic residues at positions +2 and +3, as well as a secondary proline at position -2 (Figure 5.15C-C'). The latter supports the suggestion that phosphorylations may occur within PxxP motifs; 23 sequences with increased phosphorylation exhibited this (Table 5.14). It is unlikely all phosphorylations will be a direct result of GbpC kinase activity, as many other kinases were themselves modified. The short treatment time, however, should have restricted these secondary phosphorylations, ensuring the phosphosites are more probable to be regulated by GbpC.

126
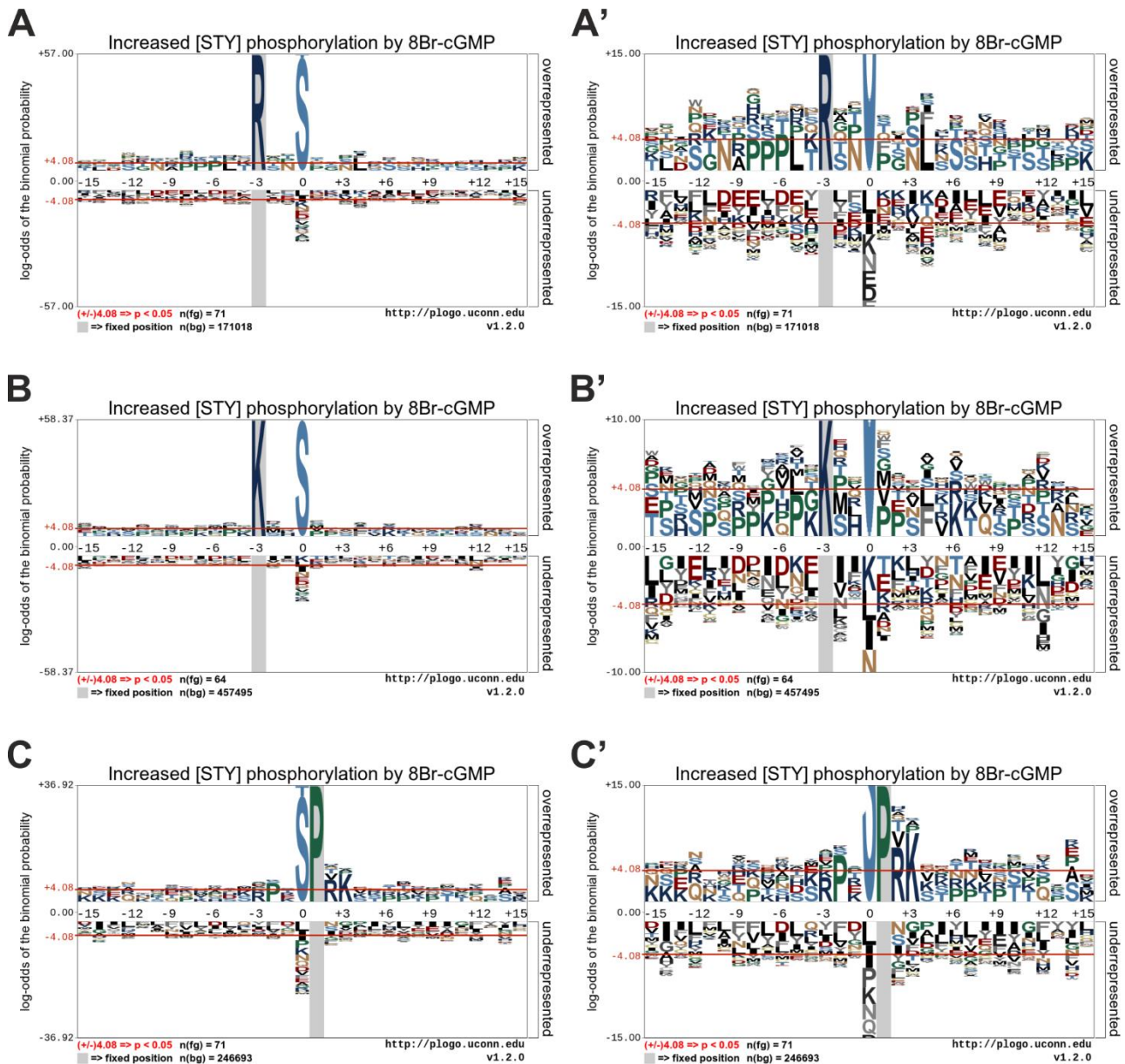
Figure 5.15 **Consensus sequences with increased phosphorylation in response to 8Br-cGMP**. Over-representation analysis of amino acids in sequence windows of significantly modified peptides in response to 8Br-cGMP treatment. Sequences were compared with a *D. discoideum* background derived from Dictybase. Letter size is proportional to probability and the red lines indicate significance thresholds. Basic residues arginine (A) and lysine (B), and aliphatic proline (C) are fixed, shaded in grey. For clarity, zoomed in alignments shown in (A'-C') to resolve residues with lower probabilities.

Targets of GbpC phosphorylation are unknown, as are the potential consensus sequences it interacts with and modifies. By comparing the consensus sequences of both GbpC-null cells (Figure 5.13) and 8Br-cGMP treated Ax3 (Figure 5.14) it was hoped to identify similarities between the independent analyses. Due to the small number of phospho-sequences in GbpC-null, no alignments with strong amino acid co-localisation were found. Despite this, prevalence of proline and basic residues was observed and found to be more striking in alignments for 8Br-cGMP treatment. Together, the results indicate a preference for target sequences either located within or in close proximity to PxxP motifs, and/or with basic residues at position -3 relative to the phosphosite.

Gene name	Protein name	Phospho-site	Fold-change	Sequence window
cplA	Putative calpain-like cysteine protease A	S601	2.273	VK**P**E[ₚS]**P**REF
DDB_G0291842	Probable protein kinase DDB_G0291842	T45	3.725	VC**P**K[ₚT]**P**TKT
DDB0184280	Uncharacterised protein	S1973	2.252	NI**P**T[ₚS]**P**KSS
DDB0184478	Uncharacterised protein	T367	2.953	TP**P**P[ₚT]**P**LKK
DDB0187414	Uncharacterised protein	S110	0.852	IK**P**Q[ₚS]**P**EIK
DDB0187697	Uncharacterised protein	S224	2.991	KR**P**T[ₚS]**P**QQL
DDB0188170	Uncharacterised protein	S1093	2.089	TN**P**V[ₚS]**P**RFV
DDB0190250	Uncharacterised protein	S695	2.152	LE**P**L[ₚS]**P**TKK
DDB0202577	Uncharacterised protein	S102	1.447	PT**P**Q[ₚS]**P**TNT
drnA	Putative RNase III	S116	3.657	QR**P**I[ₚS]**P**TIR
gacG	Rho GTPase-activating protein GacG	T515	2.840	SA**P**T[ₚT]**P**RNF
gflC	PHD zinc finger-containing protein	S583	3.993	SK**P**M[ₚS]**P**KIN
gtf2f1	General transcription factor IIF subunit 1	S470	2.730	KE**P**S[ₚS]**P**QAV
gtf2f1	General transcription factor IIF subunit 1	S470	3.976	KE**P**S[ₚS]**P**QAV
H1	Histone H1	T127	1.479	AP**P**A[ₚT]**P**TKK
mhkC	Myosin heavy chain kinase C	S367	2.383	KS**P**V[ₚS]**P**PKE
pdeD	cGMP-dependent 3',5'-cGMP phosphodiesterase A	S149	2.890	SP**P**L[ₚS]**P**QQQ
rpl6	60S ribosomal protein L6	T45	1.293	VA**P**V[ₚT]**P**VEK
sibD	Integrin beta-like protein D	Y163	1.377	MV**P**I[ₚY]**P**VTY
trfA	General transcriptional corepressor TrfA	S1294	1.113	EQ**P**E[ₚS]**P**LKK
DDB0184478	Uncharacterised protein	T363	3.877	IKE**P**[ₚT]P**P**PT
DDB0190401	Uncharacterised protein	S1093	0.524	HFT**P**[ₚS]P**P**KS
DDB0205845	Uncharacterised protein	S339	0.982	KKS**P**[ₚS]M**P**VI

Table 5.14. Phosphosites [ₚS/T/Y] identified within PxxP motifs (red) after treatment with 8Br-cGMP in Ax3.

In order to identify a specific target of GbpC, proteome and phosphoproteome datasets were compared. Ideally a phosphorylation site would have been found to be both down-regulated in GbpC-null and up-regulated in 8Br-cGMP treated Ax3. Unfortunately, no phosphosite met this criteria. Overall, the overlap between all OMICs datasets was minimal, as shown in Figure 5.16; no gene was modified in all three OMICs datasets. The only gene with altered expression and phosphorylation in GbpC-null cells was MetE. While there were 10 genes were found to exhibit altered phosphorylation status in both GbpC-null cells and 8Br-cGMP treated Ax3, the phosphosites were at different locations (Table 5.15). Furthermore, 7 of the 10 genes were uncharacterised and their relevance is unknown. Unfortunately there was no definitive consensus sequence, or specific phospho-site, modified by GbpC; assuming either exist, they remain elusive.

The goal of consensus sequence analysis was to identify GbpC target motifs. The impact of GbpC loss on the phosphoproteome was less dramatic than anticipated, which meant no clear consensus sequence was determined. Incidentally, 8Br-cGMP treatment yielded far greater changes in the phosphoproteome than anticipated, meaning some phosphorylations identified are likely secondary, tertiary etc. Nonetheless, when taken together the results provide some support to the hypothesis than GbpC is functionally related to PKG beyond their common traits of cGMP regulation and kinase capacity. Substrates identified often
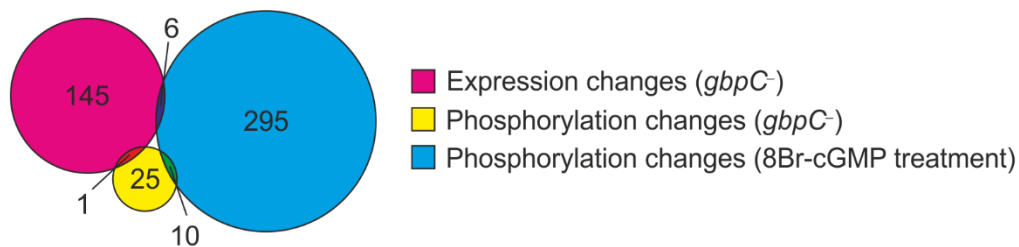
Figure 5.16 **Minimal overlap between various OMICs datasets.** Venn diagram of individual genes where any modification has taken place and the overlap between data-sets.

contains basic residues at position -3 which is consistent with PKG (Francis *et al.*, 2010). Furthermore, results suggest GbpC might specifically modify PxxP motifs to modulate binding capacity to SH3-domain containing proteins. Consistent with studies on mammalian PKG, a definitive substrate consensus sequence was not resolved. These findings, however, provide potential avenues to follow when studying candidate substrates of GbpC.

5.2.5 Concluding remarks

Stimulation of cells with 8Br-cGMP and subsequent activation of GbpC elicits a rapid and wide range of modifications. GbpC is known primarily for its role in regulation of osmotic-shock responses and cytoskeletal dynamics. The results from this experiment have supported this and provided a host of components through which it can exert its effect to those ends. Furthermore the activity of GbpC can be implicated in biological processes previously undescribed, including autophagy. It will be necessary to validate the hits identified and undertake further experiments to resolve the specific interactions and signalling pathways. This could include generating mutant cell lines where the identified gene product is knocked out or mutated at the phosphosite to produce phosphomimetic or non-phosphorylatable proteins, and testing these mutant lines to identify changes to autophagic flux under both basal conditions and 8Br-cGMP stimulation. Nonetheless, the impact of GbpC activity in *Dictyostelium* is far-reaching.

5.3 Discussion

GbpC is the only known *Dictyostelium* kinase regulated by cGMP. Thus, it acts as a master regulator of all stimuli which elevate intracellular cGMP levels, including hyper-OS (Oyama, 1996), extracellular cAMP (Van Haastert, 1983; Van Haastert and Van der Heijden, 1983) and compression (Figure 4.9C). Knowledge of downstream effectors, however, remains limited, and no GbpC substrates have been identified to date. Using mass-spectrometry, the global effect of GbpC loss on both the proteome and phosphoproteome, and the rapid changes driven by GbpC activation, have been resolved. Effectors established in literature were identified within this data, while known processes and protein groups were identified by GO analysis. These findings validated the integrity and reliability of the dataset, and consequently provided confidence that the novel modifications mediated by GbpC are genuine. Together, this has led to a greater understanding of GbpC's role within *Dictyostelium*.

The primary focus was to resolve candidate proteins which transduced cGMP signalling to the autophagic machinery. Although no hits were identified in the GbpC-null cells, altered phosphosites in 4 candidate

proteins were detected upon GbpC stimulation. TOR was phosphorylated within an unconserved region of the kinase domain C-loop (Yang *et al.*, 2013), therefore it is difficult to ascertain whether it is activating or inhibitory. It is also unclear whether this modification is specific to TORC1 or TORC2. Phosphorylations were detected in additional components of TORC2, however the TORC1 substrate FebA was also phosphorylated. The modification site aligns to an eIF4E-BP1 inhibitory phosphosite (Lekmine *et al.*, 2004) mediated by TORC1 in mammals (Hara *et al.*, 1997). Morio *et al.* (2001) concluded the site lost in *Dictyostelium* due to the absence of an adjacent proline residue, however this was based solely on peptide sequence alignment. *Dictyostelium* FebA phosphorylation at T37 and/or T46 has been detected *in vivo* after both starvation and rapamycin treatments (Rosel *et al.*, 2012) which, in combination with our detection of pT37, implies the site may be conserved. Additionally, the phosphosite fits the recently described NEK kinase substrate motif (Kooij *et al.*, 2019). Together, this suggests Tor phosphorylation may occur in both complexes. It also indicates TORC1 is active, which would inhibit autophagy initiation. As this has previously been shown not to be the case, it implies cGMP mediated autophagy induction occurs via non-canonical, Tor-independent mechanisms.

Modifications in other autophagy related proteins included Atg6b, Atg13 and Rab1A. All were phosphorylated in response to GbpC activation, but the effect of these changes remain unclear. Atg6b was modified in an unconserved region unique to *Dictyostelium*. Atg13, too, exhibits vast deviation from homologues in other organisms, making it difficult to infer function from studies on such homologues. Inhibitory phosphorylation of Atg13 protein has been reported in both humans (Puente *et al.*, 2016) and yeast (Kamada *et al.*, 2000), inhibiting autophagy in both cases. Phosphorylation of *Dictyostelium* Atg13 has not been previously reported, and the modification detected does not align to any reported sites in other organisms. Given its role as a scaffold for Atg1 and Atg101 (Mesquita *et al.*, 2015), Atg13 phosphorylation might modulate the complex to regulate autophagy. Considering the divergence between species, it is plausible phosphorylation of *Dictyostelium* Atg13 functions in an alternative manner. Finally, there is Rab1a which in mammalian cells has been shown to interact with Atg9 and localise to omegasomes (Winslow *et al.*, 2010). The *Dictyostelium* Rab1a phosphosite aligns to mammalian ATG13 although the function is unknown (Zhou *et al.*, 2013). It is promising that these genes are all involved in the early stages of autophagy and autophagosome biogenesis. Determining the functional relevance of their phosphorylation in response to 8Br-cGMP will resolve their role in mediating cGMP-regulated autophagy, and potentially uncover further detail regarding their activity in canonical autophagy.

The role of GbpC in regulating the cytoskeleton is well documented, predominantly with regard to myosin phosphorylation. While several myosins and their respective kinases were phosphorylated, a diverse array of actin-interacting proteins were identified which have not been linked to cGMP signalling. Of particular interest was the scaffold protein Carmil which localises to pseudopods, along with Arp2/3 (Jung *et al.*, 2001), MyoB (Fukui *et al.*, 1989) and MyoC (Jung *et al.*, 1996). Carmil phosphorylation change was detected within PxxP motifs essential for binding both MyoB/C (Jung *et al.*, 2001) and actin capping protein

(Remmert *et al.*, 2004). Phosphorylation change was also detected in Arp3 and MyoC. Modification of several elements of a complex provides a strong indication of GbpC regulation. Furthermore, in GbpC-null cells MyoB expression was increased which could indicate a compensatory mechanism for dysregulation of the Carmil complex. cGMP signalling regulates pseudopods at both cell poles through SgcA, refining them at the front and suppressing them at the rear of the cell (Veltman and van Haastert, 2006, 2008). Furthermore, cGMP signalling is essential for maintenance of head-tail contacts during streaming (Veltman and van Haastert, 2008), with defects reported in both GbpC (Veltman and van Haastert, 2008) and Carmil (Jung *et al.*, 2001) knockouts, although severity is markedly greater with GbpC loss. Together, it suggests cGMP signalling may influence cytoskeletal dynamics towards both poles of the cell through independent mechanisms. The identification of phosphorylated Carmil complex suggests a potential mechanism through which GbpC acts upon the actin cytoskeleton.

Another cluster of modifications was detected within the Sca1 complex. The Sca1 complex is part of a negative feedback loop involving TORC2, RasC, and PKB, which regulates F-actin and cell polarity (Charest *et al.*, 2010). 8Br-cGMP treatment resulted in increased phosphorylation of ScaA S920 and Phr S50. Neither phosphosite has been described in the literature, however (Charest *et al.*, 2010) suggested ScaA contained two phosphosites: S359 mediated by PKB, and another, unknown, site. No phosphorylation of PKB was detected, which could explain why we detected reduced phosphorylation at S359 of ScaA. Equally, no modifications were detected in the phosphatase PP2A-A, another Sca1 complex protein. Furthermore, dephosphorylation of GefH was detected and close to significance (q=0.077). As with the Carmil complex, these modifications within the same complex, along with Tor phosphorylation, hints at a role for actin cytoskeletal regulation by cGMP signalling.

The production of cGMP can be stimulated by at least two stimuli: hyper-OS (Oyama, 1996), and extracellular cAMP (Roelofs and van Haastert, 2002). Both stimuli demand substantial cytoskeletal restructuring. It is established cGMP signalling promotes myosin phosphorylation resulting in myosin filament disruption (Kuwayama *et al.*, 1996). The detection of multiple modifications in critical, actin-regulating, complexes suggest a broader role for GbpC, whereby it simultaneously disrupts myosin filaments and promotes actin regulation. Precisely what this regulation entails remains to be determined, and warrants further study. Combined with GbpC regulating gene expression through transcription factors, such as DstC (Araki *et al.*, 2003, 2010), which includes actin-interactors such as AbnA (Na, 2007; Na *et al.*, 2007), it would appear GbpC is more integral than presently understood.

GbpC is speculated as a functional homologue mammalian PKG due to their shared cGMP-regulated kinase activity. Unlike GbpC, a host of PKG substrates have been identified with many detailed in a review by (Francis *et al.*, 2010). They also concluded no single consensus motif existed for PKG, and speculated substrate specificity was directed by sub-cellular localisation rather than a target motif. The similarities between substrates of both PKA and PKG further compound the difficulty in resolving PKG-specific modifications. Recently, (Sugiyama *et al.*, 2019) showed PKG phosphorylated Rxx($_p$S), Rx($_p$S) and Kx($_p$S)

peptides approximately 6-fold, while RRx($_p$S) phosphorylation increased 31-fold. GbpC activation yielded only one RRx($_p$S) modification, however 102 phosphorylations fitting the other motifs were identified (Figure 5.14A-B, 5.15A-B). Some of these may be mediated by PKA which has an established substrate consensus Rxx($_p$S/T) (Huang *et al.*, 2007; Lee *et al.*, 2011). Worth noting is that Arp3 is phosphorylated by PKG (Huang *et al.*, 2007), as *Dictyostelium* homologue ArpC phosphorylation was detected in response to GbpC activation. The specific site appears to be phosphorylatable in mammalian cells, however it is unclear if this is specific to breast cancer cells (Mertins *et al.*, 2016). These findings add further support to the conclusion that GbpC is a functional homologue of mammalian PKG.

It was anticipated that loss of GbpC would have a minor effect on the proteome, and a more pronounced impact on the phosphoproteome. Instead, the inverse was observed. Activation of DstC by hyper-OS causes gene expression change after only 15 min, ultimately affecting 809 genes over 2 hr (Na, 2007; Na *et al.*, 2007). As hyper-OS activates cGMP production (Oyama, 1996) which acts through GbpC, and that DstC is regulated by GbpC (Araki *et al.*, 2003, 2010), it can be inferred that GbpC contributes to such expression changes. Interestingly, however, was the minimal change in the GbpC-null phosphoproteome. Basal GbpC activity perhaps remains low, and exerts its effect predominantly through activation. This appears to be the case given the diverse phosphorylation changes observed after 2 min stimulation with 8Br-cGMP. Rapid cGMP production occurs in response to 10s extracellular cAMP or folate stimulation of starved cells (Roelofs and van Haastert, 2002). It was recently these both molecules stimulated rapid phosphoproteome change (10s cAMP, 45s cAMP and folate; Nichols *et al.*, 2019). Shorter treatment with 8Br-cGMP might also achieve this, and provide clearer indication of downstream components directly modified by GbpC. Excitingly, clusters of modifications have been detected in processes not previously described. Detailed study to validate these findings will provide a greater understanding of established cGMP signalling pathways, but novel regulatory mechanisms as well. To summarise, GbpC appears to be involved in a plethora of processes, rapidly driving global cellular changes and modulating gene expression.

Chapter 6

Discussion

This PhD has been broadly split into three categories: mechanical forces, osmotic stress response and autophagy. It has investigated the connections between the three, aiming to identify the similarities and differences between mechanically-induced and osmotic stress-induced autophagy induction. Summarised below are the key findings of these areas of research, identifying unanswered questions and speculating future experiments to address them.

6.1 Developing a toolkit to study mechanical forces

Mechanical forces are ubiquitous in life, affecting all organisms from single cells to complex multicellular organisms. These forces manifest in different forms, such as compressive, shear and/or stretch forces. The frequency and magnitude also vary, ranging from large events such as breathing, blood flow, and injury during exercise, to small forces such as changes in tension within the ECM. How a cell or tissue detects and adapts to these forces is essential for maintain optimal function, and respond appropriately to environmental cues.

The literature studying mechanical force in all its forms is vast; the ability to sense touch and pain (Maksimovic *et al.*, 2014), hearing (Orr *et al.*, 2006), embryo development (Beloussov, 1980; Beloussov *et al.*, 1988; Pagliara *et al.*, 2014), compression (Gawlitta *et al.*, 2007; Huang *et al.*, 2004), cardiovascular shear (Chiu *et al.*, 1998; Lee *et al.*, 2010; Warboys *et al.*, 2014) or stretch forces (Bradley *et al.*, 2003; Sadoshima and Izumo, 1993). Equally, a diverse range of mechanisms have evolved to detect and respond to these physical cues, converting them into chemical signals (Orr *et al.*, 2006). Examples include stretch-activated ion channels (Martinac, 2004), which undergo conformation change upon increased membrane tension (Hamill and Martinac, 2001; Lammerding *et al.*, 2004; Maroto *et al.*, 2005). Interactions between the ECM and the transmembrane proteins bound to it, such as integrin (Matthews *et al.*, 2006), can trigger structural changes leading to signalling transduction at focal adhesions (FA; Burridge and Chrzanowska-Wodnicka, 1996). This includes changes in ECM tension, leading to protein unfolding (Oberhauser *et al.*, 1998), such as in cardiomyocytes (Lammerding *et al.*, 2004). The ability of cells to detect the complex array of physical cues is matched by the complexity of the response.

Understanding the detection and response to mechanical force is important to further our knowledge of both physiology and pathology. Mechanical force plays a pivotal role in development, such as osteoclastogenesis and bone density regulation (Huang *et al.*, 2004; Kanzaki *et al.*, 2002) or during embryo development (Beloussov, 1980; Beloussov *et al.*, 1988), vascular health (Davies, 1995; Sadoshima and Izumo, 1993), and maintenance of cellular health, such as modulating gene expression via tension at the nuclear envelope (Kim and Wirtz, 2015) or orienting microtubules in *Arabidopsis* leaves (Jacques *et al.*, 2013). Resolving the function of these forces and the cellular response also permits a greater understanding of the impact when these systems become disrupted.

Failure to appropriately detect and respond to mechanical force can lead to breakdown of cellular homeostasis. One well studied area is the role of mechanical force in cancer survival. Solid tumours grow in

limited space within an established, constrained tissue structure which, coupled with rapid proliferation, compresses cells within and adjacent to the tumour site (Cheng *et al.*, 2009). Changes to ECM caused by tension can impair correct expression of cell-cycle genes, attributed to cancer progression (Huang and Ingber, 1999). Furthermore compressive forces have been attributed to regulation of cancer cell progression, migrations and death (Cheng *et al.*, 2009; Kalli *et al.*, 2019; Northcott *et al.*, 2018). Metastatic cells which escape the tumour and enter the blood stream must also overcome this shear-force intensive environment, as well as cell-death mechanisms triggered by ECM detachment (Das *et al.*, 2018; Hawk and Schafer, 2018). Identification of the signalling pathways responsible to transducing force into a biological response provides an opportunity to devise new therapeutic interventions in diseases, such as cancer, which hijack such processes for survival.

To determine the intricacies of mechanotransduction requires appropriate systems to study it, methods which are suitable to each force manifestation being tested, alongside considerations for magnitude, frequency and physiological environment. A variety of approaches exist, each with their own strengths and limitations, which was reflected in the literature and remains true today. This makes comparison of results from different research groups challenging, and continues to be an issue. To resolve this, it was aimed to establish a unified mechanical force toolkit composed of the best suited methods available for studying compression, shear and stretch forces.

6.1.1 Compression
Subjecting cells to compressive force was well established, and could be undertaken with ease. Methods described in literature are diverse, ranging from use of devices capable of inducing high-pressure (Tanabe *et al.*, 2011), to magnetic beads to apply compressive force (Matthews *et al.*, 2006). Equally, there are less aggressive systems such as overlaying cells with agarose and the addition of weights to elevate the compressive force (King et al., 2011; Figure 3.2, 4.5, 4.10). Compression using agarose is cost-effective and accessible, permitting live-cell imaging and biochemical analyses e.g. transcriptome analysis (Di-Luoffo, Delarue, *et al.*, 2021).

One major limitation is that compression of cells is restricted to 2D. Consequently, experiments requiring large quantities of material are challenging. While it was possible to overcome this to determine intracellular cGMP concentration upon compression (Figure 4.10A), it would be impractical to scale for experiments which require much larger protein samples such as OMICs. However, recent developments in single-cell OMICs (Lee *et al.*, 2020) could address the issue and provide novel opportunities to study compression in this respect.

Another major drawback is the lack of a high-throughput system for screening purposes. Screening multiple cell lines is laborious and time-consuming, however an automated system does not exist. If a commercial system did become available, it might only be viable for groups able to afford it. In addition, screening is made more challenging by a practical limitation of compression itself; compression displaces media above cells limiting addition of compounds to immediately before or after application of force. An accessible

option would be mass-production of compression inserts of defined dimensions and weights, compatible with standard cluster plates, allowing application of exact and reproducible force. Furthermore, advances in microscope image analysis and automation would allow streamlining of part of the protocol. For *Dictyostelium*, creating an extrachromosomal expression vector containing both GFP-atg8 and a RFP-tagged nuclear markers would have facilitated more rapid cell detection and puncta quantification.

6.1.2 Shear forces

As with testing compression, a range of options are available for subjecting cells to shear stress which have been developed over decades. The most accessible is the orbital shaking method (Dardik *et al.*, 2005; Warboys *et al.*, 2014), used previously (see Figures 3.4 and 3.5). The main advantage is allowing high- and low-shear intensity, alongside uniform and disturbed flow patterns to be studied in tandem. This system is only suited for end-point analysis where samples are fixed for microscopy or lysed for biochemical or molecular biology analysis. Cost-effective and easier to scale up, it provides an ideal system for testing multiple conditions and samples, but live-cell study isn't possible.

For live-cell imaging studies under shear flow, again, a range of options are available. Parallel plate systems can be used, also providing sufficient surface area for biochemical analysis post-imaging (Dardik *et al.*, 2005; Lien *et al.*, 2013) however require assembly/disassembly. User-friendly commercial options are available: microscope slides with built-in channels for tuneable shear force application, even simulation of vascular bifurcations. Complete workflows comprising pumps, tubing and computer control systems are also available and designed for long-term experiments. The latter systems are restrictive in terms of cost, but comparable setups could be made using less expensive equipment. The appropriate configuration depends on the desired output.

The syringe pump used in Figure 3.3 was fully compatible with microscope systems, but limited to short treatment times due to finite media volume available. A peristaltic pump would have been more appropriate to address this. Some, but not all, microscope slides contain channels with sufficient surface area to permit biochemical analysis, allowing microscopy and biochemical data to be collected from the same sample. Given the potential cost of investing in equipment, it would be more effective to utilise the orbital shaking method for larger screens, and if follow-up study of certain conditions is desired, to employ methods that allow modulation of the shear forces being applied.

Attempts were made to subject *Dictyostelium* to shear forces. Cells cultured using ibidi™ slides and subjected to low intensity shear force were easily displaced and washed away. The orbital shaking method, even at reduced rotational speed, was sufficient to detach the majority of cells. The semi-adherent physiology of *Dictyostelium* suggest it is not a suitable model for fluid shear force. However, it has been reported that pre-treatment of surfaces with substrate poly-L-lysine improves cell adhesion sufficiently to retain cell attachment (Décavé *et al.*, 2003; Lombardi *et al.*, 2008). Additionally, there is a need to study the effects of mechanical forces on detached cells, for example of metastasising cancer cells in the blood

stream. *Dictyostelium* is suited to shaking culture and could be, instead, suitable for studying shear in a non-adherent setting.

6.1.3 Stretch

At the start of the PhD, there were few commercial options available for testing stretch forces. Methods were either small scale, limiting subsequent options for analysis, or large scale but incompatible with live-cell imaging. Of the options that were available, the cost was severely limiting. One system used a vacuum pump to stretch an elastic membrane upon which cells were cultured and while live-cell imaging was possible, it was limited to upright widefield microscopes; no high resolution imaging. To address this, the aim was to create and test a microscope stage-compatible device, capable of stretching samples to defined tensions while live-imaging.

The stretching device was based a precursor device designed and manufactured by Dr Simmons' lab (University of Florida, USA), made instead of metal to be robust and durable. The device used motors which were controlled via a laptop, and was limited to testing to a single sample at a time. Large scale experiments would be impractical, particularly for extended treatment conditions. Additionally, if multiple conditions were tested, a single device wouldn't suffice. The use of multiple devices would remedy this, however this would be expensive. Consequently, the stretching device described here would be best suited to short-tern experiments seeking to uncover the immediate effects of stretch, rather than the long-term adaptations. Most critically, it was shown to be microscope compatible and live-cell images of cells subjected to stretch were acquired (Figure 3.11).

6.1.4 Summary

In order to study mechanical forces, careful consideration is required regarding the force being tested, the time-frame of interest, the force magnitude and frequency, and the desired data output (live-cell imaging data, gene expression profiles, protein abundance etc.). Every method has advantages and disadvantages, therefore combining approaches to address the specific questions being probed is essential. Novel and innovative techniques are being devised to address this (Al-Maslamani *et al.*, 2021; Boulter and Féral, 2021; Deng *et al.*, 2017), which are essential in driving new discoveries in the field.

Across all mechanical forces detailed, the greatest limiting factors are cost and scalability. In order to advance our understanding of how mechanical forces influence cells, the systems to study them need to be affordable and accessible. Equally, to ensure rapid progress is made, high-throughput workflows need to be designed and created. Creating a toolkit or guide, similar to that of autophagy (Klionsky *et al.*, 2016), would aid in accessibility for new researchers and reproducibility of results. Together, this would facilitate advances in our understanding of how forces shape cells, tissues and life.

6.2 When under pressure, comfort eat (yourself); mechanically-induced autophagy

Since the seminal paper showing compression induced autophagy in both *Dictyostelium* and mammalian cells (King *et al.*, 2011), multiple publications have been released confirming this in other organisms as well

as under different forces. Compression induces autophagy in rat nucleus pulposus cells (Ma *et al.*, 2013), autophagy increased by compression and stretch after elevated intraocular pressure (Piras *et al.*, 2011), and shear induced autophagy in endothelial cells (Das *et al.*, 2018; Liu *et al.*, 2015). However the precise mechanism(s) connecting mechanical force and autophagy remain unclear, although several signalling pathways have been implicated.

6.2.1 Compression

The autophagic response to compression appears to be highly conserved. It has been reported in *Dictyostelium* (King *et al.*, 2011), mammalian cells (Di-Luoffo, Delarue, *et al.*, 2021; King *et al.*, 2011; Teng *et al.*, 2011), mice (Tanabe *et al.*, 2011), rat (Ma *et al.*, 2013), plants (Jacques *et al.*, 2013). Although referred to as wild-type, *Dictyostelium* Ax2 and Ax3 harbour genetic differences. To ensure any genetic variation between these two cell lines, or even different lab stocks of the same strain (Bloomfield *et al.*, 2008), it was essential to verify the response as observed in Ax3 (King *et al.*, 2011) was observed in Ax2 (Figure 3.2).

Several *Dictyostelium* knock-out cell lines were subjected compression in an attempt to identify diminished autophagy induction (Figure 4.5), although no potential candidates were found. This included PiezoA (Srivastava *et al.*, 2020), the *Dictyostelium* homologue of mammalian Piezo1, a mechanically gated ion channel capable of detecting membrane tension changes in an independent manner (Cox *et al.*, 2016; Lewis and Grandl, 2021). Initially shown to be mTOR-independent (King *et al.*, 2011), there have been reports that mTOR could be involved in some circumstances (Blawat *et al.*, 2020). Integrin-linked kinase in human periodontal ligament cells has been suggested to mediate the response to static compression (Zou *et al.*, 2021). Authors also implicate phosphatidylinositol 3-kinase (PI3K) signalling, involved in nucleation of autophagosomes (Hurley and Young, 2017). PI3K-AKT signalling has also been implicated, leading to increased expression of GABARAPL1 (Di-Luoffo, Delarue, *et al.*, 2021) and speculation that PI3K signalling may act as a hub for mechanotransduction (Di-Luoffo, Ben-Meriem, *et al.*, 2021). Significant research has been undertaken studying phosphatidylinositols in *Dictyostelium,* due to their role in phagocytosis and macropinocytosis (Buckley *et al.*, 2016; Carnell *et al.*, 2011; King and Kay, 2019) making *Dictyostelium* an excellent candidate for testing this proposal.

6.2.2 Shear

Provisional results suggested that autophagy was induced in HUVEC, but not MDA-MB-231, cells upon shear stress (Figure 3.5). This is supported by several publications regarding HUVEC autophagy induction by shear (Dong *et al.*, 2017; Liu *et al.*, 2015), as well as endothelial cells (Liu *et al.*, 2015; Vion *et al.*, 2017). Interestingly, it has been reported that non-endothelial cells, too, are shear-sensitive (Grierson and Meldolesi, 1995; Lee *et al.*, 2005), and a causal link between shear-stress and autophagy has been reported in bone (Bacabac *et al.*, 2004; Burger and Klein-Nulend, 1999), cervical cancer (Das *et al.*, 2018) and hepatocellular carcinoma cells (Wang *et al.*, 2018). In this instance, it appears MDA-MB-231 cells are not best suited for studying shear-stress induced autophagy, but several alternatives are established in the literature.

The precise signalling responsible for driving autophagy induction by shear stress is unclear, and many signalling components have been proposed. It has been shown to be mTOR-independent (Lien *et al.*, 2013), like with compression (King *et al.*, 2011). Autophagy regulation has been suggested to occur via p53 (Liu *et al.*, 2018), bone morphogenetic protein receptor Smad1/5 (Lien *et al.*, 2013), p38 MAPK (Lien *et al.*, 2013; Liu *et al.*, 2018) and both redox regulation and Sirt1 expression (Liu *et al.*, 2015). The precise signalling pathway may depend on the magnitude of the shear stress, frequency or flow direction; is it unidirectional in a vein, or disturbed? The induction of autophagy has been suggested to be atheroprotective (Vion *et al.*, 2017), which would explain why it can be hijacked for cytoprotective purposes in cancer metastasis (Das *et al.*, 2018). Identifying the signalling pathway(s) responsible for shear-induced autophagy under various shear-stress conditions could reveal novel therapeutic interventions for treating metastatic cancers or diseases of the vascular system.

6.2.3 Stretch

The earliest reported coincidence of stretch-induced damage accumulation in aging mice and elevated autophagy was by Gutmann *et al*. (1971) but a causal link was not suggested. One aim of this PhD was to determine if stretch could elicit an autophagic response. Unfortunately, the stretching device method developed was not tested to this end. However, there have been several publications released on this subject. It was previously shown that 1 hr exercise induced autophagy in mice in muscle tissues (Grumati *et al.*, 2011). Porter *et al*. (2014) reported stretch induced autophagy, highlighting it was both mTOR- and BAG3-independent, and not chaperone-assisted autophagy (CASA). BAG3 is involved in the misfolded protein response (Stürner and Behl, 2017). Other publications have also shown an autophagic response to stretch (Inaba *et al.*, 2017), suggested an adaptive role in responding to stretch and repairs damage caused (Hirt and Liton, 2017). In cardiomyocytes a potential role for angiotensin II type 1 receptors have been implicated (Lin *et al.*, 2015). At present, the least is known regarding the role of stretch-induced autophagy. Further study is necessary to determine the signalling responsible.

6.2.4 Summary

It was initially speculated that regardless of the force type (compressive, shear and tension), the signalling would either act through a single pathway, or function through a mechanotransduction master regulator akin to mTOR. As novel research was published on each type of force, it became clear this was not the case. In terms of autophagy induction, some cells are more mechanoresponsive than others, and some respond to one force and not another, such as MDA-MB-231 responding to compression but not shear (Figure 3.5C; King et al., 2011). It now appears that cells possess the capacity to detect and respond to these physical stimuli with a greater degree of complexity and specialisation. Equally, this may be due to the need for redundancy giving the prevalence of mechanical forces in life. Autophagy is an ancient process on account of it being observed highly divergent organisms such as *Dictyostelium*, mammalian organisms, yeast, and plants. Mechanical force predates autophagy, but it could be that the two have become interlinked over the millennia. Autophagy is a stress response, and if in some contexts mechanical forces are stressful and/or damaging, it could provide an appropriate survival mechanism.

6.3 Autophagy and osmotic stress

Maintaining homeostasis is essential for cell survival. Changes in osmotic environment must be detected and appropriately adapted to by all organisms, single- and multi-cellular, to maintain optimal conditions. Whether hyper- or hypo-OS, both are stresses which can impair protein structure and function, blocking interactions or activity, disrupt ion concentration gradients, and lead to rapid changes in cell volume and water content. Rectifying this changes is energetically demanding, but essential for survival.

Hyper-OS was shown to induce autophagy in *Dictyostelium*, resulting in a clear dose-response up to 100mM sorbitol (Figure 4.4). Similarly, a clear dose-response was observed between autophagy and 8Br-cGMP treatment (Figure 4.6). As it was established hyper-OS could stimulate the production of cGMP (Oyama, 1996), it was speculated that cGMP signalling could mediate the response. However upon ablation of all guanylyl cyclase activity, or of the only cGMP-regulated kinase, GbpC, autophagy appeared unaffected (Figure 4.9). Under harsh hyper-OS conditions, the cells rapidly lost water content and shrunk (Figure 4.4D). In turn, ion concentration gradients would have been disrupted which would have triggered ion pump activity and consumed ATP in the process (Lang and Föller, 2014). Low ATP would be detected by AMPK and consequently could have induced autophagy (Ranjana *et al.*, 2019). Furthermore, *Dictyostelium* contain a contractile vacuole complex which stores excess water and ions, maintained by a V-type H^+-ATPase (Plattner, 2015). Disruption by osmosis would disrupt the contractile vacuole, consume ATP to resolve it, and contribute to AMPK activity in *Dictyostelium*.

Hyper-OS has been reported to induce autophagy via AMPK in kidney (Nunes *et al.*, 2013), colon and cervical cancer (Peña-Oyarzun *et al.*, 2017), yeast (Mikawa *et al.*, 2010) and plant (Liu *et al.*, 2009) cells. It was reported that autophagy was induced by hyper-OS in nucleus pulposus cells via a calcium-dependent mTOR/AMPK pathway (Jiang *et al.*, 2015) however this has been refuted (Liu *et al.*, 2017). Furthermore, while AMPK was activated by hyper-OS, HT22 hippocampal nerve cells exhibited no increase in autophagy (Dafre *et al.*, 2019). Together, this suggests the response to hyper-OS and any effect on autophagy, is not uniform across all cell types.

The two titration experiments were undertaken in Ax2, whereas the double knockout *gcA⁻/sgcA⁻* and *gbpC⁻* cell lines were created from Ax3. Ax3 exhibited a similar maximal response to Ax2 under hyper-OS conditions, although at a lower concentration of sorbitol (50mM in Ax3 vs. 100mM Ax2; Figures 4.4B, 4.9A). Additionally, autophagic responses to both starvation (Figure 4.11) and 8Br-cGMP treatment (Figure 4.8) were lower compared with Ax2. This could be attributed to the genetic duplication present in Ax3 and Ax4 lines (Bloomfield *et al.*, 2008). It would be worthwhile creating knockout lines for both guanylyl cyclases and GbpC in an Ax2 background. The greater capacity for autophagy induction in Ax2 would provide an improved dynamic range, facilitating resolution of minor changes which is more challenging in Ax3 given the inherent biological variation in autophagic puncta counts. This would allow the extent to which cGMP is responsible for mediating the autophagic response to hyper-OS.

What also remains unclear is whether the cGMP-induced autophagic response is conserved in mammalian cells. MDA-MB-231 showed minor increases in autophagic puncta upon stimulation (Figure 4.13), but results were not as clear as observed in *Dictyostelium*. It was speculated that they might not typically utilise cGMP signalling, however it has been reported that this cell line is cGMP-sensitive (Borcherding *et al.*, 2016). It would be interesting to determine if hyper-OS induces an autophagic response in MDA-MB-231 cells, particularly if compared with cell lines adapted to osmotic stress such as renal cells or hepatocytes, or tissues with higher expression of PKG such as bladder, adrenal gland or testis (Ørstavik *et al.*, 1997). Equally, it could prove fruitful to determine if these cell lines activate autophagy, perhaps as a cytoprotective mechanism against osmotic stress.

As observed with mechanical forces, the response to hyper-OS is magnitude dependent; the greater the stress, the greater the response. Due to global impact on protein conformation, ion gradients, cellular water content, and the array of adaptations cells and tissues must undertake to survive, it is likely a diverse range of signalling pathways are triggered simultaneously. This will make it challenging to identify the specific process which leads to autophagy induction, but could identify currently unknown, non-canonical pathways.

6.4 The interplay of mechanical force, osmosis and autophagy

Both mechanical force and osmotic stress can cause sudden and drastic change to the local environment, to which cells must quickly adapt to survive. It is, therefore, unsurprising that both are commonly reported as inducing the stress response, autophagy. Significant progress has been made in elucidating the underpinning signalling pathways responsible for mediating the response to these stressors, as well as the regulation of autophagy. Still, much remains unknown.

In collaboration with Peter van Haastert (University of Groningen, Netherlands), it was shown for the first time that compression induced cGMP production in *Dictyostelium* (Figure 4.10). There is currently no literature indicating whether this response has been observed in any other organism. It was particularly exciting given the established role of cGMP in vasculature and the response to shear force (Bredt and Snyder, 1990; Nausch *et al.*, 2008), as well as its role in responding to hyper-OS stress (Oyama, 1996). While in both instances the loss of cGMP signalling did not impair or dampen the autophagic response (Figure 4.9, 10B), it does highlight a niche whether both mechanical force and the OSR overlap. The precise role remains unclear, and it would be interesting to quantify any change in intracellular cGMP levels in mammalian cells under compression.

Turnover of cGMP is rapid, quickly broken down by several PDE enzymes in *Dictyostelium* (Bader *et al.*, 2007). Due to the time taken to dismantle the compression apparatus, the real level of cGMP during compression may have been orders of magnitude greater. Compression of knockout cell lines, lacking PDEs to ablate degradation of the signal, would provide a more pronounced indication of cGMP content during compression. An alternative to the RIA method would be the use of live-cell reporters, such as fluorescent

indicators of cGMP (FlincG), which has been used in rat vascular smooth muscle cells (VSMCs; Nausch et al., 2008) and plant cells (Isner and Maathuis, 2011). There are no reports of this being used in *Dictyostelium*, however protocols indicate use of an adenoviral vector so it might not be possible. It would be suitable for testing in mammalian cell lines.

In the vasculature, activation of nitric oxide synthase (NOS) enzymes produces nitric oxide (NO) (Bredt and Snyder, 1990). This activates soluble guanylyl cyclases, leading to a rise in intracellular cGMP levels which drives activity of PKG (Francis *et al.*, 2010). This signalling pathway is also reported in osteoblasts, with shear force predicted to be comparable for that of the vasculature (Burger and Klein-Nulend, 1999; Weinbaum *et al.*, 1994). NO signalling also plays an important role in plants, also yielding intracellular cGMP production (Durner *et al.*, 1998; Wilson *et al.*, 2008). NO-cGMP signalling is not exclusive to shear, and plays a role in driving the biological response to stretch forces in both endothelial and cardiomyocytes (Casadei and Sears, 2003; Castro *et al.*, 2010).

A common adaptive response to mechanical force and hyper-OS is the rearrangement and reinforcement of the cytoskeleton. Under mechanical strain, proteins cross-linking actin filaments can become deformed, triggering an UPR similar to the heat shock response (Trotter *et al.*, 2002). Heat, like osmotic stress and mechanical tension, can alter protein conformation and impair function, to which there are heat shock proteins (HSPs) which detect these misfolded proteins. In yeast, HSPs exist with specific and redundant roles for the endoplasmic reticulum (ER) and cytosolic unfolded protein response (UPR; Geiler-Samerotte et al., 2011; Metzger and Michaelis, 2009). In ER-UPR, misfolded proteins are detected shortly after translation by chaperones, which facilitate appropriate protein conformation, or deliver the peptide for degradation via chaperone assisted autophagy (CASA; Buchberger et al., 2010).

Cytosolic UPR addresses misfolded peptides already in the cellular milieu, where their fate can be either repair or degradation, the latter via autophagy or the proteasome (Buchberger *et al.*, 2010). If misfolded proteins accumulate, they can be sequestered in aggregates which are later encapsulated and degraded by autophagy (Parsell and Lindquist, 1993; Pinto *et al.*, 1991). The cytosolic UPR system is conserved in *Arabidopsis* (Sugio *et al.*, 2009). This system could be activated in response to hyper-OS or mechanical forces if the end-point was disruption of protein conformation, and could be tested for involvement in mediating the response.

Autophagy is a dynamic and complex system which has been implicated in the response to starvation (Kamada *et al.*, 2000; Otto *et al.*, 2003), mechanical forces (King *et al.*, 2011; Porter *et al.*, 2014; Wang *et al.*, 2018), osmotic stress (Nunes *et al.*, 2013), low energy/ATP levels (Inoki *et al.*, 2012; Ranjana *et al.*, 2019), plasma membrane damage repair (López-Jiménez *et al.*, 2018) and mitochondrial damage (Palikaras *et al.*, 2018). This list is not exhaustive, nor is our understanding of the array of biological events which regulate it. In order to appropriately regulate autophagy flux to maintain homeostasis, all the upstream regulation needs to be appropriately coordinated. It is therefore unsurprising to have identified an overlap

between mechanical force and hyper-OS regarding autophagy induction, and it is anticipated more will be identified in the future.

6.5 Understanding the effects of cGMP signalling by phosphoproteomics

After determining that 8Br-cGMP was a potent inducer of autophagy, the next question was: how does it achieve this? In *Dictyostelium* it has been documented that myosins and their kinases were phosphorylated in response to cGMP signalling (Bosgraaf *et al.*, 2002). However there was a distinct lack of evidence supporting any direct link between the cGMP-regulated kinase GbpC and a substrate. Through analysis of the phosphoproteome under 8Br-cGMP stimulation, hundreds of modifications and subsequent candidate proteins were identified (Figure 5.6).

The primary aim was to identify autophagy proteins involved in signal transduction and autophagy initiation. Changes in phosphorylation status were detected in components of the initiation and nucleation stages, as well as up-stream regulation. TOR is the central protein which forms the TORC1 and TORC2 complexes, which each have distinctive roles (Charest *et al.*, 2010; Liao *et al.*, 2008). Among other roles, TORC1 activity inhibits autophagy through inhibitory phosphorylation of Atg1. The phosphorylation detected in TOR lies within the kinase domain C-loop (Yang *et al.*, 2013), suggesting it could impact kinase activity. When active, TORC1 phosphorylates various substrates, including FebA, the *Dictyostelium* homologue of mammalian 4E-BP1 (Rosel *et al.*, 2012). Detection of FebA phosphorylation suggests TORC1 is active and that autophagy would be blocked, which is not the case (Figure 4.7). This suggests not only that the response is TORC1-independent as with compression-induced autophagy (King *et al.*, 2011), but that this unknown non-canonical pathway is driving autophagy and overriding the canonical inhibitory TORC1 signalling entirely.

The Atg1 complex is essential for autophagy to take place. Atg1-null cells are commonly used as negative controls to this end, as no autophagy can occur within them. The *Dictyostelium* Atg1 complex is formed of Atg1, Atg13, Atg101 and possibly DDB_G0285767 (Mesquita *et al.*, 2017). Like Atg1, Atg13 is essential for any autophagic activity to take place (Mesquita *et al.*, 2015), making Atg13 a promising candidate for a downstream target of cGMP signalling. The purpose of the phosphorylation is unclear. Under basal conditions, Atg13 phosphorylation in both yeast and mammalian cells is inhibitory (Kamada *et al.*, 2000; Puente *et al.*, 2016), however Atg13 is highly divergent across different species (Mesquita *et al.*, 2015). Future experiments should aim to determine the function of this phosphorylation in *Dictyostelium*, e.g. T514A mutation. This should include determining whether the modification occurs solely by cGMP signalling, or whether other stressors such as hyper-OS, compression or starvation also induce this phosphorylation.

Nucleation is driven by the Beclin-1 complex, Atg6 in *Dictyostelium*. The phosphorylation occurs in the N-terminal region of Atg6B, the second Atg6 isoform present in *Dictyostelium*. Both *Dictyostelium* Atg6 genes have long N-terminal extensions not present in other organisms. It is unclear when and how these arose,

and no evidence exists regarding this. Speculating a gene fusion event, attempts were made to BLAST the unconserved regions to other organisms but yielded no candidates to this end. It has been reported that the same phosphorylation occurs under cAMP stimulation (Nichols *et al.*, 2019), indicating the modification serves a purpose and should be studied further.

In mammalian cells, Beclin-1 can be regulated by an array of mechanisms such as reduced expression, enhanced degradation, sequestration in tau bundles, and inhibitory binding to Bcl-2 proteins (Salminen *et al.*, 2013). Additionally, several reports on autophagy initiation show Beclin-1 regulation by phosphorylation: phosphoglycerate kinase 1 at S30 (Qian *et al.*, 2017), calcium-activated DAPK at T119 within the Bcl-2 homology-3 (BH3) domain (Zalckvar *et al.*, 2009), and Akt at S234 and S295 within the 14-3-3 domain for protein binding (Wang *et al.*, 2012). While *Dictyostelium* has no known Bcl-2 proteins, Akt/PkbA homologues are present within the genome. Regarding mammalian DAPK, *Dictyostelium* contain the two genes, *DDB_G0279405* and *DDB_G0272092*, which are putative kinases with possible involvement in calcium signalling. These should be studied further to determine their role in Atg6 regulation. Mutation of the specific S89 residue in Atg6B could also shed light on the role of Atg6B regulation in *Dictyostelium* autophagy. While the exact sites of phosphorylation may vary, it could the overarching regulatory mechanism by phosphorylation is what is conserved across organisms.

Rab proteins are ras-related, and implicated in regulation of endocytic trafficking, playing specific roles are defined stages in the pathway. Mammalian RAB1A has been proposed to interact with ATG9 during early autophagosome biogenesis (Winslow *et al.*, 2010), however there is currently no evidence to suggest *Dictyostelium* Rab1A functions in autophagy. It has been shown that, upon activation by chemoattractant cAMP, Rab1A binds GTP to become active, interacts with Roco2, and together they drive actin polymerisation and pseudopod extension (Kicka *et al.*, 2011). The authors mutated several residues in Rab1A to determine function, but not the T74 site identified here. Additionally, no modifications were detected in Roco2. A large number of cytoskeletal proteins were modified in response to cGMP-induction, so the detected Rab1A phosphorylation could be related to cytoskeletal signalling. As the phosphorylation is conserved in mammalian RAB1A (Zhou *et al.*, 2013), it should be studied in greater detail. This includes determining the effect of mutating the T77 amino acid, both to non-phosphorylatable and phosphomimetic residues, as well as verifying whether *Dictyostelium* Rab1A is also involved in early autophagosome biogenesis.

6.6 Summary and future questions

This PhD presents novel work on how autophagy is activated by mechanical forces and hyper-OS in *Dictyostelium*. It has shown that static compression yielded elevated intracellular cGMP which has never been previously described. Additionally, it identified 8Br-cGMP, a cGMP analogue, as a potent inducer of autophagy which stimulated *de novo* formation of autophagosomes. Finally, it attempted to identify the signalling pathway linking cGMP signalling to the autophagic machinery through phosphoproteomic analysis.

The main aim of this project was to identify the signalling pathway(s) which connected a compression stimulus to the autophagic machinery. Identification of cGMP was a promising discovery, highlighting a cross-over between force and the OSR. While it isn't the primary driver of autophagy initiation under these stress conditions, it may still contribute in ways which are not yet understood. The identification of phosphorylation changes in autophagy genes after cGMP stimulation suggests a causal link which requires further study. While cGMP signalling alone may be unable to induce autophagy, it may modulate the response to specific stressors for optimal adaption. cGMP is an established second messenger, but clearly there remain unknown functions and outcomes that need to be determined. Equally, autophagy is a complex and dynamic stress response and much remains unknown about the non-canonical mechanisms which regulate it.

This work highlights the challenges involved in establishing a novel method for studying mechanical forces, particularly with the aim to study a stress response such as autophagy. Since the final stages of device testing were completed, the next stage would be to apply the system to a biological question. Additionally, the limitation of cost remains a problem for furthering study of mechanical forces. More accessible and cost effective systems require development to facilitate further study in more research groups, particular those with limited funding.

The mechanisms responsible for transducing mechanical forces and osmotic stress into biological responses are yet to be fully understood. Due to the complexity of parallel signalling pathways being activated, combined with the contextual considerations such as specialised cell types and magnitude of stress, this will be a challenge. Further work is needed to dissect the individual elements responsible for mediating these responses, with the ultimate goal to consolidate this information into a comprehensive network of pathways showing the overlap between them. With this, it would provide opportunities for novel therapeutic interventions to target previously unknown pathways and modulate the stress response pathways.

Chapter 7

Appendix

7.1 *Dictyostelium* media and buffer osmolality
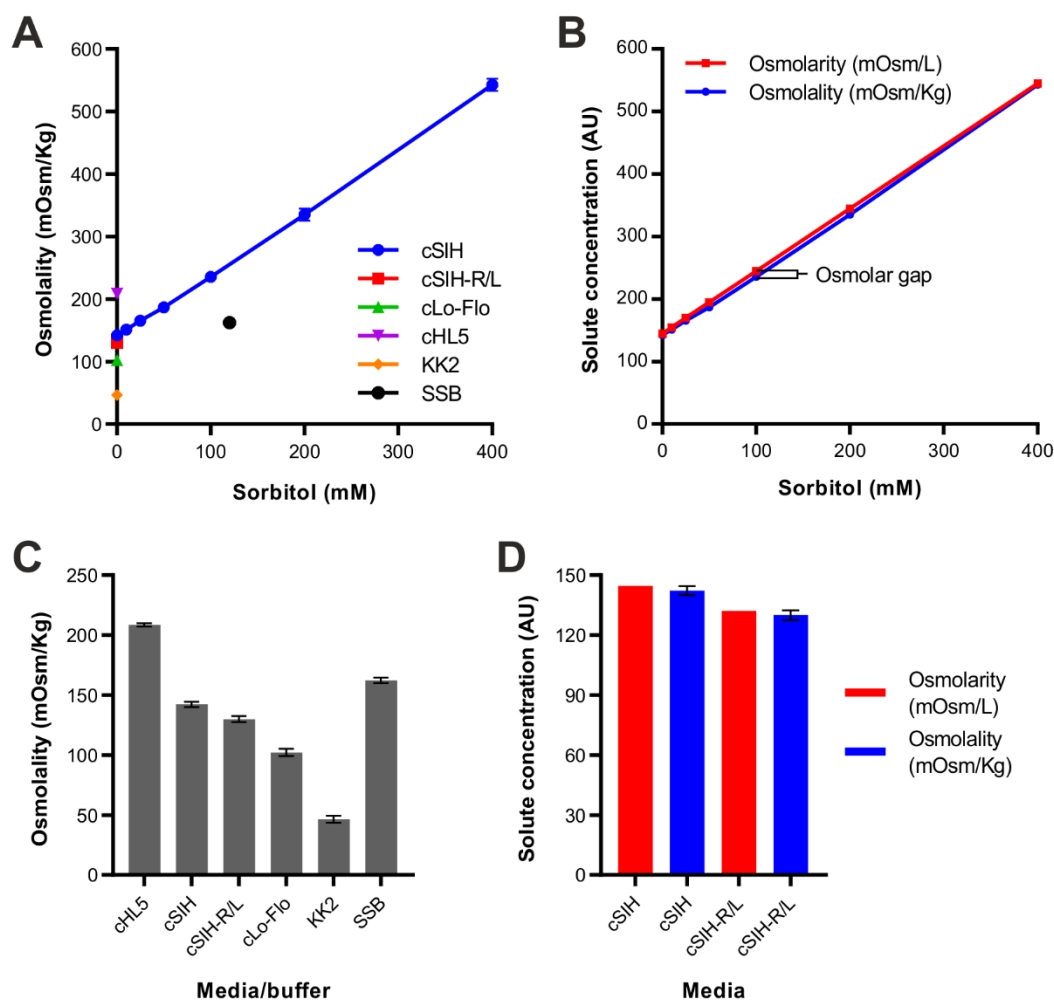
Figure 7.1 **Osmolites in common *Dictyostelium* media and buffers.** Calculated osmolarity (mOsm/L) and measured osmolality (mOsm/Kg) of various *Dictyostelium* media and buffers used for culturing, washing or starvation. Media containing 1X pen-strep prefixed with "c". (A) Osmolality of all media tested plotted against sorbitol concentration. SSB contains sorbitol as part of the recipe for balancing 1X KK2 wash buffer osmolality, while SIH is supplemented for hyper-osmotic shock treatment. Error bars denote SD (3 independent experiments). (B) cSIH supplemented with sorbitol for hyper-osmotic shock experiments. The variance between calculated osmolarity and measured osmolality is the "osmolar gap", indicated. Error bars denote SD (3 independent experiments; osmolality only). (C) Media osmolalities with no additional sorbitol beyond original recipe. Error bars denote SD (3 independent experiments). (D) Comparison of cSIH and cSIH-R/L calculated osmolarities and measured osmolalities. Error bars denote SD (3 independent experiments; osmolality only).

7.2 Exploratory test comparing 8Br-cGMP treatments in HL5 and SIH
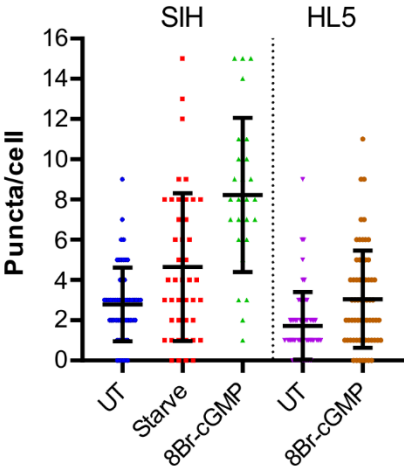
Figure 7.2 **Autophagy induction dampened in HL5 cultured cells.** AX2 expressing GFP-atg8 cultured in either SIH or HL5. Cells treated for 10 minutes with either 10mM 8Br-cGMP, arginine/lysine amino acid starvation (Starve) or untreated (UT). Each data point represents an individual cell and the puncta quantified for the conditions indicated. Bars denote mean and SD (single experiment).

7.3 GbpC-null proteome under basal conditions

Gene name	Protein name	Fold-change	-log(p)
MetE	5-methyltetrahydropteroyltriglutamate-homocysteine methyltransferase	7.280	6.372
DDB0191869	Uncharacterised protein	3.210	2.796
DDB0217648	Uncharacterised protein	3.206	4.871
Mob2	MOB kinase activator-like 2	3.005	2.530
SnrpG	Probable small nuclear ribonucleoprotein G	2.729	1.586
PykA	Pyridoxal kinase	2.481	2.193
GacG	Rho GTPase-activating protein gacG	2.229	2.324
CupG	Calcium up-regulated protein G	2.225	1.668
29C	Protein 29C	2.155	3.017
CupC	Calcium up-regulated protein C	2.097	1.863
DDB0186448	Uncharacterised protein	1.904	2.045
DDB0203213	Uncharacterised protein	1.881	2.196
DDB0217673	Uncharacterised protein	1.794	2.016
FolC	Putative folylpolyglutamate synthase	1.717	1.973
DDB0231493	Peptidase A22B family protein	1.690	1.613
DDB0168606	Uncharacterised protein	1.646	1.664
DDB0218071	Uncharacterised protein	1.591	1.533
DDB0167543	Poly [ADP-ribose] polymerase	1.561	3.377
PteN	Phosphatidylinositol 3,4,5-trisphosphate 3-phosphatase and dual-specificity protein phosphatase PTEN	1.415	1.890
PonC2	Ponticulin-like protein C2	1.377	3.762
DDB0188558	Uncharacterised protein	1.336	2.052
DDB0205122	Uncharacterised protein	1.283	2.233
CupF	Calcium up-regulated protein F	1.281	5.906
3B	Prespore-specific protein 3B	1.212	3.699
CryS	Crystal protein	1.100	4.783
DDB_G0295669	Isochorismatase hydrolase	1.099	3.215
Ncbp1	Nuclear cap-binding protein subunit 1	1.017	1.746
DDB0231482	Aldehyde dehydrogenase	0.986	2.769
PrsC	Ribose-phosphate pyrophosphokinase C	0.971	2.035
DDB0188790	Uncharacterised protein	0.970	4.850
Pdx2	Probable pyridoxal 5-phosphate synthase subunit pdx2	0.917	3.046
DDB0203975	Uncharacterised protein	0.907	3.766
DDB0230137	Methylenetetrahydrofolate reductase	0.904	3.441
DDB_G0283731	Uncharacterised transmembrane protein DDB_G0283731	0.854	3.172
DDB0186750	Uncharacterised protein	0.839	3.051
DDB_G0282243	NHP2-like protein 1 homologue	0.833	2.185
DDB0189497	Uncharacterised protein	0.818	2.451
DDB0189496	Uncharacterised protein	0.763	1.903
DD3-3	Protein DD3-3	0.740	3.933
Ndufa5	Probable NADH dehydrogenase [ubiquinone] 1 alpha subcomplex subunit 5	0.724	1.978
Mrps2	Ribosomal protein S2, mitochondrial	0.711	2.764
PonA	Ponticulin	0.686	3.010
DDB0205990	Uncharacterised protein	0.682	2.124
Nad11	NADH-ubiquinone oxidoreductase 75 kDa subunit	0.676	3.966
RsmM	Small GTPase	0.669	2.764
FhbA	Flavohemoprotein A	0.668	3.665
GadB	Glutamate decarboxylase B	0.631	2.287
MyoK	Myosin-K heavy chain	0.585	3.946
Gp130	Lipid-anchored plasma membrane glycoprotein 130	0.572	2.739
LmpB	Lysosome membrane protein 2-B	0.570	3.282
DDB0190556	Uncharacterised protein	0.565	2.406
DDB0202825	Uncharacterised protein	0.564	2.332
DDB0188841	Uncharacterised protein	0.551	2.791
KrsA	Serine/threonine-protein kinase 4 homologue A	0.550	2.458
Pdx1	Probable pyridoxal 5-phosphate synthase subunit pdx1	0.536	2.418
Rab2A	Ras-related protein Rab-2A	0.526	3.003

DDB0204712	Uncharacterised protein	0.516	2.353
GcvT	Aminomethyltransferase, mitochondrial	0.506	2.390
DDB0169117	Uncharacterised protein	0.505	3.247
GpaI	Guanine nucleotide-binding protein alpha-9 subunit	0.500	3.309
ComG	Aldehyde dehydrogenase family 3 comG	0.490	4.073
NosA	NOSA	0.476	3.730
CpnC	Copine-C	0.453	3.386
MyoB	Myosin IB heavy chain	0.441	3.058
RasG	Ras-like protein rasG	0.438	3.260
AmdA	AMP deaminase	0.421	5.551
DDB0218666	Uncharacterised protein	0.399	3.022
DDB_G0294597	Beta-lactamase family protein	0.363	3.836
DDB0215923	Uncharacterised protein	-0.363	4.010
Nubp1	Cytosolic Fe-S cluster assembly factor NUBP1 homologue	-0.390	3.189
Mhsp70	Heat shock 70 kDa protein, mitochondrial	-0.424	2.814
SodA	Superoxide dismutase [Cu-Zn] 1	-0.429	3.455
DDB0204568	Uncharacterised protein	-0.429	3.227
Pck2	Phosphoenolpyruvate carboxykinase [GTP], mitochondrial	-0.447	3.326
DDB_G0276247	Uncharacterised protein	-0.490	3.176
AlrA	Aldose reductase A	-0.492	3.621
Adprt1B	Poly [ADP-ribose] polymerase	-0.500	2.448
Timm10	Mitochondrial import inner membrane translocase subunit Tim10	-0.511	3.208
CshA	Citrate synthase, peroxisomal	-0.512	5.675
DDB_G0289609	CBS domain-containing protein DDB_G0289609	-0.545	2.628
DscA-1	Discoidin-1 subunit A	-0.566	2.378
DDB0217941	Uncharacterised protein	-0.587	3.067
DDB0190746	Uncharacterised protein	-0.593	3.254
FcsB	Fatty acyl-CoA synthetase B	-0.604	2.428
DDB0188399	Uncharacterised protein	-0.617	2.599
DymB	Dynamin-B	-0.624	2.140
SUMO	Small ubiquitin-like protein	-0.639	2.284
Metap2	Methionine aminopeptidase 2	-0.641	4.367
DDB0186928	Uncharacterised protein	-0.650	4.669
DDB0168161	DNA repair protein RAD51 homologue	-0.666	3.347
AbnA	Actobindin-A	-0.683	2.424
AAC11	AAC-rich mRNA clone AAC11 protein	-0.694	2.274
Caf17	Putative transferase caf17 homologue, mitochondrial	-0.695	2.645
PrtB	cAMP-regulated M3R protein	-0.716	3.717
DDB_G0271752	NADH:flavin oxidoreductase/NADH oxidase domain-containing protein	-0.730	2.347
DDB0188170	Uncharacterised protein	-0.746	2.182
DDB0168319	Uncharacterised protein	-0.750	2.743
AbkD	Probable serine/threonine-protein kinase abkD	-0.755	2.547
AbcG2	ABC transporter G family member 2	-0.771	3.043
DDB_G0292188	von Willebrand factor A domain-containing protein DDB_G0292188	-0.796	2.786
DDB0204153	Uncharacterised protein	-0.808	2.857
CapB	cAMP-binding protein 2	-0.832	4.483
DDB0206221	Uncharacterised protein	-0.863	2.812
DDB_G0281291	Uncharacterised protein	-0.902	4.073
DDB0217890	Uncharacterised protein	-0.907	2.682
DDB_G0290649	CCCH-type zinc finger-containing protein	-0.912	3.110
DDB_G0276291	Uncharacterised protein	-0.925	3.915
AF310893_3	Uncharacterised protein	-0.958	2.115
DDB0168017	Uncharacterised protein	-0.977	5.479
DDB0206173	DIS3-like exonuclease 2	-0.994	1.915
RliB	Protein rliB	-1.003	2.888
DDB0219578	Uncharacterised protein	-1.020	4.071
GrxB	Glutaredoxin-like protein	-1.026	3.457
Metap1	Methionine aminopeptidase 1	-1.033	5.876
DDB0186920	Uncharacterised protein	-1.037	4.001

AifA	Apoptosis-inducing factor homologue A	-1.040	2.276
DDB0169112	Uncharacterised protein	-1.049	4.393
DDB_G0280445	Glutathione-dependent formaldehyde-activating, GFA family protein	-1.079	5.576
DDB_G0291326	Putative uncharacterised transmembrane protein DDB_G0291326	-1.100	3.108
DDB_G0277599	Uncharacterised protein	-1.115	2.045
DDB_G0268948	Putative methyltransferase DDB_G0268948	-1.144	5.088
DDB_G0288011	Methyltransferase type 11 domain-containing protein	-1.166	4.578
DDB0202984	Uncharacterised protein	-1.181	4.371
DDB0189869	Uncharacterised protein	-1.302	3.407
DDB_G0282951	Uncharacterised protein DDB_G0282951	-1.303	1.595
DDB0185319	Uncharacterised protein	-1.331	1.588
DDB0167233	Uncharacterised protein	-1.347	1.786
DDB0167477	Uncharacterised protein	-1.398	2.823
DDB0188011	Uncharacterised protein	-1.468	5.867
DDB0217020	Uncharacterised protein	-1.476	3.270
DDB_G0267510	Coiled-coil domain-containing protein 43 homologue	-1.491	2.149
DDB_G0271784	Uncharacterised protein	-1.543	2.186
DDB0206525	Uncharacterised protein	-1.554	1.769
DDB0219676	Uncharacterised protein	-1.563	3.972
DDB0231514	Phosphopantothenatecysteine ligase	-1.641	1.965
DDB0168021	Uncharacterised protein	-1.758	2.197
Mrpl16	60S ribosomal protein L16, mitochondrial	-1.776	1.796
DDB_G0295779	EGF-like domain-containing protein	-1.809	1.522
DDB_G0282011	GPI transamidase subunit PIG-U family protein	-1.836	2.631
HspI	Small heat shock protein hspI, mitochondrial	-1.911	5.263
DDB_G0268776	Glutamyl-tRNA(Gln) amidotransferase subunit B, mitochondrial	-1.997	2.186
GxcJJ	Rac guanine nucleotide exchange factor JJ	-2.099	1.643
DDB0219881	Uncharacterised protein	-2.155	4.178
DDB0187945	Uncharacterised protein	-2.238	1.943
DDB0188747	Uncharacterised protein	-2.371	1.531
DDB_G0275349	Uncharacterised protein	-2.420	1.650
DDB0205698	Uncharacterised protein	-2.430	1.442
DG1091	Developmental protein DG1091	-2.591	2.825
DDB0219383	Uncharacterised protein	-2.927	3.443
DDB_G0279347	Uncharacterised protein	-3.756	1.629
DDB_G0274223	Glutathione S-transferase domain-containing protein DDB_G0274223	-4.209	4.844
Ech1	Delta(3,5)-Delta(2,4)-dienoyl-CoA isomerase, mitochondrial	-4.552	4.285

Table 7.1. Significant protein expression changes in vegetative *gbpC*⁻ cells. Significance was calculated using a combination of the T-test P-value and the fold-change, where the smaller the fold change the smaller the P-value had to be to be declared significance. The output of this is the q-value.

7.4 GbpC-null phosphoproteome under basal conditions

Phosphoproteome					Proteome	
Gene name	**Protein name**	**Phospho-site**	**Fold-change**	**-log(p)**	**Fold-change**	**-log(p)**
AF279134_1	Uncharacterised protein	S593	3.445	3.681		
Carmil	Protein CARMIL	T970	-6.270	6.757	0.275	1.686
DDB_G0277165	Probable serine/threonine-protein kinase DDB_G0277165	S351	-3.273	4.643		
		S356	-3.181	5.012		
DDB_G0277539	Probable protein kinase DDB_G0277539	T357	2.863	3.876		
DDB_G0289907	EGF-like domain-containing protein	S1500	-4.138	5.355		
DDB0167384	Uncharacterised protein	S2272	-3.644	4.234		
		S2278	-3.160	4.409		
DDB0168507	Uncharacterised protein	T517	4.285	5.237		
DDB0169506	Uncharacterised protein	S315	-6.125	5.718	0.145	1.105
DDB0184280	Uncharacterised protein	S565	-3.687	3.374	-0.328	1.473
		S568	-3.547	4.336	-0.328	1.473
DDB0184357	Uncharacterised protein	S20	4.172	5.816		
DDB0185950	Uncharacterised protein	S14	-3.542	4.110	-0.600	0.482
DDB0187697	Uncharacterised protein	T337	-4.674	5.021		
DDB0187721	Uncharacterised protein	S175	2.388	3.344		
DDB0192051	Uncharacterised protein	S350	-2.197	3.776		
DDB0202625	Uncharacterised protein	T640	-1.825	3.465		
DDB0205685	Uncharacterised protein	S181	-3.108	6.462	-0.385	0.623
		S260	-3.054	4.890	-0.385	0.623
		S261	-3.482	5.076	-0.385	0.623
DDB0205950	Uncharacterised protein	S154	-3.424	6.732		
		T155	-3.022	3.875		
DDB0216579	Uncharacterised protein	T374	-1.684	4.246		
DDB0216674	Uncharacterised protein	S984	-4.809	4.898	0.042	0.054
DDB0216929	Uncharacterised protein	T26	-3.235	3.843		
DDB0216989	Uncharacterised protein	S148	-3.085	4.537		
DDB0217693	Uncharacterised protein	S823	-4.526	4.925		
DDB0218265	Uncharacterised protein (Fragment)	S540	2.719	3.307		
DDB0220651	HMG1/2 (High mobility group) box-containing protein	T774	-2.798	3.770		
GacF	Rho GTPase-activating protein gacF	S9	-2.194	4.789		
GacH	Rho GTPase-activating protein gacH	S43	4.142	5.221		
GbpC	Cyclic GMP-binding protein C	S2322	-5.135	5.183	-1.537	1.119
GlpV	Glycogen phosphorylase 1	T10	1.151	4.375	0.046	0.246
LimD	LIM domain protein	S501	2.964	3.549	0.095	0.459
MetE	5-methyltetrahydropteroyltriglutamate-homocysteine methyltransferase	S762	3.709	3.502	**7.280**	**6.372**
MkcC	Probable serine/threonine-protein kinase mkcC	S493	-3.255	4.049	0.888	0.443
Phg2	Serine/threonine-protein kinase phg2	S705	4.870	3.509		
Pks16	Probable polyketide synthase 16	T1374	-4.691	5.819	0.162	0.796
PrlA	Proliferation-associated protein A	S2	4.558	2.940	-0.131	0.572
Rpl18a	60S ribosomal protein L18a	S118	3.853	4.620	0.025	0.076
Taf7	Transcription initiation factor TFIID subunit	S380	-2.101	3.462		

Table 7.2. Significant phosphorylation status changes in vegetative *gbpC*⁻ cells. Fold-change and significance values for changes in protein expression included for reference, where bold text denotes a significant entry. Significance was calculated using a combination of the T-test P-value and the fold-change, where the smaller the fold change the smaller the P-value had to be to be declared significance. The output of this is the q-value.

7.5 Ax3 phosphoproteome after 2 min stimulation with 8Br-cGMP

Gene name	Protein name	Phospho-site	Fold-change	-log(p)
AAC11	AAC-rich mRNA clone AAC11 protein	S223	2.233	4.170
AAC11	AAC-rich mRNA clone AAC11 protein	S436	2.547	1.771
AbcC2	ABC transporter C family member 2	S758	0.805	3.101
AbcC8	ABC transporter C family member 8	S960	3.160	4.483
AccA	Acetyl-CoA carboxylase	S1140	0.695	2.701
AF310889_1	Uncharacterised protein	S504	-1.984	2.748
ak1	Alpha-protein kinase 1	S235	-4.345	1.887
Ap3b-1	AP-3 complex subunit beta	S259	3.195	3.086
ArgB	Acetylglutamate kinase	S565	2.440	3.527
ArpC	Actin-related protein 3	S268	1.969	3.234
Atg6B	Beclin-1-like protein B	S89	2.201	1.918
Atg13	Autophagy protein 13	T514	2.000	1.827
CadA	Calcium-dependent cell adhesion molecule 1	T17	6.006	1.870
CadA	Calcium-dependent cell adhesion molecule 1	S48	-2.558	3.976
CanA	Serine/threonine-protein phosphatase 2B catalytic subunit	S525	2.249	1.690
CanA	Serine/threonine-protein phosphatase 2B catalytic subunit	S534	0.675	3.096
CanA	Serine/threonine-protein phosphatase 2B catalytic subunit	S543	1.052	3.316
Cdk11	Cyclin-dependent kinase 11	S209	4.498	4.963
CnrF	RabGAP/TBC domain-containing protein	S66	4.142	1.986
CnrM	Ankyrin repeat-containing protein	S938	2.118	5.119
CopA	Coatomer subunit alpha	S809	-1.882	2.058
CpiA	Cystatin-A1	T2	3.774	1.630
CplA	Putative calpain-like cysteine protease A	S174	1.995	3.759
CplA	Putative calpain-like cysteine protease A	S601	2.273	2.155
Dct	Dynacortin	S31	-2.989	2.352
DDB_G0267588	Probable phosphatidylinositol phosphate kinase DDB_G0267588	S122	3.473	4.240
DDB_G0267588	Probable phosphatidylinositol phosphate kinase DDB_G0267588	S159	2.031	2.499
DDB_G0267588	Probable phosphatidylinositol phosphate kinase DDB_G0267588	S238	2.401	5.018
DDB_G0267850	Ribosomal protein L1 family protein	T494	1.994	3.112
DDB_G0268328	Protein DDB_G0268328	S696	1.970	2.855
DDB_G0268948	Putative methyltransferase DDB_G0268948	S17	0.760	2.603
DDB_G0270864	Uncharacterised protein	S34	4.801	1.727
DDB_G0270864	Uncharacterised protein	S35	1.141	2.573
DDB_G0270864	Uncharacterised protein	S135	2.369	4.218
DDB_G0271358	Uncharacterised protein	T36	2.882	3.074
DDB_G0271402	Probable serine/threonine-protein kinase DDB_G0271402	S561	-1.514	1.808
DDB_G0271676	SH3 and F-BAR domain-containing protein DDB_G0271676	S398	-1.304	2.635
DDB_G0271806	PH and Rap-GAP domain-containing protein DDB_G0271806	S648	2.075	5.070
DDB_G0271806	PH and Rap-GAP domain-containing protein DDB_G0271806	S648	1.963	2.345
DDB_G0272092	Probable serine/threonine-protein kinase DDB_G0272092	S401	3.455	4.934
DDB_G0272092	Probable serine/threonine-protein kinase DDB_G0272092	S469	1.798	2.817
DDB_G0272092	Probable serine/threonine-protein kinase DDB_G0272092	S750	1.141	2.787
DDB_G0272484	Deoxynucleoside triphosphate triphosphohydrolase SAMHD1 homologue	T504	2.813	1.830
DDB_G0273095	28 kDa heat- and acid-stable phosphoprotein homologue	S135	1.823	4.420
DDB_G0274481	SPX and EXS domain-containing protein 2	S901	-4.263	1.553

DDB_G0275165	Probable serine/threonine-protein kinase DDB_G0275165	S834	2.721	4.522
DDB_G0275843	Uncharacterised protein	S24	2.016	4.268
DDB_G0275843	Uncharacterised protein	S125	4.150	5.509
DDB_G0276181	Probable serine/threonine-protein kinase DDB_G0276181	S1459	-4.009	1.652
DDB_G0276181	Probable serine/threonine-protein kinase DDB_G0276181	S1460	2.464	1.692
DDB_G0276461	Probable serine/threonine-protein kinase DDB_G0276461	S611	-4.393	5.722
DDB_G0278665	Probable serine/threonine-protein kinase DDB_G0278665	S888	1.916	2.233
DDB_G0278909	Probable inactive serine/threonine-protein kinase DDB_G0278909	S318	1.316	3.421
DDB_G0279223	SOSS complex subunit B homologue	S130	1.925	2.834
DDB_G0279653	Putative uncharacterised protein DDB_G0279653	S355	2.980	5.216
DDB_G0279831	Probable myosin light chain kinase DDB_G0279831	S143	-0.653	3.432
DDB_G0279863	Uncharacterised protein	S45	2.714	5.382
DDB_G0279863	Uncharacterised protein	S879	1.596	3.520
DDB_G0280111	Probable serine/threonine-protein kinase DDB_G0280111	S930	2.540	3.617
DDB_G0281809	Rap-GAP domain-containing protein DDB_G0281809	S1540	2.177	5.549
DDB_G0282021	Uncharacterised protein DDB_G0282021	S205	-1.537	3.390
DDB_G0285063	Uncharacterised protein	S2332	1.271	4.676
DDB_G0285119	Putative uncharacterised protein DDB_G0285119	S219	0.872	2.563
DDB_G0285119	Putative uncharacterised protein DDB_G0285119	S220	0.872	2.563
DDB_G0285189	Uncharacterised protein DDB_G0285189	S49	2.697	1.804
DDB_G0286829	Putative uncharacterised protein DDB_G0286829	S106	2.334	2.556
DDB_G0287165	Spastin	S331	3.577	4.210
DDB_G0287625	Uncharacterised protein DDB_G0287625	S458	2.375	2.105
DDB_G0287975	Putative uncharacterised protein DDB_G0287975	S143	3.483	3.146
DDB_G0287975	Putative uncharacterised protein DDB_G0287975	T146	-3.930	4.098
DDB_G0287975	Putative uncharacterised protein DDB_G0287975	S148	3.444	3.466
DDB_G0287975	Putative uncharacterised protein DDB_G0287975	S153	-4.261	5.066
DDB_G0287975	Putative uncharacterised protein DDB_G0287975	T155	3.524	4.313
DDB_G0287975	Putative uncharacterised protein DDB_G0287975	S156	1.486	2.330
DDB_G0287975	Putative uncharacterised protein DDB_G0287975	S157	3.859	3.951
DDB_G0288237	Uncharacterised protein	S1116	0.903	2.498
DDB_G0289141	Poly [ADP-ribose] polymerase	S108	-3.877	5.535
DDB_G0289263	Putative uncharacterised protein DDB_G0289263	S804	2.374	2.517
DDB_G0289829	Uncharacterised protein	S2594	2.558	2.427
DDB_G0291133	Probable protein kinase DDB_G0291133	S766	4.026	6.226
DDB_G0291301	Putative bifunctional amine oxidase DDB_G0291301	S1050	2.784	5.418
DDB_G0291301	Putative bifunctional amine oxidase DDB_G0291301	S1053	1.321	3.675
DDB_G0291842	Probable protein kinase DDB_G0291842	T45	3.725	5.506
DDB_G0291966	RNA-binding region RNP-1 domain-containing protein	S217	6.547	6.983
DDB_G0292160	Uncharacterised protein DDB_G0292160	S172	1.413	2.387
DDB_G0292354	Probable serine/threonine-protein kinase DDB_G0292354	S326	-1.680	3.224
DDB_G0292354	Probable serine/threonine-protein kinase DDB_G0292354	S331	-2.516	4.010

154

DDB_G0293276	Probable serine/threonine-protein kinase DDB_G0293276	S389	1.074	2.661
DDB_G0293920	Uncharacterised protein	S705	1.730	2.941
DDB_G0294587	Uncharacterised protein (Fragment)	S269	2.299	2.127
DDB_G0295683	LIM-type zinc finger-containing protein	S94	2.125	4.132
DDB_G0295683	LIM-type zinc finger-containing protein	S1226	1.328	3.221
DDB_G0295849	Rhomboid-like protein	S218	1.741	2.465
DDB0167554	Uncharacterised protein	S225	1.836	3.529
DDB0167929	Uncharacterised protein	T224	-1.608	2.054
DDB0167929	Uncharacterised protein	S228	1.933	3.384
DDB0168059	Uncharacterised protein	S1151	1.931	5.954
DDB0168108	Uncharacterised protein	S575	4.260	4.159
DDB0168210	Uncharacterised protein	S336	-1.867	2.445
DDB0168210	Uncharacterised protein	T338	-2.114	2.961
DDB0168507	Uncharacterised protein	S551	2.853	1.961
DDB0168793	Uncharacterised protein	S27	-0.902	3.085
DDB0168842	Uncharacterised protein	S773	1.145	2.993
DDB0168928	Uncharacterised protein	S612	2.182	2.792
DDB0183896	Uncharacterised protein	S42	3.194	6.631
DDB0183957	Uncharacterised protein	S365	2.877	2.139
DDB0184103	Uncharacterised protein	S791	4.484	1.843
DDB0184149	Uncharacterised protein	S652	1.316	3.815
DDB0184153	Uncharacterised protein	S136	1.984	2.385
DDB0184280	Uncharacterised protein	T31	1.458	2.245
DDB0184280	Uncharacterised protein	S1973	2.252	3.197
DDB0184291	Uncharacterised protein	S171	-2.584	3.789
DDB0184416	Uncharacterised protein	S178	-0.974	2.068
DDB0184478	Uncharacterised protein	T363	3.877	5.007
DDB0184478	Uncharacterised protein	T367	2.953	3.809
DDB0184503	Uncharacterised protein	S47	3.974	4.622
DDB0184542	Uncharacterised protein	S112	0.729	2.678
DDB0184565	Uncharacterised protein	S34	0.799	2.925
DDB0185569	Uncharacterised protein	S971	3.239	2.206
DDB0185666	Uncharacterised protein	S51	1.486	2.142
DDB0185950	Uncharacterised protein	T679	2.257	3.045
DDB0186124	Uncharacterised protein	S401	1.252	3.893
DDB0186293	Uncharacterised protein	S553	2.116	2.044
DDB0186471	Uncharacterised protein	S49	3.106	4.070
DDB0186499	Uncharacterised protein	S555	3.702	4.407
DDB0186526	Uncharacterised protein	T531	2.709	3.697
DDB0186987	Uncharacterised protein	S556	3.851	3.109
DDB0187046	Uncharacterised protein	S361	4.300	4.504
DDB0187142	Uncharacterised protein	T285	1.882	2.037
DDB0187142	Uncharacterised protein	S292	6.099	5.512
DDB0187414	Uncharacterised protein	S31	2.511	1.753
DDB0187414	Uncharacterised protein	S110	0.852	2.284
DDB0187697	Uncharacterised protein	S224	2.991	1.896
DDB0187710	Uncharacterised protein	S1649	-2.726	4.919
DDB0188026	Uncharacterised protein	T408	1.315	2.452
DDB0188114	Uncharacterised protein	S283	4.817	6.046
DDB0188129	Uncharacterised protein	S98	3.659	1.591
DDB0188159	Uncharacterised protein	S10	2.261	2.954
DDB0188170	Uncharacterised protein	S283	-0.890	2.628
DDB0188170	Uncharacterised protein	S1093	2.089	3.182
DDB0188214	Uncharacterised protein	S352	3.403	2.298
DDB0188218	Uncharacterised protein	S73	-3.553	2.212
DDB0188240	Uncharacterised protein	S144	-2.817	4.188
DDB0188445	Uncharacterised protein	S438	3.821	4.056
DDB0188491	Uncharacterised protein	S456	0.581	3.387
DDB0188531	Uncharacterised protein	S98	1.390	3.153
DDB0188531	Uncharacterised protein	S409	1.139	2.710
DDB0188671	Uncharacterised protein	S36	1.497	4.003
DDB0188671	Uncharacterised protein	S337	2.718	4.308

DDB0188719	Uncharacterised protein	S1310	-2.426	4.503
DDB0188846	Uncharacterised protein	S483	-1.487	2.011
DDB0188984	Uncharacterised protein	T278	4.705	4.670
DDB0189206	Uncharacterised protein	T662	2.422	3.276
DDB0189208	Uncharacterised protein	S690	3.124	1.726
DDB0189239	Uncharacterised protein	S378	3.249	3.465
DDB0189592	Uncharacterised protein	T849	1.535	2.425
DDB0189629	Uncharacterised protein	S450	3.068	3.248
DDB0189801	Uncharacterised protein	S676	2.381	3.165
DDB0189922	Uncharacterised protein	S640	1.402	3.080
DDB0190250	Uncharacterised protein	S695	2.152	2.262
DDB0190400	Uncharacterised protein	T291	2.012	1.893
DDB0190401	Uncharacterised protein	S1093	0.524	2.875
DDB0190401	Uncharacterised protein	T1122	-2.361	3.630
DDB0190401	Uncharacterised protein	S1137	3.553	4.033
DDB0190468	Uncharacterised protein	S395	2.406	1.906
DDB0190636	Uncharacterised protein	S42	1.851	2.994
DDB0190861	Uncharacterised protein	S240	1.108	3.204
DDB0190886	Uncharacterised protein	T526	2.384	1.783
DDB0190902	Uncharacterised protein	S221	2.625	1.725
DDB0191761	Uncharacterised protein	S26	1.207	2.033
DDB0191767	Uncharacterised protein	S1306	4.744	6.647
DDB0191978	Uncharacterised protein	S33	4.905	2.873
DDB0192033	Uncharacterised protein	S256	6.244	5.759
DDB0201969	Uncharacterised protein	S786	3.924	4.926
DDB0202577	Uncharacterised protein	S102	1.447	2.679
DDB0204403	Uncharacterised protein	S128	1.389	2.688
DDB0204457	Uncharacterised protein	S288	5.156	5.255
DDB0204555	Uncharacterised protein	S565	3.431	4.821
DDB0204624	Uncharacterised protein	T625	2.237	2.970
DDB0204946	Uncharacterised protein	S243	-1.052	2.608
DDB0205028	Uncharacterised protein	S284	2.590	2.271
DDB0205031	Uncharacterised protein	S203	5.574	6.255
DDB0205031	Uncharacterised protein	S281	2.092	7.199
DDB0205364	Uncharacterised protein	S244	-1.472	1.921
DDB0205492	Uncharacterised protein	S66	-1.865	2.034
DDB0205845	Uncharacterised protein	S339	0.982	2.229
DDB0205854	Uncharacterised protein	T1737	-1.420	3.509
DDB0205872	Inositol 5-phosphatase	S9	-1.933	5.113
DDB0205875	Uncharacterised protein	S249	1.831	2.111
DDB0205950	Uncharacterised protein	S159	-2.831	4.218
DDB0205958	Uncharacterised protein	S1080	1.106	3.475
DDB0206274	Uncharacterised protein	S846	2.263	1.853
DDB0206467	Uncharacterised protein	S286	1.997	2.768
DDB0215671	Uncharacterised protein	S685	2.459	4.188
DDB0215817	Uncharacterised protein	S167	2.753	2.891
DDB0215923	Uncharacterised protein	S17	2.883	2.273
DDB0216866	Uncharacterised protein	S669	2.205	2.390
DDB0216913	Uncharacterised protein	T280	3.047	3.415
DDB0216929	Uncharacterised protein	S1442	1.559	2.967
DDB0217137	Uncharacterised protein	T50	2.885	1.607
DDB0217474	Uncharacterised protein	T488	4.516	1.912
DDB0217474	Uncharacterised protein	S489	4.587	1.880
DDB0217510	Uncharacterised protein	S989	2.392	2.181
DDB0217599	Uncharacterised protein	S927	0.974	2.653
DDB0217599	Uncharacterised protein	S1668	3.701	4.592
DDB0217649	Uncharacterised protein	S119	2.001	4.033
DDB0217693	Uncharacterised protein	S1037	1.711	2.121
DDB0217806	Uncharacterised protein	T311	-0.789	3.735
DDB0217819	Uncharacterised protein	S2066	1.465	3.905
DDB0218071	Uncharacterised protein	S679	-0.584	2.861
DDB0218242	Uncharacterised protein	S1733	2.009	2.247
DDB0218242	Uncharacterised protein	S2507	2.165	1.849

DDB0218425	Uncharacterised protein	S171	3.363	4.554
DDB0218432	Uncharacterised protein	S189	1.169	3.432
DDB0218582	Uncharacterised protein	S198	1.610	4.558
DDB0218699	Uncharacterised protein	S162	1.701	5.326
DDB0218808	Uncharacterised protein	S346	1.704	2.853
DDB0218888	Uncharacterised protein	S173	2.172	2.402
DDB0219299	Uncharacterised protein	T88	1.607	2.799
DDB0219299	Uncharacterised protein	S158	5.032	4.937
DDB0219310	Uncharacterised protein	S214	2.685	4.210
DDB0219312	Uncharacterised protein	S500	4.485	3.438
DDB0219673	Uncharacterised protein	S466	-3.078	4.116
DDB0219831	Uncharacterised protein	S127	2.628	1.788
DDB0220518	Myb domain-containing protein	S288	3.324	5.332
DDB0220611	Uncharacterised protein (Fragment)	Y140	1.411	2.692
DDB0220611	Uncharacterised protein (Fragment)	S144	1.504	2.322
DDB0220640	CHD gene family protein containing chromodomain, helicase domain, and DNA-binding domain	S460	5.095	5.796
DDB0220669	SAP DNA-binding domain-containing protein	S48	4.316	1.788
DDB0220676	SAP DNA-binding domain-containing protein	S67	-1.797	1.789
DDB0230013	Rho GTPase	S365	-1.652	1.743
DDB0230057	Carboxylic ester hydrolase	S117	-2.366	1.772
DG1104	WD-40 repeat-containing protein	S2495	1.417	2.829
DG1122	Development protein	T143	2.676	3.989
DhkI-1	Hybrid signal transduction histidine kinase I	S1482	3.857	1.986
DocA	Uncharacterised protein	S762	2.941	3.024
DrnA	Putative RNase III	S116	3.657	5.306
Dst2	Serine/threonine-protein kinase dst2	S170	1.872	1.801
Dst2	Serine/threonine-protein kinase dst2	S1128	2.807	1.805
DstD	Signal transducer and activator of transcription	S102	0.915	3.716
Dyrk1	Probable serine/threonine-protein kinase dyrk1	S743	2.335	3.641
Dyrk1	Probable serine/threonine-protein kinase dyrk1	S749	-2.080	2.624
ElmoE	ELMO domain-containing protein E	S1655	4.307	4.565
ElmoE	ELMO domain-containing protein E	S1664	2.225	4.100
			3.605	3.774
ElmoF	ELMO domain-containing protein F	S1094	2.346	2.760
Eps15	Epidermal growth factor receptor substrate 15 homologue	S412	2.785	2.206
FebA	Eukaryotic translation initiation factor 4E-1A-binding protein homologue	S22	3.329	1.670
FhkC	Probable serine/threonine-protein kinase fhkC	S579	2.401	3.441
Fkbp5	FK506-binding protein 5	T1501	1.987	2.612
ForA	Formin-A	S220	-1.329	2.581
ForA	Formin-A	S222	3.827	5.114
ForB	Formin-B	S15	5.024	4.795
ForE	Formin-E	S303	1.751	2.211
Fray2	Serine/threonine-protein kinase fray2	T587	3.999	2.074
GacG	Rho GTPase-activating protein gacG	S430	2.878	4.322
GacG	Rho GTPase-activating protein gacG	T515	2.840	2.444
GacI	Rho GTPase-activating protein gacI	S473	2.427	2.574
GacJ	Rho GTPase-activating protein gacJ	S743	3.283	3.228
GacL	Rho GTPase-activating protein gacL	S100	2.648	4.566
GacP	Rho GTPase-activating protein gacP	S487	1.083	4.855
GacU	Rho GTPase-activating protein gacU	S421	3.034	1.770
GacX	Rho GTPase-activating protein gacX	S9	-0.979	3.102
GbpC	Cyclic GMP-binding protein C	T2480	1.674	3.722
GefD	Ras guanine nucleotide exchange factor D	S374	1.943	8.634

GefE	Ras guanine nucleotide exchange factor E	T237	2.450	1.989
GefF	Ras guanine nucleotide exchange factor F	S92	-3.486	2.610
GefP	Ras guanine nucleotide exchange factor P	S519	3.897	1.614
GefQ	Ras guanine nucleotide exchange factor Q	S390	0.903	4.320
GefQ	Ras guanine nucleotide exchange factor Q	S460	0.911	2.295
GefR	Ras guanine nucleotide exchange factor R	S858	1.723	3.676
GefS	Ras guanine nucleotide exchange factor S	S370	-2.493	2.542
GefV	Ras guanine nucleotide exchange factor V	S518	-6.046	3.898
GflC	PHD zinc finger-containing protein	S583	3.993	1.991
GlcS	Glycogen [starch] synthase	S646	3.829	1.726
GlpV	Glycogen phosphorylase 1	T15	1.426	1.852
GrlE	Metabotropic glutamate receptor-like protein E	S770	-3.472	1.887
Gtf2f1	General transcription factor IIF subunit 1	S470	2.730	1.979
			3.976	1.577
GuaA	GMP synthase [glutamine-hydrolyzing]	S5	3.229	1.704
GxcDD	Guanine exchange factor for Rac 30	S373	1.267	2.760
GxcGG	Uncharacterised protein	S771	2.625	1.925
GxcM	Uncharacterised protein	S257	0.839	3.055
GxcZ	RhoGEF domain-containing protein	T806	3.285	3.760
H1	Histone H1	T127	1.479	2.593
Hbx5-1	Homeobox protein 5	S482	1.287	4.706
HdaA	Type-1 histone deacetylase 1	S415	3.149	3.762
HdaC	Type-2 histone deacetylase 2	T669	2.378	4.344
HspD	Heat shock cognate 90 kDa protein	S590	2.508	3.493
Impdh	Inosine-5'-monophosphate dehydrogenase	S453	2.849	4.759
Ipo13A	Importin-13 homologue A	S295	-3.285	1.843
Kif6	Kinesin-related protein 6	S1016	-3.723	5.439
KxcB	Kinase and exchange factor for Rac B	S26	6.120	5.429
KxcB	Kinase and exchange factor for Rac B	S280	1.574	1.809
KxcB	Kinase and exchange factor for Rac B	S307	1.046	2.498
LimD	LIM domain protein	S496	7.449	6.333
LimD	LIM domain protein	S507	2.407	4.783
LvsB	BEACH domain-containing protein lvsB	S1925	1.692	3.509
LvsF	BEACH domain-containing protein lvsF	S134	1.617	1.790
LysA	Uncharacterised protein	S847	3.550	1.747
MhcA	Myosin-2 heavy chain	S1636	1.698	2.054
MhcA	Myosin-2 heavy chain	T1835	1.373	2.365
MhkA	Myosin heavy chain kinase A	S517	1.789	2.433
MhkB	Myosin heavy chain kinase B	S335	1.312	3.387
MhkC	Myosin heavy chain kinase C	S367	2.383	5.507
MhkC	Myosin heavy chain kinase C	S373	1.810	3.355
MIP1	Uncharacterised protein	S279	1.901	3.937
MkcB	Probable serine/threonine-protein kinase mkcB	T338	4.341	1.646
MkkA	Mitogen-activated protein kinase kinase kinase A	T484	3.364	3.098
MlcR	Myosin regulatory light chain	S13	1.119	2.511
MlcR	Myosin regulatory light chain	S14	1.119	2.511
Mpl3	MAP kinase phosphatase with leucine-rich repeats protein 3	S279	0.643	2.550
MybZ	Myb-like protein Z	S662	2.826	3.441
MyoC	Myosin IC heavy chain	T341	-0.834	3.042
MyoE	Myosin IE heavy chain	S334	-3.608	1.858
NdrB	Probable serine/threonine-protein kinase ndrB	S521	1.454	5.029
Nog1	Probable nucleolar GTP-binding protein 1	S613	4.390	5.202

NudE	Lis-interacting protein	S290	1.038	3.989
PakF	Serine/threonine-protein kinase pakF	S242	2.807	3.827
PatA	Calcium-transporting ATPase PAT1	S990	4.705	2.203
Pcna	Proliferating cell nuclear antigen	S132	1.632	2.997
PctA	Ethanolamine-phosphate cytidylyltransferase	S194	2.943	4.670
PdeD	cGMP-dependent 3',5'-cGMP phosphodiesterase A	S149	2.890	1.770
Pds5	Sister chromatid cohesion protein PDS5 homologue	T88	4.579	1.735
PgmA	Phosphoglucomutase-1	T118	5.468	1.713
Phr	Sca1 complex protein phr	S50	5.578	5.999
PitB	Phosphatidylinositol transfer protein 2	T183	2.041	3.339
PkaC	cAMP-dependent protein kinase catalytic subunit	S434	-3.491	1.901
PspC	Prespore-specific protein	S1023	-1.816	1.942
PspC	Prespore-specific protein	S1026	-1.431	3.413
PtpA1-1	Tyrosine-protein phosphatase 1	S35	7.190	6.930
			1.345	5.594
pXi	Probable serine/threonine-protein kinase pXi	S584	2.069	2.403
Rab1A	Ras-related protein Rab-1A	T74	0.832	2.178
RacGAP	Uncharacterised protein	S538	3.235	1.831
RacGAP	Uncharacterised protein	S1346	2.189	1.990
Racgef1	Rac guanyl-nucleotide exchange factor	S620	3.296	3.918
Racgef1	Rac guanyl-nucleotide exchange factor	S1030	-1.503	4.010
Racgef1	Rac guanyl-nucleotide exchange factor	S1200	2.122	4.627
RblA	Retinoblastoma-like protein A	S1155	1.611	1.981
RdeA	Phosphorelay intermediate protein rdeA	S187	7.651	6.911
RdiA	Putative rho GDP-dissociation inhibitor 1	S21	0.700	2.740
Rfc1	Probable replication factor C subunit 1	S531	-3.033	3.179
Roco10	Probable inactive serine/threonine-protein kinase roco10	S232	-1.921	1.937
Roco5	Probable serine/threonine-protein kinase roco5	S190	4.055	4.432
Roco6	Probable serine/threonine-protein kinase roco6	S954	1.476	4.907
Roco6	Probable serine/threonine-protein kinase roco6	S977	0.802	2.245
Roco6	Probable serine/threonine-protein kinase roco6	S1302	2.268	3.902
Roco7	Probable serine/threonine-protein kinase roco7	S2609	1.525	2.690
Roco9	Probable serine/threonine-protein kinase roco9	S764	2.165	4.207
Roco9	Probable serine/threonine-protein kinase roco9	T3295	1.612	2.525
Rpl10	60S ribosomal protein L10	S104	1.907	4.332
Rpl6	60S ribosomal protein L6	T45	1.293	2.195
Rps11	40S ribosomal protein S11	S105	2.951	2.255
Rps3	40S ribosomal protein S3	S4	2.989	2.066
Rps3a	40S ribosomal protein S3a	S36	-1.388	2.363
RpsA	40S ribosomal protein SA	T2	1.771	3.584
Rrs1	Ribosome biogenesis regulatory protein homologue	S203	1.654	2.188
ScaA	Sca1 complex scaffold protein scaA	S359	-0.956	3.721
ScaA	Sca1 complex scaffold protein scaA	S920	2.026	3.194
SepA	Serine/threonine-protein kinase sepA	T587	6.023	5.574
SgcA	Guanylyl cyclase	S2752	-2.267	2.199
SgkC	Sphingosine kinase related protein	S235	5.658	5.979
SibD	Integrin beta-like protein D	Y163	1.377	2.201
SvkA	Serine/threonine-protein kinase svkA	S318	1.369	1.985
Top2	Probable DNA topoisomerase 2	S1474	1.797	3.127
Top2	Probable DNA topoisomerase 2	S1475	1.555	3.081
Tor	Serine/threonine-protein kinase tor	S2282	3.782	5.798
TrfA	General transcriptional corepressor trfA	S852	4.872	1.979

TrfA	General transcriptional corepressor trfA	T1239	2.561	2.089
TrfA	General transcriptional corepressor trfA	S1294	1.113	2.360
TupA	General transcriptional corepressor tupA	S87	1.706	5.436
UppA	UTP--glucose-1-phosphate uridylyltransferase 1	S21	-5.338	6.407
VacA	Vacuolin-A	T9	-5.236	5.475
VilA	Villidin	S648	1.128	2.345
Vps13F	Putative vacuolar protein sorting-associated protein 13F	S3313	4.761	4.670
Vps28	Vacuolar protein sorting-associated protein 28	S78	6.306	6.889
Vps51	Vacuolar protein sorting-associated protein 51 homologue	S795	1.716	2.179
Wdr91	WD repeat-containing protein 91 homologue	S280	-1.310	2.125

Table 7.3. Significant phosphorylation status changes in 8Br-cGMP treated Ax3 cells. Significance was calculated using a combination of the T-test P-value and the fold-change, where the smaller the fold change the smaller the P-value had to be to be declared significance. The output of this is the q-value.

7.6 Microscope image processing and *Dictyostelium* GFP-atg8 puncta quantification script

```
//select directories

dir1 = getDirectory("Choose Source Directory ");

dir2 = getDirectory("Choose Destination Directory - Max Projections");

dir3 = getDirectory("Choose Destination Directory - Initial JPEG");

dir4 = getDirectory("Choose Destination Directory - Results");

//save library as individual tiffs

ids=newArray(nImages);

for (i=0;i<nImages;i++) {

    selectImage(i+1);

    title = getTitle;

    print(title);

    ids[i]=getImageID;

    saveAs("tiff", dir1+title);

}

run("Close All");

//batch process to generate Max Projections and PNGs

list = getFileList(dir1);

setBatchMode(true);

for (i=0; i<list.length; i++) {

        showProgress(i+1, list.length);

        filename = dir1 + list[i];

        if (endsWith(filename, "tif")) {

                open(filename);

                Stack.setChannel(1);

                run("Grays");

                setMinAndMax(500, 10000);
```

```
        run("Z Project...", "projection=[Max Intensity] all");

        saveAs("TIFF", dir2+"MAX "+ list[i]);

        run("Green");

        saveAs("PNG", dir3+"MAX "+ list[i]);

        close();

        close();

    }

}

//Automated dot counting

list = getFileList(dir2);

setBatchMode(true);

for (i=0; i<list.length; i++) {

        showProgress(i+1, list.length);

        filename = dir2 + list[i];

        if (endsWith(filename, "tif")) {

                open(filename);

                //cell segmentation

                run("Duplicate...", " ");

                run("Auto Threshold", "method=Triangle white");

                run("Despeckle");

                run("Remove Outliers...", "radius=10 threshold=50 which=Bright");

                run("Analyze Particles...", "size=50-Infinity show=Masks exclude add in_situ");

                roiManager("Deselect");

                roiManager("Delete");

                run("Fill Holes");

                run("Mean...", "radius=10");

                run("Make Binary");
```

162

```
run("Watershed");

run("Analyze Particles...", "size=60-Infinity show=Masks exclude add in_situ");

saveAs("Tiff", dir4+list[i]+"mask_only");

close();

roiManager("Show All with labels");

saveAs("Tiff", dir4+list[i]+"_original_mask");

run("Clear Results");

//dot counting per ROI

function scaleROI(factor) {

        type = selectionType();

        getSelectionCoordinates(x, y);

        for (i1 = 0; i1 < x.length; i1++) {

                x[i1] = x[i1];

                y[i1] = y[i1];

        }

        makeSelection(type, x, y);

        run("Find Maxima...", "noise=1250 output=Count exclude");

        saveAs("Results", dir4+list[i]+".txt");

}

factor = ("1");

count = roiManager("count");

current = roiManager("index");

for (i2 = 0; i2 < count; i2++) {

        roiManager("select", i2);

        scaleROI(factor);

        roiManager("update");

}
```

```
            if (current < 0)

            roiManager("deselect");

            else

            roiManager("select", current);

            close();

            roiManager("Deselect");

            roiManager("Delete");

      }

}



            if (current < 0)



            roiManager("deselect");
```

7.7 Image processing script for *de novo* autophagosome formation and lifetime tracking

```
//IMAGES SHOULD BE RENAMED BEFORE STARTING SO THERE ARE NO FULL STOPS

//images should be tiffs

open();

//Variables to retain file directory pathway and filename for the image opened

MainFile = File.directory+File.name;

MainDirectory = File.directory

setMinAndMax(1000, 9000);

run("Brightness/Contrast...");

run("Manual Tracking");

waitForUser("Track cells - full timecourse only");

waitForUser("Select 'Overlay Dots and Lines' option");

TitleA = getTitle();

TitleB = replace(TitleA, ".tif", "");

TitleC = replace(TitleB, "Overlay Dots & Lines ", "");

TitleD = TitleC+" Overlay Dots & Lines"

saveAs("Tiff", MainDirectory+TitleD);

wait(100);

close();

BoxSize = getNumber("Define box size", 300);

BoxSizeHalf = BoxSize/2

TimeStart = getNumber("Start time in seconds", 300);

TimeInterval = getNumber("Acquisition interval in seconds", 5);

title = getTitle

title2 = replace(title, ".tif", "");

print(title);

print(title2);
```

```
Table.rename("Results from "+title2+" in µm per sec", "Results");

getDimensions(width, height, channels, slices, frames);

results = nResults();

CellCount = nResults()/frames;

run("Revert");

for(i=0;i<CellCount;i++) {

        print("image_"+i+1);

        //Activate line below to define box size for each cell

        //BoxSize = getNumber("Define box size", 300);

        for(i2=0;i2<frames;i2++) {

                setSlice(i2+1);

                X = getResult("X",i2+(i*frames));

                Y = getResult("Y",i2+(i*frames));

                makeRectangle(X-(BoxSize/2), Y-(BoxSize/2), BoxSize, BoxSize);

                run("Duplicate...", " ");

                rename("Slice"+i2+1);

                selectWindow(title);

        }

        selectWindow(title);

        close();

        run("Images to Stack", "method=[Copy (center)] name=Stack title=[] use");

        //add timelapse

        setForegroundColor(255, 255, 255);

        run("Label...", "format=00:00 starting="+TimeStart+" interval="+TimeInterval+" x=5 y=20 font=24
text=[(mm:ss)] range=1-"+results+" use");

        saveAs("Tiff", MainFile+"_cell"+(i+1));

        close();
```

166

```
        wait(100);

        open(MainFile);

}

close();

selectWindow("Results");

saveAs("Results", MainFile+"Coordinates.txt");

run("Clear Results");

close("Results");

waitForUser("Close Tracking window");
```

References

Abeliovich, H., Dunn, W.A., Kim, J. and Klionsky, D.J. (2000), "Dissection of autophagosome biogenesis into distinct nucleation and expansion steps", *Journal of Cell Biology*, Vol. 151 No. 5, pp. 1025–1033.

Al-Maslamani, N.A., Khilan, A.A. and Horn, H.F. (2021), "Design of a 3D printed, motorized, uniaxial cell stretcher for microscopic and biochemical analysis of mechanotransduction", *Biology Open*, Vol. 10 No. 2, available at:https://doi.org/10.1242/bio.057778.

Allen, R.D. and Naitoh, Y. (2002), "Osmoregulation and contractile vacuoles of protozoa", *International Review of Cytology*, Vol. 215, pp. 351–378.

Ando, J. and Yamamoto, K. (2013), "Flow detection and calcium signalling in vascular endothelial cells", *Cardiovascular Research*, Vol. 99 No. 2, pp. 260–268.

Angelone, T., Quintieri, A.M., Pasqua, T., Filice, E., Cantafio, P., Scavello, F., Rocca, C., *et al.* (2015), "The NO stimulator, Catestatin, improves the Frank-Starling response in normotensive and hypertensive rat hearts", *Nitric Oxide-Biology and Chemistry*, Vol. 50, pp. 10–19.

Araki, T., van Egmond, W.N., van Haastert, P.J.M. and Williams, J.G. (2010), "Dual regulation of a Dictyostelium STAT by cGMP and Ca2+ signalling", *Journal of Cell Science*, Vol. 123 No. 6, pp. 837–841.

Araki, T., Tsujioka, M., Abe, T., Fukuzawa, M., Meima, M., Schaap, P., Morio, T., *et al.* (2003), "A STAT-regulated, stress-induced signalling pathway in Dictyostelium", *Journal of Cell Science*, Vol. 116 No. 14, pp. 2907–2915.

Araki, T., Vu, L.H., Sasaki, N., Kawata, T., Eichinger, L. and Williams, J.G. (2014), "Two Dictyostelium tyrosine kinase-like kinases function in parallel, stress-induced STAT activation pathways", *Molecular Biology of the Cell*, Vol. 25 No. 20, pp. 3222–3233.

Bacabac, R.G., Smit, T.H., Mullender, M.G., Dijcks, S.J., Van Loon, J.J.W.. and Klein-Nulend, J. (2004), "Nitric oxide production by bone cells is fluid shear stress rate dependent", *Biochemical and Biophysical Research Communications*, Vol. 315 No. 4, pp. 823–829.

Bader, S., Kortholt, A. and van Haastert, P.J.M. (2007), "Seven Dictyostelium discoideum phosphodiesterases degrade three pools of cAMP and cGMP", *Biochemical Journal*, Vol. 402 No. 1, pp. 153–161.

Bateman, A. (2019), "UniProt: A worldwide hub of protein knowledge", *Nucleic Acids Research*, Oxford University Press, Vol. 47 No. D1, pp. D506–D515.

Beaurivage, C., Naumovska, E., Chang, Y., Elstak, E., Nicolas, A., Wouters, H., van Moolenbroek, G., *et al.* (2019), "Development of a Gut-on-a-Chip Model for High Throughput Disease Modeling and Drug Discovery", *International Journal of Molecular Sciences*, Vol. 20 No. 22, p. 5661.

Beloussov, L. V. (1980), "The role of tensile fields and contact cell polarization in the morphogenesis of amphibian axial rudiments", *Wilhelm Roux's Archives of Developmental Biology*, Vol. 188 No. 1, pp. 1–7.

Beloussov, L.V., Lakirev, A.V. and Naumidi, I.I. (1988), "The role of external tensions in differentiation of Xenopus laevis embryonic tissues", *Cell Differentiation and Development*, Vol. 25 No. 3, pp. 165–176.

Berlot, C.H., Devreotes, P.N. and Spudich, J.A. (1987), "Chemoattractant-elicited increases in Dictyostelium myosin phosphorylation are due to changes in myosin localization and increases in kinase activity.", *Journal of Biological Chemistry*, Vol. 262 No. 8, pp. 3918–3926.

Berlot, C.H., Spudich, J.A. and Devreotes, P.N. (1985), "Chemoattractant-elicited increases in myosin phosphorylation in Dictyostelium", *Cell*, Vol. 43, pp. 307–314.

Blawat, K., Mayr, A., Hardt, M., Kirschneck, C., Nokhbehsaim, M., Behl, C., Deschner, J., *et al.* (2020), "Regulation of autophagic signaling by mechanical loading and inflammation in human PDL fibroblasts", *International Journal of Molecular Sciences*, Vol. 21 No. 24, pp. 1–15.

Bloomfield, G., Tanaka, Y., Skelton, J., Ivens, A. and Kay, R.R. (2008), "Widespread duplications in the genomes of laboratory stocks of Dictyostelium discoideum", *Genome Biology*, Vol. 9 No. 4, available at:https://doi.org/10.1186/gb-2008-9-4-r75.

Bloomfield, G., Traynor, D., Sander, S.P., Veltman, D.M., Pachebat, J.A. and Kay, R.R. (2015), "Neurofibromin controls macropinocytosis and phagocytosis in Dictyostelium", *ELife*, Vol. 4, available at:https://doi.org/10.7554/eLife.04940.

Borcherding, D.C., Tong, W., Hugo, E.R., Barnard, D.F., Fox, S., LaSance, K., Shaughnessy, E., *et al.* (2016), "Expression and Therapeutic Targeting of Dopamine Receptor-1 (D1R) in Breast Cancer", *Oncogene*, Vol. 35 No. 24, pp. 3103–3113.

Bosgraaf, L. and van Haastert, P.J.M. (2003), "Roc, a Ras/GTPase domain in complex proteins", *Biochimica et Biophysica Acta - Molecular Cell Research*, Vol. 1643, pp. 5–10.

Bosgraaf, L., Russcher, H., Smith, J.L., Wessels, D., Soll, D.R. and van Haastert, P.J.M. (2002), "A novel cGMP signalling pathway mediating myosin phosphorylation and chemotaxis in Dictyostelium", *EMBO Journal*, Vol. 21 No. 17, pp. 4560–4570.

Boulter, E. and Féral, C.C. (2021), "Cyclic uniaxial cell stretching in tissue culture using a LEGO®-based mechanical stretcher and a polydimethylsiloxane stretchable vessel", *STAR Protocols*, Vol. 2 No. 2, p. 100437.

Bradley, J.M.B., Kelley, M.J., Rose, A. and Acott, T.S. (2003), "Signaling Pathways Used in Trabecular Matrix Metalloproteinase Response to Mechanical Stretch", *Investigative Ophthalmology and Visual Science*, Vol. 44 No. 12, pp. 5174–5181.

Bredt, D.S. and Snyder, S.H. (1990), "Isolation of nitric oxide synthetase, a calmodulin-requiring enzyme", *Proceedings of the National Academy of Sciences of the United States of America*, Vol. 87 No. 2, pp. 682–685.

Breuls, R.G.M., Bouten, C.V.C., Oomens, C.W.J., Bader, D.L. and Baaijens, F.P.T. (2003), "Compression Induced Cell Damage in Engineered Muscle Tissue: An In Vitro Model to Study Pressure Ulcer Aetiology", *Annals of Biomedical Engineering*, Vol. 31 No. 11, pp. 1357–1364.

Brzostowski, J.A., Fey, P., Yan, J., Isik, N. and Jin, T. (2009), "The Elmo family forms an ancient group of actin-regulating proteins", *Communicative and Integrative Biology*, Vol. 2 No. 4, pp. 337–340.

Buchberger, A., Bukau, B. and Sommer, T. (2010), "Protein Quality Control in the Cytosol and the Endoplasmic Reticulum: Brothers in Arms", *Molecular Cell*, Elsevier Inc., Vol. 40 No. 2, pp. 238–252.

Buckley, C.M., Gopaldass, N., Bosmani, C., Johnston, S.A., Soldati, T., Insall, R.H. and King, J.S. (2016), "WASH drives early recycling from macropinosomes and phagosomes to maintain surface phagocytic receptors", *Proceedings of the National Academy of Sciences*, Vol. 113 No. 40, pp. E5906–E5915.

Burger, E.H. and Klein-Nulend, J. (1999), "Mechanotransduction in bone--role of the lacuno-canalicular network.", *FASEB Journal : Official Publication of the Federation of American Societies for Experimental Biology*, Vol. 13 Suppl, pp. S101-12.

Burridge, K. and Chrzanowska-Wodnicka, M. (1996), "FOCAL ADHESIONS, CONTRACTILITY, AND SIGNALING", *Annual Review of Cell and Developmental Biology*, Vol. 12 No. 1, pp. 463–519.

Bush, J., Franek, K., Daniel, J., Spiegelman, G.B., Weeks, G. and Cardelli, J. (1993), "Cloning and characterization of five novel Dictyostelium discoideum rab-related genes", *Gene*, Vol. 136 No. 1–2, pp. 55–60.

Calvo-Garrido, J., Carilla-Latorre, S., Kubohara, Y., Santos-Rodrigo, N., Mesquita, A., Soldati, T., Golstein, P., *et al.* (2010), "Autophagy in Dictyostelium: Genes and pathways, cell death and infection", *Autophagy*, Vol. 6 No. 6, pp. 686–701.

Calvo-Garrido, J., Carilla-Latorre, S., Lázaro-Diéguez, F., Egea, G. and Escalante, R. (2008), "Vacuole Membrane Protein 1 Is an Endoplasmic Reticulum Protein Required for Organelle Biogenesis, Protein Secretion, and Development", edited by Barr, F.A.*Molecular Biology of the Cell*, Vol. 19 No. 8, pp. 3442–3453.

Calvo-Garrido, J., King, J.S., Munoz-Braceras, S. and Escalante, R. (2014), "Vmp1 Regulates PtdIns3P Signaling During Autophagosome Formation in Dictyostelium discoideum", *Traffic*, Vol. 15 No. 11, pp. 1235–1246.

Calvo-Garrido, J., King, J.S., Muñoz-Braceras, S. and Escalante, R. (2014), "Vmp1 Regulates PtdIns3P Signaling During Autophagosome Formation in Dictyostelium discoideum", *Traffic*, Vol. 15 No. 11, pp.

1235–1246.

Cardenal-Muñoz, E., Arafah, S., López-Jiménez, A.T., Kicka, S., Falaise, A., Bach, F., Schaad, O., *et al.* (2017), "Mycobacterium marinum antagonistically induces an autophagic response while repressing the autophagic flux in a TORC1- and ESX-1-dependent manner", edited by Lewinsohn, D.M.*PLOS Pathogens*, Vol. 13 No. 4, p. e1006344.

Carnell, M., Zech, T., Calaminus, S.D., Ura, S., Hagedorn, M., Johnston, S.A., May, R.C., *et al.* (2011), "Actin polymerization driven by WASH causes V-ATPase retrieval and vesicle neutralization before exocytosis", *Journal of Cell Biology*, Vol. 193 No. 5, pp. 831–839.

Casadei, B. and Sears, C.E. (2003), "Nitric-oxide-mediated regulation of cardiac contractility and stretch responses", *Progress in Biophysics and Molecular Biology*, Vol. 82 No. 1–3, pp. 67–80.

Castro, L.R.V., Schittl, J. and Fischmeister, R. (2010), "Feedback control through cGMP-dependent protein kinase contributes to differential regulation and compartmentation of cGMP in rat cardiac myocytes", *Circulation Research*, Vol. 107 No. 10, pp. 1232–1240.

Chan, E.Y.W., Kir, S. and Tooze, S.A. (2007), "siRNA screening of the kinome identifies ULK1 as a multidomain modulator of autophagy", *Journal of Biological Chemistry*, Vol. 282 No. 35, pp. 25464–25474.

Chan, E.Y.W., Longatti, A., McKnight, N.C. and Tooze, S.A. (2009), "Kinase-Inactivated ULK Proteins Inhibit Autophagy via Their Conserved C-Terminal Domains Using an Atg13-Independent Mechanism", *Molecular and Cellular Biology*, Vol. 29 No. 1, pp. 157–171.

Chang, Y.-Y. and Neufeld, T.P. (2009), "An Atg1/Atg13 Complex with Multiple Roles in TOR-mediated Autophagy Regulation", edited by Schmid, S.L.*Molecular Biology of the Cell*, Vol. 20 No. 7, pp. 2004–2014.

Charest, P.G., Shen, Z., Lakoduk, A., Sasaki, A.T., Briggs, S.P. and Firtel, R.A. (2010), "A ras signaling complex controls the RasC-TORC2 pathway and directed cell migration", *Developmental Cell*, Elsevier Ltd, Vol. 18 No. 5, pp. 737–749.

Chen, C.L., Wang, Y., Sesaki, H. and Iijima, M. (2012), "Myosin I links PIP3 signaling to remodeling of the actin cytoskeleton in chemotaxis", *Science Signaling*, Vol. 5 No. 209, pp. 1–10.

Chen, P., Ostrow, B.D., Tafuri, S.R. and Chisholm, R.L. (1994), "Targeted disruption of the Dictyostelium RMLC gene produces cells defective in cytokinesis and development", *The Journal of Cell Biology*, Vol. 127 No. 6, pp. 1933–1944.

Chen, S.A., Zhou, L., Zhang, Y., Leng, Y., Pei, X.Y., Lin, H., Jones, R., *et al.* (2014), "Targeting SQSTM1/p62 Induces Cargo Loading Failure and Converts Autophagy to Apoptosis via NBK/Bik", *Molecular and Cellular Biology*, Vol. 34 No. 18, pp. 3435–3449.

Cheng, G., Tse, J., Jain, R.K. and Munn, L.L. (2009), "Micro-environmental mechanical stress controls tumor spheroid size and morphology by suppressing proliferation and inducing apoptosis in cancer cells", *PLoS ONE*, Vol. 4 No. 2, available at:https://doi.org/10.1371/journal.pone.0004632.

Cheong, H., Yorimitsu, T., Reggiori, F., Legakis, J.E., Wang, C.-W. and Klionsky, D.J. (2005), "Atg17 Regulates the Magnitude of the Autophagic Response", *Molecular Biology of the Cell*, Vol. 16 No. 7, pp. 3438–3453.

Chiu, J.-J., Wang, D.L., Chien, S., Skalak, R. and Usami, S. (1998), "Effects of Disturbed Flow On Endothelial Cells", *Journal of Biomechanical Engineering-Transactions of the Asme*, Vol. 120 No. 1, pp. 2–8.

Chung, C.Y., Lee, S., Briscoe, C., Ellsworth, C. and Firtel, R.A. (2000a), "Role of Rac in controlling the actin cytoskeleton and chemotaxis in motile cells", *Proceedings of the National Academy of Sciences of the United States of America*, Vol. 97 No. 10, pp. 5225–5230.

Chung, C.Y., Lee, S., Briscoe, C., Ellsworth, C. and Firtel, R.A. (2000b), "Role of Rac in controlling the actin cytoskeleton and chemotaxis in motile cells", *Proceedings of the National Academy of Sciences of the United States of America*, Vol. 97 No. 10, pp. 5225–5230.

Clancy, C.E., Mendoza, M.G., Naismith, T. V., Kolman, M.F. and Egelhoff, T.T. (1997), "Identification of a protein kinase from Dictyostelium with homology to the novel catalytic domain of myosin heavy chain kinase A", *Journal of Biological Chemistry*, Vol. 272 No. 18, pp. 11812–11815.

Clarke, M. and Spudich, J.A. (1974), "Biochemical and structural studies of actomyosin-like proteins from non-muscle cells. Isolation and characterization of myosin from amoebae of Dictyostelium discoideum", *Journal of Molecular Biology*, Vol. 86, pp. 209–222.

Coste, B., Mathur, J., Schmidt, M., Earley, T.J., Ranade, S., Petrus, M.J., Dubin, A.E., *et al.* (2010), "Piezo1 and Piezo2 are essential components of distinct mechanically-activated cation channels", *Science*, Vol. 330 No. 6000, pp. 55–60.

Côté, G.P. and Bukiejko, U. (1987), "Purification and Characterization of Myosin II Heavy Chain Kinase A from Dictyostelium", *The Journal of Biological Chemistry*, Vol. 262 No. 3, pp. 1065–1072.

Cox, C.D., Bae, C., Ziegler, L., Hartley, S., Nikolova-Krstevski, V., Rohde, P.R., Ng, C.A., *et al.* (2016), "Removal of the mechanoprotective influence of the cytoskeleton reveals PIEZO1 is gated by bilayer tension", *Nature Communications*, Nature Publishing Group, Vol. 7, pp. 1–13.

Cuervo, A.M. and Dice, J.F. (2000), "Regulation of Lamp2a levels in the lysosomal membrane", *Traffic*, Vol. 1 No. 7, pp. 570–583.

Dafre, A.L., Schmitz, A.E. and Maher, P. (2019), "Hyperosmotic Stress Initiates AMPK-Independent Autophagy and AMPK- And Autophagy-Independent Depletion of Thioredoxin 1 and Glyoxalase 2 in HT22 Nerve Cells", *Oxidative Medicine and Cellular Longevity*, Hindawi, Vol. 2019, available

at:https://doi.org/10.1155/2019/2715810.

Dardik, A., Chen, L., Frattini, J., Asada, H., Aziz, F., Kudo, F.A. and Sumpio, B.E. (2005), "Differential effects of orbital and laminar shear stress on endothelial cells", *Journal of Vascular Surgery*, Vol. 41 No. 5, pp. 869–880.

Das, J., Maji, S., Agarwal, T., Chakraborty, S. and Maiti, T.K. (2018), "Hemodynamic shear stress induces protective autophagy in HeLa cells through lipid raft-mediated mechanotransduction", *Clinical and Experimental Metastasis*, Springer Netherlands, Vol. 35 No. 3, pp. 135–148.

Davies, P.F. (1995), "Flow-mediated endothelial mechanotransduction", *Physiological Reviews*, Vol. 75 No. 3, pp. 519–560.

Décavé, E., Rieu, D., Dalous, J., Fache, S., Bréchet, Y., Fourcade, B., Satre, M., *et al.* (2003), "Shear flow-induced motility of Dictyostelium discoideum cells on solid substrate", *Journal of Cell Science*, Vol. 116 No. 21, pp. 4331–4343.

DeMali, K.A., Sun, X. and Bui, G.A. (2014), "Force Transmission at Cell–Cell and Cell–Matrix Adhesions", *Biochemistry*, Vol. 53 No. 49, pp. 7706–7717.

Dembinsky, A., Rubin, H. and Ravid, S. (1996), "Chemoattractant-mediated increases in cGMP induce changes in Dictyostelium myosin II heavy chain-specific protein kinase C activities", *Journal of Cell Biology*, Vol. 134 No. 4, pp. 911–921.

Deng, Y., Davis, S.P., Yang, F., Paulsen, K.S., Kumar, M., Sinnott DeVaux, R., Wang, X., *et al.* (2017), "Inertial Microfluidic Cell Stretcher (iMCS): Fully Automated, High-Throughput, and Near Real-Time Cell Mechanotyping", *Small*, Vol. 13 No. 28, available at:https://doi.org/10.1002/smll.201700705.

Dewey, C.F., Bussolari, S.R., Gimbrone, M.A. and Davies, P.F. (1981), "The dynamic response of vascular endothelial cells to fluid shear stress", *Journal of Biomechanical Engineering*, Vol. 103 No. 3, pp. 177–185.

Di-Luoffo, M., Ben-Meriem, Z., Lefebvre, P., Delarue, M. and Guillermet-Guibert, J. (2021), "PI3K functions as a hub in mechanotransduction", *Trends in Biochemical Sciences*, Vol. 46 No. 11, pp. 878–888.

Di-Luoffo, M., Delarue, M. and Guillermet-Guibert, J. (2021), *The Biomechanical Context Influences the Output Signaling, Independently of PIK3CA Mutations in Breast Cancer Cells*, available at:https://doi.org/https://doi.org/10.1101/2021.10.18.464825.

Dong, G., Yang, S., Cao, X., Yu, N., Yu, J. and Qu, X. (2017), "Low shear stress-induced autophagy alleviates cell apoptosis in HUVECs", *Molecular Medicine Reports*, Vol. 15 No. 5, pp. 3076–3082.

Durner, J., Wendehenne, D. and Klessig, D.F. (1998), "Defense gene induction in tobacco by nitric oxide, cyclic GMP, and cyclic ADP-ribose", *Proceedings of the National Academy of Sciences of the United*

States of America, Vol. 95 No. 17, pp. 10328–10333.

De Duve, C. and Wattiaux, R. (1966), "Functions of Lysosomes", *Annu. Rev. Physiol.*, Vol. 28, pp. 435–492.

East, M.P., Bowzard, J.B., Dacks, J.B. and Kahn, R.A. (2012), "ELMO domains, evolutionary and functional characterization of a novel GTPase-activating protein (GAP) domain for Arf protein family GTPases", *Journal of Biological Chemistry*, Vol. 287 No. 47, pp. 39538–39553.

Edelstein, A., Amodaj, N., Hoover, K., Vale, R. and Stuurman, N. (2010), "Computer control of microscopes using μManager", *Current Protocols in Molecular Biology*, Vol. 92 No. 1, pp. 14.20.1-14.20.17.

Edelstein, A.D., Tsuchida, M.A., Amodaj, N., Pinkard, H., Vale, R.D. and Stuurman, N. (2014), "Advanced methods of microscope control using μManager software", *Journal of Biological Methods*, Vol. 1 No. 2, p. 10.

Egan, D.F., Shackelford, D.B., Mihaylova, M.M., Gelino, S., Kohnz, R.A., Mair, W., Vasquez, D.S., *et al.* (2011), "Phosphorylation of ULK1 (hATG1) by AMP-activated protein kinase connects energy sensing to mitophagy", *Science*, Vol. 331 No. 6016, pp. 456–461.

Egelhoff, T.T., Lee, R.J. and Spudich, J.A. (1993), "Dictyostelium myosin heavy chain phosphorylation sites regulate myosin filament assembly and localization in vivo", *Cell*, Vol. 75 No. 2, pp. 363–371.

van Egmond, W.N., Kortholt, A., Plak, K., Bosgraaf, L., Bosgraaf, S., Keizer-Gunnink, I. and van Haastert, P.J.M. (2008), "Intramolecular activation mechanism of the Dictyostelium LRRK2 homolog Roco protein GbpC", *Journal of Biological Chemistry*, Vol. 283 No. 44, pp. 30412–30420.

Ehrenman, K., Yang, G., Hong, W.P., Gao, T., Jang, W., Brock, D.A., Hatton, R.D., *et al.* (2004), "Disruption of Aldehyde Reductase Increases Group Size in Dictyostelium", *Journal of Biological Chemistry*, Â© 2004 ASBMB. Currently published by Elsevier Inc; originally published by American Society for Biochemistry and Molecular Biology., Vol. 279 No. 2, pp. 837–847.

Eichinger, L., Pachebat, J.A., Glöckner, G. and Rajandream, M. (2005), "The genome of the social amoeba", *Nature*, Vol. 57 No. May, pp. 43–57.

Fetah, K.L., DiPardo, B.J., Kongadzem, E., Tomlinson, J.S., Elzagheid, A., Elmusrati, M., Khademhosseini, A., *et al.* (2019), "Cancer Modeling-on-a-Chip with Future Artificial Intelligence Integration", *Small*, Vol. 15 No. 50, p. 1901985.

Fok, A.K., Clarke, M., Ma, L. and Allen, R.D. (1993), "Vacuolar H(+)-ATPase of Dictyostelium discoideum. A monoclonal antibody study.", *Journal of Cell Science*, Vol. 106 (Pt 4, pp. 1103–13.

Francis, S.H., Busch, J.L. and Corbin, J.D. (2010), "cGMP-dependent protein kinases and cGMP phosphodiesterases in nitric oxide and cGMP action", *Pharmacological Reviews*, Vol. 62 No. 3, pp. 525–563.

Fujii, S., Mitsunaga, S., Yamazaki, M., Hasebe, T., Ishii, G., Kojima, M., Kinoshita, T., *et al.* (2008), "Autophagy is activated in pancreatic cancer cells and correlates with poor patient outcome", *Cancer Science*, Vol. 99 No. 9, pp. 1813–1819.

Fujita, N., Itoh, T., Omori, H., Fukuda, M., Noda, T. and Yoshimori, T. (2008), "The Atg16L Complex Specifies the Site of LC3 Lipidation for Membrane Biogenesis in Autophagy", edited by Riezman, H. *Molecular Biology of the Cell*, Vol. 19 No. 5, pp. 2092–2100.

Fukui, Y., Lynch, T.J., Brzeska, H. and Korn, E.D. (1989), "Myosin I is located at the leading edges of locomoting Dictyostelium amoebae", *Nature*, Vol. 341 No. 6240, pp. 328–331.

Fukuzawa, M., Araki, T., Adrian, I. and Williams, J.G. (2001), "Tyrosine phosphorylation-independent nuclear translocation of a Dictyostelium STAT in response to DIF signaling", *Molecular Cell*, Vol. 7 No. 4, pp. 779–788.

Funakoshi, T., Matsuura, A., Noda, T. and Ohsumi, Y. (1997), "Analyses of APG13 gene involved in autophagy in yeast, Saccharomyces cerevisiae", *Gene*, Vol. 192 No. 2, pp. 207–213.

Furuya, N., Yu, J., Byfield, M., Pattingre, S. and Levine, B. (2005), "The evolutionarily conserved domain of Beclin 1 is required for Vps34 binding, autophagy and tumor suppressor function.", *Autophagy*, Vol. 1 No. 1, pp. 46–52.

Gabriel, D., Hacker, U., Köhler, J., Müller-Taubenberger, A., Schwartz, J.M., Westphal, M. and Gerisch, G. (1999), "The contractile vacuole network of Dictyostelium as a distinct organelle: its dynamics visualized by a GFP marker protein.", *Journal of Cell Science*, Vol. 112 (Pt 2, pp. 3995–4005.

Ganley, I.G., Lam, D.H., Wang, J., Ding, X., Chen, S. and Jiang, X. (2009), "ULK1·ATG13·FIP200 complex mediates mTOR signaling and is essential for autophagy", *Journal of Biological Chemistry*, Vol. 284 No. 18, pp. 12297–12305.

Gawlitta, D., Li, W., Oomens, C.W.J., Baaijens, F.P.T., Bader, D.L. and Bouten, C.V.C. (2007), "The relative contributions of compression and hypoxia to development of muscle tissue damage: An In vitro study", *Annals of Biomedical Engineering*, Vol. 35 No. 2, pp. 273–284.

Geiger, B., Spatz, J.P. and Bershadsky, A.D. (2009), "Environmental sensing through focal adhesions", *Nature Reviews Molecular Cell Biology*, Vol. 10 No. 1, pp. 21–33.

Geiler-Samerotte, K.A., Dion, M.F., Budnik, B.A., Wang, S.M., Hartl, D.L. and Drummond, D.A. (2011), "Misfolded proteins impose a dosage-dependent fitness cost and trigger a cytosolic unfolded protein response in yeast", *Proceedings of the National Academy of Sciences of the United States of America*, Vol. 108 No. 2, pp. 680–685.

Geng, J. and Klionsky, D.J. (2008), "The Atg8 and Atg12 ubiquitin-like conjugation systems in macroautophagy", *EMBO Reports*, Vol. 9 No. 9, pp. 859–864.

Gerald, N.J., Siano, M. and De Lozanne, A. (2002), "The Dictyostelium LvsA Protein is Localized on the Contractile Vacuole and is Required for Osmoregulation", *Traffic*, Vol. 3 No. 1, pp. 50–60.

Gerisch, G., Heuser, J. and Clarke, M. (2002), "Tubular-vesicular transformation in the contractile vacuole system of Dictyostelium", *Cell Biology International*, Vol. 26 No. 10, pp. 845–852.

Glöckner, G., Lawal, H.M., Felder, M., Singh, R., Singer, G., Weijer, C.J. and Schaap, P. (2016), "The multicellularity genes of dictyostelid social amoebas", *Nature Communications*, Vol. 7 No. May, pp. 1–11.

Gnad, F., Ren, S., Cox, J., Olsen, J. V., Macek, B., Oroshi, M. and Mann, M. (2007), "PHOSIDA (phosphorylation site database): Management, structural and evolutionary investigation, and prediction of phosphosites", *Genome Biology*, Vol. 8 No. 11, available at:https://doi.org/10.1186/gb-2007-8-11-r250.

Goldberg, J.M., Bosgraaf, L., van Haastert, P.J.M. and Smith, J.L. (2002), "Identification of four candidate cGMP targets in Dictyostelium", *Proceedings of the National Academy of Sciences of the United States of America*, Vol. 99 No. 10, pp. 6749–6754.

Goldberg, J.M., Wolpin, E.S., Bosgraaf, L., Clarkson, B.K., van Haastert, P.J.M. and Smith, J.L. (2006), "Myosin light chain kinase A is activated by cGMP-dependent and cGMP-independent pathways", *FEBS Letters*, Vol. 580 No. 8, pp. 2059–2064.

Grierson, J.P. and Meldolesi, J. (1995), "Shear stress-induced [Ca2+](i) transients and oscillations in mouse fibroblasts are mediated by endogenously released ATP", *Journal of Biological Chemistry*, Vol. 270 No. 9, pp. 4451–4456.

Griffith, L.M., Downs, S.M. and Spudich, J.A. (1987), "Myosin light chain kinase and myosin light chain phosphatase from Dictyostelium: Effects of reversible phosphorylation on myosin structure and function", *Journal of Cell Biology*, Vol. 104 No. 5, pp. 1309–1323.

Grønlien, H.K., Stock, C., Aihara, M.S., Allen, R.D. and Naitoh, Y. (2002), "Relationship between the membrane potential of the contractile vacuole complex and its osmoregulatory activity in Paramecium multimicronucleatum", *Journal of Experimental Biology*, Vol. 205 No. 20, pp. 3261–3270.

Grumati, P., Coletto, L., Schiavinato, A., Castagnaro, S., Bertaggia, E., Sandri, M. and Bonaldo, P. (2011), "Physical exercise stimulates autophagy in normal skeletal muscles but is detrimental for collagen VI-deficient muscles", *Autophagy*, Vol. 7 No. 12, pp. 1415–1423.

Gudi, S.R.P., Clark, C.B. and Frangos, J.A. (1996), "Fluid flow rapidly activates G proteins in human endothelial cells: Involvement of G proteins in mechanochemical signal transduction", *Circulation Research*, Vol. 79 No. 4, pp. 834–839.

Guetta, D., Langou, K., Grunwald, D., Klein, G. and Aubry, L. (2010), "FYVE-dependent endosomal targeting
176

of an arrestin-related protein in amoeba", *PLoS ONE*, Vol. 5 No. 12, available at:https://doi.org/10.1371/journal.pone.0015249.

Gutmann, E., Hanzlíková, V. and Vyskočil, F. (1971), "Age changes in cross striated muscle of the rat", *The Journal of Physiology*, Vol. 216 No. 2, pp. 331–343.

Van Haastert, P.J.M. (1983), "Relationship between adaptation of the folic acid and the cAMP mediated cGMP response in Dictyostelium", *Biochemical and Biophysical Research Communications*, Vol. 115 No. 1, pp. 130–136.

Van Haastert, P.J.M. (1995), "Transduction of the chemotactic cAMP signal across the plasma membrane of Dictyostelium cells", *Experientia*, Vol. 51 No. 12, pp. 1144–1154.

Van Haastert, P.J.M. and Van der Heijden, P.R. (1983), "Excitation, adaptation, and deadaptation of the cAMP-mediated cGMP response in Dictyostelium discoideum", *Journal of Cell Biology*, Vol. 96 No. 2, pp. 347–353.

Van Haastert, P.J.M.M. and Kuwayama, H. (1997), "cGMP as second messenger during Dictyostelium chemotaxis", *FEBS Letters*, Federation of European Biochemical Societies, Vol. 410 No. 1, pp. 25–28.

Habourdin, C., Klein, G., Araki, T., Williams, J.G. and Aubry, L. (2013), "The arrestin-domain containing protein AdcA is a response element to stress", *Cell Communication and Signaling*, Vol. 11 No. 1, pp. 10–13.

Hacker, U., Albrecht, R. and Maniak, M. (1997), "Fluid-phase uptake by macropinocytosis in dictyostelium", *Journal of Cell Science*, Vol. 110 No. 2, pp. 105–112.

Hamill, O.P. and Martinac, B. (2001), "Molecular basis of mechanotransduction in living cells", *Physiological Reviews*, Vol. 81 No. 2, pp. 685–740.

Hanada, T., Noda, N.N., Satomi, Y., Ichimura, Y., Fujioka, Y., Takao, T., Inagaki, F., *et al.* (2007), "The Atg12-Atg5 conjugate has a novel E3-like activity for protein lipidation in autophagy", *Journal of Biological Chemistry*, Vol. 282 No. 52, pp. 37298–37302.

Hara, K., Yonezawa, K., Kozlowski, M.T., Sugimoto, T., Andrabi, K., Weng, Q.-P., Kasuga, M., *et al.* (1997), "Regulation of eIF-4E BP1 Phosphorylation by mTOR", *Journal of Biological Chemistry*, Vol. 272 No. 42, pp. 26457–26463.

Hara, T., Takamura, A., Kishi, C., Iemura, S.I., Natsume, T., Guan, J.L. and Mizushima, N. (2008), "FIP200, a ULK-interacting protein, is required for autophagosome formation in mammalian cells", *Journal of Cell Biology*, Vol. 181 No. 3, pp. 497–510.

Hardie, D.G. and Hawley, S.A. (2001), "AMP-activated protein kinase: The energy charge hypothesis revisited", *BioEssays*, Vol. 23 No. 12, pp. 1112–1119.

Hawk, M.A. and Schafer, Z.T. (2018), "Mechanisms of redox metabolism and cancer cell survival during extracellular matrix detachment", *Journal of Biological Chemistry*, Vol. 293 No. 20, pp. 7531–7537.

Hecht, E., Knittel, P., Felder, E., Dietl, P., Mizaikoff, B. and Kranz, C. (2012), "Combining atomic force-fluorescence microscopy with a stretching device for analyzing mechanotransduction processes in living cells", *The Analyst*, Vol. 137 No. 22, p. 5208.

Heid, P.J., Wessels, D., Daniels, K.J., Gibson, D.P., Zhang, H., Voss, E. and Soll, D.R. (2004), "The role of myosin heavy chain phosphorylation in Dictyostelium motility, chemotaxis and F-actin localization", *Journal of Cell Science*, Vol. 117 No. 20, pp. 4819–4835.

Heuser, J., Zhu, Q. and Clarke, M. (1993), "Proton pumps populate the contractile vacuoles of Dictyostelium amoebae.", *Journal of Cell Biology*, Vol. 121 No. 6, pp. 1311–1327.

Hirt, J. and Liton, P.B. (2017), "Autophagy and mechanotransduction in outflow pathway cells", *Experimental Eye Research*, Elsevier Ltd, Vol. 158, pp. 146–153.

Hosokawa, N., Sasaki, T., Iemura, S.I., Natsume, T., Hara, T. and Mizushima, N. (2009), "Atg101, a novel mammalian autophagy protein interacting with Atg13", *Autophagy*, Vol. 5 No. 7, pp. 973–979.

Hu, Y.L., Jahangiri, A., De Lay, M. and Aghi, M.K. (2012), "Hypoxia-induced tumor cell autophagy mediates resistance to anti-angiogenic therapy", *Autophagy*, Vol. 8 No. 6, pp. 979–981.

Huang, C.-Y.C., Hagar, K.L., Frost, L.E., Sun, Y. and Cheung, H.S. (2004), "Effects of Cyclic Compressive Loading on Chondrogenesis of Rabbit Bone-Marrow Derived Mesenchymal Stem Cells", *STEM CELLS*, Vol. 22 No. 3, pp. 313–323.

Huang, S.-Y., Tsai, M.-L., Chen, G.-Y., Wu, C.-J. and Chen, S.-H. (2007), "A Systematic Proteomics Approach for Identifying in-vitro Substrates of PKA and PKG in Rat Uteri", *Journal of Proteome Research*, Vol. 6, pp. 2674–2684.

Huang, S. and Ingber, D.E. (1999), "The structural and mechanical complexity of cell-growth control", *Nature Cell Biology*, Vol. 1 No. 5, pp. E131–E138.

Hurley, J.H. and Young, L.N. (2017), "Mechanisms of Autophagy Initiation", *Annual Review of Biochemistry*, Vol. 86 No. 1, pp. 225–244.

Ignarro, L.J., Buga, G.M., Wood, K.S., Byrns, R.E. and Chaudhuri, G. (1987), "Endothelium-derived relaxing factor produced and released from artery and vein is nitric oxide.", *Proceedings of the National Academy of Sciences of the United States of America*, Vol. 84 No. 24, pp. 9265–9269.

Ignarro, L.J., Byrns, R.E., Buga, G.M. and Wood, K.S. (1987), "Endothelium-derived relaxing factor from pulmonary artery and vein possesses pharmacologic and chemical properties identical to those of nitric oxide radical", *Circulation Research*, Vol. 61 No. 6, pp. 866–879.

Inaba, N., Kuroshima, S., Uto, Y., Sasaki, M. and Sawase, T. (2017), "Cyclic mechanical stretch contributes to network development of osteocyte-like cells with morphological change and autophagy promotion but without preferential cell alignment in rat", *Biochemistry and Biophysics Reports*.

Ingber, D.E. (1997), "TENSEGRITY: THE ARCHITECTURAL BASIS OF CELLULAR MECHANOTRANSDUCTION", *Annual Review of Physiology*, Vol. 59 No. 1, pp. 575–599.

Inoki, K., Kim, J. and Guan, K.L. (2012), "AMPK and mTOR in cellular energy homeostasis and drug targets", *Annual Review of Pharmacology and Toxicology*, Vol. 52, pp. 381–400.

Insall, R.H., Soede, R.D.M., Schaap, P. and Devreotes, P.N. (1994), "Two cAMP receptors activate common signaling pathways in Dictyostelium", *Molecular Biology of the Cell*, Vol. 5 No. 6, pp. 703–711.

Isner, J.C. and Maathuis, F.J.M. (2011), "Measurement of cellular cGMP in plant cells and tissues using the endogenous fluorescent reporter FlincG", *Plant Journal*, Vol. 65 No. 2, pp. 329–334.

Iwata, T., Popescu, N.C., Zimonjic, D.B., Karlsson, C., Höög, J.O., Vaca, G., Rodriguez, I.R., *et al.* (1995), "Structural organization of the human sorbitol dehydrogenase gene (SORD)", *Genomics*, Vol. 26 No. 1, pp. 55–62.

Jacques, E., Verbelen, J.P. and Vissenberg, K. (2013), "Mechanical stress in Arabidopsis leaves orients microtubules in a 'continuous' supracellular pattern", *BMC Plant Biology*, Vol. 13 No. 1, available at:https://doi.org/10.1186/1471-2229-13-163.

Jiang, L.B., Cao, L., Yin, X.F., Yasen, M., Yishake, M., Dong, J. and Li, X.L. (2015), "Activation of autophagy via ca2+-dependent ampk/ mtor pathway in rat notochordal cells is a cellular adaptation under hyperosmotic stress", *Cell Cycle*, Vol. 14 No. 6, pp. 867–879.

Jo, H., Sipos, K., Go, Y.M., Law, R., Rong, J. and McDonald, J.M. (1997), "Differential effect of shear stress on extracellular signal-regulated kinase and N-terminal jun kinase in endothelial cells: G(i)2- and Gβ/γ-dependent signaling pathways", *Journal of Biological Chemistry*, Â© 1997 ASBMB. Currently published by Elsevier Inc; originally published by American Society for Biochemistry and Molecular Biology., Vol. 272 No. 2, pp. 1395–1401.

Jung, C.H., Jun, C.B., Ro, S.-H., Kim, Y.-M., Otto, N.M., Cao, J., Kundu, M., *et al.* (2009), "ULK-Atg13-FIP200 Complexes Mediate mTOR Signaling to the Autophagy Machinery", edited by Schmid, S.L.*Molecular Biology of the Cell*, Vol. 20 No. 7, pp. 1992–2003.

Jung, G. and Iii, J.A.H. (1994), "The actin binding site in the tail domain of Dictyostelium myosin IC (tail homology region 2)", *FEBS Letters*, Vol. 342, pp. 197–202.

Jung, G., Remmert, K., Wu, X., Volosky, J.M. and Hammer, J.A. (2001), "The Dictyostelium CARMIL protein links capping protein and the Arp2/3 complex to type I myosins through their SH3 domains", *Journal of Cell Biology*, Vol. 153 No. 7, pp. 1479–1498.

Jung, G., Wu, X. and Hammer, J.A. (1996), "Dictyostelium mutants lacking multiple classic myosin I isoforms reveal combinations of shared and distinct functions", *Journal of Cell Biology*, Vol. 133 No. 2, pp. 305–323.

Kabeya, Y., Kamada, Y., Baba, M., Takikawa, H., Sasaki, M. and Ohsumi, Y. (2005), "Atg17 Functions in Cooperation with Atg1 and Atg13 in Yeast Autophagy", *Molecular Biology of the Cell*, Vol. 16 No. 5, pp. 2544–2553.

Kalli, M., Voutouri, C., Minia, A., Pliaka, V., Fotis, C., Alexopoulos, L.G. and Stylianopoulos, T. (2019), "Mechanical compression regulates brain cancer cell migration through MEK1/Erk1 pathway activation and GDF15 expression", *Frontiers in Oncology*, Vol. 9 No. SEP, pp. 1–17.

Kamada, Y., Funakoshi, T., Shintani, T., Nagano, K., Ohsumi, M. and Ohsumi, Y. (2000), "Tor-mediated induction of autophagy via an Apg1 protein kinase complex", *Journal of Cell Biology*, Vol. 150 No. 6, pp. 1507–1513.

Kamada, Y., Yoshino, K., Kondo, C., Kawamata, T., Oshiro, N., Yonezawa, K. and Ohsumi, Y. (2010), "Tor Directly Controls the Atg1 Kinase Complex To Regulate Autophagy", *Molecular and Cellular Biology*, Vol. 30 No. 4, pp. 1049–1058.

Kanzaki, H., Chiba, M., Shimizu, Y. and Mitani, H. (2002), "Periodontal ligament cells under mechanical stress induce osteoclastogenesis by receptor activator of nuclear factor kappa B ligand up-regulation via prostaglandin E-2 synthesis", *Journal of Bone and Mineral Research*, Vol. 17 No. 2, pp. 210–220.

Katsumi, A., Orr, A.W., Tzima, E. and Schwartz, M.A. (2004), "Integrins in Mechanotransduction", *Journal of Biological Chemistry*, Vol. 279 No. 13, pp. 12001–12004.

Khurana, B., Khurana, T., Khaire, N. and Noegel, A.A. (2002), "Functions of LIM proteins in cell polarity and chemotactic motility", *EMBO Journal*, Vol. 21 No. 20, pp. 5331–5342.

Kicka, S., Shen, Z., Annesley, S.J., Fisher, P.R., Lee, S., Briggs, S. and Firtela, R.A. (2011), "The LRRK2-related Roco kinase Roco2 is regulated by Rab1A and controls the actin cytoskeleton", *Molecular Biology of the Cell*, Vol. 22 No. 13, pp. 2198–2211.

Kihara, A., Noda, T., Ishihara, N. and Ohsumi, Y. (2001), "Two distinct Vps34 phosphatidylinositol 3-kinase complexes function in autophagy and carboxypeptidase y sorting in Saccharomyces cerevisiae", *Journal of Cell Biology*, Vol. 153 No. 3, pp. 519–530.

Kim, D.H. and Wirtz, D. (2015), "Cytoskeletal tension induces the polarized architecture of the nucleus", *Biomaterials*, Elsevier Ltd, Vol. 48, pp. 161–172.

Kim, J., Kundu, M., Viollet, B. and Guan, K.L. (2011), "AMPK and mTOR regulate autophagy through direct phosphorylation of Ulk1", *Nature Cell Biology*, Vol. 13 No. 2, pp. 132-U71.

King, J.S. (2012), "Autophagy across the eukaryotes: Is S. cerevisiae the odd one out?", *Autophagy*, Vol. 8 No. 7, pp. 1159–1162.

King, J.S. and Kay, R.R. (2019), "The origins and evolution of macropinocytosis", *Philosophical Transactions of the Royal Society B: Biological Sciences*, Vol. 374 No. 1765, available at:https://doi.org/10.1098/rstb.2018.0158.

King, J.S., Veltman, D.M. and Insall, R.H. (2011), "The induction of autophagy by mechanical stress", *Autophagy*, Vol. 7 No. 12, pp. 1490–1499.

Klionsky, D.J., Abdelmohsen, K., Abe, A., Abedin, M.J., Abeliovich, H., Arozena, A.A., Adachi, H., *et al.* (2016), "Guidelines for the use and interpretation of assays for monitoring autophagy (3rd edition)", *Autophagy*, Vol. 12 No. 1, pp. 1–222.

Kooij, B. van de, Creixell, P., Vlimmeren, A. van, Joughin, B.A., Miller, C.J., Haider, N., Simpson, C.D., *et al.* (2019), "Comprehensive substrate specificity profiling of the human nek kinome reveals unexpected signaling outputs", *ELife*, Vol. 8, available at:https://doi.org/10.7554/eLife.44635.

Kortholt, A., van Egmond, W.N., Plak, K., Bosgraaf, L., Keizer-Gunnink, I. and van Haastert, P.J.M. (2012), "Multiple regulatory mechanisms for the Dictyostelium Roco protein GbpC", *Journal of Biological Chemistry*, Vol. 287 No. 4, pp. 2749–2758.

Kuczmarski, E.R. and Spudich, J.A. (1980), "Regulation of myosin self-assembly: Phosphorylation of Dictyostelium heavy chain inhibits formation of thick filaments", *Proceedings of the National Academy of Sciences of the United States of America*, Vol. 77 No. 12, pp. 7292–7296.

Kunzt, J.B., Schwarz, H. and Mayer, A. (2004), "Determination of Four Sequential Stages during Microautophagy in Vitro", *Journal of Biological Chemistry*, Â© 2004 ASBMB. Currently published by Elsevier Inc; originally published by American Society for Biochemistry and Molecular Biology., Vol. 279 No. 11, pp. 9987–9996.

Kuroyanagi, H., Yan, J., Seki, N., Yamanouchi, Y., Suzuki, Y. ichi, Takano, T., Muramatsu, M. aki, *et al.* (1998), "Human ULK1, a novel serine/threonine kinase related to UNC-51 kinase of Caenorhabditis elegans: cDNA cloning, expression, and chromosomal assignment", *Genomics*, Vol. 51 No. 1, pp. 76–85.

Kuwayama, H., Ecke, M., Gerisch, G. and van Haastert, P.J.M. (1996), "Protection against osmotic stress by cGMP-mediated myosin phosphorylation", *Science Reports*, Vol. 271 No. 5246, pp. 207–209.

Kwak, B.R., Bäck, M., Bochaton-Piallat, M.L., Caligiuri, G., Daemen, M.J.A.P., Davies, P.F., Hoefer, I.E., *et al.* (2014), "Biomechanical factors in atherosclerosis: mechanisms and clinical implications", *European Heart Journal*, Vol. 35 No. 43, pp. 3013–3020.

De La Roche, M.A., Smith, J.L., Betapudi, V., Egelhoff, T.T. and Côté, G.P. (2002), "Signaling pathways regulating Dictyostelium myosin II", *Journal of Muscle Research and Cell Motility*, Vol. 23 No. 7–8, pp.

703–718.

de la Roche, M.A., Smith, J.L., Rico, M., Carrasco, S., Merida, I., Licate, L., Côté, G.P., *et al.* (2002), "Dictyostelium discoideum has a single diacylglycerol kinase gene with Similarity To Mammalian Θ Isoforms", *Biochemical Journal*, Vol. 368, pp. 809–815.

Lammerding, J., Kamm, R.D. and Lee, R.T. (2004), "Mechanotransduction in Cardiac Myocytes", *Annals of the New York Academy of Sciences*, Vol. 1015 No. 1, pp. 53–70.

Lang, F. and Föller, M. (2014), "Regulation of ion channels and transporters by AMP-activated kinase (AMPK)", *Channels*, Vol. 8 No. 1, pp. 20–28.

Lee, D.Y., Li, Y.S.J., Chang, S.F., Zhou, J., Ho, H.M., Chiu, J.J. and Chien, S. (2010), "Oscillatory flow-induced proliferation of osteoblast-like cells is mediated by αvβ3 and β1 integrins through synergistic interactions of focal adhesion kinase and Shc with phosphatidylinositol 3-kinase and the Akt/mTOR/p70S6K pathway", *Journal of Biological Chemistry*, Vol. 285 No. 1, pp. 30–42.

Lee, H. (1998), "The structure and function of yeast xylose (aldose) reductases", *Yeast*, Vol. 14 No. 11, pp. 977–984.

Lee, J., Hyeon, D.Y. and Hwang, D. (2020), "Single-cell multiomics: technologies and data analysis methods", *Experimental and Molecular Medicine*, Springer US, Vol. 52 No. 9, pp. 1428–1442.

Lee, J.S.H., Chang, M.I., Tseng, Y. and Wirtz, D. (2005), "Cdc42 Mediates Nucleus Movement and MTOC Polarization in Swiss 3T3 Fibroblasts under Mechanical Shear Stress", *Molecular Biology of the Cell*, Vol. 16 No. 2, pp. 871–880.

Lee, J.W., Chen, H., Pullikotil, P. and Quon, M.J. (2011), "Protein kinase A-α directly phosphorylates FoxO1 in vascular endothelial cells to regulate expression of vascular cellular adhesion molecule-1 mRNA", *Journal of Biological Chemistry*, Vol. 286 No. 8, pp. 6423–6432.

Lekmine, F., Sassano, A., Uddin, S., Smith, J., Majchrzak, B., Brachmann, S.M., Hay, N., *et al.* (2004), "Interferon-γ engages the p70 S6 kinase to regulate phosphorylation of the 40S S6 ribosomal protein", *Experimental Cell Research*, Vol. 295 No. 1, pp. 173–182.

Lewis, A.H. and Grandl, J. (2021), "Piezo1 ion channels inherently function as independent mechanotransducers", *BioRxiv*.

Liang, W., Licate, L.S., Warrick, H.M., Spudich, J.A. and Egelhoff, T.T. (2002), "Differential localization in cells myosin II heavy chain kinases during cytokinesis and polarized migration", *BMC Cell Biology*, Vol. 3, pp. 1–16.

Liao, X.H., Majithia, A., Huang, X. and Kimmel, A.R. (2008), "Growth control via TOR kinase signaling, an intracellular sensor of amino acid and energy availability, with crosstalk potential to proline

metabolism", *Amino Acids*, Vol. 35 No. 4, pp. 761–770.

Lien, S.-C., Chang, S.-F., Lee, P.-L., Wei, S.-Y., Chang, M.D.-T., Chang, J.-Y. and Chiu, J.-J. (2013), "Mechanical regulation of cancer cell apoptosis and autophagy: Roles of bone morphogenetic protein receptor, Smad1/5, and p38 MAPK", *Biochimica Et Biophysica Acta-Molecular Cell Research*, Vol. 1833 No. 12, pp. 3124–3133.

Lin, L., Xu, J., Ye, Y., Ge, J., Zou, Y. and Liu, X. (2015), "Isosorbide Dinitrate Inhibits Mechanical Stress-induced Cardiac Hypertrophy and Autophagy Through Downregulation of Angiotensin II Type 1 Receptor", *Journal of Cardiovascular Pharmacology*, Vol. 65 No. 1, pp. 1–7.

Lindmo, K. and Stenmark, H. (2006), "Regulation of membrane traffic by phosphoinositide 3-kinases", *Journal of Cell Science*, Vol. 119 No. 4, pp. 605–614.

Litschko, C., Brühmann, S., Csiszár, A., Stephan, T., Dimchev, V., Damiano-Guercio, J., Junemann, A., *et al.* (2019), "Functional integrity of the contractile actin cortex is safeguarded by multiple Diaphanous-related formins", *Proceedings of the National Academy of Sciences of the United States of America*, Vol. 116 No. 9, pp. 3594–3603.

Liu, C., Choi, H., Johnson, Z.I., Tian, J., Shapiro, I.M. and Risbud, M. V. (2017), "Lack of evidence for involvement of TonEBP and hyperosmotic stimulus in induction of autophagy in the nucleus pulposus", *Scientific Reports*, Springer US, Vol. 7 No. 1, pp. 1–13.

Liu, G., Kuwayama, H., Ishida, S. and Newell, P.C. (1993), "The role of cyclic GMP in regulating myosin during chemotaxis of Dictyostelium: Evidence from a mutant lacking the normal cyclic GMP response to cyclic AMP", *Journal of Cell Science*, Vol. 106 No. 2, pp. 591–595.

Liu, G. and Newell, P.C. (1991), "Evidence that cyclic GMP may regulate the association of myosin II heavy chain with the cytoskeleton by inhibiting its phosphorylation", *Journal of Cell Science*, Vol. 98 No. 4, pp. 483–490.

Liu, G. and Newell, P.C. (1994), "Regulation of myosin regulatory light chain phosphorylation via cyclic GMP during chemotaxis of Dictyostelium", *Journal of Cell Science*, Vol. 107 No. 7, pp. 1737–1743.

Liu, H.Z., Li, L., Chen, S.L., Wei, J.R., Zhang, J.X., Liu, J., Guo, J.W., *et al.* (2018), "Low Shear Stress Regulating Autophagy Mediated by the p38 Mitogen Activated Protein Kinase and p53 Pathways in Human Umbilical Vein Endothelial Cells", *Chinese Medical Journal*, Vol. 131 No. 9, pp. 1132–1133.

Liu, J., Bi, X., Chen, T., Zhang, Q., Wang, S.X., Chiu, J.J., Liu, G.S., *et al.* (2015), "Shear stress regulates endothelial cell autophagy via redox regulation and Sirt1 expression", *Cell Death & Disease*, Vol. 6, p. 11.

Liu, Y., Xiong, Y. and Bassham, D.C. (2009), "Autophagy is required for tolerance of drought and salt stress in plants", *Autophagy*, Vol. 5 No. 7, pp. 954–963.

Lombardi, M.L., Knecht, D.A. and Lee, J. (2008), "Mechano-chemical signaling maintains the rapid movement of Dictyostelium cells", *Experimental Cell Research*, Vol. 314 No. 8, pp. 1850–1859.

López-Jiménez, A.T., Cardenal-Muñoz, E., Leuba, F., Gerstenmaier, L., Barisch, C., Hagedorn, M., King, J.S., *et al.* (2018), "The ESCRT and autophagy machineries cooperate to repair ESX-1-dependent damage at the Mycobacterium-containing vacuole but have opposite impact on containing the infection", *PLoS Pathogens*, Vol. 14 No. 12, pp. 1–29.

Lord, S.J., Velle, K.B., Dyche Mullins, R. and Fritz-Laylin, L.K. (2020), "SuperPlots: Communicating reproducibility and variability in cell biology", *Journal of Cell Biology*, Vol. 219 No. 6, available at:https://doi.org/10.1083/JCB.202001064.

Lück-Vielmetter, D., Schleicher, M., Grabatin, B., Wippler, J. and Gerisch, G. (1990), "Replacement of threonine residues by serine and alanine in a phosphorylatable heavy chain fragment of Dictyostelium myosin II", *FEBS Letters*, Vol. 269 No. 1, pp. 239–243.

Ludbrook, S.B., Eccleston, J.F. and Strom, M. (1997), "Cloning and characterization of a rhoGAP homolog from Dictyostelium discoideum", *Journal of Biological Chemistry*, Vol. 272 No. 25, pp. 15682–15686.

Luo, X., Crawley, S.W., Steimle, P.A., Egelhoff, T.T. and Côté, G.P. (2001), "Specific Phosphorylation of Threonine by the Dictyostelium Myosin II Heavy Chain Kinase Family", *Journal of Biological Chemistry*, Vol. 276 No. 21, pp. 17836–17843.

Lusche, D.F., Kaneko, H. and Malchow, D. (2005), "cGMP-phosphodiesterase antagonists inhibit Ca2+-influx in Dictyostelium discoideum and bovine cyclic-nucleotide-gated-channel", *European Journal of Pharmacology*, Vol. 513 No. 1–2, pp. 9–20.

Ma, K.G., Shao, Z.W., Yang, S.H., Wang, J., Wang, B.C., Xiong, L.M., Wu, Q., *et al.* (2013), "Autophagy is activated in compression-induced cell degeneration and is mediated by reactive oxygen species in nucleus pulposus cells exposed to compression", *Osteoarthritis and Cartilage*, Vol. 21 No. 12, pp. 2030–2038.

Maksimovic, S., Nakatani, M., Baba, Y., Nelson, A.M., Marshall, K.L., Wellnitz, S.A., Firozi, P., *et al.* (2014), "Epidermal Merkel cells are mechanosensory cells that tune mammalian touch receptors", *Nature*, Vol. 509 No. 7502, pp. 617–621.

Marchesini, N., Ruiz, F.A., Vieira, M. and Docampo, R. (2002), "Acidocalcisomes Are Functionally Linked to the Contractile Vacuole of Dictyostelium discoideum", *Journal of Biological Chemistry*, Vol. 277 No. 10, pp. 8146–8153.

Maria Fimia, G., Stoykova, A., Romagnoli, A., Giunta, L., Di Bartolomeo, S., Nardacci, R., Corazzari, M., *et al.* (2007), "Ambra1 regulates autophagy and development of the nervous system", *Nature*, Vol. 447 No. 7148, pp. 1121–1125.

Maroto, R., Raso, A., Wood, T.G., Kurosky, A., Martinac, B. and Hamill, O.P. (2005), "TRPC1 forms the stretch-activated cation channel in vertebrate cells", *Nature Cell Biology*, Vol. 7 No. 2, pp. 179–185.

Martinac, B. (2004), "Mechanosensitive ion channels: Molecules of mechanotransduction", *Journal of Cell Science*, Vol. 117 No. 12, pp. 2449–2460.

Mato, J.M., Krens, F.A., van Haastert, P.J.M. and Konijn, T.M. (1977), "3':5'-Cyclic AMP-dependent 3':5'-cyclic GMP accumulation in Dictyostelium discoideum", *Proceedings of the National Academy of Sciences of the United States of America*, Vol. 74 No. 6, pp. 2348–2351.

Matsuura, A., Tsukada, M., Wada, Y. and Ohsumi, Y. (1997), "Apg1p, a novel protein kinase required for the autophagic process in Saccharomyces cerevisiae", *Gene*, Vol. 192 No. 2, pp. 245–250.

Matthews, B.D., Overby, D.R., Mannix, R. and Ingber, D.E. (2006), "Cellular adaptation to mechanical stress: Role of integrins, Rho, cytoskeletal tension and mechanosensitive ion channels", *Journal of Cell Science*, Vol. 119 No. 3, pp. 508–518.

McAlpine, F., Williamson, L.E., Tooze, S.A. and Chan, E.Y.W. (2013), "Regulation of nutrient-sensitive autophagy by uncoordinated 51-like kinases 1 and 2", *Autophagy*, Vol. 9 No. 3, pp. 361–373.

Mercer, C.A., Kaliappan, A. and Dennis, P.B. (2009), "A novel, human Atg13 binding protein, Atg101, interacts with ULK1 and is essential for macroautophagy", *Autophagy*, Vol. 5 No. 5, pp. 649–662.

Mertins, P., Mani, D.R., Ruggles, K. V., Gillette, M.A., Clauser, K.R., Wang, P., Wang, X., *et al.* (2016), "Proteogenomics connects somatic mutations to signalling in breast cancer", *Nature*, Nature Publishing Group, Vol. 534 No. 7605, pp. 55–62.

Mertins, P., Yang, F., Liu, T., Mani, D.R., Petyuk, V.A., Gillette, M.A., Clauser, K.R., *et al.* (2014), "Ischemia in tumors induces early and sustained phosphorylation changes in stress kinase pathways but does not affect global protein levels", *Molecular and Cellular Proteomics*, Vol. 13 No. 7, pp. 1690–1704.

Mesquita, A., Cardenal-Muñoz, E., Dominguez, E., Muñoz-Braceras, S., Nuñez-Corcuera, B., Phillips, B.A., Tábara, L.C., *et al.* (2017), "Autophagy in Dictyostelium: Mechanisms, regulation and disease in a simple biomedical model", *Autophagy*, Vol. 13 No. 1, pp. 24–40.

Mesquita, A., Tábara, L.C., Martinez-Costa, O., Santos-Rodrigo, N., Vincent, O. and Escalante, R. (2015), "Dissecting the function of Atg1 complex in Dictyostelium autophagy reveals a connection with the pentose phosphate pathway enzyme transketolase", *Open Biology*, Vol. 5 No. 8, available at:https://doi.org/10.1098/rsob.150088.

Metzger, M.B. and Michaelis, S. (2009), "Analysis of Quality Control Substrates in Distinct Cellular Compartments Reveals a Unique Role for Rpn4p in Tolerating Misfolded Membrane Proteins", edited by Walter, P.*Molecular Biology of the Cell*, Vol. 20 No. 3, pp. 1006–1019.

Mi, H., Muruganujan, A., Ebert, D., Huang, X. and Thomas, P.D. (2019), "PANTHER version 14: More genomes, a new PANTHER GO-slim and improvements in enrichment analysis tools", *Nucleic Acids Research*, Oxford University Press, Vol. 47 No. D1, pp. D419–D426.

Mikawa, T., Kanoh, J. and Ishikawa, F. (2010), "Fission yeast Vps1 and Atg8 contribute to oxidative stress resistance", *Genes to Cells*, Vol. 15 No. 3, pp. 229–242.

Mitra, S.K., Hanson, D.A. and Schlaepfer, D.D. (2005), "Focal adhesion kinase: In command and control of cell motility", *Nature Reviews Molecular Cell Biology*, Vol. 6 No. 1, pp. 56–68.

Mizushima, N. (2010), "The role of the Atg1/ULK1 complex in autophagy regulation", *Current Opinion in Cell Biology*, Elsevier Ltd, Vol. 22 No. 2, pp. 132–139.

Morio, T., Yasukawa, H., Urushihara, H., Saito, T., Ochiai, H., Takeuchi, I., Maeda, M., *et al.* (2001), "FebA: A gene for eukaryotic translation initiation factor 4E-binding protein (4E-BP) in Dictyostelium discoideum", *Biochimica et Biophysica Acta - Gene Structure and Expression*, Vol. 1519 No. 1–2, pp. 65–69.

Mun, H. and Jeon, T.J. (2012), "Regulation of actin cytoskeleton by Rap1 binding to RacGEF1", *Molecules and Cells*, Vol. 34 No. 1, pp. 71–76.

Muramoto, T., Kuwayama, H., Kobayashi, K. and Urushihara, H. (2007), "A stress response kinase, KrsA, controls cAMP relay during the early development of Dictyostelium discoideum", *Developmental Biology*, Vol. 305 No. 1, pp. 77–89.

Na, J. (2007), *Identification and Investigation of Osmostress-Induced Genes in Dictyostelium Discoideum*, available at: http://www.uni-koeln.de/med-fak/biochemie/dissertation/diss/jianbo_na.pdf.

Na, J., Tunggal, B. and Eichinger, L. (2007), "STATc is a key regulator of the transcriptional response to hyperosmotic shock", *BMC Genomics*, Vol. 8 No. 1, p. 123.

Narita, T.B., Kikukawa, T.W., Sato, Y.G., Miyazaki, S.H., Morita, N. and Saito, T. (2014), "Role of fatty acid synthase in the development of Dictyostelium discoideum", *Journal of Oleo Science*, Vol. 63 No. 3, pp. 281–289.

Nausch, L.W.M., Ledoux, J., Bonev, A.D., Nelson, M.T. and Dostmann, W.R. (2008), "Differential patterning of cGMP in vascular smooth muscle cells revealed by single GFP-linked biosensors", *Proceedings of the National Academy of Sciences of the United States of America*, Vol. 105 No. 1, pp. 365–370.

Nguyen, A.M. and Jacobs, C.R. (2013), "Emerging role of primary cilia as mechanosensors in osteocytes", *Bone*, Vol. 54 No. 2, pp. 196–204.

Nichols, J.M.E., Paschke, P., Peak-Chew, S., Williams, T.D., Tweedy, L., Skehel, M., Stephens, E., *et al.* (2019), "The Atypical MAP Kinase ErkB Transmits Distinct Chemotactic Signals through a Core Signaling

Module", *Developmental Cell*, Elsevier Inc., Vol. 48 No. 4, pp. 491-505.e9.

Noda, N.N., Fujioka, Y., Hanada, T., Ohsumi, Y. and Inagaki, F. (2013), "Structure of the Atg12-Atg5 conjugate reveals a platform for stimulating Atg8-PE conjugation", *EMBO Reports*, Nature Publishing Group, Vol. 14 No. 2, pp. 206–211.

Nolta, K. V., Padh, H. and Steck, T.L. (1993), "An immunocytochemical analysis of the vacuolar proton pump in Dictyostelium discoideum", *Journal of Cell Science*, Vol. 105 No. 3, pp. 849–859.

Northcott, J.M., Dean, I.S., Mouw, J.K. and Weaver, V.M. (2018), "Feeling stress: The mechanics of cancer progression and aggression", *Frontiers in Cell and Developmental Biology*, Vol. 6 No. FEB, pp. 1–12.

Nunes, P., Ernandez, T., Roth, I., Qiao, X.M., Strebel, D., Bouley, R., Charollais, A., *et al.* (2013), "Hypertonic stress promotes autophagy and microtubule-dependent autophagosomal clusters", *Autophagy*, Vol. 9 No. 4, pp. 550–567.

O'Shea, J.P., Chou, M.F., Quader, S.A., Ryan, J.K., Church, G.M. and Schwartz, D. (2013), "PLogo: A probabilistic approach to visualizing sequence motifs", *Nature Methods*, Vol. 10 No. 12, pp. 1211–1212.

Obara, K., Sekito, T., Niimi, K. and Ohsumi, Y. (2008), "The Atg18-Atg2 complex is recruited to autophagic membranes via phosphatidylinositol 3-phosphate and exerts an essential function", *Journal of Biological Chemistry*, Vol. 283 No. 35, pp. 23972–23980.

Oberhauser, A.F., Marszalek, P.E., Erickson, H.P. and Fernandez, J.M. (1998), "Structural protein tenascin", *Nature*, Vol. 393 No. 5429, p. 181.

Ochaba, J., Lukacsovich, T., Csikos, G., Zheng, S., Margulis, J., Salazar, L., Mao, K., *et al.* (2014), "Potential function for the Huntingtin protein as a scaffold for selective autophagy", *Proc Natl Acad Sci U S A*, available at:https://doi.org/10.1073/pnas.1420103111.

Ogura, K., Wicky, C., Magnent, L., Tobler, H., Mori, I., Mueller, F. and Ohshima, Y. (1994), "Caenorhabditis elegans unc-51 gene required for axonal elongation encodes a novel serine/threonine kinase", *Genes and Development*, Vol. 8, pp. 2389–2400.

Ohno, M., Gibbons, G.H., Dzau, V.J. and Cooke, J.P. (1993), "Shear stress elevates endothelial cGMP: Role of a potassium channel and G protein coupling", *Circulation*, Vol. 88 No. 1, pp. 193–197.

Orr, A.W., Helmke, B.P., Blackman, B.R. and Schwartz, M.A. (2006), "Mechanisms of mechanotransduction", *Developmental Cell*, Vol. 10 No. 1, pp. 11–20.

Ørstavik, S., Natarajan, V., Tasken, K., Jahnsen, T. and Sandberg, M. (1997), "Characterization of the Human Gene Encoding the Type Iα and Type Iβ cGMP-Dependent Protein Kinase (PRKG1)", *Genomics*, Vol. 42, pp. 311–318.

Ostrow, B.D., Chen, P. and Chisholm, R.L. (1994), "Expression of a myosin regulatory light chain phosphorylation site mutant complements the cytokinesis and developmental defects of Dictyostelium RMLC null cells", *Journal of Cell Biology*, Vol. 127 No. 6 II, pp. 1945–1955.

Ott, A., Oehme, F., Keller, H. and Schuster, S.C. (2000), "Osmotic stress response in Dictyostelium is mediated by cAMP", *The EMBO Journal*, Vol. 19 No. 21, pp. 5782–5792.

Otto, G.P., Wu, M.Y., Kazgan, N., Anderson, O.R. and Kessin, R.H. (2003), "Macroautophagy is required for multicellular development of the social amoeba Dictyostelium discoideum", *Journal of Biological Chemistry*, Vol. 278 No. 20, pp. 17636–17645.

Otto, G.P., Wu, M.Y., Kazgan, N., Anderson, O.R. and Kessin, R.H. (2004), "Dictyostelium Macroautophagy Mutants Vary in the Severity of Their Developmental Defects", *Journal of Biological Chemistry*, Vol. 279 No. 15, pp. 15621–15629.

Oyama, M. (1996), "cGMP accumulation induced by hypertonic stress in Dictyostelium discoideum", *Journal of Biological Chemistry*, Vol. 271 No. 10, pp. 5574–5579.

Pagliara, S., Franze, K., McClain, C.R., Wylde, G.W., Fisher, C.L., Franklin, R.J.M., Kabla, A.J., *et al.* (2014), "Auxetic nuclei in embryonic stem cells exiting pluripotency", *Nature Materials*, Vol. 13 No. 6, pp. 638–644.

Palikaras, K., Lionaki, E. and Tavernarakis, N. (2018), "Mechanisms of mitophagy in cellular homeostasis, physiology and pathology", *Nature Cell Biology*, Springer US, Vol. 20 No. 9, pp. 1013–1022.

Pandit, R., Leinenga, G. and Götz, J. (2019), "Repeated ultrasound treatment of tau transgenic mice clears neuronal tau by autophagy and improves behavioral functions", *Theranostics*, Vol. 9 No. 13, pp. 3754–3767.

Papatheodorou, I., Moreno, P., Manning, J., Fuentes, A.M.P., George, N., Fexova, S., Fonseca, N.A., *et al.* (2020), "Expression Atlas update: From tissues to single cells", *Nucleic Acids Research*, Vol. 48 No. D1, pp. D77–D83.

Parsell, D.A. and Lindquist, S. (1993), "The function of heat-shock proteins in stress tolerance: Degradation and reactivation of damaged proteins", *Annual Review of Genetics*, Vol. 27, pp. 437–496.

Pauly, T.A., Ekstrom, J.L., Beebe, D.A., Chrunyk, B., Cunningham, D., Griffor, M., Kamath, A., *et al.* (2003), "X-ray crystallographic and kinetic studies of human sorbitol dehydrogenase", *Structure*, Vol. 11 No. 9, pp. 1071–1085.

Pejchal, R. and Ludwig, M.L. (2005), "Cobalamin-independent methionine synthase (MetE): A face-to-face double barrel that evolved by gene duplication", *PLoS Biology*, Vol. 3 No. 2, pp. 0254–0265.

Pelham, R.J. and Wang, Y. -l. (1997), "Cell locomotion and focal adhesions are regulated by substrate

flexibility", *Proceedings of the National Academy of Sciences*, Vol. 94 No. 25, pp. 13661–13665.

Peña-Oyarzun, D., Troncoso, R., Kretschmar, C., Hernando, C., Budini, M., Morselli, E., Lavandero, S., *et al.* (2017), "Hyperosmotic stress stimulates autophagy via polycystin-2", *Oncotarget*, Vol. 8 No. 34, pp. 55984–55997.

Pinto, M., Morange, M. and Bensaude, O. (1991), "Denaturation of proteins during heat shock: In vivo recovery of solubility and activity of reporter enzymes", *Journal of Biological Chemistry*, Vol. 266 No. 21, pp. 13941–13946.

Piras, A., Gianetto, D., Conte, D., Bosone, A. and Vercelli, A. (2011), "Activation of autophagy in a rat model of retinal ischemia following high intraocular pressure", *PLoS One*, Vol. 6 No. 7, p. e22514.

Plattner, H. (2015), "The contractile vacuole complex of protists-New cues to function and biogenesis", *Critical Reviews in Microbiology*, Vol. 41 No. 2, pp. 218–227.

Porter, K.M., Jeyabalan, N. and Liton, P.B. (2014), "MTOR-independent induction of autophagy in trabecular meshwork cells subjected to biaxial stretch", *Biochimica et Biophysica Acta - Molecular Cell Research*, Elsevier B.V., Vol. 1843 No. 6, pp. 1054–1062.

Puente, C., Hendrickson, R.C. and Jiang, X. (2016), "Nutrient-regulated phosphorylation of ATG13 inhibits starvation-induced autophagy", *Journal of Biological Chemistry*, Vol. 291 No. 11, pp. 6026–6035.

Qian, X., Li, X., Cai, Q., Zhang, C., Yu, Q., Jiang, Y., Lee, J.-H., *et al.* (2017), "Phosphoglycerate Kinase 1 Phosphorylates Beclin1 to Induce Autophagy", *Molecular Cell*, Vol. 65 No. 5, pp. 917-931.e6.

Queval, A., Ghattamaneni, N.R., Perrault, C.M., Gill, R., Mirzaei, M., McKinney, R.A. and Juncker, D. (2010), "Chamber and microfluidic probe for microperfusion of organotypic brain slices", *Lab on a Chip*, Vol. 10 No. 3, pp. 326–334.

Rai, A., Nöthe, H., Tzvetkov, N., Korenbaum, E. and Manstein, D.J. (2011), "Dictyostelium dynamin B modulates cytoskeletal structures and membranous organelles", *Cellular and Molecular Life Sciences*, Vol. 68 No. 16, pp. 2751–2767.

Ranjana, M., Rakesh, K. and Saran, S. (2019), "AMPKα promotes basal autophagy induction in Dictyostelium discoideum", *Journal of Cell Physiology*, pp. 1–13.

Ravid, S. and Spudich, J.A. (1989), "Myosin heavy chain kinase from developed Dictyostelium cells. Purification and characterization.", *The Journal of Biological Chemistry*, Vol. 264 No. 25, pp. 15144–15150.

Reggiori, F. and Klionsky, D.J. (2013), "Autophagic processes in yeast: Mechanism, machinery and regulation", *Genetics*, Vol. 194 No. 2, pp. 341–361.

Remmert, K., Olszewski, T.E., Bowers, M.B., Dimitrova, M., Ginsburg, A. and Hammer, J.A. (2004), "CARMIL

Is a Bona Fide Capping Protein Interactant", *Journal of Biological Chemistry*, Vol. 279 No. 4, pp. 3068–3077.

Rice, K.M., Kakarla, S.K., Mupparaju, S.P., Paturi, S., Katta, A., Wu, M., Harris, R.T., *et al.* (2010), "Shear stress activates Akt during vascular smooth muscle cell reorientation", *Biotechnology and Applied Biochemistry*, Vol. 55 No. 2, pp. 85–90.

Robinson, D.N., Ocon, S.S., Rock, R.S. and Spudich, J.A. (2002), "Dynacortin is a novel actin bundling protein that localizes to dynamic actin structures", *Journal of Biological Chemistry*, Vol. 277 No. 11, pp. 9088–9095.

Roczniak, A. and Burns, K.D. (1996), "Nitric oxide stimulates guanylate cyclase and regulates sodium transport in rabbit proximal tubule", *American Journal of Physiology-Renal Physiology*, Vol. 270 No. 1, pp. F106–F115.

Roelofs, J. and van Haastert, P.J.M. (2002), "Characterization of two unusual guanylyl cyclases from Dictyostelium", *Journal of Biological Chemistry*, Vol. 277 No. 11, pp. 9167–9174.

Roelofs, J., Meima, M., Schaap, P. and van Haastert, P.J.M. (2001), "The Dictyostelium homologue of mammalian soluble adenylyl cyclase encodes a guanylyl cyclase", *EMBO Journal*, Vol. 20 No. 16, pp. 4341–4348.

Roelofs, J., Snippe, H., Kleineidam, R.G. and van Haastert, P.J.M. (2001), "Guanylate cyclase in Dictyostelium discoideum with the topology of mammalian adenylate cyclase", *Biochemical Journal*, Vol. 354 No. 3, pp. 697–706.

Rohlfs, M., Arasada, R., Batsios, P., Janzen, J. and Schleicher, M. (2007), "The Ste20-like kinase SvkA of Dictyostelium discoideum is essential for late stages of cytokinesis", *Journal of Cell Science*, Vol. 120 No. 24, pp. 4345–4354.

Roper, J.A., Williamson, R.C., Bally, B., Cowell, C.A.M., Brooks, R., Stephens, P., Harrison, A.J., *et al.* (2015), "Ultrasonic Stimulation of Mouse Skin Reverses the Healing Delays in Diabetes and Aging by Activation of Rac1", *Journal of Investigative Dermatology*, Elsevier Masson SAS, Vol. 135 No. 11, pp. 2842–2851.

Rosel, D., Khurana, T., Majithia, A., Huang, X., Bhandari, R. and Kimmel, A.R. (2012), "TOR complex 2 (TORC2) in Dictyostelium suppresses phagocytic nutrient capture independently of TORC1-mediated nutrient sensing", *Development*, Vol. 139 No. 5, available at:https://doi.org/10.1242/jcs.077040.

Sadoshima, J. and Izumo, S. (1993), "Mechanical Stretch Rapidly Activates Multiple Signaling Pathways in Cardiac Myocytes: potential involvement of an autocrine/paracrine mechanism", *The EMBO Journal*, Vol. 12 No. 4, pp. 1681–1692.

Sakoh-Nakatogawa, M., Matoba, K., Asai, E., Kirisako, H., Ishii, J., Noda, N.N., Inagaki, F., *et al.* (2013), "Atg12-Atg5 conjugate enhances E2 activity of Atg3 by rearranging its catalytic site", *Nature Structural*

and Molecular Biology, Vol. 20 No. 4, pp. 433–439.

Salminen, A., Kaarniranta, K., Kauppinen, A., Ojala, J., Haapasalo, A., Soininen, H. and Hiltunen, M. (2013), "Impaired autophagy and APP processing in Alzheimer's disease: The potential role of Beclin 1 interactome", *Progress in Neurobiology*, Elsevier Ltd, Vol. 106–107, pp. 33–54.

Salvador, N., Aguado, C., Horst, M. and Knecht, E. (2000), "Import of a Cytosolic Protein into Lysosomes by Chaperone-mediated Autophagy Depends on Its Folding State", *Journal of Biological Chemistry*, Â© 2000 ASBMB. Currently published by Elsevier Inc; originally published by American Society for Biochemistry and Molecular Biology., Vol. 275 No. 35, pp. 27447–27456.

Schuster, S.C., Noegel, A.A., Oehme, F., Gerisch, G. and Simon, M.I. (1996), "The hybrid histidine kinase DokA is part of the osmotic response system of Dictyostelium", *EMBO Journal*, Vol. 15 No. 15, pp. 3880–3889.

Shah, M.R., Wedgwood, S., Czech, L., Kim, G.A., Lakshminrusimha, S., Schumacker, P.T., Steinhorn, R.H., *et al.* (2013), "Cyclic Stretch Induces Inducible Nitric Oxide Synthase and Soluble Guanylate Cyclase in Pulmonary Artery Smooth Muscle Cells", *International Journal of Molecular Sciences*, Vol. 14 No. 2, pp. 4334–4348.

Shaw, R.J. (2009), "LKB1 and AMP-activated protein kinase control of mTOR signalling and growth", *Acta Physiologica*, Vol. 196 No. 1, pp. 65–80.

Sheng, Z., Zhang, S., Bustos, D., Kleinheinz, T., Le Pichon, C.E., Dominguez, S.L., Solanoy, H.O., *et al.* (2012), "Ser1292 autophosphorylation is an indicator of LRRK2 kinase activity and contributes to the cellular effects of PD mutations.", *Science Translational Medicine*, Vol. 4 No. 164, available at:https://doi.org/10.1126/scitranslmed.3004485.

Sigurdson, W.J., Sachs, F. and Diamond, S.L. (1993), "Mechanical perturbation of cultured human endothelial cells causes rapid increases of intracellular calcium", *American Journal of Physiology - Heart and Circulatory Physiology*, Vol. 264 No. 6 33-6, available at:https://doi.org/10.1152/ajpheart.1993.264.6.h1745.

Silveira, L.A., Smith, J.L., Tan, J.L. and Spudich, J.A. (1998), "MLCK-A, an unconventional myosin light chain kinase from Dictyostelium, is activated by a cGMP-dependent pathway", *Proceedings of the National Academy of Sciences of the United States of America*, Vol. 95 No. 22, pp. 13000–13005.

Smith, E.W., Lima, W.C., Charette, S.J. and Cosson, P. (2010), "Effect of starvation on the endocytic pathway in Dictyostelium cells", *Eukaryotic Cell*, Vol. 9 No. 3, pp. 387–392.

Smith, J.L., Silveira, L.A. and Spudich, J.A. (1996), "Activation of Dictyostelium myosin light chain kinase A by phosphorylation of Thr166.", *The EMBO Journal*, Vol. 15 No. 22, pp. 6075–6083.

Sontheimer-Phelps, A., Chou, D.B., Tovaglieri, A., Ferrante, T.C., Duckworth, T., Fadel, C., Frismantas, V., *et*

al. (2020), "Human Colon-on-a-Chip Enables Continuous In Vitro Analysis of Colon Mucus Layer Accumulation and Physiology", *Cellular and Molecular Gastroenterology and Hepatology*, Vol. 9 No. 3, pp. 507–526.

Srivastava, N., Traynor, D., Piel, M., Kabla, A.J. and Kay, R.R. (2020), "Pressure sensing through Piezo channels controls whether cells migrate with blebs or pseudopods", *Proceedings of the National Academy of Sciences of the United States of America*, Vol. 117 No. 5, pp. 2506–2512.

Steinman, D.A. (2000), "Simulated pathline visualization of computed periodic blood flow patterns", *Journal of Biomechanics*, Vol. 33 No. 5, pp. 623–628.

Stürner, E. and Behl, C. (2017), "The Role of the Multifunctional BAG3 Protein in Cellular Protein Quality Control and in Disease", *Frontiers in Molecular Neuroscience*, Vol. 10, available at:https://doi.org/10.3389/fnmol.2017.00177.

Sugio, A., Dreos, R., Aparicio, F. and Maule, A.J. (2009), "The cytosolic protein response as a subcomponent of the wider heat shock response in arabidopsis", *Plant Cell*, Vol. 21 No. 2, pp. 642–654.

Sugiyama, N., Imamura, H. and Ishihama, Y. (2019), "Large-scale Discovery of Substrates of the Human Kinome", *Scientific Reports*, Springer US, Vol. 9 No. 1, pp. 1–12.

Sun, B., Hui, M. and Firtel, R.A. (2003), "Dictyostelium Stress-activated Protein Kinase α, a Novel Stress-activated Mitogen-activated Protein Kinase Kinase Kinase-like Kinase, Is Important for the Proper Regulation of the Cytoskeleton", *Molecular Biology of the Cell*, Vol. 14 No. 11, pp. 4526–4540.

Takizawa, Y., Kosuge, Y., Awaji, H., Tamura, E., Takai, A., Yanai, T., Yamamoto, R., *et al.* (2013), "Up-regulation of endothelial nitric oxide synthase (eNOS), silent mating type information regulation 2 homologue 1 (SIRT1) and autophagy-related genes by repeated treatments with resveratrol in human umbilical vein endothelial cells", *British Journal of Nutrition*, Vol. 110 No. 12, pp. 2150–2155.

Tan, J.L. and Spudich, J.A. (1990), "Dictyostelium myosin light chain kinase. Purification and characterization", *Journal of Biological Chemistry*, Vol. 265 No. 23, pp. 13818–13824.

Tanabe, F., Yone, K., Kawabata, N., Sakakima, H., Matsuda, F., Ishidou, Y., Maeda, S., *et al.* (2011), "Accumulation of p62 in degenerated spinal cord under chronic mechanical compression Functional analysis of p62 and autophagy in hypoxic neuronal cells", *Autophagy*, Vol. 7 No. 12, pp. 1462–1471.

Tanida, I., Sou, Y.S., Ezaki, J., Minematsu-Ikeguchi, N., Ueno, T. and Kominami, E. (2004), "HsAtg4B/HsApg4B/autophagin-1 cleaves the carboxyl termini of three human Atg8 homologues and delipidates microtubule-associated protein light chain 3-and GABA(A) receptor-associated protein-phospholipid conjugates", *Journal of Biological Chemistry*, Vol. 279 No. 35, pp. 36268–36276.

Tanida, I., Tanida-Miyake, E., Ueno, T. and Kominami, E. (2001), "The human homolog of Saccharomyces cerevisiae Apg7p is a protein-activating enzyme for multiple substrates including human Apg12p,

GATE-16, GABARAP, and MAP-LC3", *Journal of Biological Chemistry*, Vol. 276 No. 3, pp. 1701–1706.

Teng, B.T., Pei, X.M., Tam, E.W., Benzie, I.F. and Siu, P.M. (2011), "Opposing responses of apoptosis and autophagy to moderate compression in skeletal muscle", *Acta Physiologica*, Vol. 201 No. 2, pp. 239–254.

Thomason, P.A., Traynor, D., Stock, J.B. and Kay, R.R. (1999), "The RdeA-RegA system, a eukaryotic phospho-relay controlling cAMP breakdown", *Journal of Biological Chemistry*, Vol. 274 No. 39, pp. 27379–27384.

Titus, M.A., Warrick, H.M. and Spudich, J.A. (1989), "Multiple actin-based motor genes in Dictyostelium.", *Cell Regulation*, Vol. 1 No. 1, pp. 55–63.

Trotter, E.W., Kao, C.M.F., Berenfeld, L., Botstein, D., Petsko, G.A. and Gray, J. V. (2002), "Misfolded proteins are competent to mediate a subset of the responses to heat shock in Saccharomyces cerevisiae", *Journal of Biological Chemistry*, Â© 2002 ASBMB. Currently published by Elsevier Inc; originally published by American Society for Biochemistry and Molecular Biology., Vol. 277 No. 47, pp. 44817–44825.

Tsao, P.S., Lewis, N.P., Alpert, S. and Cooke, J.P. (1995), "Exposure to shear stress alters endothelial adhesiveness: Role of nitric oxide", *Circulation*, Vol. 92 No. 12, pp. 3513–3519.

Tung, S.M., Ünal, C., Ley, A., Peña, C., Tunggal, B., Noegel, A.A., Krut, O., *et al.* (2010), "Loss of Dictyostelium ATG9 results in a pleiotropic phenotype affecting growth, development, phagocytosis and clearance and replication of Legionella pneumophila", *Cellular Microbiology*, Vol. 12 No. 6, pp. 765–780.

Urrutia, R.A., Jung, G. and Hammer, J.A. (1993), "The Dictyostelium myosin IE heavy chain gene encodes a truncated isoform that lacks sequences corresponding to the actin binding site in the tail", *BBA - Gene Structure and Expression*, Vol. 1173 No. 2, pp. 225–229.

Vaillancourt, J.P., Lyons, C. and Côté, G.P. (1988), "Identification of two phosphorylated threonines in the tail region of Dictyostelium myosin II.", *The Journal of Biological Chemistry*, Vol. 263 No. 21, pp. 10082–10087.

Veltman, D.M. and van Haastert, P.J.M. (2006), "Guanylyl Cyclase Protein and cGMP Product Independently Control Front and Back of Chemotaxing Dictyostelium Cells", *Molecular Biology of the Cell*, Vol. 17 No. September, pp. 3921–3929.

Veltman, D.M. and van Haastert, P.J.M. (2008), "The role of cGMP and the rear of the cell in Dictyostelium chemotaxis and cell streaming", *Journal of Cell Science*, Vol. 121 No. 1, pp. 120–127.

Vion, A.C., Kheloufi, M., Hammoutene, A., Poisson, J., Lasselin, J., Devue, C., Pic, I., *et al.* (2017), "Autophagy is required for endothelial cell alignment and atheroprotection under physiological blood flow", *Proceedings of the National Academy of Sciences of the United States of America*, Vol. 114 No. 41, pp.

E8675–E8684.

Walczak, M. and Martens, S. (2013), "Dissecting the role of the Atg12-Atg5-Atg16 complex during autophagosome formation", *Autophagy*, Vol. 9 No. 3, pp. 424–425.

Wang, P., Leung, A.W. and Xu, C. (2011), "Low-intensity ultrasound-induced cellular destruction and autophagy of nasopharyngeal carcinoma cells", *Experimental and Therapeutic Medicine*, Vol. 2 No. 5, pp. 849–852.

Wang, R.C., Wei, Y., An, Z., Zou, Z., Xiao, G., Bhagat, G., White, M., *et al.* (2012), "Akt-Mediated Regulation of Autophagy and Tumorigenesis Through Beclin 1 Phosphorylation", *Science*, Vol. 338 No. 6109, pp. 956–959.

Wang, X., Lin, Q., Zhang, T., Wang, X., Cheng, K., Gao, M., Xia, P., *et al.* (2019), "Low-intensity pulsed ultrasound promotes chondrogenesis of mesenchymal stem cells via regulation of autophagy", *Stem Cell Research and Therapy*, Stem Cell Research & Therapy, Vol. 10 No. 41, pp. 1–11.

Wang, X., Liu, Q., Wang, Z., Wang, P., Zhao, P., Zhao, X., Yang, L., *et al.* (2010), "Role of autophagy in sonodynamic therapy-induced cytotoxicity in S180 cells", *Ultrasound in Medicine and Biology*, Vol. 36 No. 11, pp. 1933–1946.

Wang, X., Wang, P., Zhang, K., Su, X., Hou, J. and Liu, Q. (2013), "Initiation of autophagy and apoptosis by sonodynamic therapy in murine leukemia L1210 cells", *Toxicology in Vitro*, Elsevier Ltd, Vol. 27, pp. 1247–1259.

Wang, X., Zhang, Y., Feng, T., Su, G., He, J., Gao, W., Shen, Y., *et al.* (2018), "Fluid shear stress promotes autophagy in hepatocellular carcinoma cells", *International Journal of Biological Sciences*, Vol. 14 No. 10, pp. 1277–1290.

Warboys, C.M., de Luca, A., Amini, N., Luong, L., Duckles, H., Hsiao, S., White, A., *et al.* (2014), "Disturbed Flow Promotes Endothelial Senescence via a p53-Dependent Pathway", *Arteriosclerosis Thrombosis and Vascular Biology*, Vol. 34 No. 5, pp. 985–995.

Weinbaum, S., Cowin, S.C. and Zeng, Y. (1994), "A model for the excitation of osteocytes by mechanical loading-induced bone fluid shear stresses", *Journal of Biomechanics*, Vol. 27 No. 3, pp. 339–360.

West, A.B., Moore, D.J., Biskup, S., Bugayenko, A., Smith, W.W., Ross, C.A., Dawson, V.L., *et al.* (2005), "Parkinson's disease-associated mutations in leucine-rich repeat kinase 2 augment kinase activity", *Proceedings of the National Academy of Sciences of the United States of America*, Vol. 102 No. 46, pp. 16842–16847.

White, E. and DiPaola, R.S. (2009), "The Double-Edged Sword of Autophagy Modulation in Cancer", *Clinical Cancer Research*, Vol. 15 No. 17, pp. 5308–5316.

Wilson, I.D., Neill, S.J. and Hancock, J.T. (2008), "Nitric oxide synthesis and signalling in plants", *Plant, Cell and Environment*, Vol. 31 No. 5, pp. 622–631.

Winslow, A.R., Chen, C.-W., Corrochano, S., Acevedo-Arozena, A., Gordon, D.E., Peden, A.A., Lichtenberg, M., *et al.* (2010), "α-Synuclein impairs macroautophagy: implications for Parkinson's disease", *The Journal of Cell Biology*, Vol. 190 No. 6, pp. 1023–1037.

Wong, Y.C. and Holzbaur, E.L.F. (2014), "The Regulation of Autophagosome Dynamics by Huntingtin and HAP1 Is Disrupted by Expression of Mutant Huntingtin, Leading to Defective Cargo Degradation", *Journal of Neuroscience*, Vol. 34 No. 4, pp. 1293–1305.

Wu, Y., Liu, X., Qin, Z., Hu, L. and Wang, X. (2018), "Low-frequency ultrasound enhances chemotherapy sensitivity and induces autophagy in PTX-resistant PC-3 cells via the endoplasmic reticulum stress-mediated PI3K/Akt/mTOR signaling pathway", *OncoTargets and Therapy*, Vol. 11, pp. 5621–5630.

Xie, Z. and Klionsky, D.J. (2007), "Autophagosome formation: Core machinery and adaptations", *Nature Cell Biology*, Vol. 9 No. 10, pp. 1102–1109.

Yamamoto, A., Tagawa, Y., Yoshimori, T., Moriyama, Y., Masaki, R. and Tashiro, Y. (1998), "Bafilomycin A1 Prevents Maturation of Autophagic Vacuoles by Inhibiting Fusion between Autophagosomes and Lysosomes in Rat Hepatoma Cell Line, H-4-II-E Cells.", *Cell Structure and Function*, Vol. 23 No. 1, pp. 33–42.

Yamamoto, H., Fujioka, Y., Suzuki, S.W., Noshiro, D., Suzuki, H., Kondo-Kakuta, C., Kimura, Y., *et al.* (2016), "The Intrinsically Disordered Protein Atg13 Mediates Supramolecular Assembly of Autophagy Initiation Complexes", *Developmental Cell*, Elsevier Inc., Vol. 38 No. 1, pp. 86–99.

Yan, J., Mihaylov, V., Xu, X., Brzostowski, J.A., Li, H., Liu, L., Veenstra, T.D., *et al.* (2012), "A Gβγ Effector, ElmoE, Transduces GPCR Signaling to the Actin Network during Chemotaxis", *Developmental Cell*, Elsevier Inc., Vol. 22 No. 1, pp. 92–103.

Yang, H., Rudge, D.G., Koos, J.D., Vaidialingam, B., Yang, H.J. and Pavletich, N.P. (2013), "mTOR kinase structure, mechanism and regulation", *Nature*, Nature Publishing Group, Vol. 497 No. 7448, pp. 217–223.

Yang, Z.F. and Klionsky, D.J. (2010), "Eaten alive: a history of macroautophagy", *Nature Cell Biology*, Vol. 12 No. 9, pp. 814–822.

Young, A.R.J., Chan, E.Y.W., Hu, X.W., Köchl, R., Crawshaw, S.G., High, S., Halley, D.W., *et al.* (2006), "Starvation and ULK1-dependent cycling of mammalian Atg9 between the TGN and endosomes", *Journal of Cell Science*, Vol. 119 No. 18, pp. 3888–3900.

Yumura, S., Yoshida, M., Betapudi, V., Licate, L.S., Iwadate, Y., Nagasaki, A., Uyeda, T.Q.P., *et al.* (2005), "Multiple Myosin II Heavy Chain Kinases: Roles in Filament Assembly Control and Proper Cytokinesis in

Dictyostelium", *Molecular Biology of the Cell*, Vol. 16 No. September, pp. 4256–4266.

Zalckvar, E., Berissi, H., Mizrachy, L., Idelchuk, Y., Koren, I., Eisenstein, M., Sabanay, H., *et al.* (2009), "DAP-kinase-mediated phosphorylation on the BH3 domain of beclin 1 promotes dissociation of beclin 1 from Bcl-XL and induction of autophagy", *EMBO Reports*, Vol. 10 No. 3, pp. 285–292.

Zhang, H., Wessels, D., Fey, P., Daniels, K., Chisholm, R.L. and Soll, D.R. (2002), "Phosphorylation of the myosin regulatory light chain plays a role in motility and polarity during Dictyostelium chemotaxis", *Journal of Cell Science*, Vol. 115 No. 8, pp. 1733–1747.

Zhao, Y., Xiong, X., Jia, L. and Sun, Y. (2012), "Targeting Cullin-RING ligases by MLN4924 induces autophagy via modulating the HIF1-REDD1-TSC1-mTORC1-DEPTOR axis", *Cell Death and Disease*, Vol. 3 No. 9, available at:https://doi.org/10.1038/cddis.2012.125.

Zhou, H., Di Palma, S., Preisinger, C., Peng, M., Polat, A.N., Heck, A.J.R. and Mohammed, S. (2013), "Toward a comprehensive characterization of a human cancer cell phosphoproteome", *Journal of Proteome Research*, Vol. 12 No. 1, pp. 260–271.

Zhu, H., Wang, D., Zhang, L., Xie, X., Wu, Y., Liu, Y., Shao, G., *et al.* (2014), "Upregulation of autophagy by hypoxia-inducible factor-1α promotes EMT and metastatic ability of CD133+ pancreatic cancer stem-like cells during intermittent hypoxia", *Oncology Reports*, Vol. 32 No. 3, pp. 935–942.

Zou, R., Wu, S., Wang, Y., Kang, X., Zhao, S., Shi, H., Zheng, D., *et al.* (2021), "Role of integrin-linked kinase in static compressive stress-induced autophagy via phosphatidylinositol 3 kinase in human periodontal ligament cells", *International Journal of Molecular Medicine*, Vol. 48 No. 3, pp. 1–11.